Control of the Long-Range Self-Organization of Polycyclic Aromatic Hydrocarbons for Device Applications

Dissertation zur Erlangung des Grades
"Doktor der Naturwissenschaften"

am Fachbereich Chemie und Pharmazie
der Johannes Gutenberg-Universität in Mainz

Wojciech Pisula

geb. in Cieplice Slaskie Zdroj

Mainz 2005

Tag der mündlichen Prüfung: 28.09.2005

Contents

Index of Abbreviations

AFM	atomic force microscopy
CD	circular dichroism
DSC	differential scanning calorimetry
FET	field-effect transistor
FFT	fast Fourier transformation
g	gram
HBC	hexa-*peri*-hexabenzocoronene
HDMS	hexamethyldisilazane
HOPG	highly oriented pyrolytic graphite
HR-TEM	high-resolution transmission electron microscopy
ITO	indium-tin oxide
LB	Langmuir-Blodgett
LC	liquid crystal
LED	light emitting diode
NMR	nuclear magnetic resonance
POM	polarized optical microscopy
PAH	polycyclic aromatic hydrocarbons
Pc	phthalocyanine
PTFE	poly(tetrafluoroethylene)
THF	tetrahydrofuran
TOF	time-of-flight
UV-Vis	ultraviolet/visible
WAXS	wide-angle X-ray scattering
XRD	X-ray diffraction

Introduction

Nowadays, people are surrounded by a variety of different and complex electronics with integrated circuits which are established in plenty of areas. These electronics are integrated in devices which are of essential importance for our daily life and improve substantially the peoples standard of living. But due to the rapid technological progression and the introduction of novel electronics, our close environment is exposed to permanent changes.

Most of the technology is based on metals and inorganic semiconductors. Undoubtedly, these materials possess excellent conductive properties, but nevertheless other materials with novel properties are intensively investigated which could fulfill the great demand for further device miniaturization on the one hand and allow low cost production of these devices on the other. Following these requirements organic materials appear to be currently the most potential candidates for the partial replacement of metals and silicon in field-effect transistor, light-emitting diodes or photovoltaic devices. Furthermore, organic semiconductors are very promising due to their low cost and their easy processibility. Both academic and industrial research put considerable effort in the investigation of the suitable organic materials for electronic devices. For instance, the number of scientific publications concerning organic compounds exploited in electronic devices increased extremely since the beginning of the 90'ies, whereby many of the reports were placed in high-ranking journals. Recently, Siemens announced the successful construction of a photovoltiac cell based on organic compound with an efficiency of more than five percent being a breakthrough in this field. These two examples should emphasize the great impact of the field of organic semiconductors. Thereby, the most essential parameter is the charge carrier mobility in these materials, which determinates in a high degree the successful application of the compounds.

One can distinguish between two technological progresses; on one hand the ongoing circuits miniaturization leads to molecular devices (*molecular electronics*) which consists of only one single molecule. These devices are characterized by a very high electronic efficiency. For instance, a single carbon nanotube exploited in a FET device showed recently mobilities up to 79,000 cm^2/Vs.[1] This value is significantly higher in comparison to the common MOSFETs (1000 cm^2/Vs) based on the inorganic counterpart silicon.[2] On the other hand there is a great demand of producing cheap electronics (*plastic electronics*) in mass production for one-way use which is not possible by using inorganic materials. For the latter kind of application the electronic performance is secondary, since device mobilities up to 1.0

cm²/Vs are necessary in order to replace amorphous silicon, which is mainly used today in cheap devices.

One concept for the fabrication of low-cost devices is to apply organic materials, consisting of molecules which show the tendency to self-assembly. These molecules which can be regarded as single building blocks, self-organize via specific intermolecular interactions into complex supramolecular structures. One group of this kind of materials is **polycyclic aromatic hydrocarbons (PAHs)** consisting of a planar aromatic core which can be substituted in order to control the bulk properties. Due to π-interactions between the aromatic cores these molecules self-organize into supramolecular columnar structures along which a one-dimensional charge carrier migration takes place. Local charge carrier mobilities of up to 1.1 cm²/Vs for hexa-*peri*-hexabenzocoronene derivatives have been observed making these compounds very promising for practical application.

However, the transfer of these properties into electronic devices is difficult and requires a detailed investigation of adequate processing techniques. In devices the most essential requirement for an undisturbed one-dimensional charge migration along the columns is a high long-range order in the active layer which is deposited between the electrodes. Local defects at domain boundaries in unoriented layers can trap the charge carriers and decrease considerably the device performance leading to significantly lower charge carrier mobilities.

Thus, the development of appropriate processing techniques became an essential challenge for the fabrication of unperturbed long-range oriented organic semiconductors. This close relationship between supramolecular structure and electronic properties has been investigated impressively for thiophene oligomers and polymers or phthaloyanines. However, no breakthrough could be achieved in the design of a processing technique, so that the performance of the devices based on these organic compounds is still under the desired properties for practical application. The most important requirement is surely the fabrication of highly ordered samples resulting in excellent device performance. Today no processing technique could completely satisfy this demand. Vacuum deposition is an exception which however is not in agreement with the next requirement of simplicity in manufacturing and low cost fabrication. An additional need from the industrial point of view is the production of large ordered areas, which is mainly possible by solution processing.

One reason for the general lack of success in processing of organic materials might be the insufficient consideration of the intrinsic behavior of the compounds in solution or in the isotropic phase for the processing procedure. Transfer of knowledge between the synthesis and the final application is only possible by the establishment of a materials scientist as a link which can give a feedback to the supramolecular chemistry. The morphology formation is a

fundamental property for any processing method and their detailed investigation leads to the successful processing of the materials. Moreover, the nucleation and growth ability of compounds, consisting of molecules which self-assemble into superstructures, depends strongly on the degree of interaction between the single building blocks controlled by the molecular design. Therefore, all aspects such as the molecular architecture, the self-assembly into complex supramolecular structures, bulk properties and finally processing conditions have to be considered for a successful implementation of the material in electronic devices.

In this study, the **fundamental understanding** of the relationship between the molecular architecture and the supramolecular organization in various discotic systems based on polycyclic aromatic hydrocarbons plays a key role. Since the supramolecular arrangement of the single building blocks has a great effect on the one-dimensional intrinsic charge carrier mobility and on the device performance, one major objective is the investigation of the intra- and intercolumnar organization of the discotic molecules in bulk dependent on the aromatic core size and the length and architecture of the substituents.

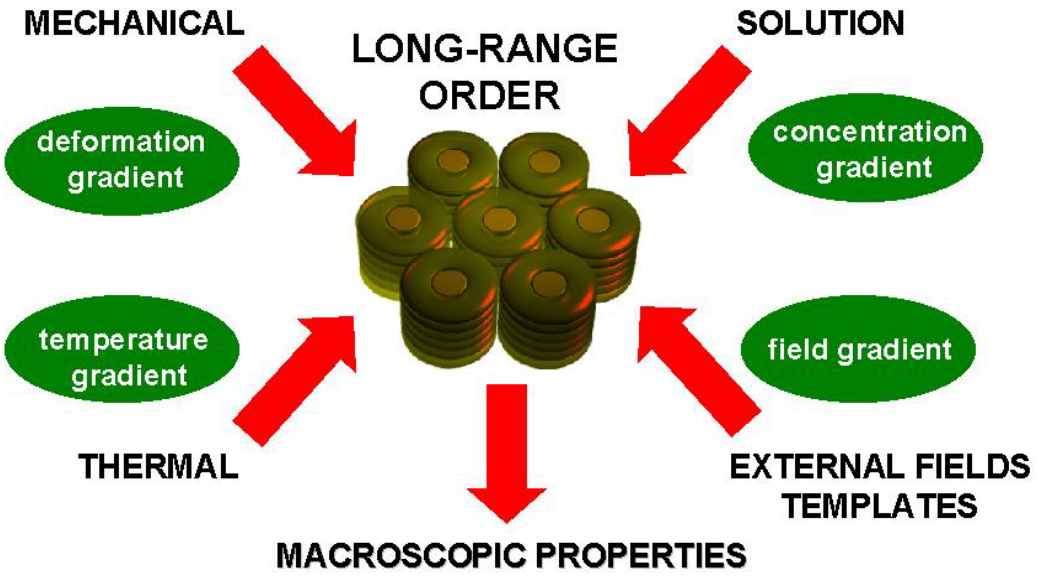

Figure 2.1. *Overview of the different processing techniques by which the long-range order of discotic molecules can be controlled. Each alignment technique is based on a gradient along which the materials are transformed into highly ordered systems within the defined zone.*

Another important subject of this work is the influence of the different substituents on the interaction between molecules and therefore the self-aggregation into the superstructures which is essential for the processibility of the materials from the solution and the isotropic

phase. Therefore, the relationship between the self-aggregation of different discotic derivatives and their morphology formation in both solution processed and crystallized from the isotropic state films is studied. Since the latter processing method requires a low isotropization temperature of the materials, the control of the thermal behavior by using different substituents is a fundamental point. The final major objective in this work is the transfer of the morphology formation in the bulk into the processing from solution or the isotropic phase. Different processing techniques (schematic overview shown in Figure 2.1) have to be developed in strong correlation with the optimal nucleation and growth abilities of the materials in different environments, which are closely connected with the degree of self-aggregation of corresponding materials. Furthermore, it is important to compare the supramolecular structure of the highly oriented systems with the organization in the bulk in order to reveal the most essential processing parameters.

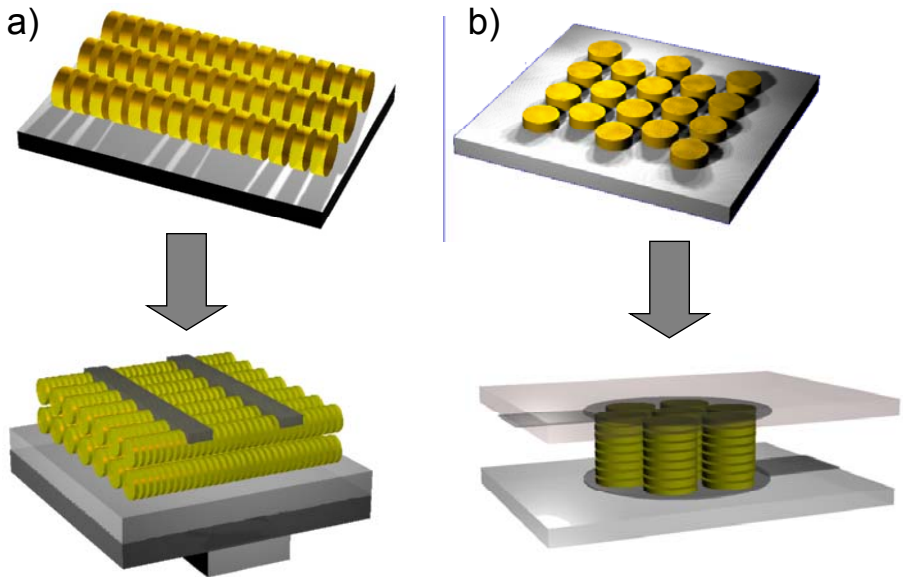

Figure 2.2. *Two characteristic supramolecular organizations of discotic molecules on surfaces; a) the edge-on arrangement with uniaxially oriented columns required for FET devices and b) the molecular face-on organization leading to homeotropic alignment demanded for the design of photovoltaic cells.*

A further point represents the interaction of the molecules during nucleation with polar surface. Discotic molecules can adopt two characteristic supermolecular arrangements which are required for electronic devices with different geometries. In FETs the edge-on arrangement of the molecules is needed (Figure 2.2a) with columns uniaxially oriented and

organized in-plane to the substrate to ensure the charge migration between the electrodes. For this orientation specific alignment techniques are applied by processing the material from solution or the isotropic state. One the other hand, homeotropical alignment is expected to be beneficial for the performance in photovoltaic cells (Figure 2.2b), but requires the processing from the isotropic state. In literature the mechanism leading to this orientation of discotics is not clear. It is claimed that specific chemical units introduced within the side chains can effectively increase the affinity of the molecules towards surfaces; however, the homeotropic alignment has not been studied for all-hydrocarbon discotics as a function of the side chain length. Therefore, a detailed investigation is necessary in order to gain insight into the exact mechanism of the homeotropic orientation for discotic materials.

Chapter 1

Supramolecular Organization of Discotic Liquid Crystals

1.1. Discotic Liquid Crystals

The definition of mesophases was first given by the discoverer, Chandrasekhar,[3] of the discotic liquid crystals 1977 as a state of order between crystals and liquids revealing long-range orientation and imperfect positional order. Two different mesomorphisms were found. Lyotropic phases are formed by dissolving amphiphilic compounds under certain conditions in suitable solvents,[4] whereby thermotropic liquid crystals are formed by heating a solid or cooling an isotropic liquid. Thermotropic mesogens consist of a rigid conjugated aromatic core with flexible side chains. These specific geometries of the molecules such as rods or discs lead to an enhanced packing of the mesogens accompanied by the nanophase separation of the different intramolecular segments and to the formation of the liquid crystalline state.

Liquid crystalline materials can be assigned on the basis of their molecular shape into calamitic mesogens, characterized by the rod-like shape of the molecules, and discotic mesogens, characterized by the disc-like shape of the molecules. Since the discovery of the first discotic molecules, this research field developed immense bringing up a large variety of discotic molecules.[5] The most prominent discotic molecules are presented in Figure 1.1

showing as examples triphenylenes,[6-9] phthalocyanines (Pc),[10-13] porphyrins[14,15] and hexabenzocoronenes (HBCs)[16-18].

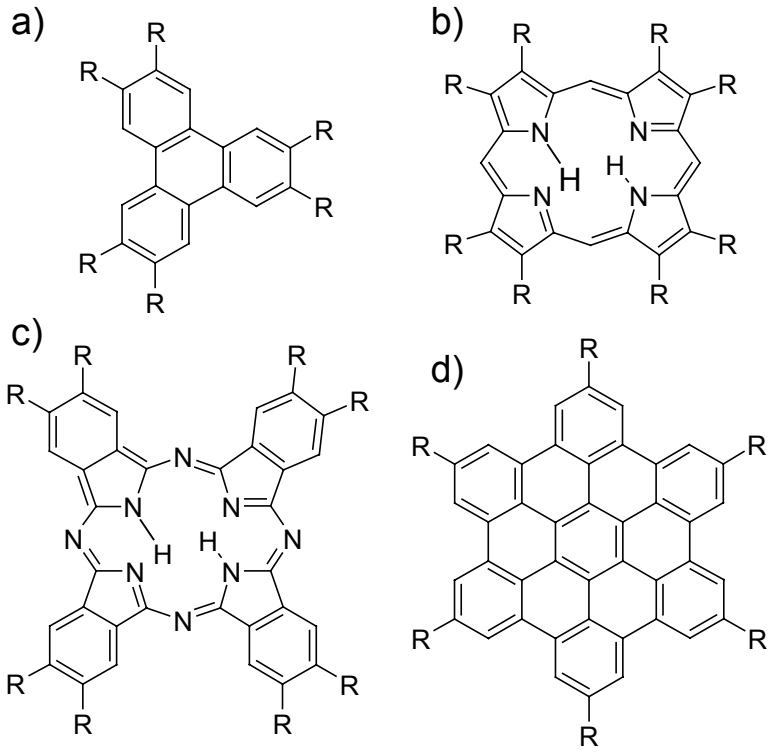

Figure 1.1. *Examples of some of the most prominent discotic liquid crystals such as a) triphenylenes, b) porphyrins, c) phthalocyanines and d) hexabenzocoronenes.*

The discotic molecules consist of a flat and rigid aromatic core peripheral substituted by a different number long alkyl side chains. Today the aromatic core size varies from a simple benzene ring[19] to extended large cores consisting of more than 132 carbon atoms[20] belonging to the class of large polyaromatic hydrocarbons (PAHs).

The main organization types which were found for these disc-like molecules can be divided into columnar, discotic-nematic, columnar-nematic and lamellar (smectic-like) phases, whereby the first organization type is the most common one (Figure 1.2.) The nematic phases reveal an orientationally ordered arrangement of the discs, but no long-range translational order. In the columnar phase the discotic molecules stack one on top of each other into columns which in turn arrange laterally into a two-dimensional unit cell. Thereby, different intercolumnar arrangements are possible which were found by Levelut.[21,22]

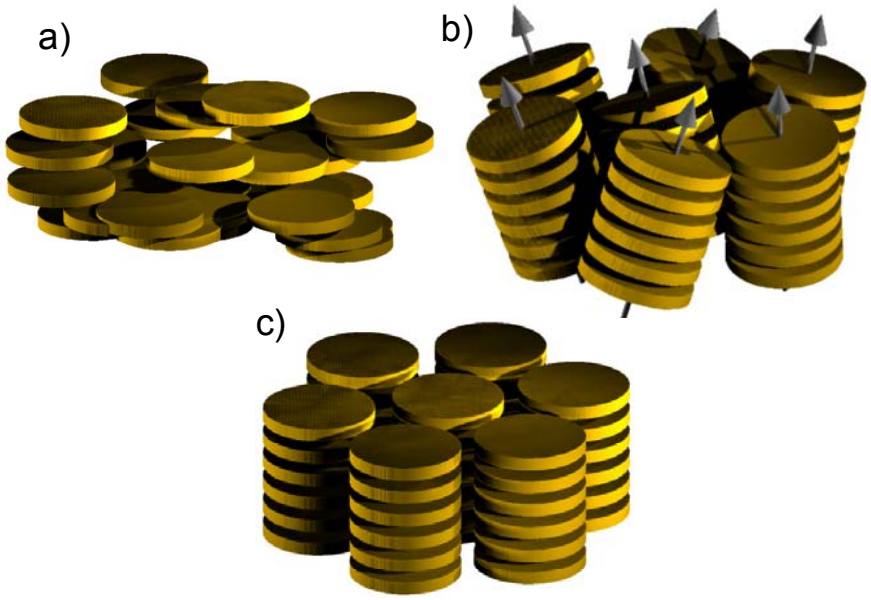

Figure 1.2. *Illustration of the different mesophases of discotic liquid crystals with a) discotic-nematic, b) columnar-nematic and c) columnar arrangement.*

He found that the main columnar structures can be attributed to a hexagonal lattice (Col_h), rectangular lattice (Col_r), or an oblique lattice (Col_{ob}) which are presented in Figure 1.3. During the self-assembling into the columnar structures the intermolecular interactions play a significant role. The main driving force for the columnar self-assembly is the so-called π stacking. When specific side groups are introduced into the side chains, hydrogen bondings can also dominate the intermolecular interaction.[23-25] In same cases these two different interaction forces act cooperatively leading to the formation of more stabilized columnar superstructures.[26-29] The third possible forces are metal coordinations.

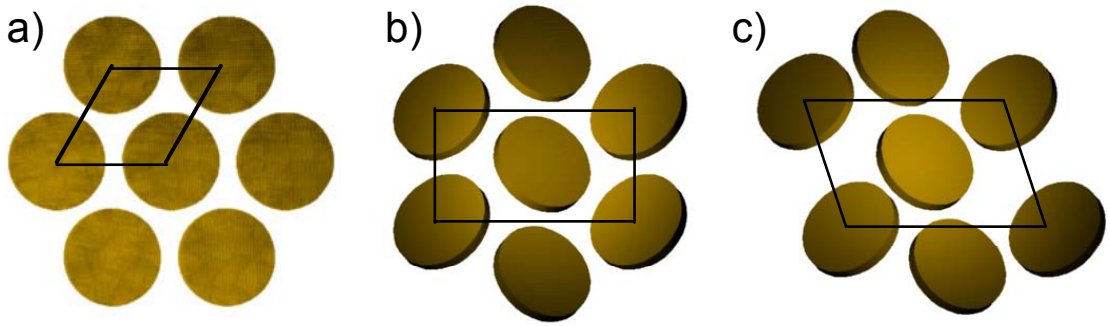

Figure 1.3. *Different two-dimensional intercolumnar arrangements with a) hexagonal (Col_h) lattice, b) rectangular lattice (Col_r) and c) an oblique lattice (Col_{ob}).*

Discotic liquid crystals possess three important phases presented in Figure 1.4. The phases are characterized by the order and the mobility of the molecules. The low temperature phases show higher intracolumnar organization, whereby the side chains are in a disordered state in the core periphery. Typically, due to the packing conditions of the two nanophases and the reduced molecular mobility, the aromatic cores are tilted with respect to the columnar axis as schematically shown in Figure 1.5. In general this phase is assigned as crystalline, what might be not correct in the precise sense. Nevertheless, in order to follow the nomenclature used to assign the different phases for triphenylenes, this term will be used in this study to refer to this higher order phase. The designation "plastic crystalline" distinguishes another low temperature phase also with high structural order, but points out the increase of molecular mobility. Also in the plastic crystalline the molecules can reveal a tilted arrangement.

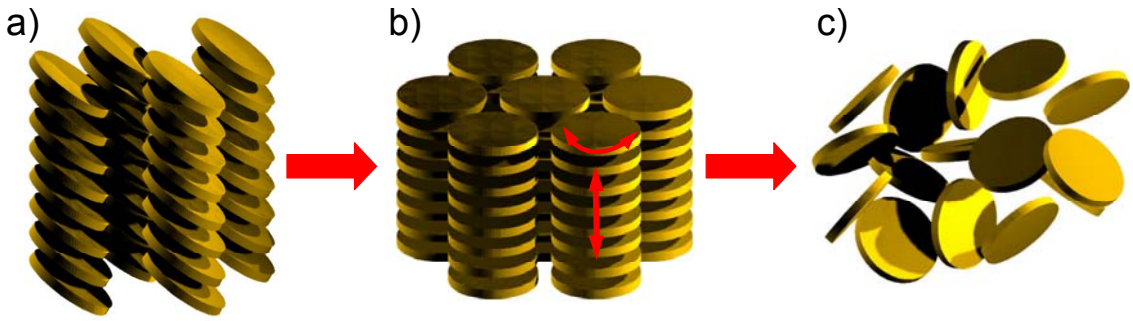

Figure 1.4. *Schematic illustration of the characteristic phases of discotic liquid crystals with a) the crystalline phase at low temperatures, b) the intermediate liquid crystalline state and c) the isotropic phase.*

The phase transition to the liquid crystalline phase is accompanied by a significant increase in molecular mobility such as the rotation of the discs about the columnar axis. Both the intra- and intercolumnar organization changes in comparison to the low temperature phase. The discotic molecules adopt an orthogonal arrangement with parallel cores being perpendicular to the columnar axis. However, due to a higher steric demand of the side chains the interaction between the aromatic cores can be disturbed leading to a disordered columnar phase. This effect is more pronounced at higher temperatures at which the molecular dynamics reaches the maximum value and the steric hindrance of the side chains increases significantly. For symmetrically substituted derivatives a hexagonal columnar organization is characteristic for the mesophase.

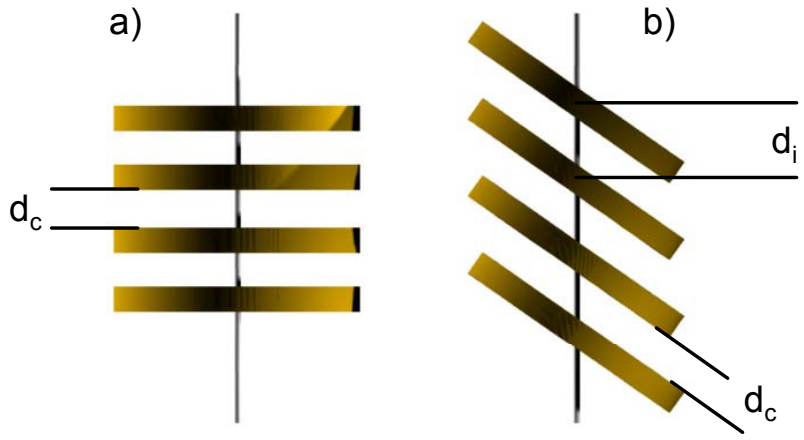

Figure 1.5. *Schematic illustration of the different molecular intracolumnar arrangements with a) the orthogonal organization of the discs and b) the tilted arrangement with respect to the columnar axis. Two distances are characteristic: the cofacial distance (d_c) and the intracolumnar period (d_I) .*

At the transition to the isotropic phase the columnar aggregates break leading to a disordered liquid. The isotropization temperature depends strongly on the steric requirements of the side chains and their influence on the π-π interaction of the aromatic cores. For discotics with larger cores the isotropic phase occurs at usually very high temperatures, which are often even higher than the onset of decomposition.

The thermotropic phase behavior of discotic liquid crystals is usually studied by using differential scanning calorimetry (DSC), polarized optical microscopy (POM), thermogravimetric analysis (TGA), wide-angle X-ray scattering and solid-state nuclear magnetic resonance (NMR). DSC is used to determine the phase temperatures and enthalpy changes related to each transition providing information about the relative change during the phase transitions, whereas by using POM it is possible to assign the type of mesophase due to the appearance of specific birefringence of the corresponding optical textures. The thermal stability is investigated by the TGA which is important for possible thermal processing of the material. The intra- and intercolumnar order and the corresponding packing parameters in each phase can be studied in detail by using X-ray diffraction.[30-32] Furthermore, this method provides information about the change in the supramolecular structure due to thermal treatment or any other processing. Solid-state NMR is one of the most powerful tools for the study of the molecular dynamics.[33,34] By using this method it is possible to distinguish between the dynamics of different intramolecular elements and to derive independent conclusions about the rotation of the core or about the peripheral mobility of side chains. Thus, each phase can be assigned exactly on the basis of the solid-state NMR results.

Moreover, due to different electronic environments of the aromatic protons in the intracolumnar packing, the tilted arrangement of the discs in the solid phase can be determined as well. In general, for the successful materials science dealing with discotic liquid crystals it is necessary to apply these experimental methods complementary in order to gain a full picture about the bulk behavior.

1.2. Mechanism of the Charge Carrier Transport

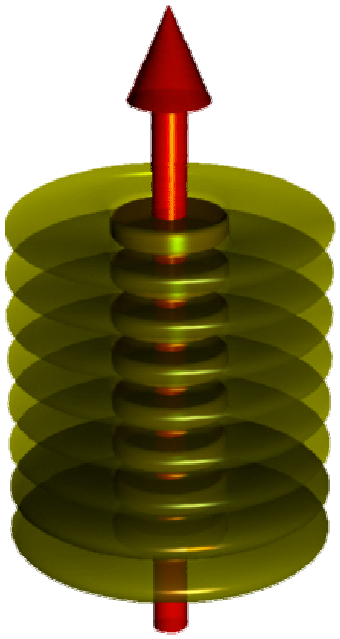

Figure 1.6. *Columnar pathway for charge migration.*

Discotic molecules have extensive molecular π-orbitals in which the electrons are delocalized. Due to the interaction between the π-orbitals of adjacent cores a one-dimensional pathway for charge migration along the columnar structures is possible (Figure 1.6). Thereby, the peripheral substitution of the aromatic cores with long aliphatic hydrocarbon chains provides an insulation of the conducting core. In such cases one can regard these supramolecular structures as "nanowires". The charge transfer takes place via hopping between localized states of neighboring aromatic molecules with assumed jump-time between 75 to 750 fs for HBCs in the mesophase[35] being in an identical range as for phthalocyanines[36]. The main difference between the delocalized, which is characteristic for the hopping in metals, and localized transport is that, in the former, the transport is limited by phonon scattering, whereas in the latter, it is phonon assisted.[37] The localization of the states in organic semiconductors, which leads to lower mobilities, has origins such as weak interactions between the single building blocks and disorder.[38]

A detailed study of the charge transport mechanism in discotic liquid crystalline materials was performed by van de Craats by using the pulse-radiolysis time-resolved microwave conductivity (PR-TRMC) technique.[39] By using this PR-TRMC method it is possible to determine the charge carrier mobility on a nanometre length scale (interface effects caused by electrodes are avoided and electric field effects are minimized), so traps caused by structural defects and impurities are far less disturbing. It is very important to emphasize that the charge carrier mobilities determined by this technique provide different information than techniques such as time-of-flight (TOF)[40-44] or field-effect transistor (FET) experiments. The

PR-TRMC technique reveals only intrinsic or local charge carrier mobilities which migrate only between several molecules, whereas the mobilities in the bulk, which are obtained by the TOF and FET experiments, are usually several orders of magnitude lower due to a higher degree of disorder and possible trapping sites at grain boundaries. These latter values are strongly dependent also on the long-range order of the sample which can be prepared by different processing techniques. The charge carrier mobilities revealed by the PR-TRMC technique can be considered as the maximum possible values. For triphenylenes it was possible to confirm the intrinsic mobility by TOF measurements.[37]

In general, the charge transfer along an ideal conjugated system is more efficient than the charge hopping between neighboring aromatic molecules. Nevertheless, high mobilities up to 1.1 cm^2/Vs at room temperature for the columnar discotics were obtained due to their pronounced self-organization propensity into highly ordered supramolecular structures,[45] which might be considered to be an upper limit attainable for non-covalently-bonded materials.

It was found that the charge carrier mobility in the hexagonal liquid crystalline phase is more dependent on the size of the aromatic core than on the cofacial distance between neighboring cores within the columnar stack.[46] This relationship was explained by the increased π-π interaction in the case of the larger aromatic cores leading to a more stable columnar structure thus increasing the intracolumnar charge transport. The mobility increased from 0.1 cm^2/Vs for triphenylenes[39,47,48] over 0.7 cm^2/Vs for phthalocyanines[49-51] up to 1.0 cm^2/Vs for HBCs,[52] whereby the influence of the chain length on the charge carrier mobility became negligible for discotic compounds with larger aromatic cores.

1.3. Electronic Devices based on Organic Materials

The device geometry of an organic light emitting diode (OLED) is shown schematically in Figure 1.7. The simplest type of an OLED consists of a thin film of an organic emitter is sandwiched between a transparent anode and a metallic cathode. Under an external voltage electrons and holes, which are injected into the lowest unoccupied molecular orbital (LUMO) and highest occupied molecular orbital (HOMO), drift

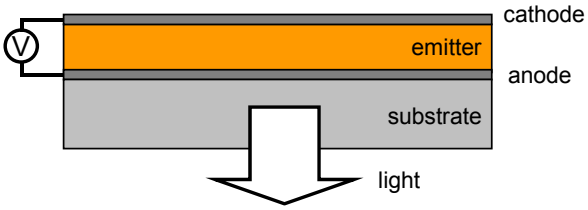

Figure 1.7. *Schematic representation of a single layer organic light emitting diode.*

though the material under the influence of the electric field until they encounter each other and recombine to form an exciton which can emit light.

For an efficient performance of the OLED, discotic liquid crystals have to possess a high charge carrier mobility accompanied with a high fluorescence quantum efficiency. Examples of successfully incorporated discotics in charge transporting/compensating layers have been reported.[53] The fabrication of multilayers OLEDs is performed by expensive techniques such as vapor deposition. Furthermore, another requirement for the design of an OLEDs is the homeotropical alignment of the discotics in order to ensure an unhindered charge transport which occurs due to the device geometry in the direction perpendicular to the substrate.

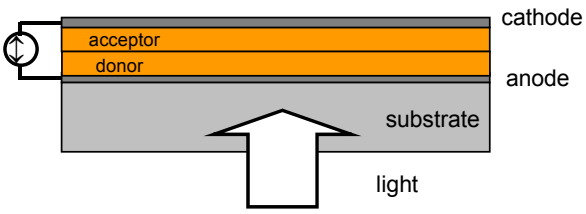

Figure 1.8. *Schematic illustration of an organic photovoltaic cell.*

The device construction of a photovoltaic cells based on organic materials is similar to the OLEDs (Figure 1.8). One way to obtain high efficiency of the photovoltaic device is the blending if two organic compounds with different relative preferences for positive and negative charges. Thereby it is important to increase the interfacial areas between the two materials. The absorbed light photogenerates electron-hole pairs which charge-separated and then transported due to the applied electrical field for collection at the cathode and anode, respectively. The ideal segregation of the acceptor-donor domains into an interpenetrating network seems to be the most desired morphology in photovoltaics ensuring the high charge separation as well as the pathway of charges to the electrodes. Therefore, the most desired organization of the discotic columnar structures is a homeotropical alignment which might enhance the charge migration across the layers and the charge collection.

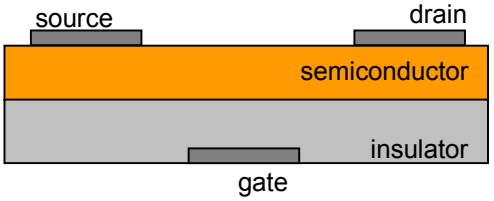

Figure 1.9. *Schematic illustration of a field-effect transistor in the top-contact geometry.*

In Figure 1.9 one typical top-contact FET configuration is shown (the other possible geometry is the bottom-contact). In a FET the current between source and drain contacts depends on the gate voltage. For instance, the accumulation of charges in a hole-transporting semiconductor within the channel between the source and drain occurs when the gate voltage is negative with respect to the source. The variation of the gate voltage allows the control of the charge carrier density in the channel at a given source-to-drain voltage. The efficiency of a

FET is determined by the time which the charge carriers require to drift through the channel. The mobility is strongly dependent on the long-range order of the organic semiconductor exploited between the contacts. Grain boundaries or single defects of unoriented layers can trap the charges and significantly reduce the device performance. In order to attain high mobilities of the discotics materials it is necessary to uniaxially align the columnar structures in the direction of the applied electrical field between the source and drain.

1.4. Homeotropic Alignment

Various device configurations require specific modes of order between the electrodes which are accomplished by different processing techniques. The main charge transport in field-effect transistors takes place parallel to the insulating substrate and therefore requires an edge-on arrangement (schematic illustration in Figure 1.10a) of the discotic molecules with uniaxial columnar orientation in charge transport direction. In general, edge-on arrangement of the molecules results from a minimization of the surface contact of molecules with the substrate of different polarity. But the uniaxial long-range columnar order requires adequate processing techniques which will be presented in the next section.

In contrast, optimized photovoltaic devices or OLEDs require a migration of charges foremost perpendicular to the substrate. Different discotic systems reveal spontaneous face-on arrangement (see Figure 1.10b) inducing macroscopic homeotropic alignment with the columnar axis perpendicular to the substrate. The surface affinity of the molecules can be modified by changing the chemical nature of the aromatic core or of the side chains.[11] During solution processing of alkylated HBC on molybdenum disulfide[12] or highly oriented pyrolitic graphite[13] the interaction between the aromatic core with the surfaces plays an important role during the alignment leading to monolayer formation with molecules lying flat on the substrate. On the other hand, examples of homeotropic alignment from the isotropic state of triphenylenes[14] and phthalocyanines[15] bearing heteroatoms in the side chains imply a strong influence of the substituents on the arrangement of the molecules. This was confirmed for triphenylene derivatives self-assembled in monolayers on gold.[54]It was shown that the discotic molecules could be oriented either face-on or edge-on only depending on the number and position of the tethering points.

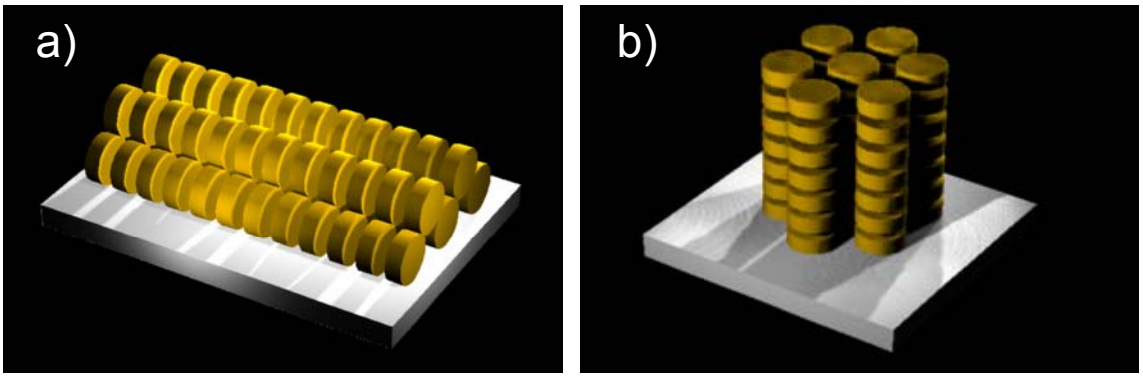

Figure 1.10. *Schematic representation of the different type of supramolecular arrangement on surfaces with a) edge-on orientation of the molecules, where the columnar axis is oriented parallel to the substrate and b) face-on arrangement resulting in homeotropical order.*

Since the homeotropic alignment of these materials takes place only at the liquid – solid phase transition, a low viscosity in the isotropic state is essential to ensure a sufficient molecular mobility. Furthermore, a low temperature of the isotropic phase transition is important for adequate processibility. But it occurs at still too high temperatures for discotic systems based on larger aromatic cores such as alkylated HBC derivatives.[16] A substitution of the HBC core by 3,7,11,15-tetramethylhexadecyl (HBC-$C_{16,4}$) led to an isotropization temperature (T_i) decrease to 231 °C in comparison to the alkylated HBCs with a T_i of 420 °C.[17] The lowered processing temperature allowed homeotropic alignment of this material between two ITO surfaces and the investigation of the relationship between photoconductivity and columnar order. Short circuit photocurrents were 5 times higher at better-ordered regions compared to those in poorly oriented parts. Another efficient way to determine the relationship between the homeotropic orientation and electronic properties are time-of-flight experiments. Thereby, the sample, which is sandwiched between semitransparent electrodes, is illuminated by a short laser pulse which generates charges. Due to an applied electrical field, the generated charges can migrate through the sample to the opposite electrode of the contrary polarity, whereby the transit time is monitored. Until now only TOF examples on aligned triphenylenes have been carried out.[41-44,47,55-57]

1.5. Alignment Techniques

Since the first investigations of FET devices based on organic materials the importance of molecular order within the active layer was realized.[58] Already at that time it was predicted that the increase of the degree of order and orientation would significantly improve the device performance by the reduction of possible trapping sites such as defects and grain boundaries for charge carriers. Indeed, a half decade later the first processing technique was applied for the FET fabrication of the organic semiconductors leading to an increase in performance.[59,60] This triggered an enormous progress in this research field which maintains until today and brings out new device designs with new record values.[38,61] In the following section, which is not restricted to discotic liquid crystals, the main processing techniques discussed in the literature will be presented.

1.5.1. Single Crystal Growth

The fabrication of single crystals is limited to small weight molecules such as perylene, anthracene[62] and rubrene[63] and is connected a high technical effort. On the other hand, single crystals provide atomically perfect structures leading to unique electronic properties in the bulk. The investigation of the electronic transport is thereby not limited to any structural defects and can be undertaken in an extraordinarily detailed manner. Typically the time-of-flight experiments were the only possible way to determine the charge transport in single crystals.[64,65] But recently, the first single-crystal FETs were realized which opened a new type for the study of charge transport in highly ordered molecular systems.[66,67] The application of single-crystal FETs is of high interest because this experimental tool enables the investigation of aspects of charge transport in organic materials that could not be determined in the TOF experiments. One of the important distinctions between these two types of experiments is the magnitude of carrier densities.[62] This is the reason why the progress in this research field has been remarkably rapid, with new record values of carrier mobility for the FETs being achieved like for pentacene up to 3 cm^2/Vs [68](thin film device) and for rubrene (single-crystal) even up to 15 cm^2/Vs,[63] new promising organic materials being introduced, and new device processing techniques being developed.

1.5.2. Vacuum Deposition

Similar to the growth of single crystals the fabrication of highly ordered samples by vacuum deposition is limited to a certain group of materials. The sublimation can take place in

a variety of vacuum deposition systems, utilizing techniques in which the deposition parameters vary widely. In general, the main advantages of this technique are the facile control of the thickness, high purity and high order of the obtained films. Furthermore, the optimal processing parameters can be easily controlled by the monitoring of the deposition rate and the temperature of the substrate. However, similar to the preparation of single crystals the fabrication of highly ordered sample requires also instrumental effort. Furthermore, due to the high application temperature compounds such as polymers or molecules substituted by longer side chains tend to decompose by cracking during the processing. The most prominent examples for the successful preparation of highly ordered surface layers by this technique are small molecules such as pentacene,[69] which holds the highest bulk charge carrier mobility of 1.5 cm^2/Vs for vacuum deposited films, π-conjugated rod-like molecules such as thiophene oligomers[70-72] and unsubstitued disc-shape molecules like phthalocyanine derivatives. For vacuum deposited thin layers of phthalocyanine, the mobility varied between 10^{-4} cm^2/Vs for nickel Pc[73]and 0.02 cm^2/Vs for copper Pc.[74,75] In all cases the large p-conjugation length along the long axis of the molecules and close molecular packing of the molecules along at least one of the short molecular axes lead to π-stacking and to good performance in FETs.

1.5.3. Simple Solution Processing (Spin-Coating, Drop-Casting)

The simple coating of a solution onto a spinning substrate is one of the most elegant ways to realize a homogenous film of an organic material. The only requirement for any processing technique based on solution processing is a sufficient solubility of the organic compound. Therefore, most of the larger molecules have to be substituted by alkyl chains in order to provide the solubility. This technology is believed to have the highest potential impact on manufacturing costs of soluble organic semiconductors. When the spin-coating technique is well handled, it allows the production of very homogeneous films with perfect control of their thickness over relatively large areas. This is in contrast to drop-cast surface layers which are often non-uniform in thickness, morphology, and electrical properties due to an irregular deposition of the material during the solvent evaporation. In general, the film morphology depends strongly on the processing conditions which can be controlled by solution concentration, substrate temperature during casting, solvent choice, and environmental conditions during film drying. The relation between these parameters is very complex for the morphology formation in a drop-cast film. Field-effect measurements were mainly carried out on spin-coat or drop-cast films based on thiophenes oligomers and polymers[76,77] due to simplicity of the morphology control. Molecules with self-assembly

propensity require first a detailed investigation of their self-association in solution in order to understand the morphology formation. Furthermore, the interaction of the molecules with the corresponding surfaces of different properties is extremely important, but also quite complex. This relation has to be regarded for every system separately. For the disc-shaped molecules different molecular arrangements are possible leading to changes in the supramolecular organization and different properties of the surface layers.

1.5.4. Langmuir-Blodgett Technique

An alternative means to produce well-organized thin films is the Langmuir-Blodgett (LB) technique,[78,79] which is one of the most conventional methods of nano-film fabrication allowing fine control of both the structure and thickness of the films. However, the LB technique is in principle restricted to amphiphilic molecules and macromolecules. Monolayers can be fabricated at the air-water interface by lateral compression and deposited onto a solid support by either vertical transfer or a horizontal lift.[80]

The LB technique and its variations have also been explored for the preparation of poly(3-alkylthiophene) FETs.[81-83] The maximum mobility measured from these multilayer LB films was 0.02 cm^2/Vs.[83] Intensive investigations of LB films consisting of planar molecules such as triphenylenes, phthalocyanines and prophyrins[84-91] were also carried out.[92] One essential goal was to obtain highly ordered superstructured surfaces layers and to enhance their stability by the chemical modification of the molecules. In order to obtain the desired organization like a molecular edge-on arrangement on the substrate a hydrophilic side group has to be introduced to the aromatic core which leads to the corresponding arrangement of the discs at the air – water interface. The principle of the processing of discotic molecules by the LB technique is presented in Figure 1.11. Surface spreading pressure isotherm measurements indicated that depending on their architecture, discogenic phthalocyanines typically exhibit one of two possible orientations when placed at the air-water interface. In one case the core lies flat on the water surface and the hydrocarbon chains extend away from the interface leading to the face-on arrangement. This molecular configuration can be achieved if the core of the molecules is capable of hydrogen bonding, and it also maximizes the configuration space available to the aliphatic tails. In the other case the core sits perpendicular to the interface with two or more side chains submerged in the water resulting in the edge-on arrangement. Such a configuration maximizes the π-stacking interactions between the conjugated cores if the molecules are arranged into columns parallel to the water surface forming a two-dimensional columnar phase.

The phthalocyanine ring is rigid, conjugated and hydrophobic and tends therefore to aggregation in face-to-face dimers, at least when the central metallic ion does not bear any bulky axial ligand. Thus, anchoring the phthalocyanine ring parallel to the water surface requires strong polar substituents, either in the center[93-95] or on the periphery[96-99] of the macrocycle.

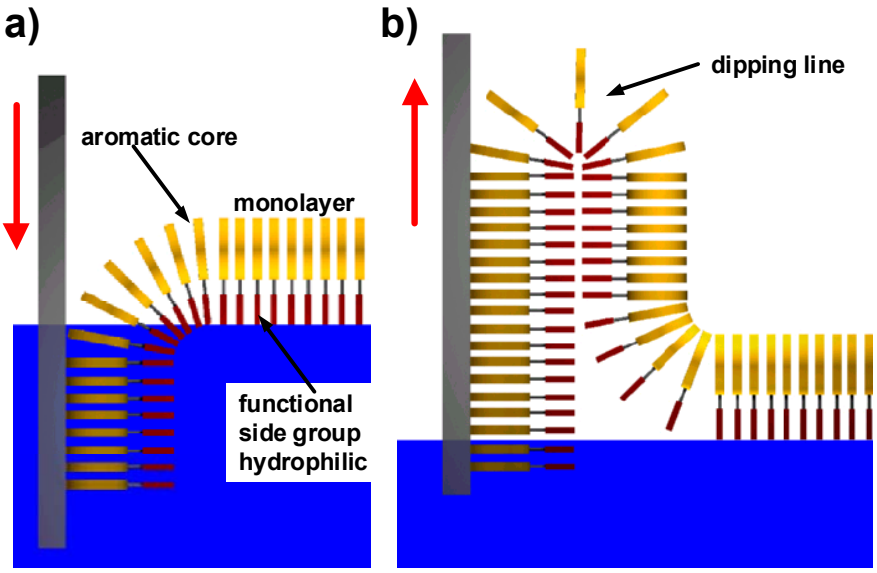

Figure 1.11. *Schematic illustration of the fabrication of the Langmuir-Blodgett films of on the example of discotic molecules onto a substrate with the edge-on arrangement: a) formation of the first monolayer at the substrate surface during the first downstroke dip. A monolayer is formed at the air-water interface with hydrophilic side chains bearing a functional group spread over the water surface with the hydrophilic side groups oriented towards the air and is transferred onto the hydrophobized substrate surface, b) a second molecular layer with opposite orientation of discotic groups is formed on top of the first monolayer during the upstroke mode.*

The orientation obtained from Pc molecules bearing weak polar groups is very difficult to predict, since it results from the competition between the affinity of the polar substituents for the water surface and the aggregation ability of the Pc derivatives. Three different strategies were designed to get edge-on Pc rings in LB films. One way was to use asymmetrically substituted phthalocyanines, which bear strong polar groups only on one part of its core[95,100-105] Another possibility was to prepare LB films from polymeric phthalocyanines such as phthalo-cyaninato-polysiloxanes[106-109] or just rely on fully symmetrical mesogenic phthalocyanines,[110-116] able to form stable columnar assemblies at the air-water interface without any amphiphilic character. Among the latter examples, one exhibits, by far, the best order parameters. The highest charge carrier mobility for the LB

aligned phthalocyanine films was found to be up to 10^{-4} cm²/Vs.[117-121] This is a significantly lower value in comparison to vacuum deposited Pc derivatives. It is suggested than the introduction of flexible side chains, which are required for the LB processing, increase considerably the intracolumnar disorder.

The study of the LB alignment of triphenylene derivatives was not carried out in such intensive manner, as was the case for the above described phthalocyanines and porphyrins. The main work was performed in the early 90ies independently by two different groups, by Ringsdorf and his coworkers[122-124] and on the other side Heiney et al.[125,126] Both groups studied first the edge-on arrangement of asymmetrically substituted amphiphilic triphenylenes and reported later a high uniaxial columnar orientation in the dipping direction.[127-129] In further studies the behavior of triphenylene oligomers and polymers was investigated and a similar edge-on configuration was found as it was the case for the monomers.[130-133] The face-on arrangement of triphenylenes at the air-water surface was not reported.

1.5.5. Epitaxial Growth on PTFE Alignment Layers

A breakthrough in the epitaxial growth of various materials on polymer films, which were pre-oriented, was achieved by Wittmann and Smith by the introduction of friction-deposited poly(tetrafluoroethylene) (PTFE) surface layers.[134] The principle of the preparation technique is schematically illustrated in Figure 1.12. A bar of solid PTFE is moved against a smooth counterface such as glass at a controlled rate and temperature, while applying a controlled pressure. This simple procedure leaves a thin layer of highly oriented PTFE on the glass surface. It was reported that the film thickness of the deposited layer could vary from 2 nm to 100 nm. Structure investigations revealed that the chain axis of the PTFE macromolecules was oriented parallel to the glass surface and along the sliding direction. A single-crystalline order over the whole film could be established. The one of the main advantages of PTFE is its very high melting temperature (340 °C) and excellent resistance against most of the chemicals.

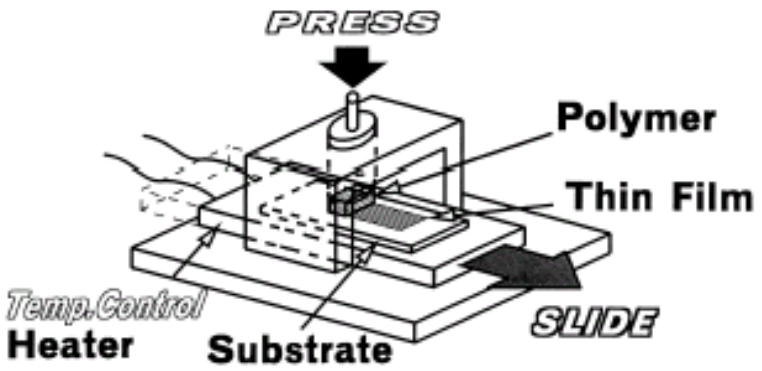

Figure 1.12. *Schematic illustration of the fabrication of the friction-deposited PTFE polymer layers (taken from [135]).*

Wittmann and Smith observed that most of the materials such as polymers, liquid crystals, and small molecules were highly aligned by depositing the substances onto the pre-oriented PTFE layer. Thereby, the high orientation of the molecules was achieved by crystallization from the isotropic state, by casting from solution or by vapor deposition. The orienting capacity of the PTFE layers was explained by the combination of a specific surface topography and a favorable crystal structure.

Besides the investigation of only the crystallization behavior of various polymers[136-141] and small molecules[142-145] on the pre-oriented PTFE films, Wittmann and Smith realized already in their first work the impact of this alignment technique on the fabrication of electronic devices based of organic materials. The successful alignment of small molecules such as sexithiophene,[146-150] pentacene[151] and phthalocyanine derivatives,[152-154] which were all vacuum sublimated, opened the possibility of the exploitation in FETs. Mobilities up to 0.25 cm²/Vs for pentacene and 0.023 cm²/Vs for phthalocyanines were observed.[155] Recently, polymers such as poly(3-alkylthiophene)s semiconductors were oriented on the PTFE layers revealing a hole mobility along the drawing direction which was enhanced by a factor of 25 compared with that of spin-coated films.[156-158]Besides the alignment of classical liquid crystals,[159-163] examples for the processing of discotic liquid crystal are rare. The alignment of triphenylene is the only case, next to the one of HBC which will discussed more in detail later, for a PTFE aligned discotic molecule.[164]

The discotic liquid crystal was based on 2-hydroxy-3,6,7,10,11-penta-(1-butoxy)triphenylene, which was derivatized with 1-adamantenecarboxylic acid (Ada-PBT) and 10-undecenoic acid (ˆ-undecenoyl-PBT), respectively. By spin-coating this material onto the PTFE orientation layer a uniaxial in-plane alignment of columns along the orientation

direction was determined from the high optical anisotropy observed in polarized optical microscopy and absorption. Annealing of the films at higher temperatures at which the material was in its hexagonal mesophase even increased the degree of orientation.

Recently, it was shown that polyimide is an alternative material to PTFE for the utilization as a pre-oriented polymer layer.[165-167] Moreover, it was shown that the dioctylfluorene-bithiophene copolymer (F8T2), which is a nematic liquid crystalline conjugated polymer semiconductor, can be preferentially oriented by rubbed polyimide layers, and when used as the active channel in FETs it exhibits a mobility of 0.02 cm^2/Vs and an on/off ratio of 10^5.[168,169]

1.5.6. Alignment from the Isotropic Phase

The natural nucleation and growth influence to a great extent the morphology and structure of a material and are dependent on the change of the temperature within the time scale. The solidification of the material from the isotropic phase is characterized by its crystallization kinetics. It is also known that the temperature gradient leads to anisotropic spherulite shapes and affects the directions of spherulite growth. The growth takes place along a temperature gradient (change of the temperature along a defined distance), being normal to the growth front. Lovinger was the first who applied this technique for the investigation of the crystallization of poly(ethyleneoxide) at steady conditions.[170] This concept was afterwards also applied for other polymeric systems.[171,172] The changes in interspherulitic boundary shapes have also been reported. Recently, it was shown that the temperature gradient could accelerate the conversion of the melt into spherulites. An identical technique is applied for the alignment of inorganic crystals at surfaces.[173,174]

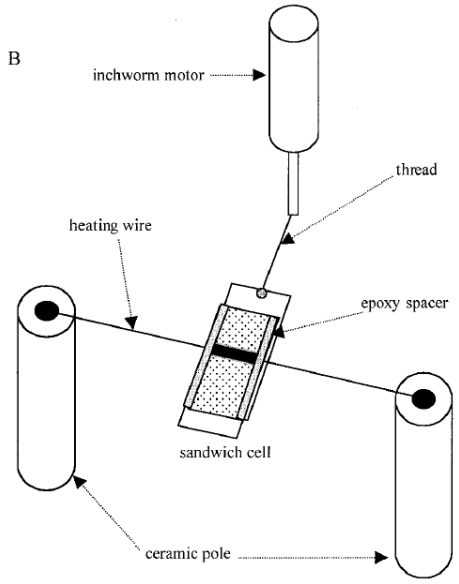

Figure 1.13. *Schematic illustration of the zone-melting apparatus applied by Bard et al.*[174]

Bard and his coworkers picked up this technique to fabricate highly oriented films based on porphyrin derivatives.[175] They used a home-build device which is schematically shown in Figure 1.13. This zone-melting technique was based on an electrically heated wire which generated a narrow molten zone on the organic

layer sandwiched between two pieces of glass. When the molten zone was moved slowly across the layer from one end of the sample to the other, it was reported that a single-crystal film was produced after a single pass. An additional effect was the significant improvement of the purity of the materials due to the zone-refinement effect. After this treatment, the steady-state short-circuit photocurrent was improved by several orders of magnitude.

1.5.7. Alignment from Solution along a Concentration Gradient

The first time this processing technique was applied in the early 80ies in order to align polycarbonate films doped with a tetrathiotetracene-tetracyanoquinodimethane complex. At optimum conditions a high alignment was observed which was characterized by the high anisotropy in electrical conductivity up to 10^8.[176] Later similar results were made for the alignment of poly(ethylene) and polypropylene.[177] The zone-casting technique will be discussed more in detailed concerning the alignment of discotic materials. The principle of this technique was also used by another group which applied a slightly changed device in order to distribute latex particles into a two-dimensional array onto a glass surface.[178,179]

1.6. Alignment of HBC molecules

The general synthetic route for six-fold alkyl substituted HBC is presented in Figure 1.14a. First, the cyclotrimerization of 4,4´-diphenylacetylene in the presence of dicobalt octacarbonyl yields the hexaphenylbenzol. It should be noted that diphenylacetylene can be obtained by different ways. Afterwards the cyclodehydrogenation reaction of the hexaphenylbenzo gives the desired product. The synthesis of asymmetrically substituted HBC derivatives requires another route which is presented in Figure 1.14b. Thereby, 2,3,4,5-tetraarylcyclopenta-2,4-dien-1-one, which is the product of a double Knoevenagel condensation between a 4,4'-substituted benzil and a 1,3-diarylacetone, is transformed by the Diels-Alder reaction into the hexaphenylbenzene.

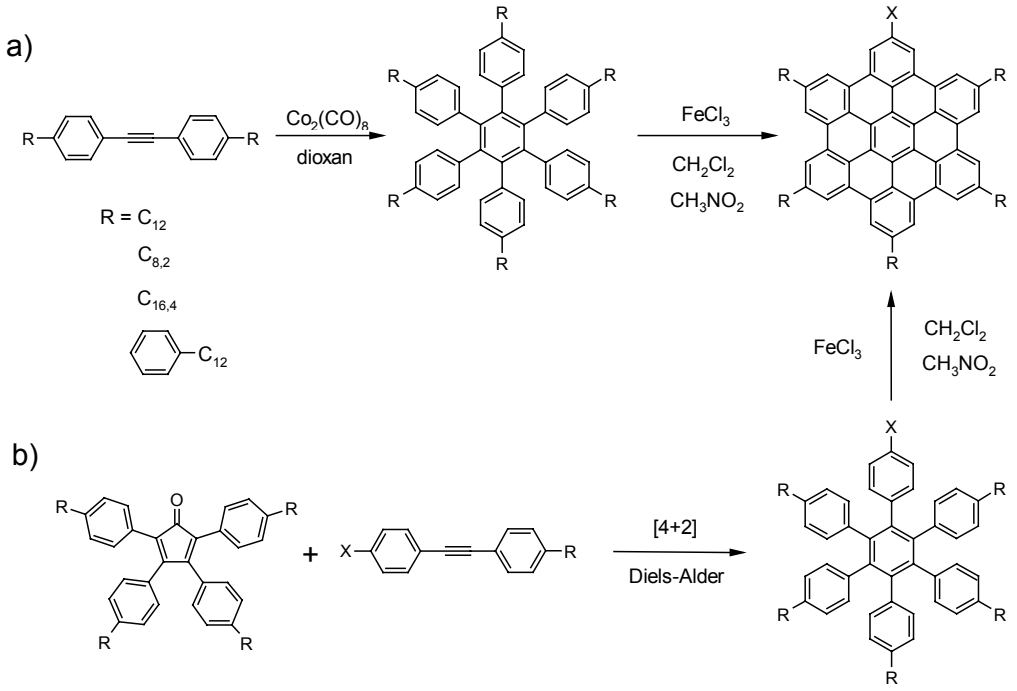

Figure 1.14. *General synthetic route for a) six-fold substituted and b) asymmetrical hexa-peri-hexaenzocoronene derivatives.*

The history of discotic liquid crystalline hexa-*peri*-hexabenzocoronene (HBC) derivatives as semiconductors is significantly shorter than that of phthalocyanines, porphyrins and triphenylenes. Therefore, only few different alignment techniques were applied to enhance the supramolecular alignment of different HBC derivatives.

The most frequently applied method was the LB technique which is currently well established for the orientation of HBCs. Similar to the above described counterparts, HBC molecules were also asymmetrically substituted (first terminated by a carboxylic acid group) leading to the desired amphiphilic character.[180] The molecules formed well-defined LB films when spread from a solution at the air-water interface. Grazing-incidence X-ray diffraction and X-ray reflectivity studies of the LB monolayer revealed two crystallographic phases at room temperature which depended on the surface pressure applied to the film. Amphiphilic HBC molecules were also prepared by the LB technique on poly(ethylene imine) functionalized silicon wafers acting as an anchor point for the first layer.[181-183] A macroscopic in-plane orientation of the columns with their main axis parallel to the dipping direction was determined by polarized UV-vis spectroscopy.

A further enhancement in the fabrication of LB films was the introduction of a polar anthraquinone group as an electron acceptor moiety.[184] It was shown that these amphiphilic

HBCs formed well-defined Langmuir monolayers at the air-water interface, with a π-stacked columnar structure where the HBC cores were rotated around the surface normal and tilted relative to the water surface. The HBCs were confined to form a layer lying on top of the layer of polar groups that were in contact with the water subphase. Efficient transfer of the monolayer of the anthraquinone-substituted HBC derivative to hydrophobic quartz substrates by vertical dipping gave well-defined multilayer films. Thermal processing by simple heating the films resulted in an irreversible rearrangement to a single macroscopically aligned phase of hexagonally packed columns oriented along the dipping direction with disk planes perpendicular to the columnar axes and stacked in a cofacial manner.

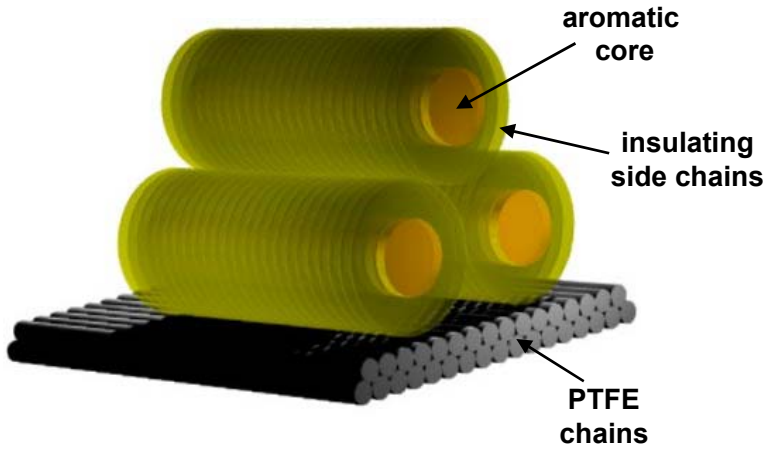

Figure 1.15. *Schematic illustration of the aligned HBC molecules on the friction-deposited PTFE layer.*

The alignment of the friction-deposited PTFE film was another technique which was successfully used for other materials and was then applied to obtain oriented HBC layers. Thereby, the discotic HBC materials were cast from solution and the solvent slowly evaporated. Indeed, this method yielded well-aligned films based on the HBC derivatives and the structure evaluation revealed a parallel orientation of the columnar stacks underlying PTFE chains (as in Figure 1.15 presented).[185,186] Furthermore, the epitaxial organization of the 2D unit cell of the HBC molecules fitted with a certain number of the PTFE chains as Wittmann had predicated for a successful alignment.[187] The exploitation in a FET of these aligned HBC layers showed promising device performance with mobilities up to $5x10^{-3}$ cm^2/Vs and a high anisotropy in conductivity with maximum value obtained for the direction along the columnar alignment.

As described above, it is very difficult to control the morphology and structure in a spin-coated surface layer. However, it was shown that when a mixture of HBC and perylene

diimide (PDI) is spin-coated from solution, a controlled phase separation was obtained which produces vertical layers of both compounds separated by a rough interface.[188-190] Moreover, these multilayers revealed a very high efficiency when incorporated into a photovoltaic cell with an external quantum efficiencies as high as 34% at a wavelength of ~ 490 nm. This high efficiency was explained by the large surface contact area between the materials and the absence of charge trapping 'islands'. Therefore, the performance of the HBC derivative in photovoltaic cells was significantly more efficient than their liquid crystalline phthalocyanine counterparts which resulted in photovoltaics with low efficiency, probably due to poor alignment of the liquid crystal. [191,192]

Chapter 2

Materials and Alignment Techniques

2.1. Materials

The materials investigated in this work were all provided by the Müllen group at the Max-Planck Institute for Polymer Research in Mainz.

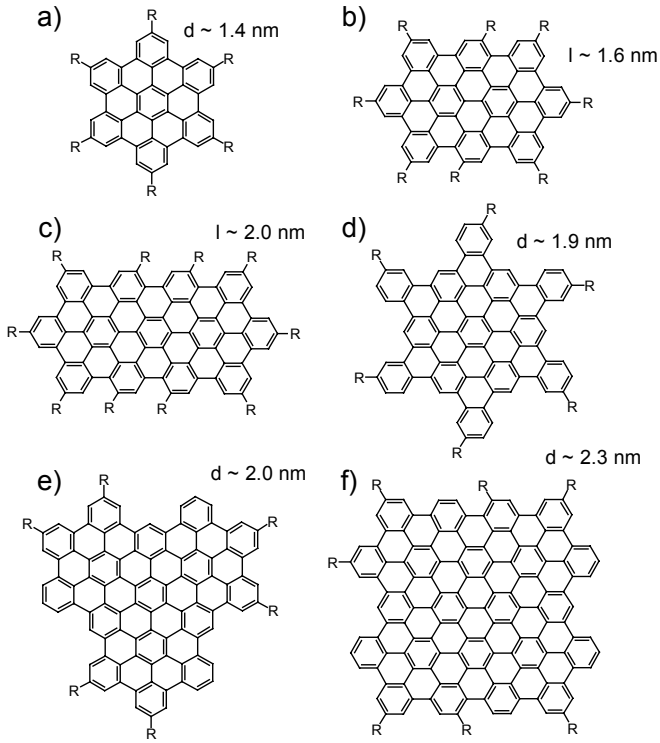

Figure 2.1. *Chemical structures of the investigated polycyclic aromatic hydrocarbons with different core sizes, a) HBC (C42),[20] b) C60, c) C78, d) C78-Star, e) C96[21] and f) C132.*

For this study the size of the polycyclic aromatic hydrocarbons (PAHs) were varied from the hexa-peri-hexabenzocoronene (HBC) core to the extended aromatic core consisting of 132 carbon atoms, whereby the HBC derivatives were the most intensively investigated compounds. Since the IUPAC nomenclature is very complex for derivatives with a core larger than 42 carbon atoms, the PAHs are assigned by the number of carbon atoms. The chemical structures of the different PAHs are presented in Figure 2.1. These unsubstituted graphite sheets are planar discs which do not show solubility. The isotropization temperature is far above the investigated temperature range.

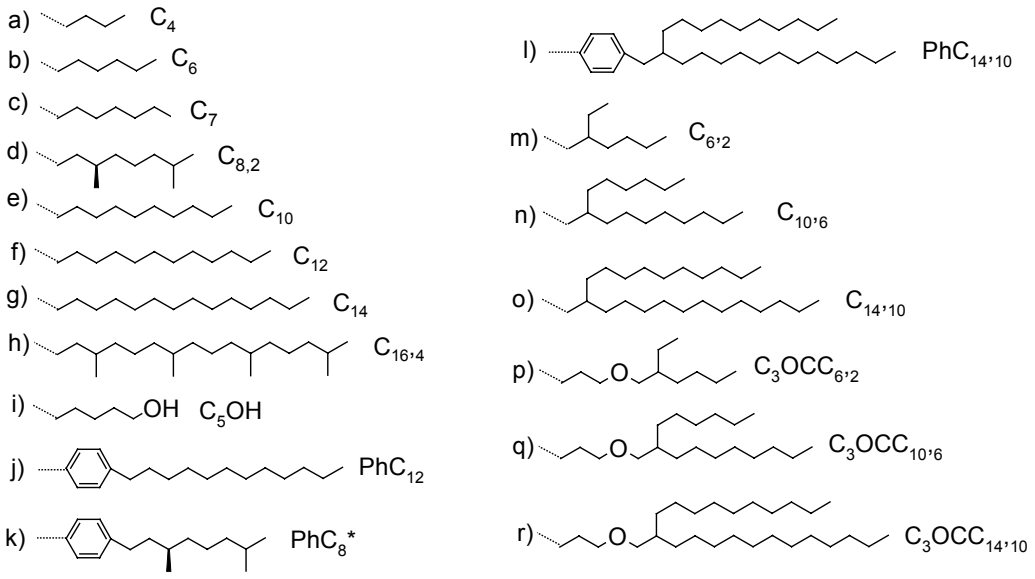

Figure 2.2. *Structures of different side chains used for the symmetrical substitution of the aromatic cores. The alkyl chains are described by the number of carbon atoms. The branched chains are labeled in a separate way.*

In order to control the supramolecular organization and the bulk properties such as solubility and thermal behavior of these materials, the substitution of the aromatic core by various substituents such as alkyl chains bearing for instance functionalized groups play a fundamental role in the molecular design of the single building blocks. Therefore, the influence of various alkyl chains of different length and mass distribution were evaluated. Figure 2.2 shows the different side chains which were symmetrically attached to the aromatic cores, whereby in most of the cases the HBC core was used. The side chains were characterized also by the number of carbon atoms. The branched chains are assigned in an additional way.

An additional tool in the tuning the properties of the self-assembly molecules is the asymmetrical substitution of the aromatic core. The chemical structures of these PAHs are presented explicitly in the following (Figures 2.3 and 2.4). Additionally, perylene, terrylene and quaterrylene diimide derivatives were investigated as pure materials and in blends with other HBC derivatives (Figure 2.5).

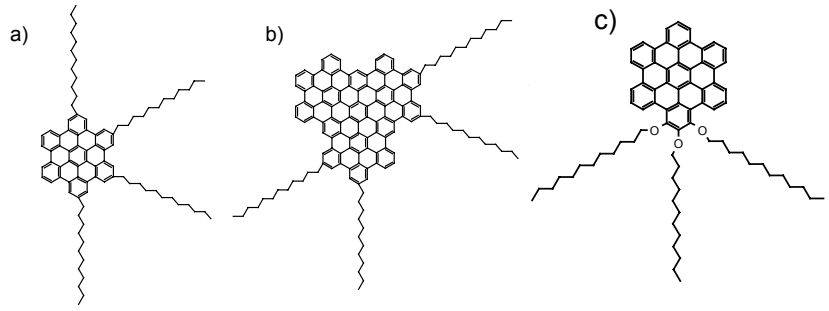

Figure 2.3. *Chemical structures of a) HBC-$(C_{12})_4$, b) C96 -$(C_{12})_4$ and c) trialkoxy HBC-$(OC_{12})_3$.*

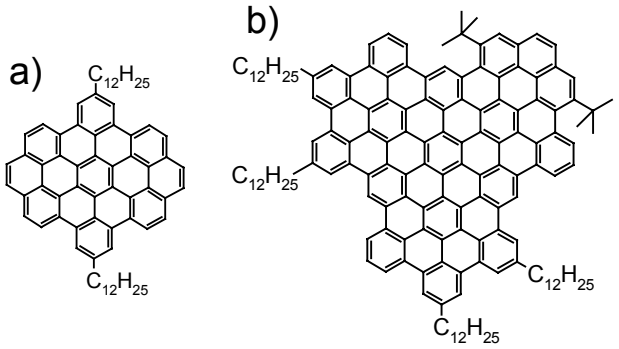

Figure 2.4. *Chemical structure of a) C46-$(C_{12})_2$ and b) C98-$(C_{12})_4(^tBu)_2$.*

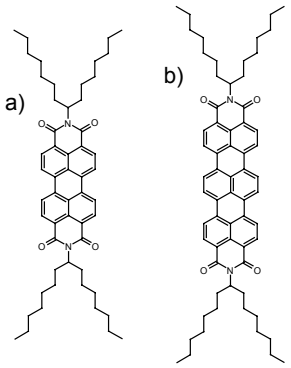

Figure 2.5. *Chemical structures of a) N,N'-Di(1-Heptyloctylperylene-3,4:11,12-tetracarboxdiimide (PDI) and b) N,N'-Di(1-Heptyloctyl)terrylene-3,4:11,12-tetracarboxdiimide (TDI).*

Since not each PAH was substituted by the same side chains all investigated compounds are listed in Table 2.1.

Table 2.1. *Summery of all investigated compounds in this study.*

Sample	C core	C side chain	f	Reference
HBC	42	0	6	
HBC-C_4	42	4	6	
HBC-C_6	42	6	6	
HBC-$C_{8,2}$	42	10	6	[193]
HBC-C_{10}	42	10	6	[194]
HBC-C_{12}	42	12	6	[194]
HBC-C_{14}	42	14	6	[194]
HBC-$C_{16,4}$	42	20	6	[195]
HBC-$(C_{12})_4$	42	12	4	[196]
HBC-PhC_{12}	42	18	6	[197]
HBC-PhC_8*	42	16	6	[198]
HBC-$PhC_{14,10}$	42	30	6	[199]
HBC-$C_{6,2}$	42	8	6	[200]
HBC-$C_{10,6}$	42	16	6	[200]
HBC-$C_{14,10}$	42	24	6	[200]
HBC-$C_3OCC_{6,2}$	42	11	6	[201]
HBC-$C_3OCC_{10,6}$	42	20	6	[201]
HBC-$C_3OCC_{14,10}$	42	28	6	[201]
HBC-C_5OH	42	5	6	[196]
unwrapped HBC-$(OC_{12})_3$	42	12	3	[202]
C46-$(C_{12})_2$	46	12	2	[196]
C60-$C_{8,2}$	60	10	8	[203]
C60-C_{12}	60	12	8	[203]
C78-C_{12}	78	12	10	[204]
C78-Star-$C_{16,4}$	78	20	6	[204]
C96	96	0	6	[205]
C96-C_7	96	7	6	[205]
C96-$C_{8,2}$	96	10	6	[205]
C96-C_{12}	96	12	6	[205]
C96-$C_{16,4}$	96	20	6	[205]
C96-$(C_{12})_4$	96	12	4	[206]
C96-$C_{14,10}$	96	24	6	[206]
C98-$(C_{12})_4(^tBu)_2$	98	12	4	[206]
C132-C_{10}	132	10	8	[204]
C132-$C_{16,4}$	132	20	8	[204]
PDI	24	16	2	[207]
TDI	34	16	2	[207]

2.2. Zone Processing Methods

The morphology and structure formation of each material is determined by its natural nucleation and growth which are dependent on parameters changed during the time (Figure 2.6a). The principle of the zone processing methods is based on the knowledge obtained from the investigation of the structure formation. Thereby, the temperature, deformation rate or solvent concentration are changed within a defined zone resulting in a parameter gradient which is the driving force for the directed growth. The raw material is moved along this processing gradient with a certain velocity (Figure 2.6b). The optimal processing parameters depend strongly on the natural nucleation and directed growth of the material which is simultaneously a limitation for these processing techniques. In the following work, it will be shown that only materials with a directed growth ability can be aligned by these techniques.

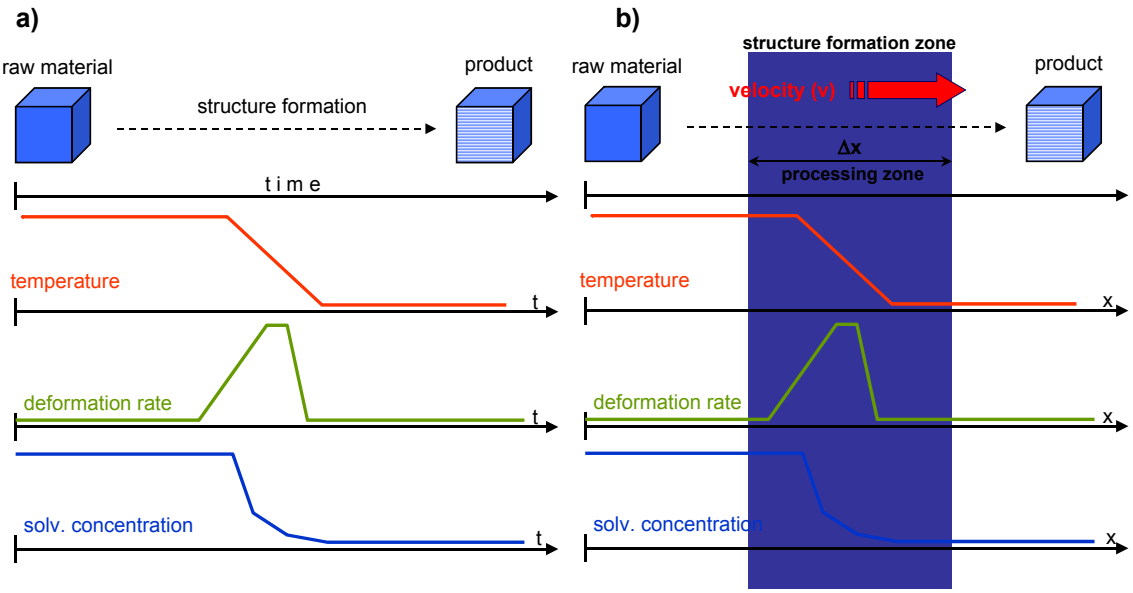

Figure 2.6. *a) Structure formation during natural nucleation and growth determined by the change of the parameters in time, b) concept of the zone-casting where the operating parameters are changed within a defined zone resulting in a processing gradient. The different label of the axes in each case should be noted.*

The innovation of this concept is the great simplicity. As it was mentioned in the introduction, the exploitation and the development of low cost electronics is based on an efficient performance of the used material, but also on the easy fabrication of the devices. To the knowledge of the author, up to now there is no processing technique for organic semiconductors described in literature which could satisfy the requirement of efficiency and simplicity simultaneously.

It should again be mentioned that the processing techniques described in this work were occasional reported by different groups. However, this is *the first time* that the whole principle is recovered and discussed in great detail to transfer the processing on a whole group of materials, alkyl substituted PAHs, with regard to the practical application of these materials in devices.

2.2.1. Filament Extrusion

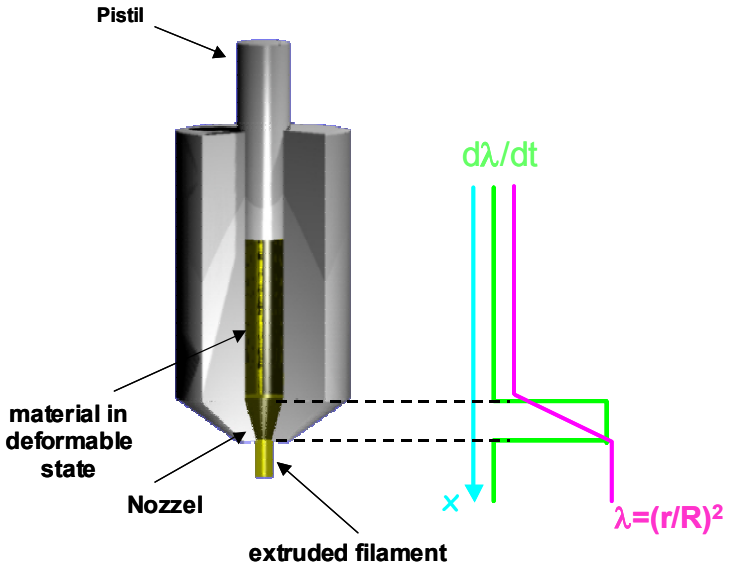

Figure 2.7. *Schematic representation of the filament alignment by extrusion using a mini-extruder. The maximum shear forces act at the contraction of the nozzle.*

Shear-induced alignment of liquid crystalline materials is quite known and was studied mainly during rheology experiments.[208-211] For this work the samples were prepared by filament extrusion using a home-built mini-extruder which is presented schematically in Figure 2.7. Therein, the material is heated up to a phase at which it becomes plastically deformable and is extruded as thin filament by a constant-rate motion of the piston along the cylinder. This mechanical processing is controlled by a number of parameters: the velocity of the piston, diameters of cylinder and orifice and the die shape. The ratio of the cylinder to orifice diameters defines the macroscopic draw ratio ($\lambda = (R/r)^2$) and the shape of the die defines the drawing rate profile. In the case of the conical die, as in the example shown in Figure 2.7, the drawing rate is constant within the die and is zero within the cylinder and at the die orifice. In the extruder used, the cylinder had an inner diameter of 2.0 mm and the orifice diameter was 0.7 mm. In this way, 0.7 mm thick filaments drawn to nearly λ=8 were obtained. The piston has been moved typically with the rate of 5 mm/s which resulted in a

high drawing rate within the die ($d\lambda/dt=20/s.$).

The X-ray diffraction experiments revealed that under such conditions the columns are in all cases well oriented in the direction of the extrusion. No effect of drawing rate on the structure could be detected.

2.2.2. Zone-casting

The principle of the zone-casting technique is based on observations performed during the solvent evaporation of a drop-cast solution. One can observe, that the deposited material is mainly oriented in the direction of the solvent evaporation. Theoretically, at adequate conditions it should be possible to obtain from simple drop-casting a homogeneous film with a radial alignment of the superstructure. However, this is quite difficult, since the concentration within the solution drop changes with ongoing evaporation of the solvent and material precipitation. Therefore, it is not possible to achieve stationary conditions and a homogenous film morphology by drop-casting. At close inspection of the drop-cast layer, one can notice that most of the material is deposited at the rim of the coffee spot, whereas the film interior is poor of material. Practically, before the investigation of the optimal zone-casting conditions, first it is important to study the film morphology from solution prepared by drop-casting by using different concentrations, different solvents (differing in the evaporation temperature) and casting temperatures. These findings are essential for the application of the appropriate processing parameters.

For the orientation of large ordered areas without the application of additional alignment layers it was necessary to find a processing technique based on solution processing that could work at stationary conditions for a sufficient long processing time. The casting process, which is based on the findings from drop-casting, should be carried out directly on the desired substrate. The logical consequence was the development of the zone-casting technique which ensured a simple stationary processing of highly ordered surface layers.

The principle of this technique is presented in Figure 2.8a. A solution is spread out by means of a nozzle onto a moving support such as glass or silicon. Thereby, a meniscus is formed between the nozzle and the support. During the solvent evaporation, a concentration gradient adjusts within the meniscus. When the critical concentration is attained, the material begins to precipitate or to nucleate from the solution and then crystallizes directionally onto the moving support forming in this way the aligned thin layer. The film morphology can be controlled by the processing parameters which were e.g. the evaporation temperature and

polarity of the solvent, concentration, temperatures of the heating blocks, solvent flow, substrate velocity etc. The optimized zone-casting conditions depend strongly on the solution behavior of the material. In the case of π-stacking molecules, such as the alkyl substituted PAHs, the solubility depends strongly on the self-aggregation. The relation between the zone-casting processing and the solution aggregation will be discussed more in detail in Chapter 4.

Figure 2b illustrates schematically the concentration within the meniscus as a function of the distance within the deposition zone. The model shows that with the attained critical concentration within the solidification zone, the concentration increases rapidly until the solidification on the support is reached.

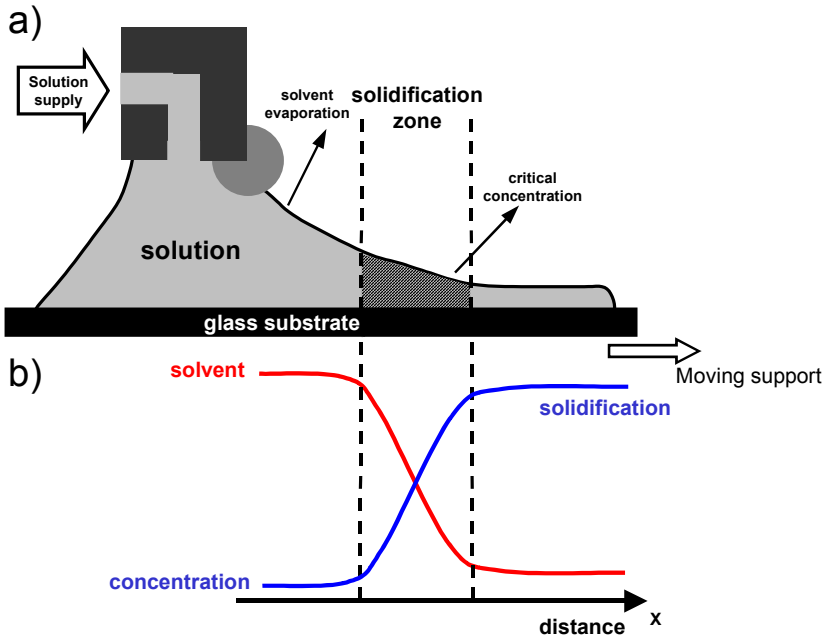

Figure 2.8. *a) Schematic illustration of the principle of the zone-casting technique with b) the concentration and solidification plot as a function of the distance within the meniscus. The solidification zone in which the material deposition takes place is emphasized within the meniscus.*

The zone-casting apparatus is constructed in a strong collaboration with Dr. Adam Tracz from the Centre of Molecular and Macromolecular Studies, Polish Academy of Sciences, Lodz (Poland) and home-build in the Max-Planck Institute for Polymer Research in Mainz.

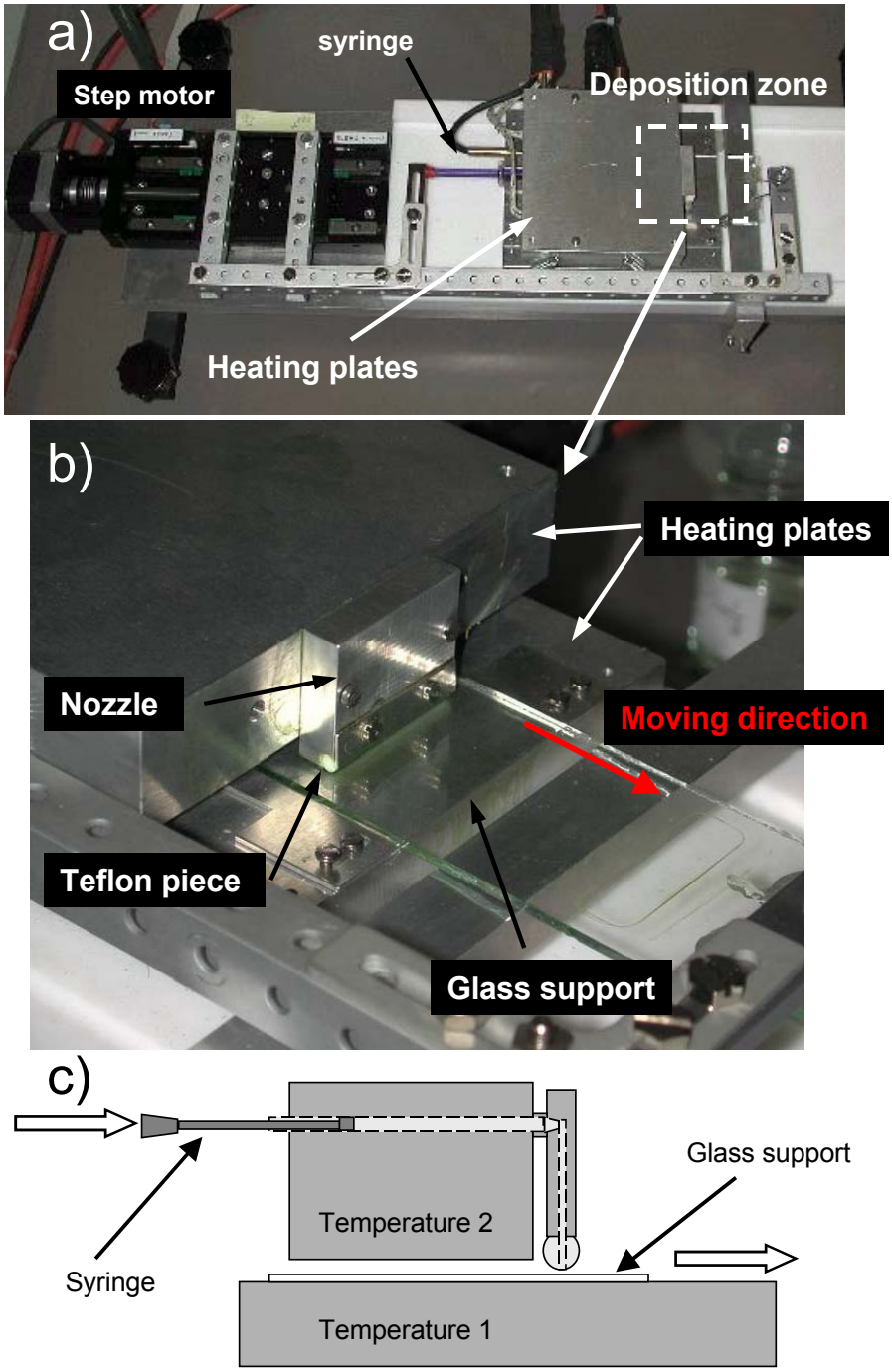

Figure 2.9. *a) The home-build zone-casting device in reality (the set-up here is shown with only one step motor, whereas the experiments were performed by using two motors), b) the deposition zone with the specially designed nozzle (the moving direction of the support is indicate by the red arrow), c) schematic presentation of the zone-casting set-up with the two heating blocks, which can be controlled individually, the syringe placed in the upper block (heated to the temperature T_2) and the support is positioned on the bottom block (at T_1).*

The apparatus, which is shown in Figure 2.9, consists of two heating blocks and two step motors, whereby the second one was additionally introduced. By using only one step motor the support velocity was dependent on the equilibrium conditions between the solution flow and the evaporation of the solvent, which ideally should be equal. This limited the number of variable parameters extremely. By using two motors it is now possible to drive the support independent from the solution supply and solvent evaporation which are then only dependent on the applied temperature of the heating blocks.

A syringe of 1 ml volume filled with the solution is placed into the upper heating block, whereas the support, on which the material is deposited, is positioned on the lower block. Both blocks are thermally controlled independently from each other. In order to form a meniscus between the nozzle and the support, it has been found that the temperature of the upper block has to be higher or equal than that of the lower block. In generally, a fluid tends to flow in the direction of the lower temperature. The solution flow was controlled by the step motor which was pressing out over a bridging construction the solution from the syringe at a constant flow. The flow rate was determined by using the syringe volume and the required time. The other motor was moving the support at a controlled speed under the nozzle. Under appropriate rates of the solvent evaporation and the solution supply, a stationary gradient of concentration is formed within the meniscus. The nozzle consisted of a metal block and a Teflon piece which ensured a homogeneous distribution of the solvent onto the support over the whole nozzle width (which was ca 3 mm). The distance between the nozzle and the support, which also regulated the size of the meniscus and therefore the evaporation area, was controlled by using different spacers. Furthermore, it was important to position the nozzle exactly parallel to the support in order to ensure a uniform film thickness.

Generally, the size or length of the surface layer prepared by the zone-casting processing is only restricted to the limited volume of the applied syringe. Theoretically, it is possible to zone-cast film of unlimited length, as long as the conditions are not changed during the process.

2.2.3. Zone-crystallization

For the alignment of the material from the isotropic phase along a temperature gradient, a home-build zone-crystallization device was used, consisting of two heating blocks which independently could be thermally controlled. The set-up of the device is shown schematically in Figure 2.10a. During the process, the sample was moved at a controlled velocity from a heating block with temperature T_1, at which the material was at the isotropic state, to a cooled

block with a lower temperature T_2, lower than the crystallization temperature. The intermediate distance of the blocks was 3 mm, in which the crystallization took place.

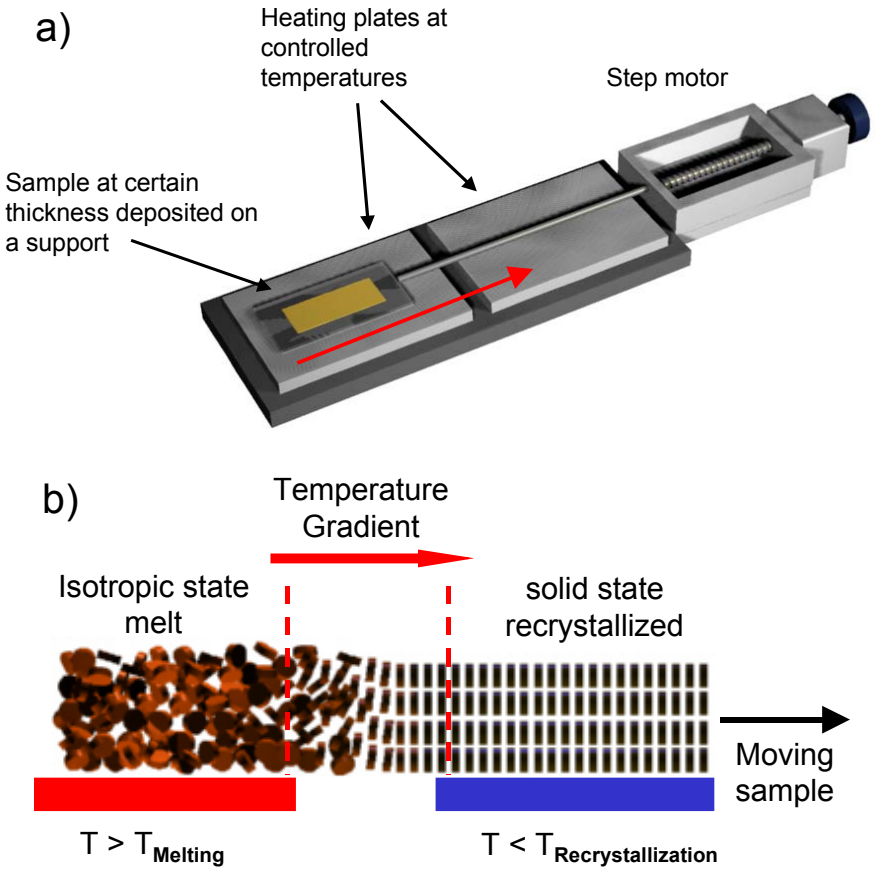

Figure 2.10. a) *Schematic presentation a) of the zone-crystallization apparatus and b) of zone-crystallization process, whereby the HBC molecules are illustrated as simple discs.*

The processing conditions depend mainly on the crystallization kinetics of the material. The model of the crystallization process of the material based on the discotic molecules is displayed in Figure 2.10b. On the plate heated above the isotropization temperature of the material the molecules does not reveal any order. When the sample is moved gradually from the heating plate above the gap, a nucleation center initiated the crystallization and thus the growth of the material. At optimized conditions, which can be controlled by the temperatures of the heating plates, by the temperature difference and the gap size between the two plates, by the velocity of the moving support and by the film thickness, only one nucleation point appears from which the unhindered growth takes place in the direction of the temperature gradient. In the case of columnar self-assembly, first a molecules arrange in the nucleation center at which the columnar growth continuities.

Chapter 3

Relation between the Molecular Architecture and the Supramolecular Organization in Bulk

The understanding about the relation between the molecular architecture of the single building blocks and the resulting supramolecular structure is of essential importance for the application of discotic systems based on polycyclic aromatic hydrocarbons in electronic devices. Since the supramolecular arrangement has a great effect on the one-dimensional intrinsic charge carrier mobility and on the device performance, one major objective is the investigation of the bulk intra- and intercolumnar organization of the discotic molecules in dependence of the design of the aromatic core and the substituents.

3.1. Relationship between Core Size, Side Chain Length and the Supramolecular Organization in the Hexagonal Mesophase

In this section the structural study of a broad spectrum of discotic compounds, which are substituted by linear side chains, is presented. The core size is varied from the HBC core consisting of 42 carbon atoms up to a large aromatic core of 132 carbon atoms. The longest substituted side chain consisted of 20 carbons, whereas plain HBC and C96 cores were also studied. The large number of materials studied, as listed in Table 3.1, reasonably covers the whole range of the possible architectures and related range of volume fractions of the constituents.

Table 3.1. *Summery of the investigated compounds, given are the chemical composition, thermal behavior, intercolumnar packing parameters for the hexagonal phase and intracolumnar cofacial distance.*

Sample	C core	C side	f	Transition temperatures [°C]	$a_{(hex)}$ [nm]	d [nm]
HBC	42	0	6	not observed	1.28	0.342
HBC-C_4	42	4	6	not observed	1.85	0.347
HBC-C_6	42	6	6	not observed	2.20	0.353
HBC-$C_{8,2}$	42	10	6	(Cr) 81 (Col_h) ~ 420 (I)	2.64	0.361
HBC-C_{10}	42	10	6	(Cr) 124 (Col_{ho}) ~420 (I)	2.63	0.362
HBC-C_{12}	42	12	6	(Cr) 107 (Col_{ho}) ~420 (I)	2.83	0.363
HBC-C_{14}	42	14	6	(Cr) 114 (Col_{ho}) ~420 (I)	3.02	0.360
HBC-$C_{16,4}$	42	20	6	(Col_p) -36 (Col_{ho}) 231 (I)	3.37	0.370
HBC-$(C_{12})_4$	42	12	4	(Col_p) 146 (Col_{ho})	2.52	0.354
C60-$C_{8,2}$	60	10	8	(Cr) 109 (Col_{ho})	2.74	0.372
C60-C_{12}	60	12	8	(Cr) 104 (Col_{ho}) >450 (I)	3.13	0.376
C78-C_{12}	78	12	10	(Cr) 87 (Col_{ho}) >450 (I)	3.25	0.394
C78-Star-$C_{16,4}$	78	20	6	not observed	3.78	0.342
C96	96	0	6	not observed	2.0	0.343
C96-C_7	96	7	6	not observed	2.75	0.346
C96-$C_{8,2}$	96	10	6	not observed	3.09	0.344
C96-C_{12}	96	12	6	38 (no change in structure)	3.35	0.343
C96-$C_{16,4}$	96	20	6	not observed	3.91	0.344
C96-$(C_{12})_4$	96	12	4	not observed	3.47	0.347/0.462*
C96-$C_{14,10}$	96	24	6	not observed	3.47	0.36/0.471*
C132-C_{10}	132	10	8	not observed	3.32	0.351
C132-$C_{16,4}$	132	20	8	not observed	4.19	0.354

Cr – crystalline phase
Col_p – plastic phase
Col_{ho} – hexagonal ordered mesophase
*) d (tilted) / period along the column

Figure 3.1 presents examples of 2D-WAXS patterns characteristic for the mesophase of discotics consisting of different core sizes and different substituents. The distinct meridional and equatorial reflections indicate a pronounced order within the extruded filaments. The meridional reflections corresponding to the intracolumnar correlations resulting from the π-stacking of the molecules imply the orthogonal arrangement of the discs to the columnar axis

in all analyzed cases. The equatorial reflection distribution can be fitted to a lateral 2D unit cell which characterizes the intercolumnar organization. The characteristic 2D hexagonal lattice was assigned for all systems being in the mesophase. In most cases, such a structure was indicated by the typical peak positions of $1:\sqrt{3}:2:\sqrt{7}$, whereby the proportions of intensities at various positions were system dependent. An explanation of this effect is briefly discussed in the Appendix where the scattering effects from the hexagonal columnar arrangement are considered as being dependent on the core size and the volume fraction of the side chain phase i.e. the parameters which have been varied in a broad range in the studied samples. It is pointed out in the Appendix that a disappearance or weakness of higher order reflections must not necessarily be correlated with the range and degree of the columnar order but can also result from specific volume ratios between aromatic columns and the peripheral side chains.

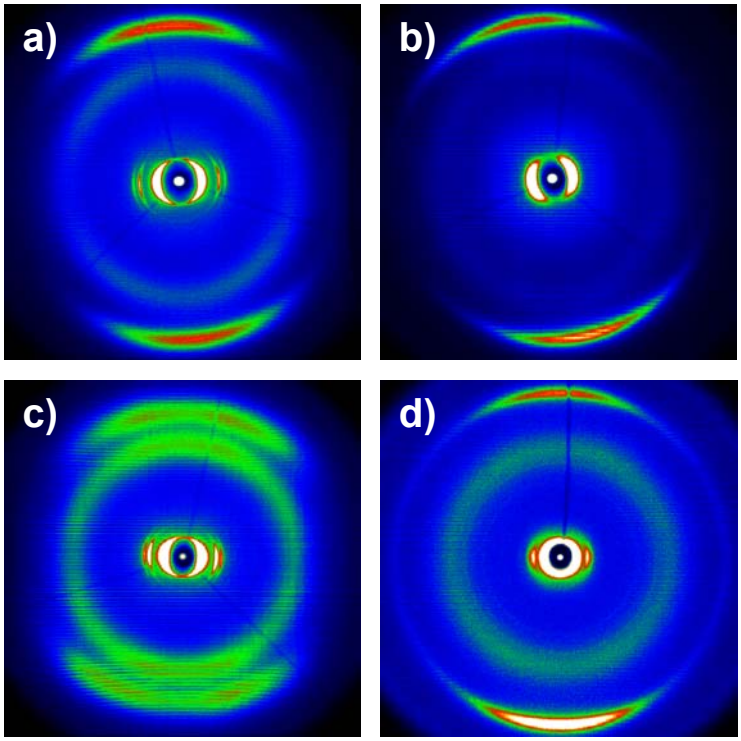

Figure 3.1. *Characteristic 2D-WAXS patterns of a) HBC-$(C_{10})_6$, b) C96-$(C_7)_6$, a) C60-$(C_{12})_8$ and C78-Star-$C_{16,4}$; all compounds were heated to the mesophase.*

The effects of the variation of the architectural parameters, such as the side chain length and the aromatic core size, of the discotic molecules on the scattering intensity distributions are illustrated in Figures 3.2 and 3.4. As an example, the scattered intensity distributions, averaged over the azimuthal angle, shown in Figure 3.2 illustrate impressively the relation

between the side chain length and the parameters of the lateral packing of columns for different HBC derivatives. The intensity distributions are plotted as a function of the scattering vector s (defined as $s = 2\sin\theta/\lambda$, where 2θ is the scattering angle). The results show a shift of the reflections to lower s values with increasing side chain length. This shift can be correlated to increasing unit cell parameters which expand from 2.69 nm determined for HBC-C_{10} to 3.37 nm found for HBC-$C_{16,4}$.

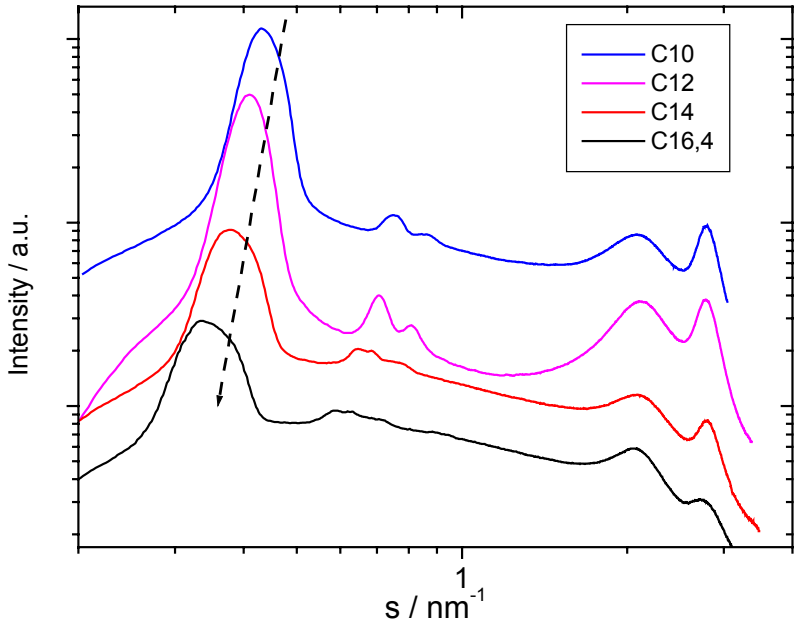

Figure 3.2. *Intensity distribution as a function of the scattering vector for HBC derivatives substituted by side chains of different length.*

However, differences in the degree of the intracolumnar order for HBCs substituted by side chains of different length were obvious. One can differentiate between a disordered and an ordered intracolumnar packing of the discs. As examples for both packing possibilities, characteristic 2D-WAXS patterns of HBC-$C_{16,4}$ and HBC-C_{10} are presented in order to clarify the difference.

The temperature-dependent 2D-WAXS measurements of the HBC-$C_{16,4}$ extruded filament are shown in Figure 3.3. A hexagonal intercolumnar organization was observed over the whole temperature range, whereby the unit cell parameters varied slightly from 2.89 nm in the low temperature phase at –100 °C, to 3.27 nm at room temperature up to 3.34 nm at 150 °C. In contrast to the columnar arrangement, the intracolumnar order of the molecules revealed more pronounced differences in the investigated temperatures. For the low

temperature phase a disc tilting with respect to the columnar axes was assigned due to the appearance of a distinct meridional reflection related to the intracolumnar period of 0.47 nm, rather than due to the very weak off-meridional reflection peaks. Therefore, this low temperature phase was attributed to the plastic crystalline state due to this characteristic supramolecular order and the pronounced plastic deformation of the material. At room temperature the HBC-$C_{16,4}$ compound revealed a very waxy consistence and the extruded filament is almost transparent.

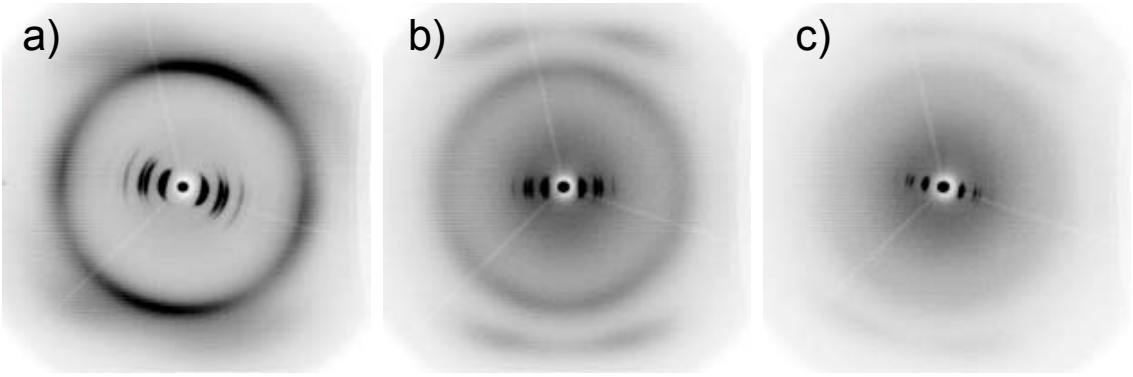

Figure 3.3. *Temperature-dependent 2D-WAXS measurements of filament extruded HBC-$C_{16,4}$ at a) –100 °C, b) room temperature and c) at 150 °C.*

At room temperature the compound was assigned to the disordered columnar phase due to the weak intensity of the meridional reflections. Moreover, the molecules do not change their arrangement to the typical orthogonal intracolumnar order for a liquid crystalline phase, but remained slightly tilted. At higher temperatures these meridional reflection disappear almost completely. It can be assumed that the high steric demand of the bulky side chains hindered a close approach of the aromatic cores to each other leading to a decrease of the intracolumnar order which was indicated by the diffuse meridional reflections.

In contrast to the disordered intracolumnar arrangement in the mesophase, HBC-C_{10} revealed an ordered packing of the discotic molecule. In Figure 3.3a a characteristic 2D-WAXS pattern of this compound for the mesophase is shown. Thereby, the distinct meridional reflections indicate a considerably higher correlation between the discs in comparison to the organization of the HBC-$C_{16,4}$ molecules due to a lower steric hindrance of the relatively short C_{10} alkyl chains.

While the lateral organization of columns is strongly dependent on the substituents the intracolumnar period in the mesophase remains in the typical range between 0.34 nm and 0.37 nm for the investigated HBC derivatives, whereby the value increases slightly with increasing

side chains length. This difference of the intracolumnar dimensions can be correlated with the increase of the steric requirements of longer side chains which hinder a closer approach of the aromatic cores. Additionally, a characteristic amorphous halo was observed for each HBC compound at a correlation distance of 0.46 nm.

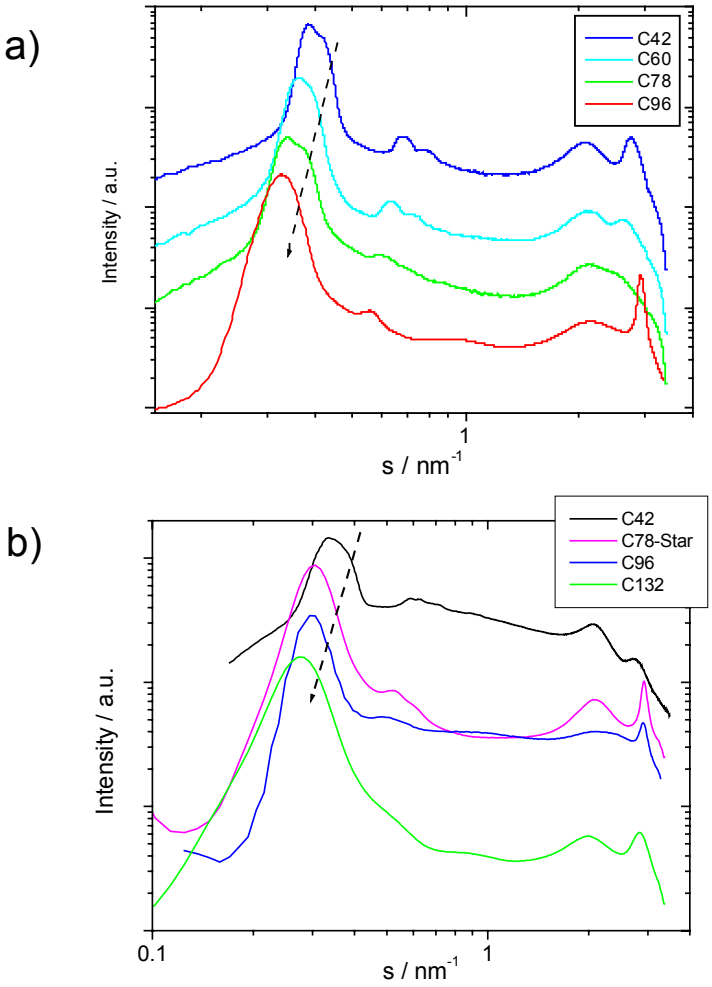

Figure 3.4. *Intensity distribution as a function of the scattering vector for different discotic molecules each substituted by a) C_{12} alkyl chains and b) $C_{16,4}$.*

The X-ray diffractogram in Figure 3.4 reveals effects of core size on the unit cell parameters describing the columnar packing. The structures of discotic molecules with different core sizes, but each substituted by C_{12} alkyl chains, are taken into account here. It has been found that the intercolumnar distance increases with increasing core size as indicated by the shift of the reflections to smaller scattering values. The aromatic core size of the compounds shown in Figure 3.4 varies from HBC with a diameter of approximately 1.4 nm to the C96 core with a size of about 2.0 nm. This difference in core size is also reflected in the

different hexagonal unit cell parameters obtained for these compounds which were a = 2.83 nm for HBC-C_{12} and a = 3.35 nm for C96-C_{12}. It should be noted that the cores C42, C78-Star and C96 were six-fold substituted by the C_{12} alkyl chains, whereas eight side chains were attached to the C60 core. Nevertheless, the trend of the increasing unit cell dimensions with larger core size is obvious. Furthermore, it can be supposed that the symmetric shape of the core is not essential since the molecules perform a lateral rotation due to their high mobility in the mesophase resulting in an average effective core geometry.

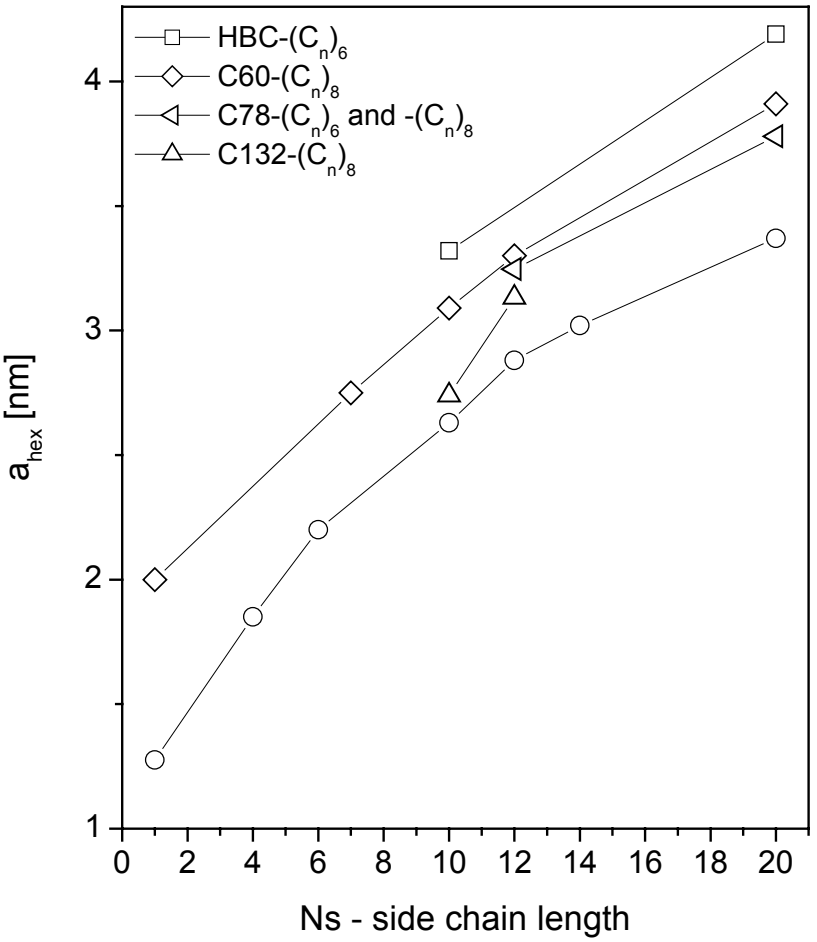

Figure 3.5. *Hexagonal unit cell dimensions as a function of the side chain length and core size.*

Similar dependence between the core size and the unit cell parameters was observed for discotics substituted by branched $C_{16,4}$ side chains (Figure 3.4b). The intercolumnar packing dimensions increased also with increasing core size.

In Figure 3.5, the hexagonal intercolumnar spacings for all the investigated compounds

are summarized as a function of the side chain length for various core sizes. A similar dependence of the lattice parameters on the side chain length is observed for the HBC and C96 cores. Both dependencies reveal the same trend, whereas all the C96 packing parameters are shifted by ca. 0.6 nm to higher distances due to the larger core disc. Both curve shapes are not linear and seem to level off for longer substituents. This behavior provides a strong indication that the side chains in the mesophase arrange themselves into a continuous intercolumnar phase filling the space between the columns, whereby the degree of interdigitation of the side chains can be considered as becoming higher for longer chains. Similar packing behavior has been reported for triphenylene derivatives.[212] In Figure 3.6, the intercolumnar hexagonal arrangement is illustrated for two HBC derivatives substituted by short and long alkyl side chains taken as examples.

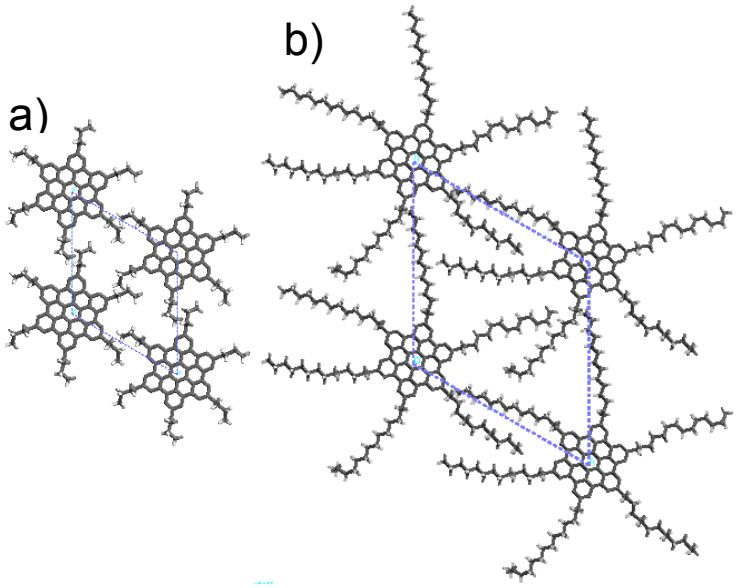

Figure 3.6. *Two hexagonal lattice arrangements consisting of a) HBC-C_4 and b) HBC-C_{14}.*

Since, both the HBC six-fold substituted by linear C_{10} alkyl chains and the HBC substituted by branched $C_{8,2}$ side chains reveal the same lattice parameters, it is assumed that the packing possibilities related to the number of carbon atoms within the side chains has a larger influence on the intercolumnar organization than the details of the chemical architecture. However, this statement is not valid generally. An exception has been observed for longer dove-tailed side chains with very much different mass distribution in the side groups and will be discussed in the following section. Branching of side chains close to the discotic core can result in a high steric demand and increase chain interactions in the disc

periphery which are too large to allow the orthogonal arrangement of discs in the columns preserving the characteristics for strong π–stacking distances. Such constraints can, however, relax through a tilt of discs with respect to the columnar axes which in effect leads to an extension of columns and increase of the space around them. The tilt of discs with respect to the columnar axes in the mesophase has been observed in two samples considered here, C96-$(C_{12})_4$ and C96-$(C_{10,14})_6$, for which the behavior will be discussed in more detail later.

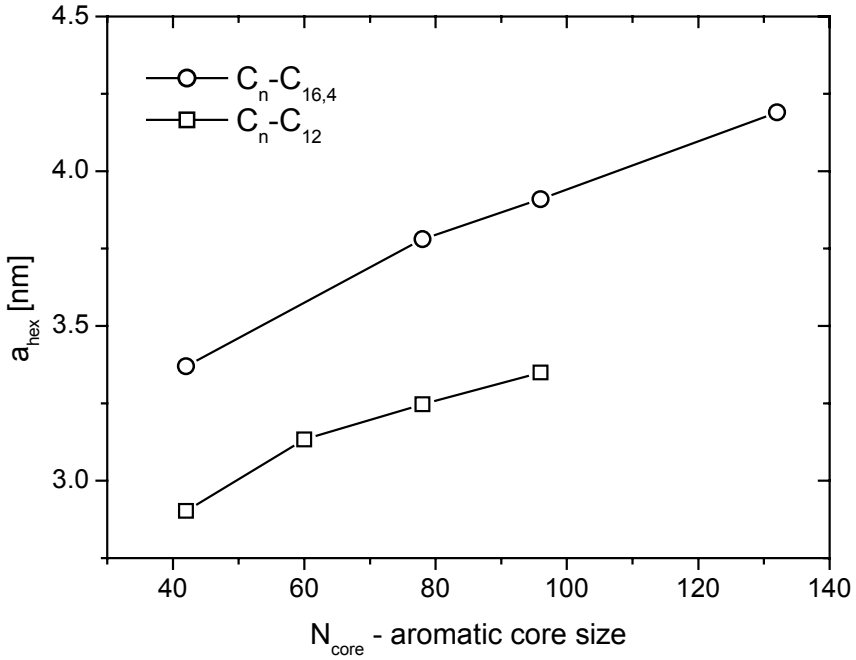

Figure 3.7. *Hexagonal unit cell parameters as a function of the core size.*

The dependence between the core size and the 2D unit cell parameters of the columnar packing is presented in Figure 3.7 for two lengths of the side chains. The aromatic core mass is expressed by the number of carbon atoms and the intercolumnar packing lattice parameters for discs substituted by the linear C_{12} alkyl chains and the branched $C_{16,4}$ chains are given. All the results presented indicate that the morphological parameters of the studied systems are related to the packing possibilities in the two phases: the aromatic columnar cores and the aliphatic chains constituting the periphery. The disc cores forming the columns in all systems obviously remain at distances between 0.34 and 0.36 nm which are only slightly higher than the interlayer distances of graphite. This suggests that the density of the columns is nearly that of the graphite (ρ_c=2.25 g/cm^3). Such packing within the columns has to be in balance with the packing of the aliphatic side chains filling the space between them. Assuming the density

ρ_s=0.9 g/cm^3 (corresponding nearly to amorphous wax) for the side chain phase, the intercolumnar distances can be related to the spatial requirements of the side chains given by their length and number. This can be expressed by the following relation based on the geometry illustrated in Figure 3.6

$$\frac{a_{hex}^2 d\sqrt{3}}{2} = V_{core} + V_{sc} \tag{3.1}$$

where V_{core} and V_{sc} are volume fractions of the core and the side chain phases per repeating distance d along the column, respectively. Considering relations between these volume fractions and the molecular weights of the corresponding molecular moieties, the intercolumnar distance a_{hex} can be given by the following relation

$$a_{hex} = \sqrt{\frac{2}{dN_A\sqrt{3}}\left(\frac{M_c}{\rho_c} + \frac{fM_s}{\rho_s}\right)} \tag{3.2}$$

where N_A is the Avogadro number, M_c and M_s are molecular masses of the core and a single side chain, respectively and f is the number of side chains in the discotic molecule.

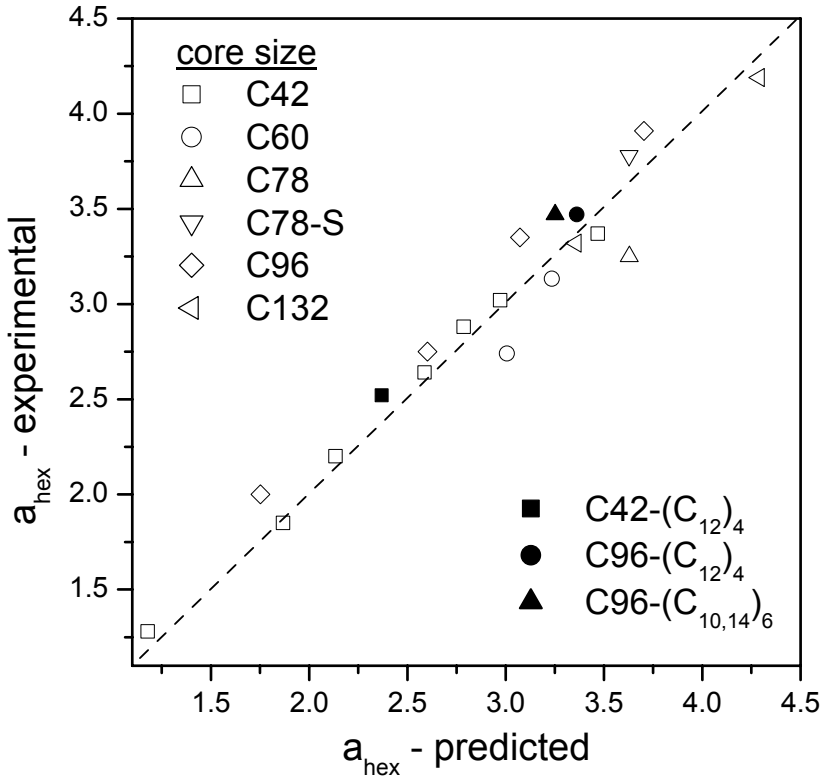

Figure 3.8. *Comparison of the predicted and experimental values of the hexagonal lattice constants for columnar bulk structures.*

This relation allows predictions concerning intercolumnar distances in the hexagonal arrangement when the molecular parameters (M_c, M_s and f) are known. The values predicted of the hexagonal lattice constants are compared in Figure 3.8 with the values determined experimentally on the bases of the X-ray diffraction intensities. The correlation can be regarded as very satisfying if one assumes that there occur no adjustable parameters in it. This means that relation (3.2) very well describes the packing conditions of the discotic molecules. Modifications of the assumed densities could further improve the correlation.

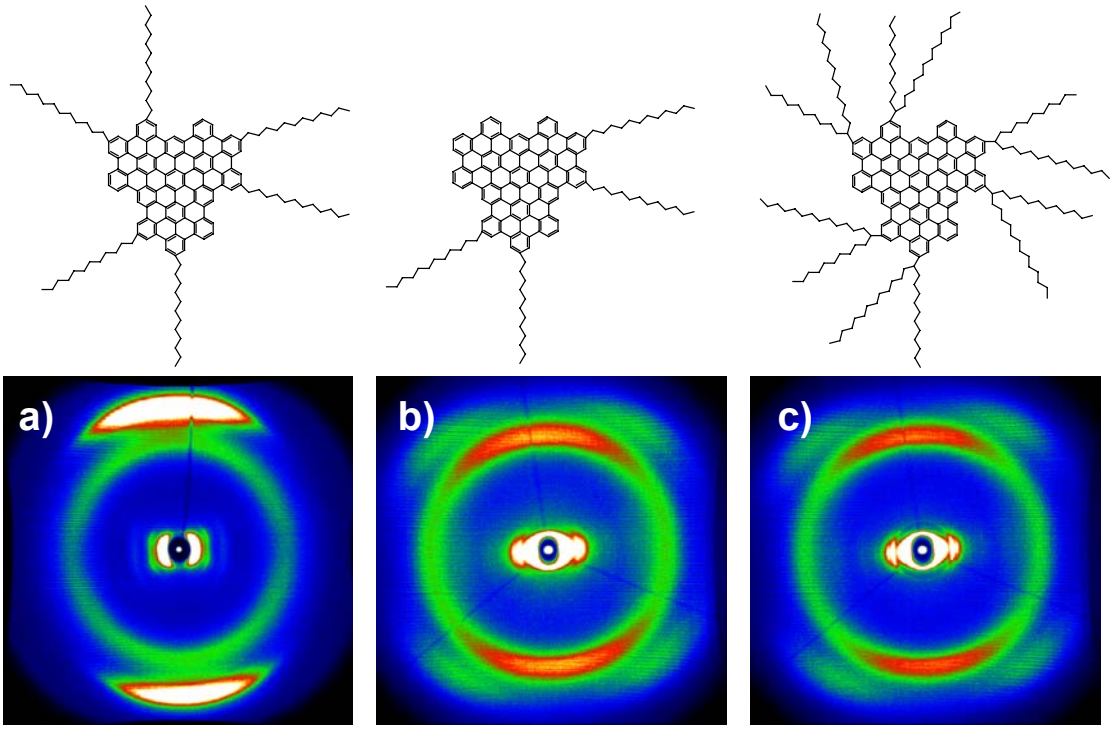

Figure 3.9. *Structure investigation by using 2D-WAXS experiments dependent on the number of side chains substituted to the C96 core with a) C96-$(C_{12})_6$,, C96-$(C_{12})_4$ and c) C96-$(C_{14,12})_6$.*

The number of alkyl chains attached to the aromatic core can also influence the intercolumnar packing. The supramolecular organization of some discotic cores with a reduced number of side chains i.e. HBC-$(C_{12})_4$, C96-$(C_{12})_2$, C96-$(C_{12})_4$ and with dove-tailed side chains C96-$(C_{14,12})_6$ have, therefore, been investigated. Examples of the 2D-WAXS patterns for the systems with different side chain numbers are shown in Figure 3.9. The sample C96-$(C_{12})_2$ was not processable by filament extrusion due to strong π-stacking and the reduced degree of freedom of the side chains leading to insufficient plasticity of the material. The powder X-ray diffraction of this material revealed only one broad small angle peak at s=0.38 nm^{-1} and therefore the lattice could not be assigned precisely. In the other cases,

independent of the asymmetry of some molecules, the hexagonal 2D lattices were detected. In some cases, however, a tilting of discs with respect to the columnar axis was observed which resulted in increased periods along the columns. The lattice constants of the intercolumnar packing in such systems are also considered in the comparison between experimental and predicted values presented in Figure 3.8.

For the system HBC-$(C_{12})_4$ in which the typical orthogonal disc orientation with respect to the column axes was detected for the mesophase (Figure 3.10b), the comparison reveals a good agreement. In the crystalline state the disc adopted the characteristic tilted intracolumnar arrangement (Figure 3.10c). Contrary to that, in the system C96-$(C_{12})_4$ (Figure 3.9b), the tilt of discs was detected also in the mesophase and the hexagonal lattice constant was not satisfying the relation (3.2) when columns of cross-section corresponding single discs area were considered. The by far too large lattice constant observed experimentally can, however, be understood when columns build up of pairs of coplanar adjacent discs are considered. Such pairs with 8 arms each constitute more symmetric elements and, when tilted, fit to a nearly cylindrical cross-section of the columns which better fit to the detected hexagonal symmetry of the columnar arrangement.

The other system with the detected tilt, C96-$(C_{14,12})_6$ (Figure 3.9c), is also in good agreement with the relation (3.2) when the increased periodicity along the columns is considered. The tilt in this case has probably a different reason than in the other case. As discussed earlier in this section the crowd of side chains at the periphery of the discs requires column extension in order to be accommodated at the density characteristic for the side chain phase. This extension is realized by the tilt of discs with respect to the column axis. The observed agreement of the experimental and predicted lattice parameters for this system with the tilt taken into account strongly supports such a hypothesis.

The results presented indicate that the characteristic supramolecular structures and related parameters are controlled by packing possibilities of the stiff planar cores and the flexible side groups into separate phases of different densities. The balance of these packing possibilities with the π–interactions in the columns should impose the structure stability and corresponding transition temperatures. In all the systems investigated, the structures reported extend over a very broad temperature range often exceeding the range of accessible temperatures because of chemical decomposition. This indicates that for the studied molecular architectures, there is no conflict between packing possibilities and conditions for effectiveness of the π–interactions. A lowered temperature of the isotropization was only observed for the sample HBC-$C_{16,4}$ for which the effect can be related to the low fraction of the columnar phase. It can, however, be expected that in the systems with the tilt of discs,

where the effectiveness of the π–stacking becomes reduced at the expense of satisfaction of packing conditions, the stability of structures will become reduced as well.

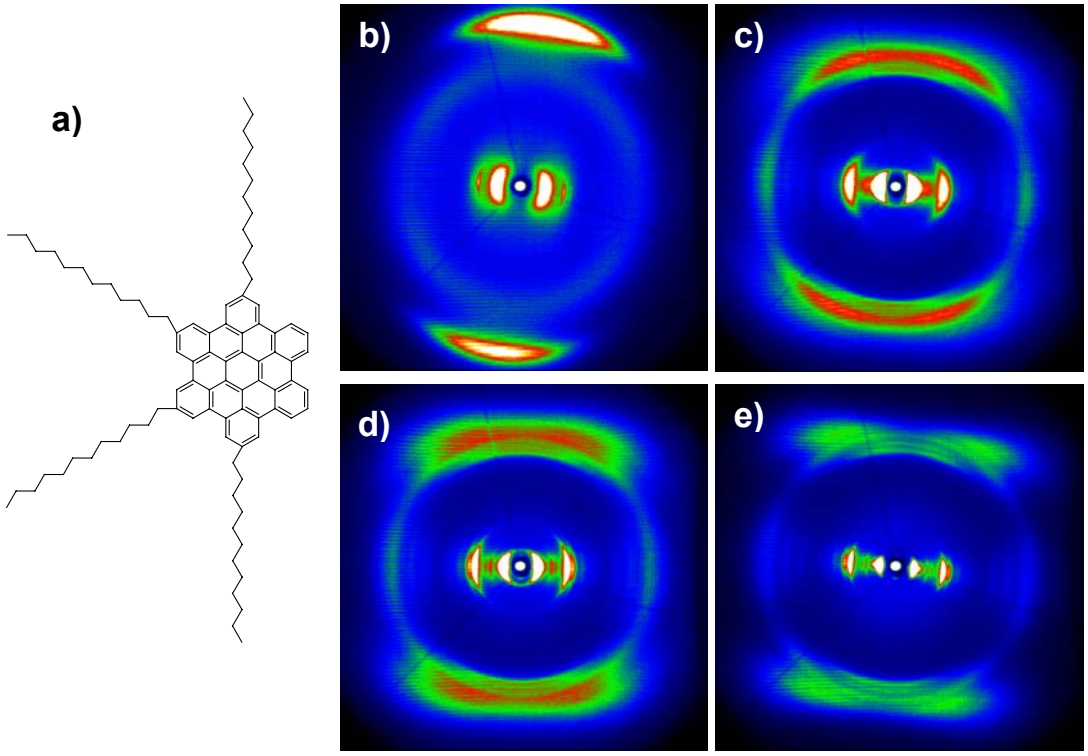

Figure 3.10. *a) Chemical structure of HBC-$(C_{12})_4$, 2D-WAXS for an extruded HBC-$(C_{12})_4$ filaments b) in the mesophase, c) at the initial state before annealing, c) after the first annealing in the mesophase and d) after the second annealing (the patterns in c) to e) are recorded under the same conditions and are displayed in the same contrast).*

For the system HBC-$(C_{12})_4$ in which the typical orthogonal disc orientation with respect to the column axes was detected for the mesophase (Figure 3.10b), the comparison reveals a good agreement. In the crystalline state the disc revealed the characteristic tilted intracolumnar arrangement (Figure 3.10c-3.10e). Thereby, the degree of the supramolecular order was strongly dependent on the thermal treatment of the extruded sample. After annealing at the mesophase the X-ray pattern for the crystalline phase exposed more distinct reflections. Finally, the off-meridional reflections corresponding to the disc tilting were separate (Figure 3.10e). Unusually, the intercolumnar arrangement was improved as well being reflected by more pronounced equatorial reflections. The unit cell for the crystalline phase was fitted to two different arrangements; a hexagonal lattice with a unit cell of a = 3.60 nm, and an orthorhombic lattice with a = 1.81 nm and b = 3.13 nm. The equatorial scattering intensity distribution is presented in Figure 3.11. Due to the asymmetrical substitution of the

aromatic core, a lamellar arrangement of alternating single rows of aromatic cores and alkyl side chains can be assume. The proposed superstructure is presented as the inset in Figure 3.11.

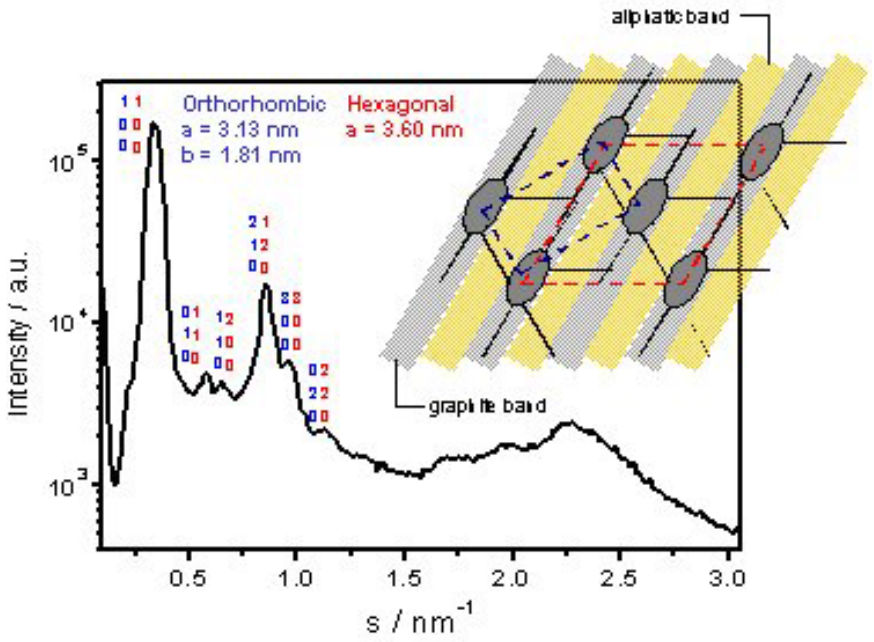

Figure 3.11. *Equatorial scattering intensity distribution as a function of the scattering vector, the reflection positions are assigned by the Miller's indices according to the hexagonal (red) and orthogonal (blue) lattice; inset shows the illustration of the supramolecular arrangement with alternating aromatic core and alkyl chain rows (the side chains are indicated as straight lines due to simplicity).*

It has been revealed that the supramolecular organization is determined to a high degree by the molecular architecture. Thus, the intercolumnar packing dimensions are strongly dependent on the aromatic core size, the side chain length and number of side chains. Thereby, the number of carbon atoms for linear or methylene containing side chains is in relation with the length. Triphenylenes, substituted with different side chains but having the same total number of peripheral carbon atoms, revealed identical intercolumnar packing parameters.[212,213] In the present study it was additionally confirmed that the influence of the different molecular parameters on the hexagonal lattice constant of derivatives substituted by linear alkyl chains can be summarized in the relationship taking into account the two phase packing with for each phase characteristic density. The unit cell parameters increase with the core size, whereas the interdigitation plays a major role with increasing side chain length being in accordance with results reported for triphenylenes.[212,213] The only correlation between the molecular architecture and the intercolumnar parameters with the thermal

behavior was found for HBC derivatives which is discussed in Chapter 5. Compounds consisting of larger aromatic cores did not exhibit any phase transition. Finally, the conclusions play an important role in the control of the supramolecular organization of discotic liquid crystalline molecules, consisting of extended polycyclic aromatic hydrocarbons, by varying the aromatic core size and the number and size of the substituents.

3.2. Investigation of the Supramolecular Structure of Dove-Tailed HBCs

3.2.1. Alkyl Side Chains with Branching at the β-position

The relation between the branching at the β-position of alkyl chains and the supramolecular organization has been investigated on a series of HBC derivatives: HBC-$C_{6,2}$, HBC-$C_{10,6}$ and HBC-$C_{14,10}$.

The distinct equatorial reflections in the 2D-WAXS pattern of the investigated compounds suggested a well-ordered supramolecular structure of the macroscopically oriented filaments with columns aligned in extrusion direction. The patterns for HBC-$C_{6,2}$ and HBC-$C_{10,6}$ are shown in Figure 3.12, whereas the pattern of HBC-$C_{14,10}$ is exhibited in Figure 3.13.

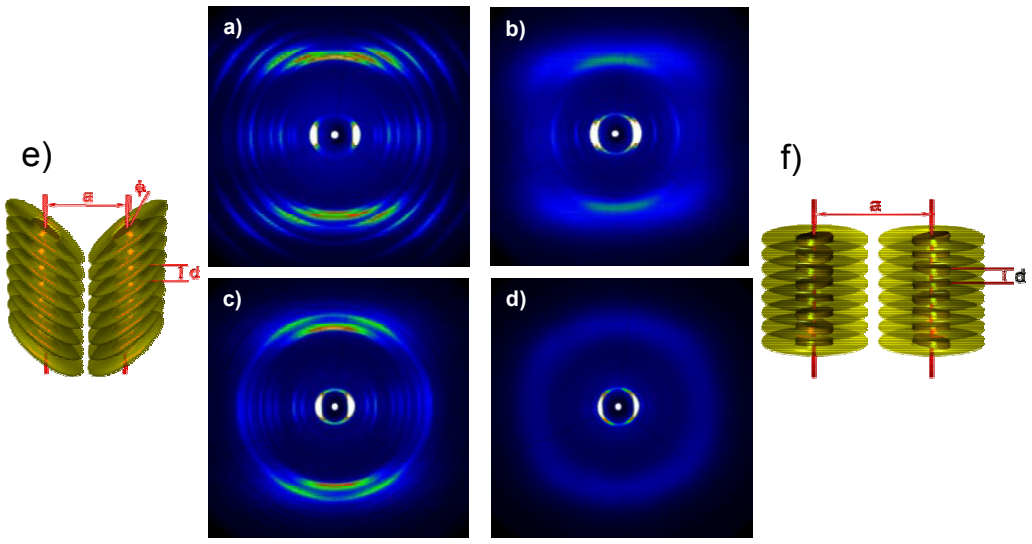

Figure 3.12. *2D-WAXS pattern of filament extruded HBC-$C_{6,2}$ a) in the plastic crystalline phase and b) in the mesophase, and HBC-$C_{10,6}$ c) in the crystalline phase and d) in the mesophase at 60 °C; e) schematic representation of the herringbone structure observed at room temperature for the three investigated compounds and f) the Col_d phase determined for HBC-$C_{6,2}$ and HBC-$C_{10,6}$.*

The high degree of order of these samples at room temperature is obvious from the large number of higher order reflections in these patterns. The intracolumnar packing is identical for the three investigated HBCs, which was not surprising, as the chemical structures were similar. The meridional reflexes indicated a tilting of the discotic cores with respect to the columnar axis leading to the herringbone arrangement (Figures 3.12a and 3.12c for HBC-$C_{6,2}$ and HBC-$C_{10,6}$, Figure 3.13a for HBC-$C_{14,10}$). The intracolumnar packing of HBC-$C_{6,2}$ is exceptionally well pronounced indicated by the high number of higher-order, off-meridional reflections arising from the intracolumnar but also strong intercolumnar correlations between the discs. Contrary to HBC-$C_{10,6}$ and HBC-$C_{14,10}$, where the corresponding phase due to the absence of long-range correlation is assigned to a plastic-crystalline phase, HBC-$C_{6,2}$ forms a crystalline phase at room temperature. Based on the intracolumnar period of 0.48 nm and the maximum off-meridional peaks correlating to the cofacial distance of 0.37 nm, a tilting angle between 30° and 40° could be determined for the investigated compounds. Figure 3.14 shows Cerius[2] simulated 2D-WAXS patterns for HBC discs with different tilting angles. These simulations clarify the difficulty of the exact assignment of the molecular tilting angle by the determination of the azimuthal angle of the maximum reflection peak in the off-meridional. By increasing the tilt angle, the reflections with the highest intensity appear at higher azimuthal angle of the off-meridional, whereby the intracolumnar period of 0.49 nm is correlated with the meridional peak which is identical for all investigated tiling angles. However, it is not possible to correlate a definite reflection peak with the disc tilt.

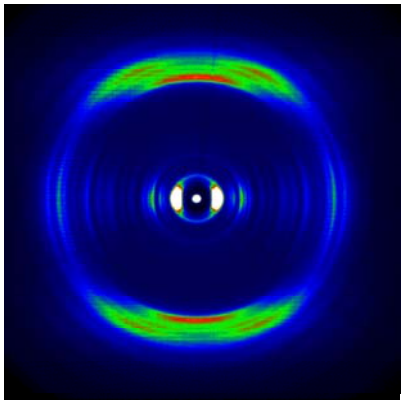

Figure 3.13. *2D-WAXS pattern of filament extruded HBC-$C_{14,10}$ a) in the plastic crystalline phase.*

The high meridional reflection intensity and the number of higher order reflexes corresponding to the stacking correlation, as observed for HBC-$C_{6,2}$, also suggest a well organized intracolumnar packing. The distribution of the equatorial reflections corresponds

the lateral intercolumnar arrangement, which was assigned from the powder X-ray scattering results.

When heated to the mesophase, the intracolumnar order of both materials HBC-$C_{6,2}$ and HBC-$C_{10,6}$ underwent a significant change obvious from the 2D-WAXS patterns (Figures 3.12b and 3.12d). In both cases, the meridional reflections corresponding to the disc-to-disc distance became considerably undefined and diffuse. Moreover, for HBC-$C_{10,6}$ these reflections became continuously weaker with increasing temperature until they completely disappeared at 60 °C, indicating a significant decrease of the intracolumnar order in the higher temperature liquid crystalline phase. Therefore, this state was assigned as columnar disordered Col_d. Cooling back to room temperature again, the meridional reflections return reversibly after a certain time.

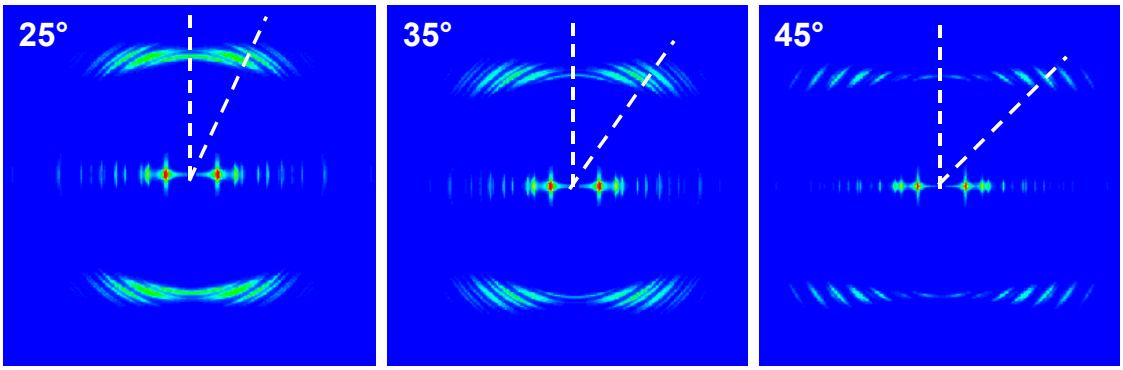

Figure 3.14. *Cerius*^{2} *simulated 2D-WAXS diffraction patterns for HBC discs with different molecular tilting angles placed in an arbitrary chosen hexagonal unit cell.*

The intercolumnar arrangement of the materials in different phases was investigated using powder X-ray scattering. The intercolumnar organization was characterized by using a 2D lateral lattice, which was determined by fitting a mathematical relation to the reflection positions. Due to the complexity of the diffractogram, it was very difficult to find a close correlation between the peaks. A lateral 2D monoclinic model gave the best fits for the intercolumnar organization (Table 3.2). The gamma angle of $\gamma = 60°$ is identical for all studied materials at room temperature with packing parameters depending on the side chain length.

Figures 3.15a presents a characteristic powder X-ray scattering intensity distribution as a function of the scattering vector s for HBC-$C_{6,2}$. The high intensity of the reflections in the wide-angle range (2 – 3 nm^{-1}) points out once again the high degree of the intracolumnar order. Upon heating the sample to the Col_d phase, a considerable structural change can be observed as described by the change of the scattering pattern (Figure 3.15b). Surprisingly, the

columnar arrangement in this phase could not be assigned to a hexagonal lattice, which is unusual for C6-symmetric HBCs. Nevertheless, as implied by the high intensity of the split small angle peaks, a well-ordered intercolumnar packing was observed. In contrary, the reflections corresponding to the molecular stacking disappeared verifying the 2D-WAXS results.

Table 3.2. *2D lateral unit cell assignment for the three investigated compounds in their corresponding phases. In the right: a schematic example of the monoclinic columnar arrangement is presented.*

Compound	Phase	Unit cell	Parameters [nm]
HBC-$C_{6,2}$	C_r	monoclinic	a = 2.21 b = 1.88, γ=62°
	Col_d	monoclinic	a = 2.67 b = 1.63, γ =45°
HBC-$C_{10,6}$	Col_p	monoclinic	a = 2.98 b = 2.50, γ = 60°
	Col_d	orthorhombic	a = 4.32 b = 2.36
HBC-$C_{14,10}$	Col_p	monoclinic	a = 3.73 b = 2.84, γ=62°

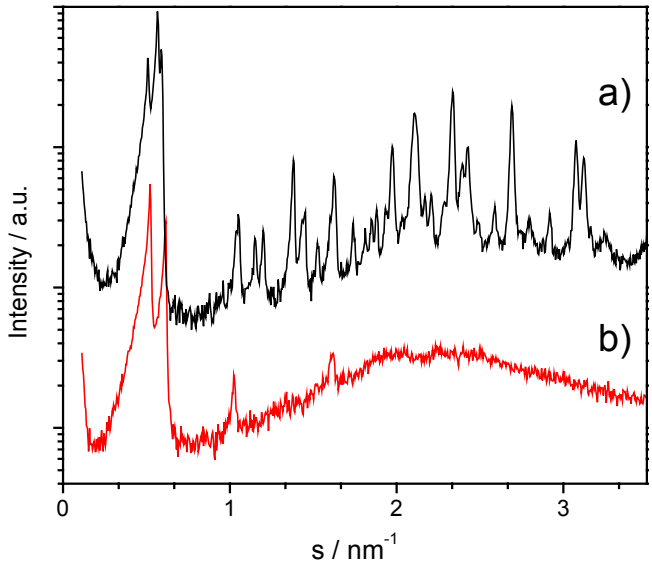

Figure 3.15. *Powder X-ray diffraction of HBC-$C_{6,2}$ at a) room temperature in the plastic crystalline phase and b) at the Col_d mesophase.*

The identical supramolecular order at room temperature was also observed for HBC-$C_{10,6}$ (see Figure 3.17a) and HBC-$C_{14,10}$ (see Figure 3.16a) in the powder X-ray diffractogram for the Col_p phase. The phase transition of HBC-$C_{10,6}$ to the liquid crystalline Col_d state is accompanied by a considerable transformation in the intra- and intercolumnar packing. Analogously to HBC-$C_{6,2}$, the high intercolumnar arrangement is maintained, but cannot be fitted to a 2D lateral hexagonal lattice. The degree of intracolumnar organization decreases significantly. While heating the sample to the optically isotropic state, a small-angle reflection appeared corresponding to a repeating distance of 2.21 nm as derived from the X-ray scattering diffraction in Figure 3.17c. This reflection can be attributed to position correlation of molecular aggregates possessing electron density contrast between the aromatic core stacks and the substituents. Assuming only nearest neighbor relations, the correlation distance should be

$$d = \frac{1.23}{s_{max}}. \qquad (3.3)$$

This value allows to estimate the number of stacking molecules consisting in the aggregate as a spherical unit of volume

$$\frac{\pi}{6} d^3 \qquad (3.4)$$

which is related to the molecular mass M by the following equation:

$$\frac{\pi}{6} d^3 = \frac{M \cdot n}{\rho \cdot N_A} \qquad (3.5),$$

where n is the number of molecules, ρ is the density assumed here 1 g/cm³ for both nanophases (the aromatic core and the alkyl shell) and N_A is the Avogadro's number. For this relationship, the most probable stacking number of nearly 4 HBC-$C_{10,6}$ molecules was determined suggesting that the molecules in the isotropic state are not isolated, but form aggregates consisting of several discs. The stacking number for HBC-$C_{14,10}$ was also determined from the X-ray scattering pattern recorded for the isotropic state revealing an identical value of 4 molecules. This might be an explanation for the isotropic phase charge carrier mobilities being observed by TOF[47] and PR-TRMC[214] independently for triphenylene derivatives and phthalocyanines[215].

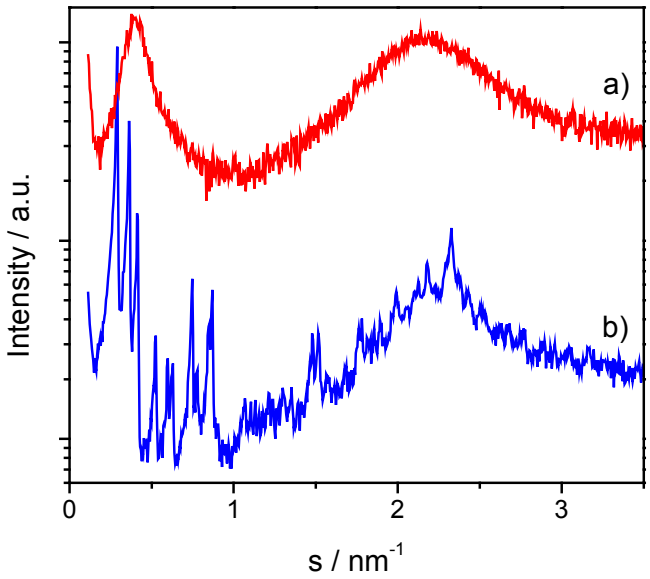

Figure 3.16. *Powder X-ray diffraction of HBC-$C_{14,10}$ at a) in the isotropic phase and b) slowly cooled back to the plastic crystalline phase Col_p at room temperature.*

After cooling the sample back to the disordered LC phase, the X-ray diffraction was again recorded suggesting that the supramolecular order of bulk HBC-$C_{10,6}$ was considerably influenced by the thermal treatment. The X-ray diffractogram displayed a similar intensity distribution as before the heating to the isotropic phase (Figure 3.17d). However, an additional small-angle reflection at 0.234 nm^{-1} appeared directly after cooling. Furthermore, a significant shift of the reflections towards the wide-angle region can be observed, indicating a decrease in the packing parameters and, as suggested by the new small-angle peak, a formation of higher order supramolecular organization. Thus, the thermal treatment of the HBC-$C_{10,6}$ material has a great influence on the packing, which has not been seen for the two other HBC derivatives. The reflection peak positions in the Col_d phase could not be fitted to any unit cell, but the appearance of the discrete small-angle allowed to assign an orthorhombic lattice for the liquid crystalline state.

In order to relate the supramolecular organization of the dove-tailed HBC derivatives with the electronic properties of the materials, the charge carrier mobility has been investigated. The results presented in this section are the direct outcome of a strong collaboration with Jorge Piris in the group of Dr. Warman, TU Delft. The sum of the one-dimensional charge carrier mobilities, $\Sigma\mu_{1D}$, has been derived from the pulse-radiolysis time-resolved microwave conductivity technique (PR-TRMC). Since the values of $\Sigma\mu_{1D}$ were monitored as a function of temperature, it was possible to correlate these values with the supamolecular arrangement in different phases. Generally, the extended intra-columnar

ordering and improved processibility shown by the materials described in this section is highly desired for applications as unidirectional conductors in electronic devices.

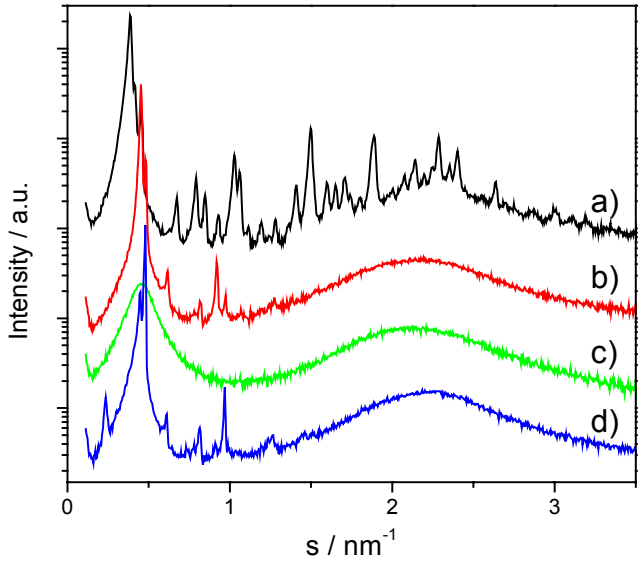

Figure 3.17. *Powder X-ray diffraction of HBC-$C_{10,6}$ at a) room temperature in the plastic crystalline phase, b) in the Cold liquid crystalline state, c) in the isotropic phase, and d) slowly cooled back to the plastic crystalline phase at room temperature.*

Table 3.3. C*harge carrier mobilities for the dove-tailed HBC derivatives.*

Sample	Phase	$\Sigma\mu_{1D}$ / $cm^2V^{-1}s^{-1}$
HBC-$C_{6,2}$	C_r	0.25
	Col_d	0.29
HBC-$C_{10,6}$	Col_p	0.73
	Col_d	0.08
HBC-$C_{14,10}$	Col_p	0.47

From the end-of-pulse conductivity the sum of the charge carrier mobilities, $\Sigma\mu_{1D}$, has been determined as a function of temperature. The values obtained for the different phases are summarized in Table 3.3. The temperature behavior of the present compounds differs notably from the previously studied HBC derivatives; in general, the mobility increases slightly with temperature in the crystalline phase until it experiences a sudden decrease by a factor ca. 2 on entering the mesophase. Most HBC derivatives studied to date shower a similar $\Sigma\mu_{1D}$ value of

ca. 0.3 cm^2/Vs in their discotic columnar hexagonal phase. In contrast, the mobility values for HBC-$C_{6,2}$ did not experience any significant change when going from the crystalline to the liquid crystalline phase (Figure 3.18). In general, the mobility does not change at transitions between phases with identical supramolecular structure as observed for HBC-PhC_{12}[52] or alkyl-thiosubstituted phthalocyanines[50,215]. The relatively low conductivity of HBC-$C_{6,2}$ despite the high crystallinity at room temperature can only be explained by the lack of high solubility and the possibility of better purification. The similarity of the intracolumnar packing in both solid-state phases, in which the disc molecules adopted a tilted arrangement, resulted in the constant charge carrier mobility over the investigated temperature range.

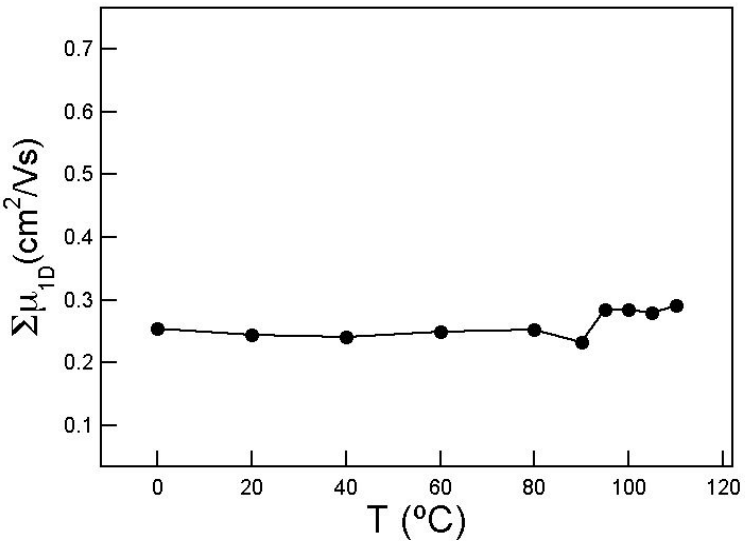

Figure 3.18. *Temperature dependence of the intracolumnar charge carrier mobility of HBC-$C_{6,2}$.*

Figure 3.19 represents the temperature behavior of the intracolumnar charge carrier mobility for HBC-$C_{10,6}$. The room temperature value $\Sigma\mu_{1D}$ = 0.73 cm^2/Vs is the highest measured for a non-crystalline phase and is only overcome by the crystalline HBC-C_{14} linear chain derivative ($\Sigma\mu_{1D}$ = 1.00 cm^2/Vs)[52]. Upon heating the mobility decreases almost linearly with temperature until it experiences a sudden drop of almost an order of magnitude upon conversion to the liquid crystalline phase. The very low conductivity values obtained in this phase compared with previously studied HBCs indicates a rather weak interdisc interaction and a rather low columnar organization. This is in good agreement with the X-ray results presented in the previous section. In comparison to phthalocyanines and porphyrins, such a pronounced mobility drop at the phase transition has not been reported.[39,50] Only discotics consisting of small aromatic cores as triphenylenes revealed such significant differences in the

mobility accompanied by the increase of columnar disorder between the phases.[48,216] In addition, high fluidity and the small enthalpy change on entering the isotropic phase are further indications of the similarity of both phases of HBC-$C_{10,6}$. As already indicated by the DSC studies, upon cooling there is a very large hysteresis before a partial recovery of the initial values could be observed. Only after extended periods of time further recovery could be observed.

Compound HBC-$C_{14,10}$ is also plastic crystalline at room temperature and accordingly shows a mobility value comparable to the crystalline HBC derivatives. As it converts directly from the plastic crystalline phase to the isotropic liquid, no temperature dependence was recorded.

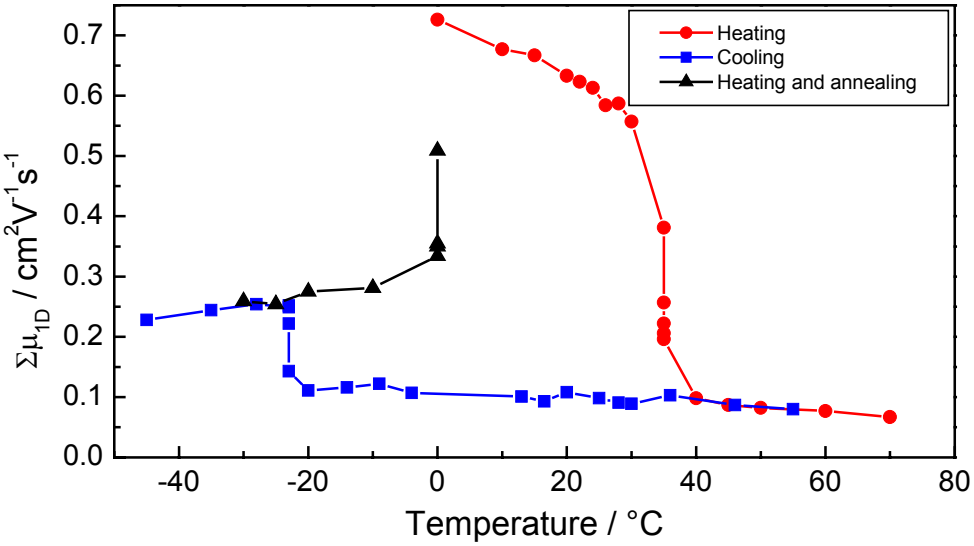

Figure 3.19. *Temperature dependence of the intracolumnar charge carrier mobility of HBC-$C_{10,6}$.*

The PR-TRMC measurements provided detailed information about the charge carrier mobility in the different phases and was correlated to the structural evaluation. It has been shown that the one-dimensional charge carrier transport along the columnar structures was strongly dependent on the intracolumnar order and the molecular packing. Disorder resulted in a drastic lowering of the mobility as observed for the liquid crystalline phase of HBC-$C_{10,6}$. On the other hand, the high purity of the derivatives with the longest side chains, HBC-$C_{10,6}$ and HBC-$C_{14,10}$, yielded very long life-times of charges and charge carrier mobilities which were comparable with highly crystalline HBCs. These two features are important requirements for the application in electronic devices and make these materials very attractive as organic semiconductors.

3.2.2. Branched Side Chains bearing Ether Linkages

In contrast to the dove-tailed side chains branched at the β-position, the branching after the ether linkage has a significantly different influence on the packing of the discotic molecules which has been studied also on a series of HBC derivatives: HBC-$C_3OC_{6,2}$, HBC-$C_3OC_{10,6}$ and HBC-$C_3OC_{14,10}$. Additionally, the supramolecular organization of HBC-$C_3OC_{8,2}$ has been analyzed on order to complete the picture.

These compounds also revealed a pronounced macroscopic alignment of columns along the filaments which was indicated by the intense and sharp equatorial reflections corresponding to the intercolumnar arrangement, strongly correlated to the phase of the compounds.

For the HBC-$C_3OC_{10,6}$, HBC-$C_3OC_{6,2}$ and HBC-$C_3OC_{8,2}$ an identical supramolecular order Col_{hd} was determined for the higher temperature solid-state. Based on X-ray scattering results, the intercolumnar arrangement of the three materials was assigned to a two-dimensional (2D) lateral, hexagonal, disordered columnar phase Col_{hd} and showed a significant dependence of the packing parameters on the length of the side chains. The bulk hexagonal lattice dimensions decreased from a = 3.07 nm for HBC-$C_3OC_{10,6}$ to a = 2.65 nm for HBC-$C_3OC_{6,2}$ and a = 2.78 nm for HBC-$C_3OC_{8,2}$ indicating a dependence of the packing parameters on the side chains length. Figure 3.21a shows a typical intensity distribution of the derivative HBC-$C_3OC_{10,6}$ in the higher temperature solid-state phase. The material, as obtained from solution, revealed a well-organized, two-dimensional, lateral, hexagonal intercolumnar structure as implied by the large number of higher order reflections with peak positions corresponding to a relationship $1 : \sqrt{3} : 2 : \sqrt{7} : 3$.

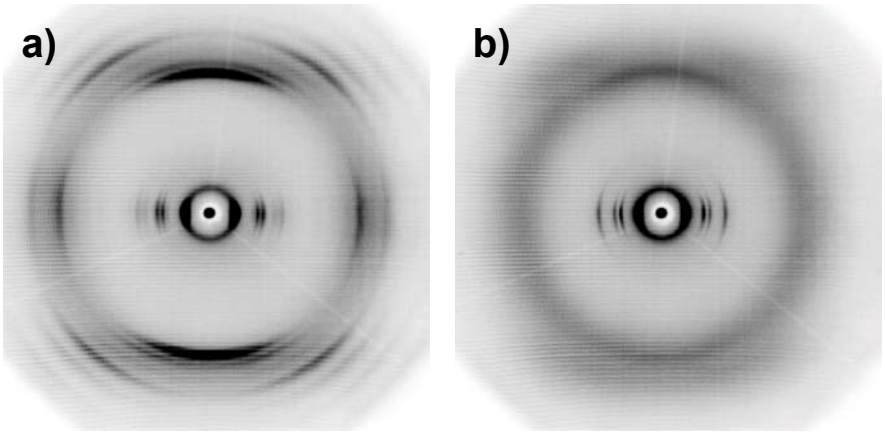

Figure 3.20. *Typical 2D-WAXS pattern of HBC-$C_3OC_{10,6}$, prepared as an extruded filament, at a) the plastic crystalline phase, and b) in the Col_{hd} phase.*

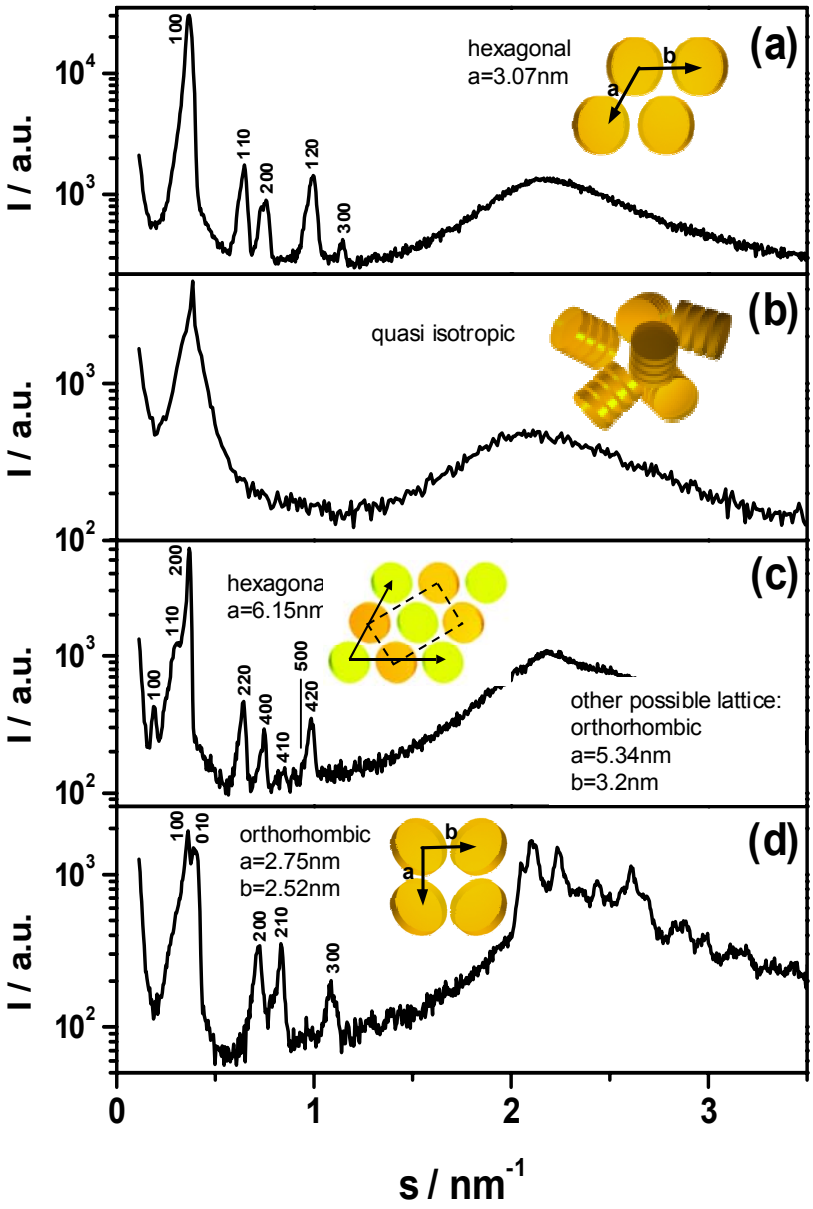

Figure 3.21. *Phase dependent powder diffraction of HBC-$C_3OC_{10,6}$; the intensity distribution is plotted against scattering vector; a) at room temperature Col_{hd} phase, b) at the isotropic state (inset drawing illustrates schematically the aggregation behavior in this phase), c) cooled back to room temperature (inset presents the two unit cells, arrows indicate the hexagonal lattice and dashed line the orthorhombic unit cell), d) cooled to the plastic crystalline phase. Reflections are indexed by using the Miller's indexes (hk0).*

The intracolumnar arrangement was characterized by temperature dependent 2D-WAXS experiments. Figure 3.20 presents examples of characteristic patterns of HBC-$C_3OC_{10,6}$ as an

extruded filament. In the mesophase, diffuse meridional reflections in the pattern (Figure 3.20b) resulted from the disordered intracolumnar packing. Weak off-meridional peaks suggested that the discs kept their tilting also in this state. Identical patterns were also obtained for compounds HBC-$C_3OC_{6,2}$ and HBC-$C_3OC_{8,2}$ in their Col_{hd} mesophase. The supramolecular order of bulk HBC-$C_3OC_{10,6}$, however, was considerably influenced by the thermal treatment when heated to the optically isotropic phase. In the isotropic state a small-angle reflection appeared at s = 0.385 nm^{-1} as derived from the maximum peak in the X-ray diffraction in Figure 3.21b. The reflection of this kind can be attributed to position correlation of molecular aggregates possessing electron density contrast between the aromatic core stacks and the aliphatic substituents. Assuming only nearest neighbor relations, the correlation distance can be described by means of equation 3.3. It allows to estimate the number of stacking molecules consisting in the aggregate as a spherical unit of volume which is related to the molecular mass M by equation 3.5. For this relationship, a most probable stacking number of nearly 5 molecules was determined for HBC-$C_3OC_{10,6}$ suggesting that the molecules in the isotropic state are not isolated (an identical number of 5 molecules was also calculated for HBC-$C_3OC_{14,10}$), but form aggregates consisting of even more discs in comparison to the HBC derivatives dove-tailed at the β-position.

After slow cooling the sample from the isotropic state, a supplementary small angle reflection appeared due to the enhanced higher order structure (Figure 3.21c). Two unit cells were determined from the peak positions and could be assigned to a pseudo-hexagonal arrangement. Both, a hexagonal lattice with twice the dimensions as before the thermal treatment and an orthorhombic unit cell with a = 5.34 nm and b = 3.2 nm, where $a \approx b\sqrt{3}$, can be alternatively be assigned to the observed scattered intensity distributions. The relationship between the packing parameters *a* and *b* of the orthorhombic lattice did not fit exactly to the pseudo-hexagonal model because the central column could be displaced slightly from the center of the cell.[20]

The phase transition from the Col_{hd} to the plastic crystalline phase was accompanied by a considerable structural change for the HBC-$C_3OC_{10,6}$, HBC-$C_3OC_{6,2}$ and HBC-$C_3OC_{8,2}$. During cooling, the degree of intracolumnar order improved which was reflected by a significant intensity increase of the off-meridian reflections in the 2D-WAXS patterns. These off-meridional peaks correspond to a molecular tilting with respect to the columnar axes. Figure 3.20a illustrates a characteristic 2D-WAXS result of extruded HBC-$C_3OC_{10,6}$ in the Col_p phase. The meridional peak is attributed to the intracolumnar periodicity of 0.43 nm, whereas the off-meridional reflections are related to the cofacial distance of 0.34 nm. These two values indicate a tilting of the discs between an angle of 30° and 40° which was also

observed for the HBC-$C_3OC_{6,2}$ and HBC-$C_3OC_{8,2}$.

Table 3.4. *Summery of the 2D lateral unit cells and packing parameters determined for the investigated HBC derivatives by assigning the reflection peak positions in the corresponding X-ray powder diffractograms. The shown lattices represent the best fits.*

Compound	Phase	Unit cell	Packing parameter / nm
HBC-$C_3OC_{14,10}$	Col_p	Orthorhombic	a = 3.52
			b = 3.71
HBC-$C_3OC_{10,6}$	Col_p	Orthorhombic	a = 2.75
			b = 2.52
	Col_{hd}	Hexagonal	a = 3.07
HBC-$C_3OC_{6,2}$	Col_p	Monoclinic	a = 2.75
			b = 2.52; γ = 65°
	Col_{hd}	Hexagonal	a = 2.65
HBC-$C_3OC_{8,2}$	Col_p	Orthorhombic	a = 2.40
			b = 2.08
	Col_{hd}	Hexagonal	a = 2.78

The intercolumnar arrangement was determined from the low-angle reflection distribution in the powder X-ray diffraction. The lattice of HBC-$C_3OC_{10,6}$ fit well to a 2D orthorhombic unit cell with a = 2.75 nm and b = 2.52 nm as illustrated in the powder diffraction in Figure 3.21d. The wide-angle part of the scattered intensity distribution revealed discrete periodicities at distances below 0.5 nm which suggests high intracolumnar correlation between the discotic molecules indicating an order improvement during cooling leading to an increase in intensity of the off-meridian reflections which corresponded to the molecular tilting. Interestingly, the intensity of reflections corresponding to the characteristic intracolumnar periodicity of 0.48 nm was almost identical to the main peak according to the intercolumnar distances suggesting a high intracolumnar correlation between the discotic molecules.

Both materials HBC-$C_3OC_{6,2}$ and HBC-$C_3OC_{8,2}$ underwent also great structural changes at the transition to the plastic crystalline phase as observed for HBC-$C_3OC_{10,6}$. Both compounds showed also a transformation from the columnar disordered phase to the

characteristic high intracolumnar order with molecules tilted towards the columnar axis in the plastic crystalline state. The unit cell parameters are summarized in Table 3.4.

Interestingly, an exceptional phase behavior was observed for the derivative HBC-$C_3OC_{14,10}$ for which no intermediate state between the plastic crystalline phase and the isotropic state phase was detected, what is in strong contrast to other discotic compounds.

The relationship between the alkyl substituents and the intracolumnar order of discotic molecules has been studied in detail for different HBC derivatives carrying side chains with different architecture. Since the charge carrier transport takes place along the columnar stacks and depends strongly on the aromatic core interaction and thus on the packing of the discotic molecules, the control of the intracolumnar arrangement of the single building blocks is one of the most essential aspects.[217,218]

For the structural assignment two important terms were used which will be elucidated in the following.

The term “plastic” was the first time defined by Gray and Winsor to describe “a particular class of mesophase in which the molecules reveal minor fluctuations in positions, at the points of a cubic lattice”.[219]. Afterwards this term was used to classify thermotropic hexagonal phases in polymers.[220] Wendorff and his coworkers described a new phase formed by the asymmetrically substituted triphenylene (3,6,7,10,11-pentapentyloxytriphenylene-2-ly pivaloate) by assigning the material as “plastic columnar discotic”.[42,221] A three-dimensional positional order of the molecules, as in the crystalline phase, and a rotational mobility were reported to be characteristic for this columnar phase.[222]

In this study the term “plastic crystallinity” was applied to emphasize the difference to the crystalline phase and was characterized by a molecular arrangement identical to the crystalline phase possessing, however, only short-range ordering. Furthermore, the consistence of the plastic crystalline materials was waxy and soft at room temperature in contrast to the crystalline powder. Solid-state NMR studies at temperatures between 6-16 °C of the β-branched HBCs revealed higher side chain mobilities leading to the short-range ordering observed in the X-ray scattering pattern.

The term “disordered” columnar was related to the intracolumnar arrangement of the HBC discs in the mesophase which possess a significantly decreased intermolecular correlation as indicated by the diffuse meridional reflections. The disordered columnar mesophase is in high contrast to the mesophase organization of HBC-PhC_{12} or HBC-C_{12} for which a pronounced π-stacking distance was observed. In general, for discotic materials, such as triphenylenes[223,224] and phthalocyanaines[225,226], disordered columnar phases are quite

common and appear when the substituents have a strong influence on the intracolumnar organization due to the high side chains dynamics. Only few examples with 2D-WAXS patterns have been reported in literature for phthalocyanines substituted by linear[227] or branched[228] alkoxy side chains. In both examples similar X-ray patterns were obtained indicating an identical degree of intracolumnar disorder in HBCs and phthalocyanines in the mesophase.

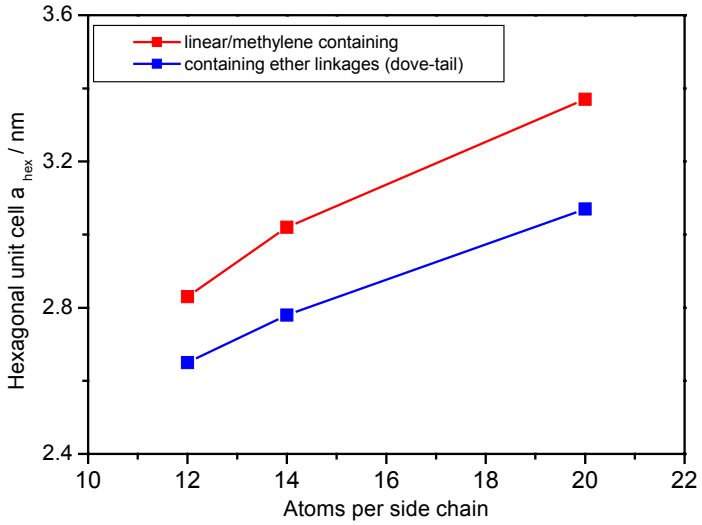

Figure 3.22. *Comparison of the hexagonal unit cell parameter a_{hex} for HBC derivatives substituted by linear and dove-tailed side chains.*

Since the ether linkages containing dove-tailed HBC derivatives revealed a hexagonal phase, it was possible to compare their unit cell parameter with HBCs substituted by linear side chains with the same number of atoms. Thereby, the carbon atoms and oxygen atoms are treated as identical, since the molecular masses are close. In Figure 3.22 it is obvious that the ether linkages containing dove-tailed HBC derivatives possess significantly smaller unit cell parameters in comparison to the linear side chains substituted HBCs. This is in good agreement with the molecular architecture, since the linear side chains are much longer. On the other hand, the dove-tailed side chains are more space-filling and bulky leading to a higher steric requirement in the aromatic core periphery. The increased steric demand and decrease of intracolumnar order have also a strong influence on the melting temperature of the materials and will be discussed in detailed in Chapter 5. However, it should be noted that the HBC derivative assigned in Figure 3.22 as dove-tailed with 14 atoms per chains is HBC-$C_3OC_{8,2}$ which is not dove-tailed substituted. HBC-$C_{16,4}$ does not bear any linear side chains, but is assigned as linear substituted. Since both compounds fit exactly into the relationship, there might be an additional effect based on the higher degree of freedom at the ether linkages

which enhance the side chains packing in the core periphery leading to a decrease of the lattice parameters. This in turn results in a high degree of intracolumnar disorder and an extension of the intracolumnar period which compensates in this way the steric demand of the dove-tailed substituents. This effect is amplified when the branching position of the side chains is placed at the core vicinity as it was the case for the β-branched HBC derivatives. The increased mobility and therefore higher steric demand of the β-position dove-tailed side chains hindered an approaching of the aromatic cores and led to extreme longitudinal and lateral displacements of the disc which was verified also by solid-state NMR results (not shown). Therefore, no intracolumnar correlations periods for HBC-C10,6 were observed. This behavior had fundamental consequences on the charge carrier transport along the columnar stacks. The charge carrier mobility decreased dramatically in the mesophase of this compound due to the intracolumnar disorder and lack of a pronounced overlap of the π-orbitals of the aromatic cores.

The observed intracolumnar disorder in the liquid crystalline phase highlights a crucial problem. On the one hand, the space filling side chains provoke this disorder in the intracolumnar packing, which encloses considerable disadvantages for applications in electronic devices, since the major charge carrier transport takes place along the columns. TOF[40] and PR-TRMC[229] measurement independently indicated for different discotic materials that increased disorder in the mesophase is accompanied with a decrease of the charge carrier mobility. But on the other hand, these bulky substituents are necessary to decrease the aggregation of the molecules and therefore to lower the processing temperature (Chapter 5) which is essential for processing. This problem is a new challenge for the design of new single building blocks which include both the facile processing from the isotropic state resulting in the desired alignment of the material and the strong self-association leading a high supramolecular order.

3.3. Examples for pronounced Supramolecular Order

The self-assembly of discotic molecules is determined by the aromatic core size and therefore by the π-stacking interactions. In order to increase the stability within the columns hydrogen-bonding interaction can be utilized. In general, hydrogen bonds are not the strongest non-covalent interaction, but they are essential for the self-assembly of complex superstructures executing as the single main driving force or commonly in combination with the π-π interactions.[230] The relatively weak hydrogen-bonding interaction can be improved by the introduction of multiple H-bonds or H-bonds supported by additional forces. The application of hydrogen bonds opens the opportunity to control the formation of the discotic

core[231,232] as well as of the columnar structures[233].

For a number of HBCs, bearing five dodecyl- or dimethyloctanyl side chains mono- and difunctionalized, by carboxylic acid functions or alcohol groups spaced by different linear chains from the aromatic core the bulk behavior has been analyzed. It was found that the influence of the functionality has only little influence on the thermal behavior. All these HBC derivatives revealed a phase transition to the hexagonal columnar mesophase at ca 100 °C.[234-237], whereby the shortening of the spacer resulted in an increase of the mesophase transition to 221 °C.[238] In contrast, the six-fold functionalization by carboxy or alcohol groups with long tethers decreased the phase transition by about 50 °C.[236]

The HBC derivative (HBC-C_5OH) presented in this work was six-fold substituted by C_5 linear chains each of them bearing an alcohol group. It was expected that alcohol groups interact by hydrogen bonding with units of molecules stacked in the adjacent columns improving the stability of the superstructure. Indeed, the high stability was expressed by the thermal behavior, as the phase transition from the crystalline to the mesophase was shifted to 225 °C in comparison to HBCs substituted by linear side chains. Furthermore, the compound revealed a very poor solubility. For the sample preparation, the material was extruded as a filament above the transition of 225 °C. The temperature-dependent 2D-WAXS patterns are shown in Figure 3.23.

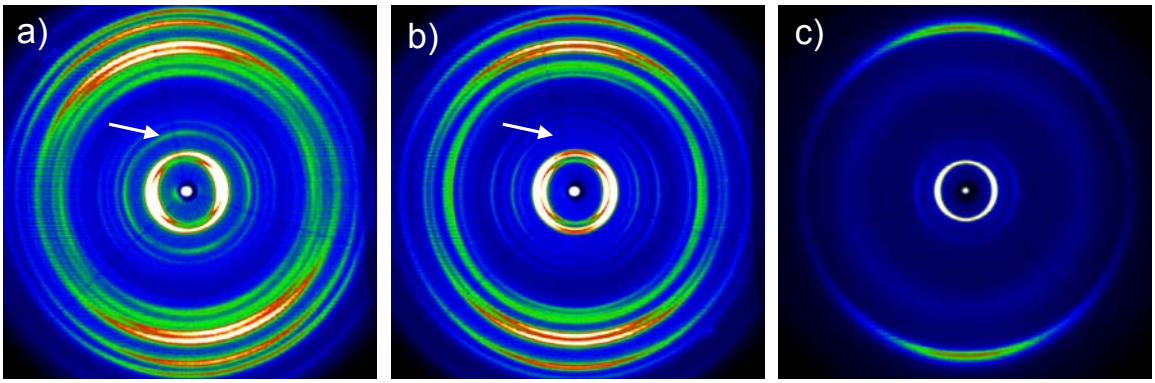

Figure 3.23. *2D-WAXS of HBC-C_5OH at a) room temperature, b) 150 °C and c) 250 °C.*

Figure 3.23a shows a typical 2D X-ray pattern for HBC-C_5OH at room temperature. The large number of the distinct reflections indicted a high degree of crystallinity. The equatorial reflection distribution was fitted to a monoclinic lattice with a=1.84nm, b=1.61nm and γ= 68°. More interesting was the very untypical appearance of several meridional wide-angle reflections. Commonly, non-tilted discs arranged in the columnar structures give rise to

the appearance of only one meridional reflection corresponding to the π-stacking distance. In the case of HBC-C_5OH it can be assumed that the discs are also in the non-tilted intracolumnar order, since no off-meridional reflection were displayed. The meridional reflections appeared at the correlation positions of 0.48 nm, 0.41 nm, 0.39 nm, 0.35 nm and 0.33 nm, whereby the scattering reflections at 0.41 nm and 0.39 nm revealed the highest intensities. Additionally, a meridian reflection at the middle-angle region was observed corresponding to 0.96 nm.

The fix-fold alcohol groups positioned at the relatively short alkyl chains provide an extremely high intracolumnar stability and order. Hydrogen interactions between molecules in adjacent columns, but also between molecules within the same columnar are assumed. This kind of network formation leads to a decrease of the molecular dynamics and therefore to one of the highest degree of intracolumnar order observed for the HBC derivatives. The meridional reflection related to the repeating distance of 0.96 nm suggests a higher order period along the stacking direction. Upon heating this period disappears due to an increased molecular dynamics (Figure 3.23b). Finally, above the phase transition of 225 °C the hydrogen bonding breaks and the molecular mobility reaches the maximum resulting in the characteristic hexagonal mesophase with an intercolumnar packing parameter of 2.22 nm and an orthogonal arrangement of the disc with the π-stacking repeating distance of 0.36 nm (Figure 3.23c). After cooling back to room temperature the high crystalline order of the sample could be reversibly recovered.

In comparison to HBCs monofunctionalized by C_4OH (phase transition from the crystalline phase to the mesophase at 87 °C)[239] and six-fold substituted by C_{11}OH (156 °C)[236], HBC-C_5OH revealed a significant increase of the mesophase transition. This extreme stability of the crystalline phase can be related to the strong hydrogen interactions, whereby the short C_5 side chains seem to support these interactions by peripheral order. The high intracolumnar stability was reflected by the multiple meridional reflections in the 2D-WAXS pattern which have never been observed for discotic materials. These results indicate the important role of the length of the tether and the number of functionalized groups both leading to an improved stabilization of the columnar structures. A similar conclusion was derived for HBC derivatives mono-functionalized by carboxy-groups.[238] Thereby, the phase transition to the mesophase shifted from 70 °C for a spacer C_{10} to 221°C for a C_3 tether.

Another efficient route to introduce columnar stability is the reduction of the number of disordering alkyl side chains. In this case the aromatic core of C46-$(C_{12})_2$ (Figure 2.4a) was symmetrically substituted by two dodecyl chains. The “unwrapping” of side chains plays also an important role for the improvement of the charge migration along the columnar stacks.

Thus, it will be discussed later in Chapter 5. Here the consequences of the reduction of the number of the side chains should be only described. It is well know that asymmetry induces also disorder in the columnar organization resulting in a lowering of the phase transitions and in increasing solubility as reported for HBCs, [240] triphenylenes,[241-243] porphyrins[244,245] As discussed above, HBC(C_{12})$_4$, which is another example for an "unwrapped" disc, did not display an enhanced columnar stability due to the asymmetrical substitution. Since the aromatic core of the C46-(C_{12})$_2$ is symmetrically two-fold substituted by dodecyl side chains, the π-stacking is particularly pronounced leading to high intracolumnar order. Nevertheless, a transition to the liquid crystalline phase was determined at 235 °C which opened the opportunity for the extrusion of the material in a deformable mesophase and the investigation of an oriented sample in the crystalline phase. The 2D-WAXS pattern for the room temperature phase is shown in Figure 3.24. No structural changes were observed by heating the sample above the phase transition.

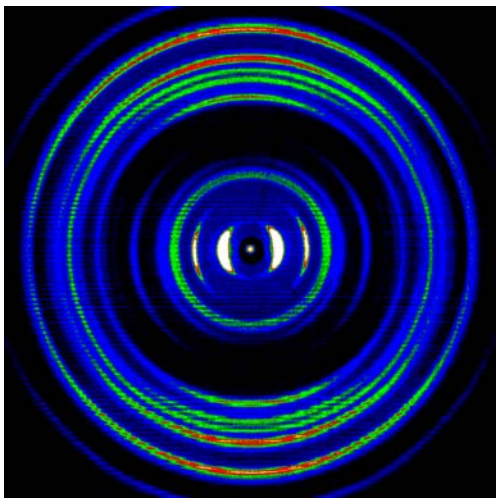

Figure 3.24. *Room temperature 2D-WAXS pattern of C46-(C_{12})$_2$.*

The 2D-WAXS of C46-(C_{12})$_2$ indicates also exceptionally high crystallinity which was based in this case on the reduction of the number of side chains and the symmetrical substitution leading to a pronounced interaction of the aromatic cores. Again, the asymmetrical "unwrapping" in the cases of HBC-(C12)4 and the trialkoxy substituted HBC-(OC12)$_3$ (Chapter 5) resulted in a less ordered supramolecular structure. In the latter case, the isotropization temperature decreased significantly in comparison to the six-fold alkyl substituted HBC derivatives from ca 400 °C to 170 °C due to the high asymmetry. The unit cell of C46-(C_{12})$_2$ was assigned to an orthorhombic lattice with a = 2.55 nm and b = 1.02 nm. Furthermore, numerous of sharp meridional reflections appeared which were positioned at

identical correlation positions, as it was the case for HBC-C_5OH: 0.49 nm, 0.44 nm, 0.42 nm, 0.40 nm, 0.35 nm indicating that the intracolumnar arrangement for both compounds might be the same. Additionally, the appearance of a weak reflection for C46-$(C_{12})_2$ corresponding to a distance of 0.96 nm suggests the same high order period along the columns.

It has been shown that two concepts can lead to the increase of intracolumnar stability. In the first case, functional groups are introduced into the side chains which interact by hydrogen bondings and support the π-stacking interaction. Thereby, the comparison to results reported in literature indicated that the degree of stabilization depends strongly on the length of the tether between the aromatic core and the hydrogen-bond forming group. Hydrogen bonding between side chains of discs in adjacent columns induce also a high intracolumnar order by the formation of a kind of cross-linking. The other possible route is the reduction of side chains which induce disorder and interact on the π-stacking. Thereby, symmetrical substitution of the aromatic core plays an important role for the molecular interaction and ensures the crystallinity. Besides the control of the intracolumnar order, the "unwrapping" is also a concept for the improvement of the charge migration along the columns and will be discussed in Chapter 5.

In comparison to molecules with a high π-stacking interaction which results in the absence of solubility and the formation of a mesophase, both discussed materials revealed a liquid crystalline phase at high temperatures ensuring processibility. On the other hand, the major disadvantages of a pronounced columnar stability are a too high transition temperature to the isotropic phase and a significantly reduced solubility. Both properties limit the processibility of these materials.

3.4. Control of the Superperiodicity along Columnar Structures

The discovery of the double-helix of DNA proved that this supramolecular organization is the most essential and stable structure in which molecules can pack.[246] Following these impressive examples in nature, the leading principle is the transfer of the intrinsic information from the molecular level onto the superstructure. The self-organization takes place by nonbonded packing interactions such as intramolecular hydrogen-bonding or aromatic π-π interactions.[247] The major challenge in supermolecular chemistry is the understanding of these processes and the design of synthetic molecular architectures leading to identical conformations. This would open an important pathway to effectively control the properties of the material.

The appearance of helicity along the stacking direction of the molecules has been reported for various systems and has different origins. The architecture of the central core of helicates plays an essential role during the self-assembly promoted by pi interactions. Thereby, the helical arrangement of helicates[248-252] is driven by the helical and rigid shape of their aromatic cores resulting in a large corkscrew twist. The introduction of steric elements into the periphery of the discotic molecules is another possibility to control helical superstructures. Phthalocyanine derivatives substituted by crown ethers and chiral alkoxy side-chains[10] or by chiral bulky helicenes[253] aggregate into uniformly twisted columnar structures, whereby the chirality of the substituents promotes one-hand sense. In contrary to that, phthalocyanine formed by their achiral counterparts are not.[254]

Interestingly, it is observed by "sergeant and soldiers" experiments[255] that supramolecular chirality can be induced into a columnar achiral system by a relatively small amount of chiral molecules.[256,257] This principle is based on the steric interaction between the chiral and achiral molecules within the column.

3.4.1. Hexa-*peri*-hexabenzocoronenes

For this study two HBC derivatives were prepared with pendant optically active (S)-3,7-dimethyloctanyl branched side chains (HBC-PhC_8^*) and dodecyl linear side chains (HBC-PhC_{12}) each with a phenylene spacer. Both studied compounds consist of an aromatic core substituted by six phenyl rings each. In the first case for HBC-PhC_8^*, (S)-3,7-dimethyloctanyl chains are attached to the phenyl rings carrying a stereogenic center which gives the molecule the chiral character. On the other hand, the second compound, HBC-PhC_{12}, is an achiral dodecylphenyl-substituted hexa-peri-hexabenzocoronene.

The thermal behavior was determined by DSC measurements for a temperature range between –100 °C and 250 °C. It is found that chiral HBC-PhC_8^* reveals no phase transition in the investigated temperature range, whereas achiral HBC-PhC_{12} shows a first board transition at 15.3 °C and a second sharp one at 79.8 °C.

Circular dichroism (CD) experiments were carried out in order to study the effect of the helical supramolecular organization on the optical activity of the materials. The chirality in the solubilizing side chains of HBC-PhC_8^* allowed the investigation of the three-dimensional structure of the aggregates within the films in comparison to the achiral compound HBC-PhC_{12} using CD spectroscopy. CD spectroscopy is a powerful tool to investigate the supramolecular helical organization of molecules which ensemble by interactions. The shape and intensity of the Cotton effect is strongly dependent on the aggregation, which is in turn

temperature-dependent, of the species in solution and indicates the type of organization of functionalized monomer units,[25] oligomers[258,259] and discs shaped molecules[26,260]. Since the CD spectra of helicenes in solutions with higher concentrations and in solid-state films obtained from solution revealed identical information,[249,250] it is assumed that the CD spectra obtained for the HBC derivatives give information about the intracolumnar organization of aggregated disc molecules. An identical experimental procedure has been reported for the analysis of the optical behavior for chiral HBC six-fold substituted by dimethyloctanyl chains.[193]

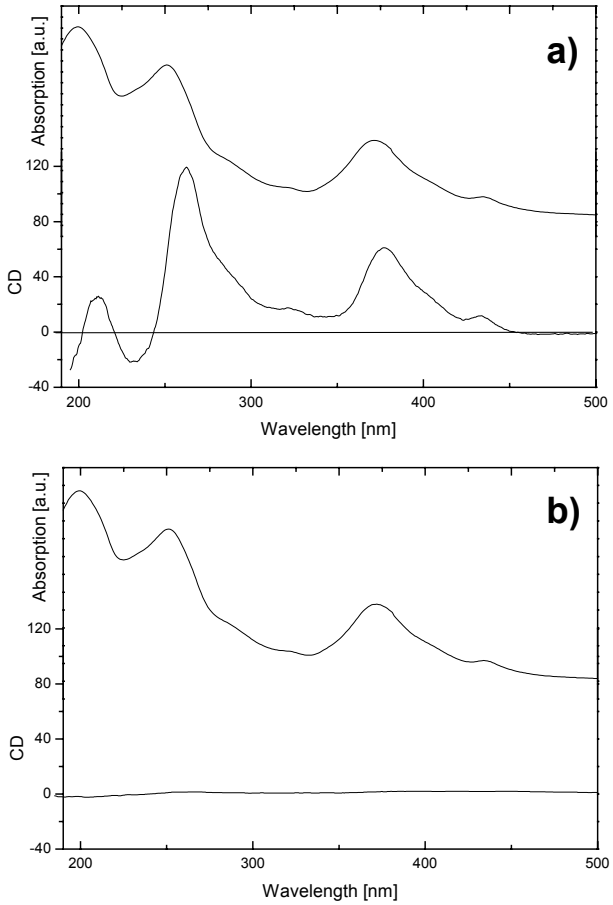

Figure 3.25. *UV-Vis and Circular dichroism of a) chiral HBC-PhC$_8^*$ and b) achiral HBC-PhC$_{12}$, both prepared as a thin film by spin-coating.*

The samples were investigated at room temperature in the solid-state as spin-coated on quartz glass from a chloroform solution. Both UV-Vis and CD spectra were recorded at the same conditions. The two compounds show identical UV-Vis spectra, which are presented in Figure 3.25, due identical molecular architecture. However, a strong difference in CD effect

be can observed.

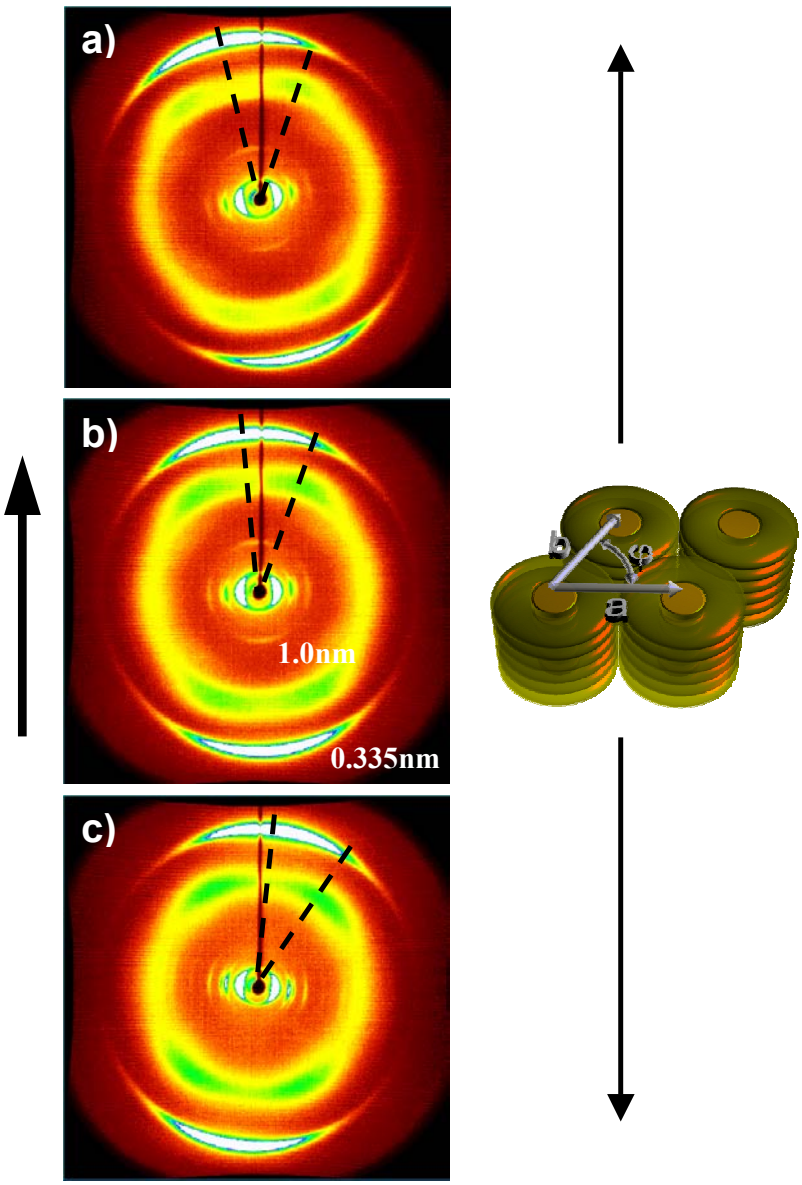

Figure 3.26. *2D-WAXS of an oriented filaments consisting of chiral HBC-PhC$_8$* at a) –100 °C, b) 30 °C and c) at 130 °C. The extrusion direction is indicated by the arrow. The hexagonal unit cell is displayed as a model valid for each investigated temperature.*

The analysis of the CD spectra were performed in analogy to the results reported for triphenylenes[261] and phthalocyanines.[36,262] As expected for an achiral system, HBC-PhC$_{12}$ does not reveal any circular dichronism, whereas chiral HBC-PhC$_8$* displays three strong characteristic CD signals with a positive Cotton-effect at the positions 210 nm, 377 nm and 262 nm. The latter most distinctive signal can be assigned to the pending phenyl rings which

are strongly effected by the neighboring stereogenic center. The peak at 375 nm results from the individual molecule and can be assigned to the aromatic band which is also present in the UV-Vis spectra.[263] From the CD analysis one can assume that chirality in the side chains has an effect on the regularity of the intracolumnar order and therefore on the handedness of the helical twist. In consequence, the achiral compound displays an identical columnar organization however without a preferred rotation of the molecules.

X-ray diffraction studies of both compounds chiral HB-PhC$_8^*$ and achiral HBC-PhC$_{12}$ are presented for three representative temperatures. Therefore intra- and intercolumnar organization is investigated in the different thermal states of the materials. Figure 3.26 shows typical 2D-WAXS patterns for a highly oriented HBC-PhC$_8^*$ filament recorded at different temperatures. The distribution of the distinct reflections in the equatorial plane indicates the considerable orientation of columns in filaments axis and therefore in extrusion direction. This obvious orientation is maintained over the whole investigated temperature range. The appearance of many higher order equatorial reflections is correlated to the pronounced intercolumnar order. The relation of the positions of these scattering intensities suggests a two-dimensional lateral unit cell for the columnar arrangement. The relative reciprocal spacing of the equatorial arcs indicates a hexagonal columnar packing for HBC-PhC$_8^*$ in all the investigated temperatures. The assignment of the scattered intensities by the Miller's indices is presented in Figure 3.27. The unit cell parameters decreases slightly with temperature decrease due to a slight mobility decrease of the substituted side chains.

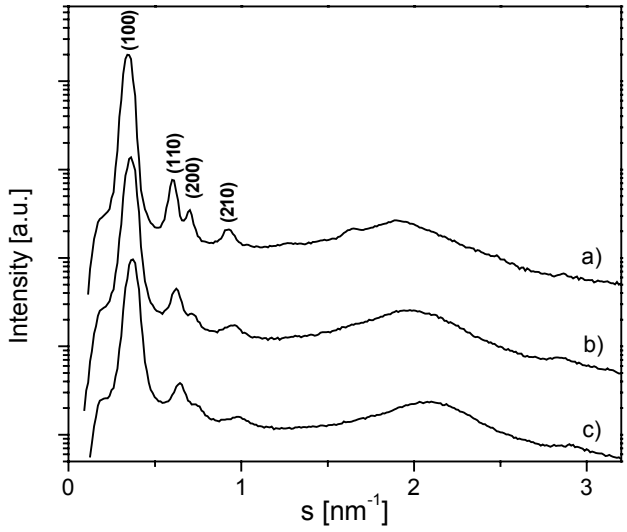

Figure 3.27. *Assignment of scattering intensities by the hexagonal Miller indexes hk0 for the chiral HBC-PhC$_8^*$ measured at a) 130 °C, b) 30 °C and c) –100 °C.*

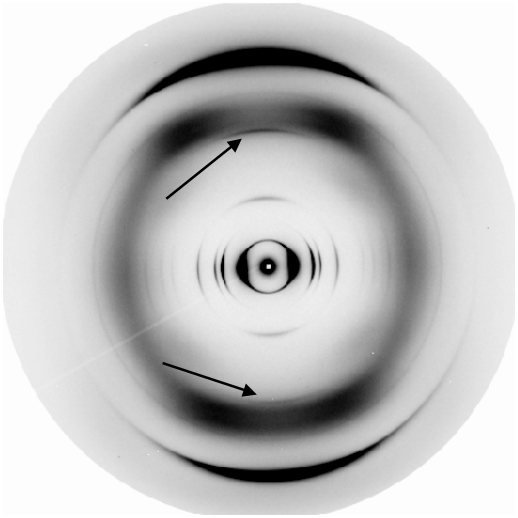

Figure 3.28. *Scattering of microfocus synchrontron radiation for HBC-PhC$_{12}$ (performed by Dr. Mari Cruz García Gutiérrez at Grenoble, France). The arrows indicate the reflections.*

The two distinct meridional reflections at wide-angle region correlate to the cofacial π-π stacking of 0.33-0.34 nm of molecular discs along the columns. Thereby, the aromatic core molecular planes are perpendicular to the columnar. This distance is in agreement with the characteristic π-π distance. Additionally, a further peak at the meridian is observed in the middle-angle region corresponding to an intracolumnar period of 1.0 nm. Although, this meridian reflection is less intensive than the π-π stacking peak, the two distances are in strong relation suggesting an additional long-range periodicity along the columns. This can be verified by the calculation of 1.0/0.33=3 revealing that exactly each fourth molecule is in correlation. An additional 2D WAXS experiment using a synchrotron radiation with a microfocus beam revealed another higher order reflection at the meridional corresponding to 0.5 nm (see Figure 3.28). This confirms that a helical arrangement with laterally rotating molecules is the only explanation for the appearance of these meridional peaks which are in strong relation with each other. The calculated correlation makes clear that the helical pitch consists of three molecules. On the other hand, this helical period of each fourth molecule over a longer range is less distinctive than the correlation between two adjacent molecules. By taking into account that each fourth molecule has to perform a turn of 60° in order to achieve the same configuration, it is possible to determine the turn of each disc towards the next molecule. Dividing the rotation angle by the number of molecules in each helix 60°/3 results in the rotation angle of 20° for each molecule with respect to the neighboring molecule. The weakly pronounced superperiod might be also the reason of a certain variation of the rotation angle around 20°.

To investigate whether the helical supramolecular arrangement is dominated by the chiral nature of the substituents, the structure of a second HBC derivative was studied bearing also six-fold phenyl rings at the corona of the core, but linear C_{12} side chains (HBC-PhC$_{12}$). Figure 3.29 presents the characteristic X-ray pattern for this compound recorded at the same temperatures as for HBC-PhC$_8$[*]. The extruded HBC-PhC$_{12}$ sample reveals pronounced long-range orientation indicated by the distinct reflections in the equatorial corresponding to the intercolumnar distances. The obvious similarity of the 2D WAXS pattern to that of HBC-

PhC_8^* indicates strongly an identical helical superperiodicity along the columns. Identical peak positions were found in the meridional as described already above. On the other hand, the intercolumnar arrangement at room temperature differs from that at the low and high temperature phases as suggested by the equatorial scattering intensity distribution. The unit cell at room temperature is assigned to an orthorhombic lattice, whereas the low and high temperatures phases indicate identical hexagonal unit cells. The assignment of the Miller indices of the three relevant temperatures is displayed in Figure 3.29. The unit cell parameters and assigned phases determined for both compounds in the investigated temperatures are summarized in Table 3.5 which are based on both thermal phase behavior and structure analysis.

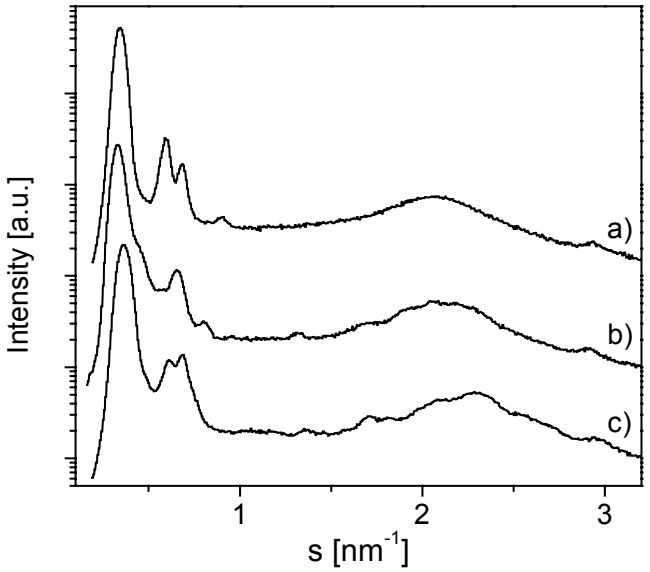

Figure 3.29. *Assignment of the scattering intensity distribution by using the hexagonal Miller indexes hk0 for achiral HBC-PhC$_{12}$ at a) 130 °C, b) 30 °C and c) –100 °C.*

Besides the scattering intensities related to the intra- and intercolumnar correlations, a diffuse isotropic halo ring appears in the WAXS patterns for both compounds HBC-PhC_8^* and HBC-PhC_{12} which can be assigned to the alkyl chains located in the columnar periphery. Furthermore, two split broad and distinct reflections are obvious in the off-meridian wide-angle range at 2.22 nm^{-1} superimposing the amorphous scattering of the alkyl chains at this position. To obtain the most favorite intramolecular configuration the energy of the molecules has to be minimized by a propeller-like tilting of phenyl rings towards the aromatic core plane. The split reflections indicate a tilting angle of 20° and 30° of the phenyl rings depending on the thermal phase. For all investigated temperatures the correlation distance of

the reflections remains at the same correlation position of 0.45 nm. Interestingly, the calculation of the cosine of 0.45 nm and 0.33 nm reveals an angle of 42.5° which is in excellent accordance with the helical arrangement of the molecules. Since each disc performs a turn of 20° to the adjacent molecule, the phenyl rings in the periphery are shifted 20° and 40°, respectively, to the phenyl rings belonging to the adjacent molecule.

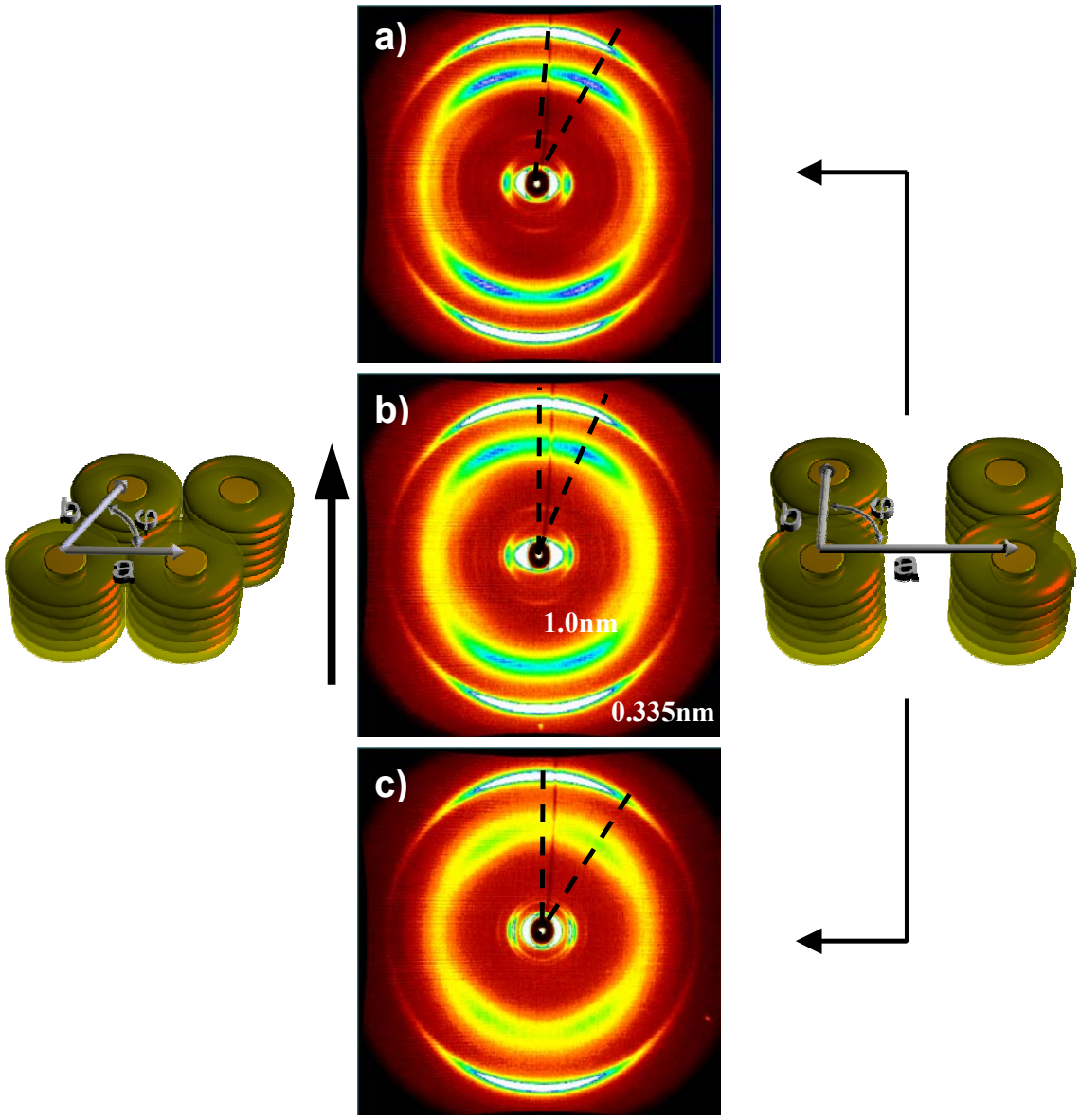

Figure 3.30. 2D Wide-angle X-ray diffraction the achiral HBC-PhC_{12} of oriented filaments at a) –100 °C, b) room temperature and c) 130 °C. The arrow indicates the extrusion direction.

It seems that the correlation of the phenyls of adjacent molecules being shifted 40° in respect to each other is the origin of the discussed reflections. A schematic molecular model demonstrates in Figure 3.31 the helical arrangement of four molecules together with the calculated values. Solid-state NMR experiments revealed that the phenylene rings are tilted out of the core plane by flipping between angles of –20° and 20° being in good agreement with the X-ray results.[264] The resulting structure is a propeller-like arrangement of the phenyl rings in the periphery of the cores as displayed in Figure 3.31 which seems to be the most efficient organization in the stacks.

It is interesting to note that these split reflections observed for the HBC-PhC_{12} sample are in all phases broader than for HBC-PhC_8^*, especially at the low temperature region. The reason might be the difference of the substituted side chains; one bearing a stereogenic center, while the other compound carries a linear alkyl chain. Both compounds revealed identical intracolumnar packing, however molecules of with different rotation sense. CD spectroscopy indicates a 1:1 of both right and left-handedness for HBC-PhC_{12}. In the case of HBC-PhC_8^*, the phenyl rings lying near the stereogenic center of the branched alkyl chains are more strongly influenced and transform the chirality to the core resulting in a uniform rotation sense giving rise to peaks in the CD spectra in the range between 200 – 450 nm. This in turn generates a better packing of the phenyl rings in the periphery reflected in sharper scattering intensities of these split peaks.

Table 3.5. *Unit cell parameters of chiral HBC-PhC_8^* and achiral HBC-PhC_{12} resulting form wide-angle X-ray diffraction.*

Compound	Temperature	Unit cell parameters [nm]	Assigned phase
HBC-$PhC_{8,2}^*$	-100 °C	a = b = 3.06	Col_{hho}
	30 °C	a = b = 3.18	Col_{hho}
	130 °C	a = b = 3.25	Col_{ho}
HBC-PhC_{12}	-100 °C	a = b = 3.43	Col_{hho}
	30 °C	a = 3.02 b = 2.13	Col_{oho}
	130 °C	a = b = 3.45	Col_{ho}

Abbreviations: Col_{hho} - ordered hexagonal helical columnar phase, Col_{ho} - ordered hexagonal columnar phase, Col_{oho} - ordered orthorhombic helical columnar phase.

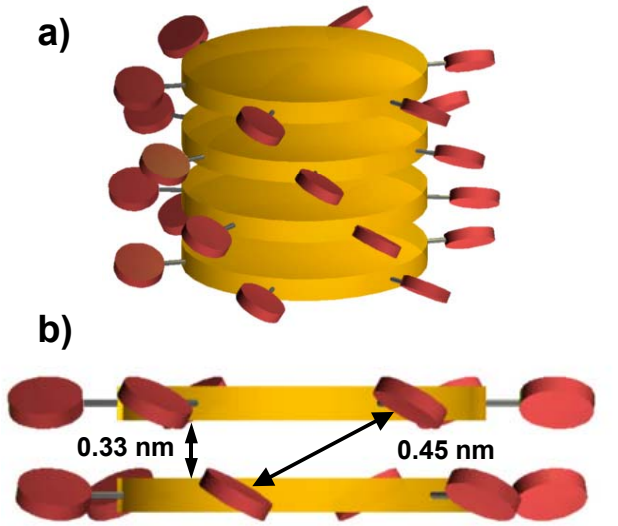

Figure 3.31. *a) Model for the intracolumnar arrangement within one helical pitch; b) representation of the correlation between the substituted phenyl rings of adjacent molecules. The phenyl rings of a corresponding disc are tilted by ca 25° to the core plane. Due to simplicity the alkyl chains attached to the phenyl rings are not shown. Therefore, this model is valid for both materials the chiral HBC-PhC$_8$* and the achiral HBC-PhC$_{12}$.*

Helical assemblies have been investigated most frequently by CD spectroscopy in solution and in bulk,[265] but relatively rarely by scattering techniques. [32,266,267] This study is a rare case where both techniques are applied complementary as performed for the investigation of the supramolecular organization of oxazoline-derived ligands.[268]

The superstructure of both materials, HBC-PhC$_{12}$ and HBC-PhC$_8$*, fulfills the strict classification of a plastic columnar discotic material which possesses three-dimensional order with minor fluctuations in positions, which have been determined earlier by solid-state NMR experiments[30], at the points of a cubic lattice.[219] The presented superstructure is the second unique helical plastic phase reported for a HBC derivative. Recently, Wu et al. described a helical arrangement for HBC derivatives substituted by rigid diphenylacetylene arms bearing bulky mono- or trialkoxy groups.[31,269] The discs are rotated successively by 15° with respect to each other leading to a helical pitch of 5 molecules. The appearance of plastic phases in columnar structures is rare and has only been reported also for triphenylens[221] and self-organized dendrimers[270,271].

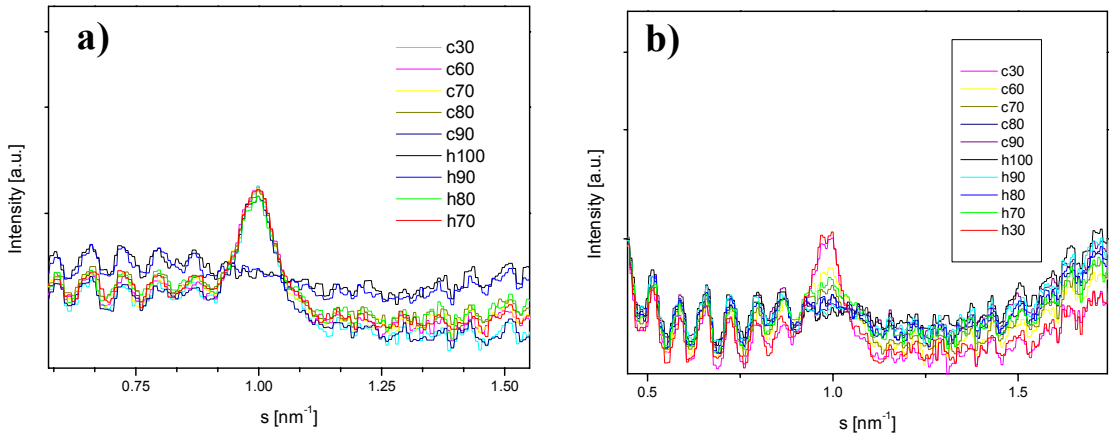

Figure 3.32. *Temperature dependent WAXS analysis of the meridian reflection at s=1 nm^{-1} corresponding to the helical pitch for a) HBC-PhC$_{12}$ and for b) HBC-PhC$_8$*. The change of the peak intensity with temperature is reversible.*

It has been also shown for the HBC derivatives substituted by the rigid diphenylacetylene arms that the degree of helical supramolecular organization decreased in the high temperature phase.[31,269]Both phenyl-substituted compounds reveal a comparable behavior upon heating the samples which was monitored by temperature-dependent X-ray scattering measurements (see Figure 3.26c for HBC-PhC$_8$*and Figure 3.30c for HBC-PhC$_{12}$). For both cases the middle angle reflection in the meridian disappears indicating the loss of helical organization at the higher temperature range. A precise temperature dependent WAXS experiment of this temperature regime proved (Figure 3.32) that the meridian reflection corresponding to the helical pitch disappears at the same temperature for both compounds. Thereby, a sharp decrease of the intensity in the case of HBC-PhC12 takes place between 80 °C and 90 °C, whereas it declines for HBC-PhC$_8$* continuously. By cooling back the samples the characteristic helical arrangement returns. The high lateral and longitudinal mobility of the molecules is an explanation for the decline of the helical organization, since this structural change it is accompanied for HBC-PhC$_{12}$ also with the solid-solid thermal phase transition.

Another interesting effect could be observed during investigating the same extruded HBC-PhC$_{12}$ specimens after six month annealing it at ambient conditions. Surprisingly, this sample reveals numerous new distinct higher order reflections which mainly appear off-meridional. Figure 3.33 illustrates the extent of structural change between the sample directly after extrusion and the annealed one indirectly by intensity analysis of a 2θ integration between 15° and 17°. Furthermore, it is important to note that this state is thermally reversible. The unit cell as well as the intracolumnar distances did not change during the structural transition in comparison to the primary sample indicating that the main molecular

rearrangement takes place only in the intracolumnar long-range. This reorganization is considered as a relaxation process which is possible due to the high lateral and longitudinal mobility of the HBC-PhC$_{12}$ molecules at that phase. Moreover, it describes the ability for self-healing which is an essential factor in electronic device applications. In contrary, chiral HBC-PhC$_8^*$ does not reveal such a relaxation phenomena what is quite surprising due to the chemical similarity to HBC-PhC$_{12}$. One possible explanation could be the different mobility of the discotic molecules and therefore the ability to reorganize.

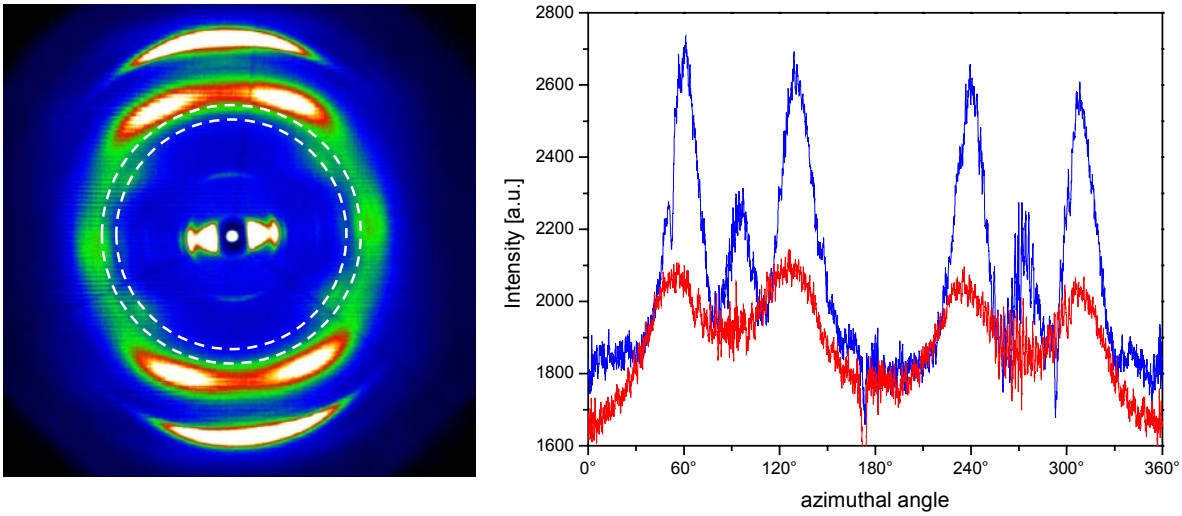

Figure 3.33. *Left: WAXS pattern of extruded filament of HBC-PhC$_{12}$ after relaxation for six months. The dashed circle indicates the theta-theta integration in this pattern as well as in Figure 3.30b. Right: intensities dependence from the azimuthal angle for HBC-PhC$_{12}$ directly after extrusion processing (red) and the same sample after six month (blue).*

In this study the formation of helical superstructures and the role of molecular design on intracolumnar arrangement in columnar systems based on two hexa-peri-hexabenzocoronene derivatives has been investigated which are of almost identical molecular architecture. Both compounds indicate an identical helical intracolumnar long-range order, with small differences in the intercolumnar arrangement, which depend on the thermal phase of the corresponding material. The phenyl rings directly to the aromatic core attached influence decisively the intracolumnar organization due to their bulky size in the columnar periphery. Additionally to their bulky size the phenyl rings have to perform a tilt towards the core plane in order minimize energy. The only conceivable possible arrangement of the discotic molecules is a rotation of each molecule caused by these steric interactions of the phenyl rings which cannot be placed exactly above each other resulting in the helical

arrangement. Although, the tilt angle of the phenyls changes slightly at different phases, the periodicity of the helix is not influenced. On the contrary, the attached alkyl chains differ in the chirality and control the uniformity of the handedness. Thus, helicity is induced by steric interactions of the substituents, whereas supramolecular chirality depends on the chiral character of the side chains and the stereogenic centers, respectively. However, these latter elements are no obligation for helicity. The mobility of the molecules is another important factor which dominates the helical organization. At room temperature (ordered hexagonal helical columnar phase) at which the mobility of the molecules decreases and the phenyl rings reach their maximum rigidity, the highest supramolecular order has been observed, whereas with increasing molecular mobility the degree of helical arrangement declines significantly. Initially, it was assumed that at the low temperature range a more ordered long-range conformation of the helix appears leading to a more distinct wide-angle meridian reflection. At this temperature range the mobility of the molecules decreases and the phenyl rings reach their maximum rigidity. However, we could not observe a more ordered helical structure.

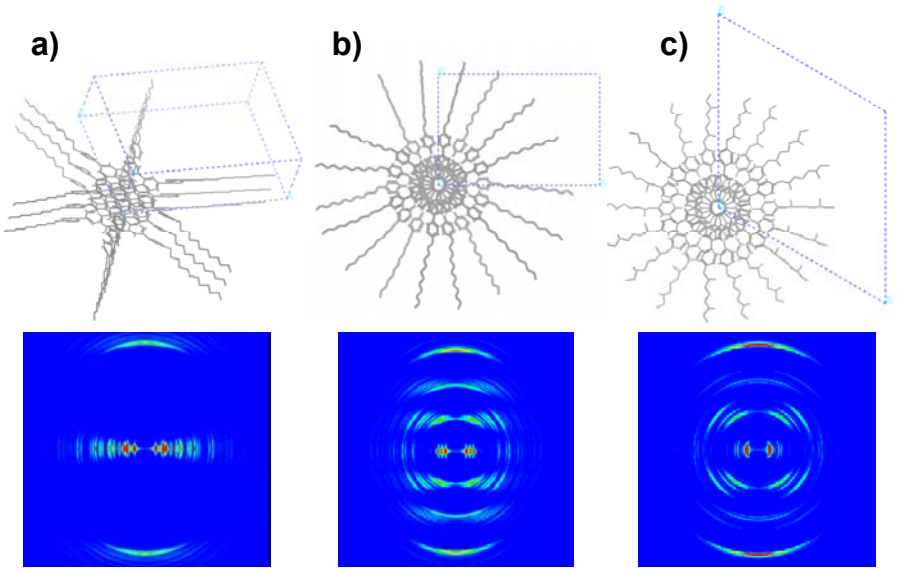

Figure 3.34. Cerius[2] simulations of the 2D WAXS scattering pattern for different intracolumnar periods with a) the typical orthogonal intracolumnar arrangement of the HBC-PhC$_{12}$ discotic molecules within the determined orthorhombic lattice, b) the HBC-PhC$_{12}$ molecules with the assigned molecular rotation and c) HBC-PhC$_8$* discs organized in the intracolumnar helix in the hexagonal lattice found for the room temperature arrangement.

Computer simulations can confirm the supramolecular organization of polymers[272-274] or discotics[31,266] derived from scattering experiments. The simulations will clarify the role of the helix within the HBC-PhC$_8^*$ and HBC-PhC$_{12}$ columnar structure on the X-ray scattering

pattern. As presented in Figure 3.34a and 3.34b the assigned columnar arrangement for HBC-PhC_{12} in an orthorhombic unit cell with and without helicity was studied. The unit cell without the helical superstructure (molecules stack orthogonal into the columnar structure) shows only reflections on the meridian at wide-angle region corresponding to the intracolumnar order within the columns, namely the π-π stacking distance of 0.34 nm, and reflections at the equatorial small-angle range related to the intercolumnar distance and the unit cell formation. When a helix with the same characteristics as revealed in this study is introduced into the columns additional scattering intensities appear in the meridian at low- and middle-angle regions assigned as (hk1) and (hk2), respectively. These reflections are split in off-meridional peaks and none of these is positioned exactly on the meridian.

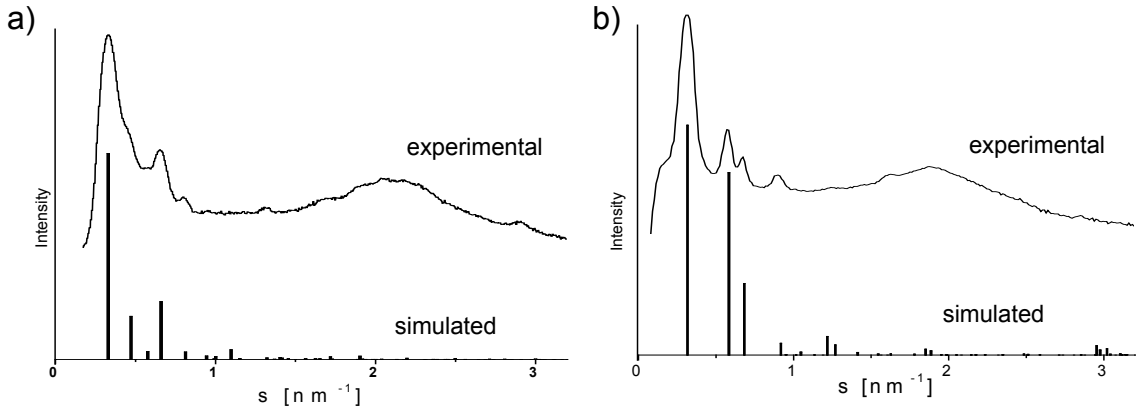

Figure 3.35. *Cerius[2] simulations of the scattering intensity distribution and the comparison to the experimental plots for a) HBC-PhC_{12} and b) HBC-PhC_8[*].*

When the molecular orientation decreases these reflections become broader and finally overlap each other at the meridian. The most intensive peaks besides the inter- and intracolumnar distances are the split ones at the low-angle range indicating the (hk1) helical pitch. In our experiment these reflections are not split and are in comparison to the simulation results quite weak. A reason for the less distinctive correlation of the helical pitch is the high disorder which is related to the liquid crystalline molecular rotations and intracolumnar fluctuations. Therefore, only intracolumnar disc correlation is possible leading to the appearance of the meridional reflections. In contrast, the Cerius[2] simulations consider only crystal structures and not liquid crystalline state with a higher molecular dynamic. Therefore, in the simulations also intracolumnar disc correlation are possible which lead to the appearance of higher order reflections in the (hk1) and (hk2) lines. In general, the simulations make clear that for a higher ordered helical structure meridional reflections are not possible, except for the simple molecular distance. The variation of the rotation angle of 20° for each

molecule could also influence the distinction of the helical pitch. The (hk2) reflections are superpositioned by the split peaks related to the tilted phenyl rings.

3.4.2. Extended Aromatic Cores of C96

In the following the effect of the peripheral substituted bulky phenyl rings onto the intracolumnar organization of a C96 derivative is studied which possesses in comparison to HBC discs a much more extended aromatic core. Thereby it is important to investigate if the supramolecular structure and the plastic phase can be found in systems consisting of larger aromatic cores, but also phenyl-substituted as the HBC derivatives described above. It should be also note that the attachment of the phenyls results in a considerably higher solubility and a broaden of the liquid crystalline phase for the HBC derivatives.

The investigated C96 derivative was therefore also six-fold dodecylphenyl-substituted (C96-PhC_{12}). Due to the larger π-stacking area in comparison to the HBCs, C96-PhC_{12} did not reveal any phase transition or significant solubility. The strong π-interaction between the molecules prevented also a plasticity formation of the material which could allow to prepare a specimen by filament extrusion for the 2D-WAXS experiments. Therefore, only a powder X-ray was recorded which is presented in Figure 3.36a. One can observe a small-angle reflection corresponding to 3.06 nm and a second reflection related to the π-stacking distance of 0.35 nm. However, besides the amorphous halo of the side chains no other reflection peaks could be observed indicating the absence of any higher intracolumnar order related to helical disc arrangement. It might be assumed that the influence of the peripheral phenyl rings is limited to smaller aromatic cores due to the strong π-interactions of the C96 aromatic cores which presents any lateral fluctuations of the disc. The formation of a plastic or liquid crystalline phase requires an adequate interaction between the solubilizing alkyl chains in the periphery and the π-stacking interactions which is not fulfilled for C96-PhC_{12}. This behavior is relatively unexpected, since C96-C_{12} revealed a high solubility and a liquid crystalline behavior and is in strong contrast to HBC-C_{12} and HBC-PhC_{12}.[205] It can be only guessed that the poor processibility of C96-PhC_{12} might be the origin of a helical stacking of the discs provoked by the bulky phenyl rings leading to an interlocking of the molecules. This increased intracolumnar interaction between the C96 molecules could result therefore in the poor solubility and absence of plasticity of the material which disables an investigation of the helical packing.

Since C96-C_{12} possesses liquid crystallinity, two *t*-butyl groups were attached asymmetrically as bulky substituents, which could induce a rotation of discs with respect to

each other, to a C96 derivative (Figure 3.36b). It is well known that *t*-butyl groups are bulky and induce high sterical requirements in the periphery of the aromatic cores.[275-277] For instance, the investigation of the aggregation in solution revealed that hexa-*t*-butyl-hexa-*peri*-hexabenzocoronene does not self-assembly and that the molecules are monomeric at any concentration in 1,1,2,2-tetrachloroethane-d_2.[238] This behavior is explained by the high steric impact of the *t*-butyl groups which hinder the disc approaching leading to the absence of π-stacking.

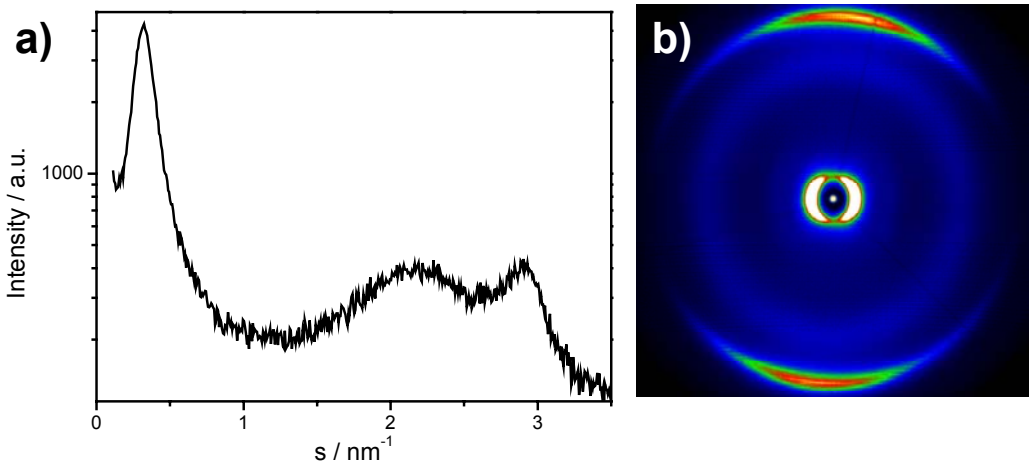

Figure 3.36. a) *X-ray diffractogram of C96-PhC_{12} and b) 2D-WAXS pattern of an extruded filament of C98-$(C_{12})_4(^tBu)_2$ (both at room temperature).*

In the case of C98-$(C_{12})_4(^tBu)_2$ (Figure 2.4b) it was assumed that the two *t*-butyl groups induce a steric hindrance on one side of the aromatic core which would provoke a rotation of the molecules towards the adjacent disc. The 2D-WAXS pattern of an extruded filament (Figure 3.36b) exhibits only two characteristic reflections: one broad corresponding to 2.57 nm (2.96 nm within a hexagonal lattice, in comparison to a = 3.35 nm of the fully substituted C96-C_{12}) and the π-stacking reflection related to 0.34 nm. Meridional reflection indicating the helical arrangement of the discotic molecules could not be observed. It is suggested that steric requirements of the two *t*-butyl groups are not high enough to influence the stacking.

The introduction of columnar helicity with C96 discs as building blocks does not follow the correlations found for HBC derivatives. In both presented C96 cases, no helical superstructures could be observed. One reason might be the strong π-interaction of the extended aromatic cores which do not allow a significant face-to-face displacement by rotation. Furthermore, the steric effect of the substituents might be also too poor since the area of a C96 disc is twice that of an HBC core.

Chapter 4

Self-organization in Solution and in Solution Processed Thin Films

A pronounced high long-range order is required in a thin active layer consisting of an organic semiconductor in order to reveal a good performance in a field-effect transistor. For the fabrication of such films adequate processing techniques are required. Furthermore, these processing methods have to fulfill the industrial requirements of simplicity in manufacturing and low cost fabrication. The processing from solution is the only possible proceeding being in agreement with these prerequisites. Since the nucleation and growth of the HBC derivatives determine the optimal processing conditions during the zone-casting, as the initial step, the self-aggregation in solution and morphology formation in drop-cast films has been investigated. It will be shown that the steric influence of the side chains plays an important role in the self-organization in solution and solution processed films. The study is divided into crystalline and non-crystalline materials, whereby the former are substituted by linear and branched alkyl side chains. The chapter is completed by comparing the self-aggregation in solution of the different compounds concerning both the molecular architecture and the processibility.

4.1. Solution Processing of Crystalline Hexa-*peri*-hexabenzocoronenes

4.1.1. Hexakis-dodecyl-hexa-*peri*-hexabenzocoronene

4.1.1.1. Self-Aggregation in Solution and in Drop-Cast Films of HBC-C_{12}

Several studies of the self-aggregation in solution of planar aromatic molecules such as macrocycles,[278-2803] helicenes,[281,282] porphyrins,[283] and phthalocyanines[276,284,285] revealed that ^{1}H NMR spectroscopy is a powerful tool for the investigation due to stacking interaction. Thereby, the ^{1}H NMR chemical shifts are strongly concentration dependent and provide insight into the structural arrangement of the aggregates. Very recently, Kastler et al. have analyzed the aggregation in solution of HBC substituted by different alkyl chains.[238] In general, in comparison to other systems, such as shape persistent phenylacetylene macrocycles (PAMs), the self-association for HBCs occurs in a concentration range, which is at least one order of magnitude lower. The ^{1}H NMR experiments were carried out at a temperature of 30 °C using 1,1,2,2-tetrachloroethane-d_2 as solvent and revealed that HBC-C_{12} possessed the highest self-aggregation among the studied HBC derivatives. The aromatic resonance for this compound reached a plateau at a concentration lower than approximately $1x10^{-6}$ M indicating monomeric molecules in the solution. The self-association constant of K_a = 898 $Lmol^{-1}$ in the above mentioned solvent for HBC-C_{12} was determined by curve fitting of the ^{1}H NMR results emphasizing that the solution aggregation was pronounced, as evidenced by a lower solubility. At a concentration of $4.75x10^{-5}$ M, the average aggregate of HBC-C_{12} consisted of approximately six discs, but with a broad distribution.

Since solution processing is an important step during the fabrication of electronic devices based on organic materials, it is essential to relate the self-aggregation of the HBC derivatives in solution with the surface morphology. Therefore, the self-assembly of the HBC molecules, which were deposited by drop-casting and spin-coating, at the interface between solvent and substrate is investigated. [286-288]

Single long nanofibers were found from a 10^{-7} M solution of HBC-C_{12} in THF, which were 1.2 nm high and ca. 20 nm wide, exceeding even several hundreds of nanometers in length (Figure 4.1a). These fibers seemed to consist of a monomolecular layer with several columns lying parallel along the fiber axis, whereby the molecules were arranged edge-on. By using a higher concentration of 10^{-4} M the film from HBC-C_{12} under same conditions exhibited high anisotropy in the structure (Figure 4.1b), which consisted in mono- and/or

bilayers.

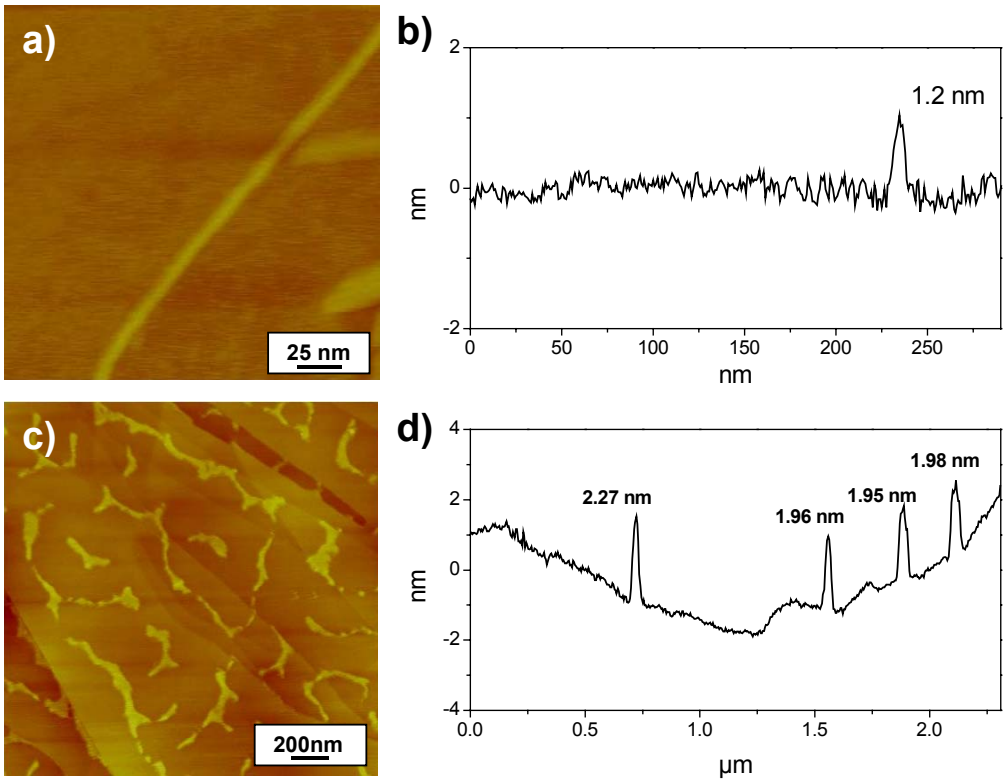

Figure 4.1. *AFM images in tapping made on HOPG surface of spin-coated films of HBC-C_{12} from a) a 10^{-7} M (cross-section is shown in b)) and c) and 10^{-4} M THF solution, d) presents the height cross-section of the image in c).*

The morphology of a drop-cast film (10^{-4} M in toluene) of HBC-C_{12} (shown is Figure 4.2) consisted of several hundred micrometer long, birefringent microfibers which are displayed also in the AFM topography images in Figure 4.4. Their dimensions slightly changed with different solvents. By casting from toluene longer, but thinner microfibers were observed in comparison to the films prepared from THF or other solvents with lower evaporation temperatures. In all cases, the morphology was uniform within the drop-cast film, whereby the columnar alignment coincided with the microfiber axis as it was previously proven.[234] This tendency to create highly anisotropic structures was even observed within a polymer matrix.[289] A closer inspection by means of the electron microscopy, which is shown in Figure 4.3c, of the supramolecular organization of a spin-coated HBC-C_{12} layer on a coal support revealed large domains with well arranged columnar structures oriented mainly in the deposition direction.

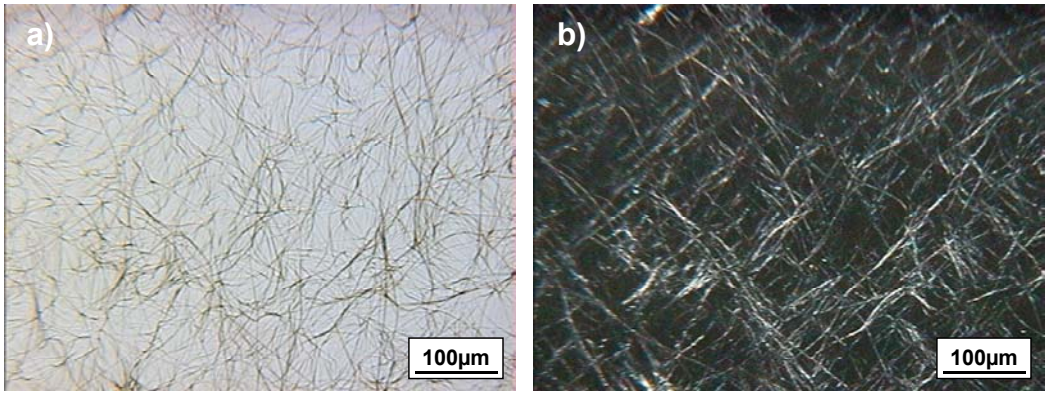

Figure 4.2. *POM image of drop-cast HBC-C12 from a 10^{-4} M toluene solution a) without and b) with cross-polarizers.*

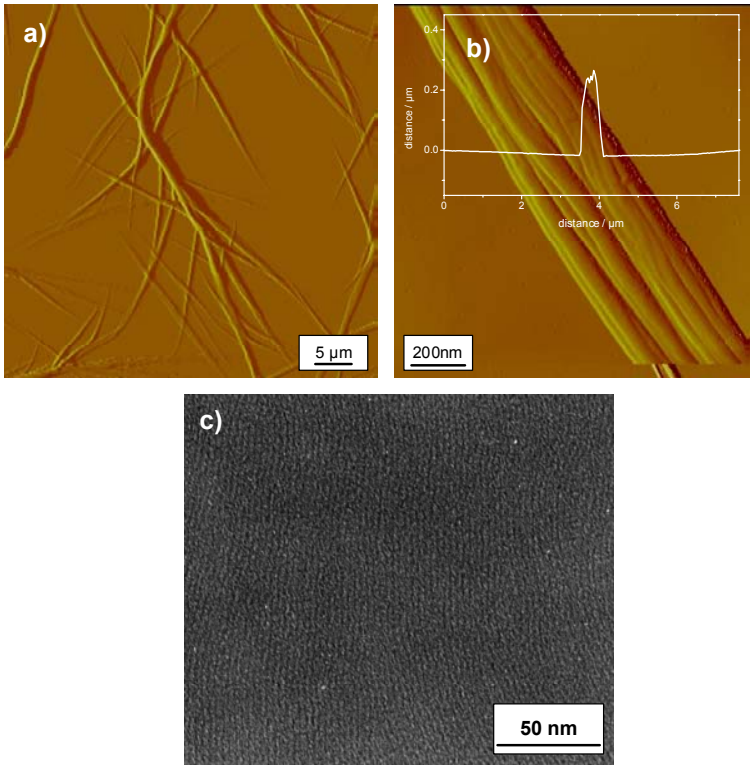

Figure 4.3. a) *AFM topography of the microfiber morphology of a drop-cast HBC-C_{12} drop-cast film, b) higher resolution AFM image (inset: cross-section of the microfiber), c) electron microscopy image of a spin-coated HBC-C_{12} film on a coal support.*

The solution aggregation study and the investigation of the morphology from solution of HBC-C_{12} have revealed an extremely high self-association of the molecules in several solvents in comparison with other HBC derivatives. Furthermore, HBC-C_{12} drop-cast from

solution such as THF or Toluene forms long ribbons exceeding a length of several micrometers indicating the strong aggregation in solution. Due to this pronounced self-aggregation leading to directed growth, this compound revealed to be a promising candidate for the zone-casting processing. However, the morphology and structure of the zone-cast HBC-C_{12} thin layers were strongly dependent on the processing conditions.

4.1.1.2. Zone-casting of HBC-C_{12}

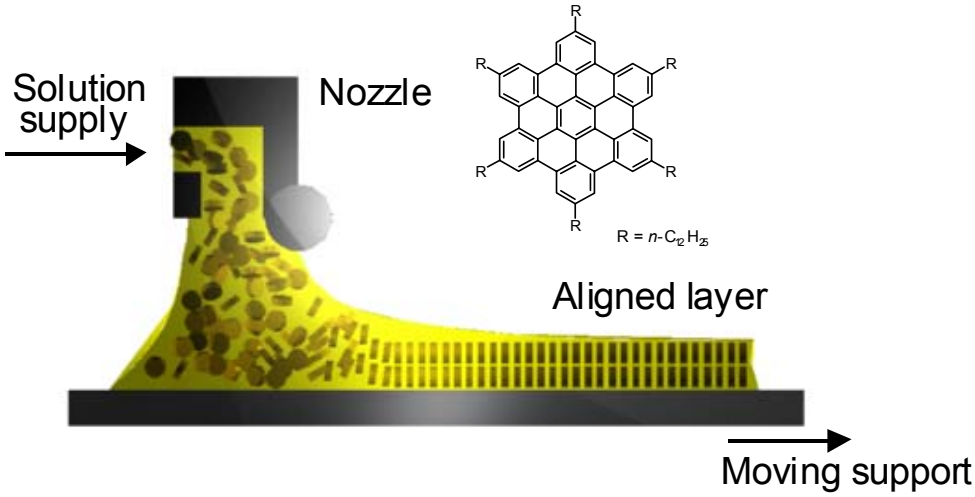

Figure 4.4. *Schematic illustration of the zone-casting of discotic HBC-C_{12}.*

Figure 4.4 presents a schematic model of the zone-casting procedure of the self-organizing discotic HBC-C_{12}. Since the solution aggregation study showed that the HBC-C_{12} molecules are only monomeric below concentrations of 10^{-6} M, but above this concentration the discotic molecules assemble into aggregates consisting of up to 6 molecules, the illustration in Figure 4.4 of single discs in the solution might be not fully true. But nevertheless, one can imagine not ordered species which are deposited in the solvent onto the support.

Following the concentration at a fixed point on the surface of the support, it can be observed that during the solvent evaporation the concentration increases until the saturation is attained. Thereby, the size of the aggregates in the solution increases due to the increasing concentration. At the critical concentration these long aggregates nucleate at the support undergoing in the same time kind of a lyotropic phase. Afterwards the material crystallizes directionally on the moving support. At the aggregates already nucleated at the surface, new molecules assembled creating in this way a homogeneous film.

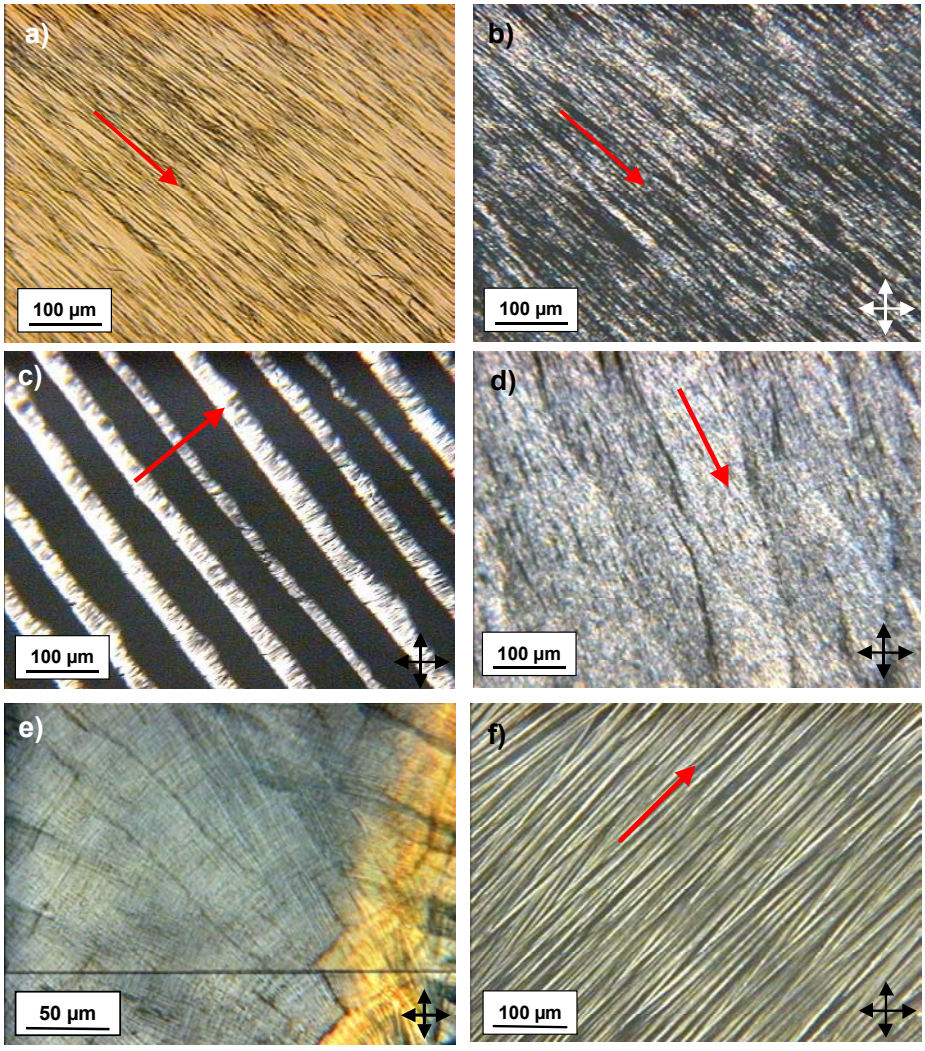

Figure 4.5. *POM images of examples of different morphologies of zone-cast HBC-C_{12} at different processing conditions as 0.6 mg/ml THF, 50 °C/40 °C 35 µm/s a) without and b) with cross-polarizers; c) 0.1 mg/ml, 50 °C/40 °C, 35 µm/s; d) 0.8 mg/ml THF, 55 °C/40 °C 35 µm/s, e) 1 mg/ml toluene, 93 °C/93 °C 75 µm/s, f) 0.5 mg/ml THF, 55 °C/40 °C 35 µm/s (first temperature is the solution temperature, whereas the second was determined for the support, the velocity is given for the support). The red arrow in the images indicates the moving direction of the support.*

Figure 4.5 shows the different film morphologies obtained from different zone-casting conditions which differed significantly from each other indicating the high sensitivity of the organization of the molecules at the surface on the processing parameters. In general, it was found that at adequate conditions identical film morphologies can be acquired as observed for the drop-cast layers, but aligned in the deposition direction. When HBC-C_{12} was zone-cast from THF at a concentration of 0.6 mg/ml, the characteristic ribbon structures appeared,

which were also in this case highly birefringent in polarized light (maximum birefringence at 45° of the fiber axes toward the polarizer/analyzer axes) and uniaxially oriented in the moving direction of the support (see Figures 4.5a and 4.5b). The density of these microfibers was strongly dependent on the concentration. So, by increasing the concentration to 0.8 mg/ml in THF the alignment of the ribbons was maintained, but the number of these structures per area increased significantly as it can be seen in Figure 4.5c. The lowering of the amount of material in ml THF resulted in an interesting periodic morphology which often appeared for not optimized processing conditions and which was also observed in some parts of the drop-cast films. The reason for this characteristic morphology pattern is a too low concentration. At such processing conditions the solvent evaporates from the meniscus, but due to the too low concentration the material does not nucleate onto the support. However, since the concentration within the meniscus increases with further solvent evaporation and new material is supplied, finally the compound crystallizes onto the support resulting in turn in a lowering of the concentration in the meniscus. This leads to a breakdown of further material deposition. And again this cycle begins with the solvent evaporation from the meniscus in which the concentration is again too low for material nucleation. As the POM image displays, the periodicity of the deposited material is relatively regular. The distance between the periods in which the compound nucleates can be controlled by the concentration. The application of toluene as solvent did not show any success in the zone-casting. This is in good accordance with the ribbons obtained by drop-casting using toluene which were significantly thinner in comparison with structures attained from THF. Finally, at adequate conditions these fibrous features transformed slowly into a homogeneous film morphology (Figure 4.5f).

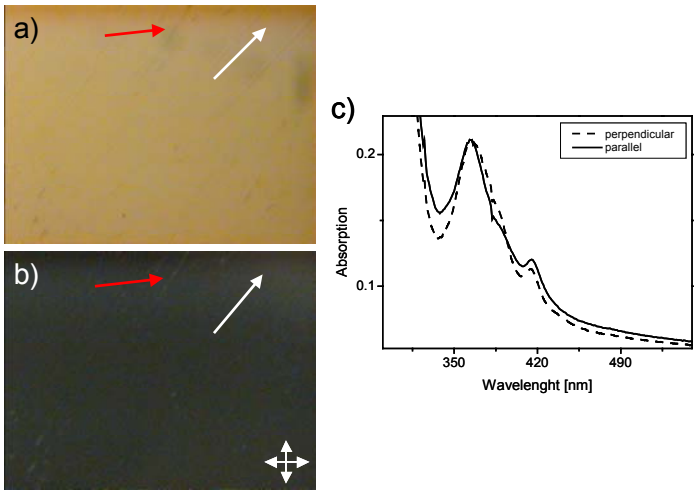

Figure 4.6. *a) Optical image of zone-cast HBC-C_{12} at optimized processing conditions, b) the same sample in polarized light (the white arrow indicates the casting direction, whereas the white one shows the same part on the film), c) absorption in polarized light measured parallel and perpendicular to the casting direction.*

At optimized conditions of 0.3 mg/ml, 51 °C/42 °C and 35µm/s, it was possible to zone-cast a homogenous film over the whole width of the nozzle (Figure 4.6a). Interestingly, these surface layers did not reveal any birefringence in polarized light in any position with respect to the polarizer/analyzer axes as presented in Figure 4.6b. A supporting result was obtained from the investigation of the absorption of polarized light measured parallel and perpendicular to the casting direction. The absorption intensity in both directions was identical leading to a dichroic ration of 1 (see Figure 4.6c). Such optical behavior is characteristic for isotropic structures, but not for oriented surface layers which typically reveal a high optical anisotropy with the change of the position in polarized light. The reason for this characteristic behavior in polarized light will be given after the structure evaluation of the films.

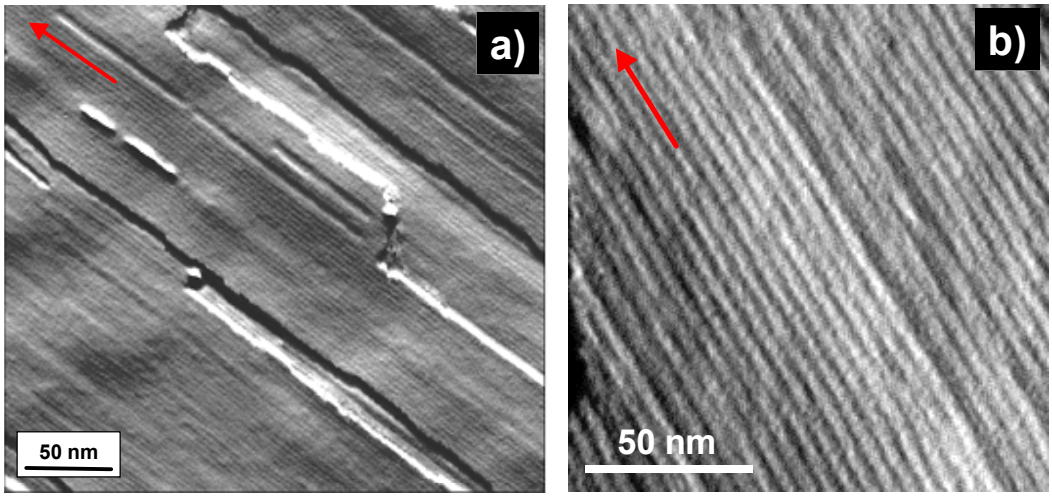

Figure 4.7. *AFM topography (amplitude images) of the HBC-C_{12} zone-cast surface layer as taken in the tapping mode with a) the large AFM scan and b) scan of image a) with a significantly smaller scan size (red arrows indicate the deposition direction).*

Atomic force microscopy (AFM) is one of the most effective tools applied extensively in chemistry and biology to investigate surface topographies in nanometer scale of various specimens. Therefore, this technique was also used in order to study the topography of the zone-casting surface layers obtained at the optimized conditions. The scans of the film surface were first performed in the tapping mode in order to avoid possible damage of the film features. At room temperature the AFM investigation revealed a homogeneous film morphology over a large area. Furthermore, a terrace-like morphology can be observed in Figure 4.7a with step-heights which are multiples of ca. 2.1 nm indicating a monomolecular or multimolecular arrangement. A film thickness of ca 20 nm was determined by using the AFM method after removing the layer in some places. Scans with higher magnifications shown in Figure 4.7b reveal the layer surface as a columnar structure on the molecular level.

The columns are uniaxially oriented in the deposition direction with exceptionally high column length and typically coherent over distances on the order of 200-500 nm, corresponding to more than 400 molecules (assuming an intracolumnar spacing of ca 0.5 nm). An apparent spacing of 5.2 nm of the columns is visible which is twice the value of the simple intercolumnar distance of 2.6 nm and in this case the average lateral column spacing. This result might indicate a packing of paired columns which could result from the characteristic intracolumnar herringbone arrangement of the discotic molecules.

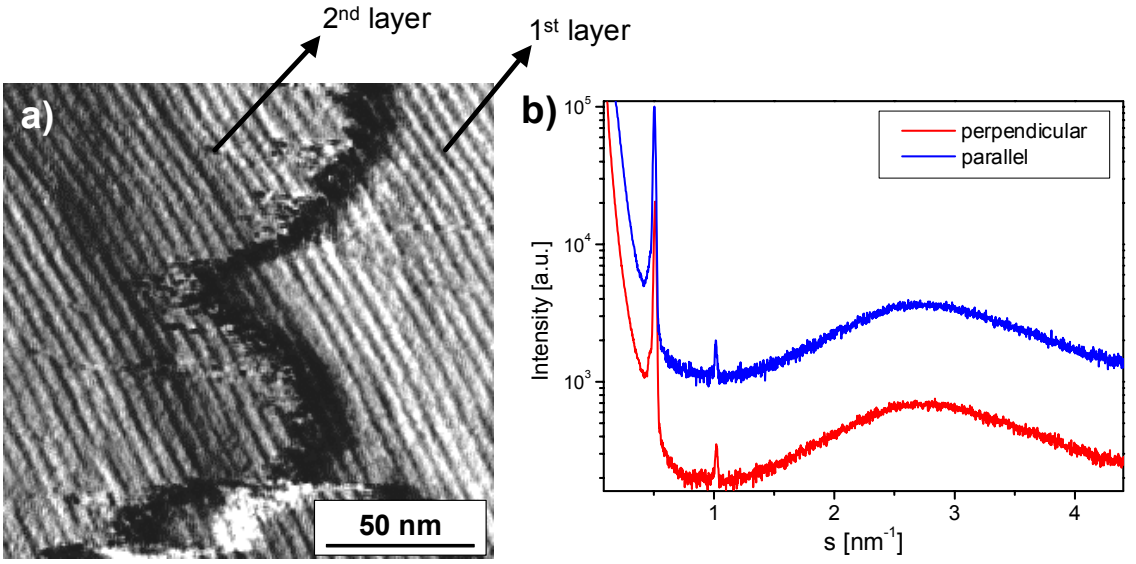

Figure 4.8. *a) AFM topography (amplitude image) taken in the tapping mode of the zone-cast HBC-C_{12} film, by removing parts of the first monolayer the second one is visible; b) large area X-ray diffraction in reflection mode of zone-cast HBC-C_{12} measured parallel and perpendicular to the casting direction.*

Additionally, by scan-induced etching the first monolayer was scratched away and the underlying layer of columns (see Figure 4.8a) became visible. Thereby, the pairs of columns in successive layers lay one on top of each other with the same uniaxial alignment. The step height of both layers was determined to be 2.1 nm. The large-area X-ray diffraction (XRD) in reflection mode (Figure 4.8b) revealed only one sharp reflection and its 2nd order at 1 nm^{-1} corresponding to the step height observed by AFM. Since in this experimental set-up the scattering vector is oriented perpendicular to the surface only periodicities which are arranged to the surface normal can be displayed. Therefore, the correlation distance of 1.98 nm can be related to the out-of-plane arrangement of the columns. The appearance of only one reflection peak indicates that there is little variability in the layer spacing normal to the surface. Moreover, the second order reflection suggests a highly ordered out-of-plane structure over the whole film thickness. The XRD measurement performed parallel to the columnar

alignment is identical in intensity and peak positions to the one taken perpendicular to the orientation confirming again the high order. It is important to note that the intracolumnar periodicities did not appear in the XRD recorded parallel to the columnar axis. This is exact correlation with the supramolecular structure as this result indicates a parallel orientation of the columnar axis to the plane of the support and a possible edge-on arrangement of the discotic molecules.

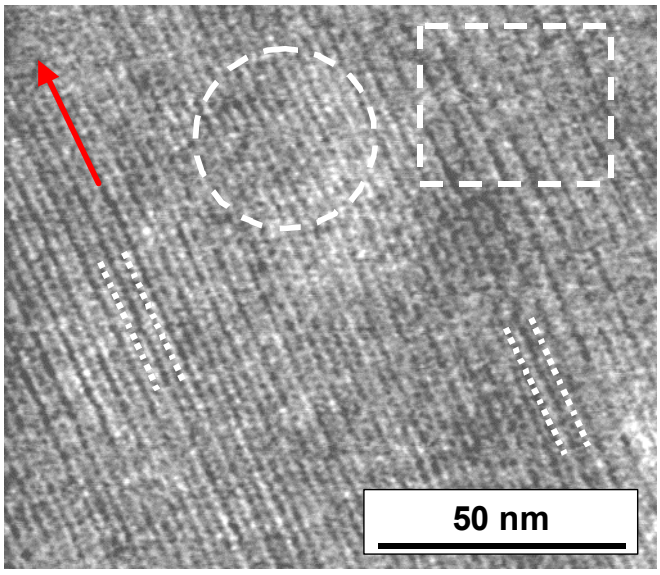

Figure 4.9. *High magnification AFM scan of the topography taken in the contact mode of the zone-cast HBC-C_{12} layer. (red arrow indicates the deposition direction).*

Since in the tapping mode the tip is exposed to all the force interactions with the surface and during the scanning procedure is for a short time in contact with the surface, it is more sensitive to the film surface, but possesses therefore a poorer resolution in comparison to the contact mode. In the latter scanning mode the tip is in the attractive force regime and in permanent contact with the surface resulting in an enhanced resolution of the surface morphology. Indeed, Figure 4.9 displays an AFM image of zone-cast HBC-C_{12} taken in the contact mode where one can see single columnar features which visualized in the tapping mode consisted of two columns. Due to this enhanced resolution, one can see more than one contrast pattern: first, the contrast is the same for adjacent columns (circle), second, paired columns form rows (square), or third, every second column gives stronger contrast (dotted lines), leading to apparent spacing of ca. 5.2 nm. This effect is probably due to different local packing of aliphatic chains which, however, does not influence considerably the average lateral column spacing of ca. 2.6 nm.

The step height of 2.1 nm of the columnar layers determined from Figure 4.8 and the

lateral distance of columns of 2.6 nm give together a two-dimensional rectangular unit cell which assigns the intercolumnar packing. But this is in strong contrast to the lattice determined for bulk HBC-C_{12} which was found to be also rectangular, but with considerably larger dimensions of a = 2.38 nm and b = 3.05 nm. In general, unit cell dimensions are highly dependent on alkyl chain packing, and it is expected that the packing differs significantly between the bulk and at the solid-air interface of these films. In regards to the apparent existence of different domains at the surface, three immediate explanations exist. The most simple is that there is a unique unit cell and the variability results from one or the other plane of the rectangular column packing, (100) or (010), being parallel to the film surface. Another possibility is surface reconstruction, which though not commonly reported for organic materials, has been observed in phase separated block copolymers. A third possibility is the coexistence of more than one unit cell (polymorphism) with sides parallel to the surface corresponding to the different lateral spacings seen in Figure 4.9.

In order to gain a deeper insight into the supramolecular arrangement of the discotic HBC-C_{12} within the zone-cast surface layers, the structure was additionally studied by using high-resolution transmission electron microscopy (HR-TEM) combined with electron diffraction. HR-TEM images as presented in Figure 4.10a confirm the homogenous morphology of the HBC-C_{12} zone-cast film which was already observed by using the AFM technique down to the nanometer scale. At higher HR-TEM magnification single columnar features appear along the casting direction with perfect columnar orientation suggesting a high supramolecular order. The in-plane average intercolumnar distance of 2.48 nm was derived from the Fast-Fourier-Transformation (FFT) pattern (inset in Figure 4.10a) which also revealed higher-order peaks emphasizing the long-range uniformity of columnar alignment in the casting direction, whereby the column length exceeded by far the investigated area. The intracolumnar stacking period of the discotic molecules of 0.49 nm was determined from the low intensity meridional peaks in the FFT pattern. Although, these periodic features were very sensitive to the high energetic electron radiation, the filtered inverse FFT image revealed an obvious intracolumnar periodicity corresponding to the stacking of the discs. From the fact that these columnar superstructures are formed by the self-assembly of the discotic molecules, an edge-on arrangement of the molecules was concluded. The columnar orientation visible in the HR-TEM image in Figure 4.10a is very similar to the one visualized by means of atomic force microscopy (AFM). Taking into account that AFM gives information only about the surface and HR-TEM gives the information about "bulk" morphology of the thin layer, the similarity of the images obtained by these techniques is very important. Strong contrast in the HR-TEM image with a periodicity corresponding to the distance between the columns proves that the columns in successive layers are positioned one on top of each other, correlating to a

rectangular columnar packing.

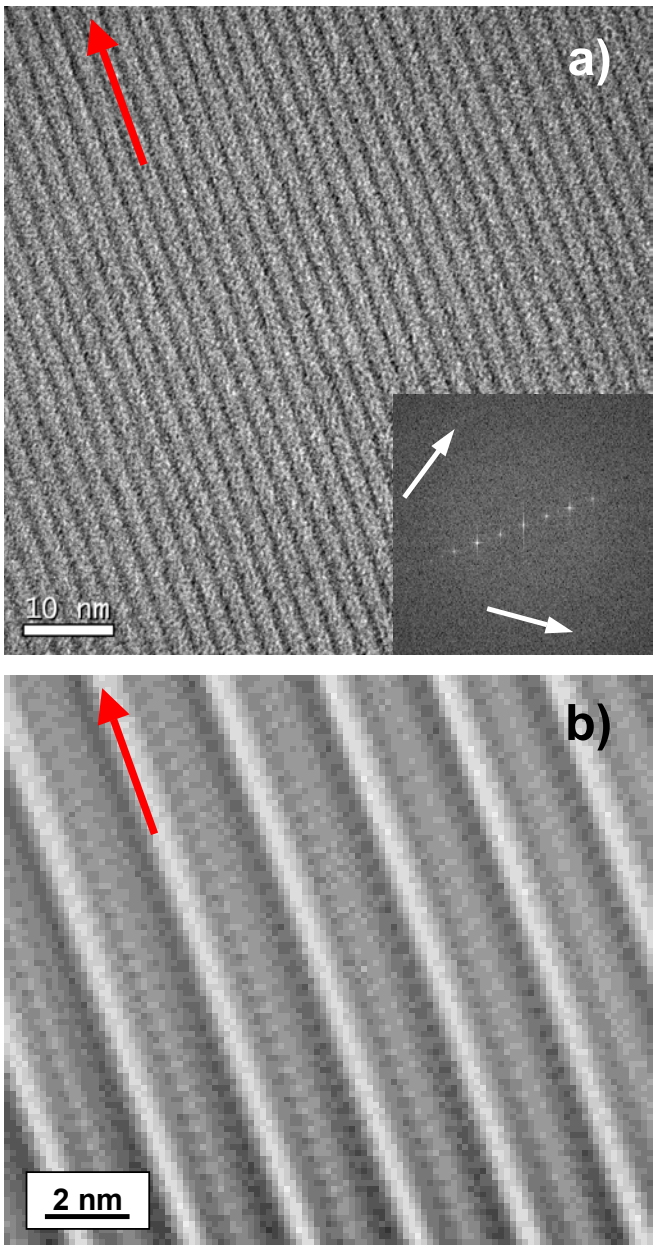

Figure 4.10. *a) Large area image from high-resolution transmission electron microscopy of a zone-cast HBC-C_{12} layer displaying a homogeneous film formation with single columnar features lying in zone-casting direction, inset: Fast-Fourier transform (FFT) image confirmed structural order of columns with an intercolumnar distance of 2.48 nm. The equatorial higher order peaks indicate the pronounced columnar orientation. The intracolumnar stacking is represented by weak and diffuse meridional peaks (indicated by white arrows), b) Filtered inverse FFT (IFFT) image showing the intermolecular periodicity within the columns. The red arrows indicate again the deposition direction.*

The visualization of single columns by itself already suggests a high supramolecular order, because only well defined elements can be seen as a projection in transmission mode of the electron microscopy as it is schematically presented in Figure 4.11. This conclusion is further supported by the electron diffraction studies described below. On the other hand, since the intracolumnar periodicity is barely visible in the HR-TEM image, the positions of the discotic molecules within adjacent columns cannot be strongly correlated. A converse molecular tilting angle in columns lying on top of each other might be a reason for the invisibility of these periodic features.

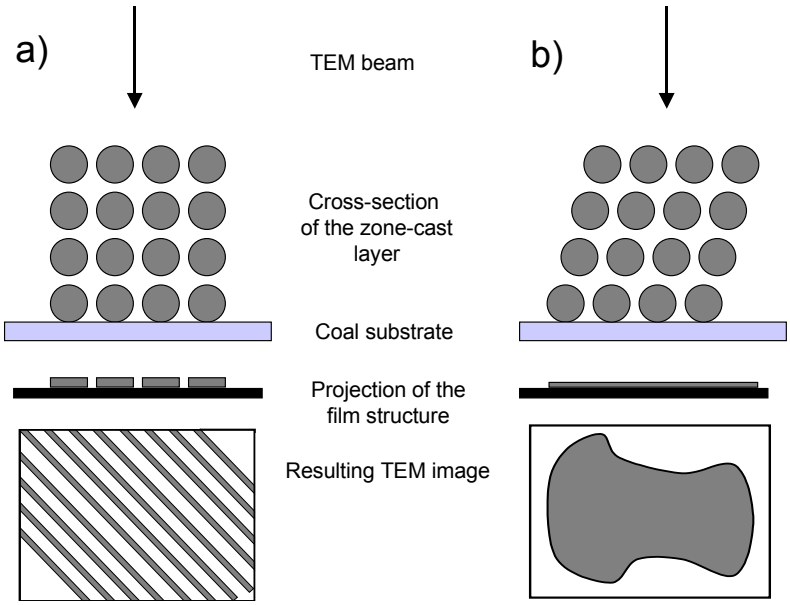

Figure 4.11. *Schematic representation of the HR-TEM results obtained for the zone-cast HBC-C_{12} layer, the visualization of the columnar structures in the transmission mode indicates that the columns are positioned one on top of each other as in a), this is in contrast to the intercolumnar arrangement in b) which would not reveal any information about the order.*

The electron diffraction shown in Figure 4.12 exhibits a pattern characteristic of a crystalline and highly ordered zone-cast HBC-C_{12} layer at room temperature. Furthermore, this pattern includes essential information about all characteristic in-plane inter- and intracolumnar periodicities. The regular columnar organization with a repeating distance of 2.48 nm seen in the TEM image was also evident as the first peak in the equatorial reflection distribution assigned as the (h00) plane. Since the columnar arrangement corresponds to a herringbone structure the (100) reflection, being double the value of the simple in-plane intercolumnar distance, was not displayed.

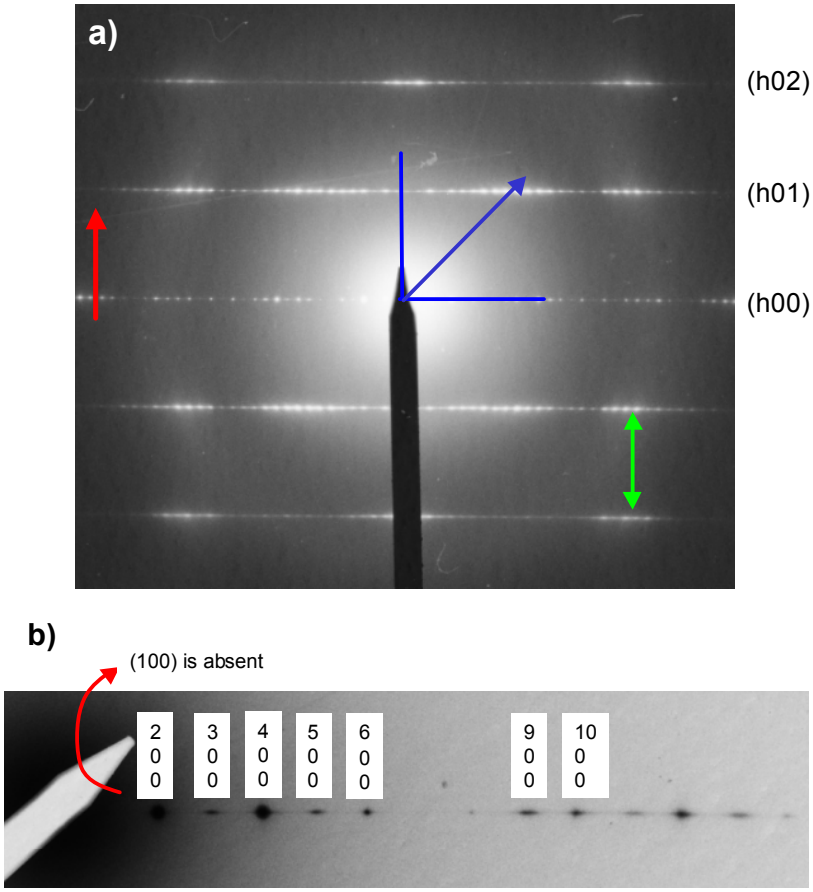

Figure 4.12. *a) Electron diffraction of a zone-cast HBC-C_{12} layer (red arrow indicates the casting direction, the blue one outlines the reflections corresponding to the molecular tilting and the green one shows the intracolumnar periodicity), c) assignment of the equatorially distributed reflections indicating the in-plane intercolumnar order by using the Miller's indexes (hkl).*

The assumption of the absence of this peak corresponding to a period of 4.96 nm was verified when the positions of the equatorial reflections were fitted to a mathematical relation assigning these reflections to one packing parameter of a two-dimensional unit cell. The significant difference in intensity between the odd and even (h00) reflections emphasized the relation of adjacent columns with discs of different tilt (herringbone structure).[290] The resulting tilting angle of the molecules was calculated from the reflections with maximum intensity in the (h01) line. The determined angle was approximately 45° towards the columnar axis with a rotation axis perpendicular to the support. The characteristic cofacial distance of 0.34 nm is related to the maximum intensity of the (h01) reflections, whereas the intracolumnar period of 0.49 nm corresponds to the positions of the reflection lines.

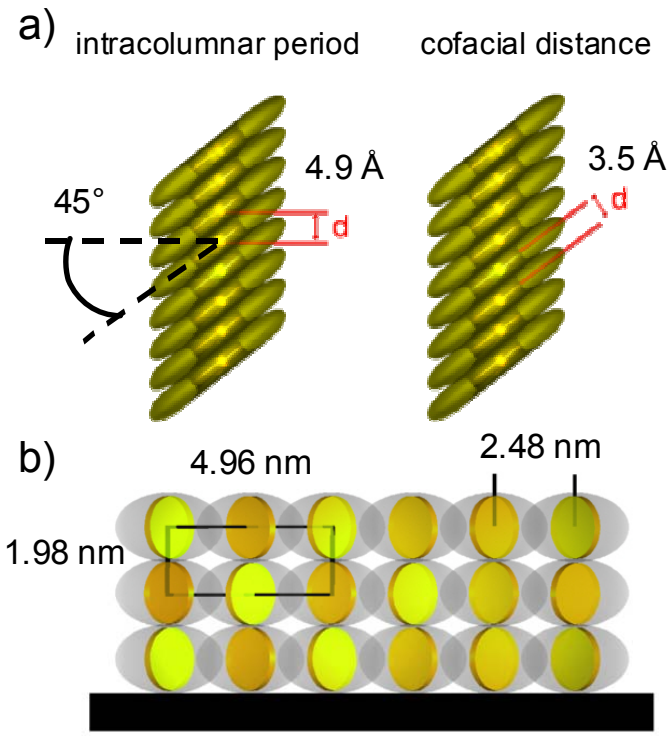

Figure 4.13. *a) Schematic illustration of the intracolumnar arrangement in the zone-cast HBC-C_{12} layers. Discotic molecules show a molecular tilting of 45° which gives two characteristic reflections corresponding to the intracolumnar period and the cofacial distance between two adjacent discs and b) primary schematic presentation of a cross-section of a zone-cast HBC-C_{12} layer. The 2D lateral orthorhombic unit cell assignment of the HBC-C_{12} columnar arrangement in the crystalline phase is based on TEM and XRD results (the aromatic core is represented as the disc and the side chains are shown schematically as surrounding ellipsoids).*

By combining the data from both the X-ray and electron scattering techniques, an orthorhombic unit cell consisting of tilted HBC-C_{12} molecules in the crystalline phase was identified as presented schematically in Figure 4.13. The small out-of-plane correlation distance can be explained by an irregular distribution of the alkyl chains in the core periphery.

A more detailed picture of the supramolecular structure of the zone-cast films has been obtained by using Grazing Incidence X-ray Diffraction which was performed in a collaboration with Dr. Dag W. Breiby, Dr. Oliver Bunk and Dr. Theis I. Sølling from the group of Dr. Martin M. Nielsen, Danish Polymer Center, Risø National Laboratory, Roskilde, Denmark. The GID studies were carried out at the z-axis diffractometer at the wiggler beamline BW2 at HASYLAB, DESY, in Germany. The results have been reported in great detail elsewhere,[291] but nevertheless one example of the results is presented in Figure 4.14.

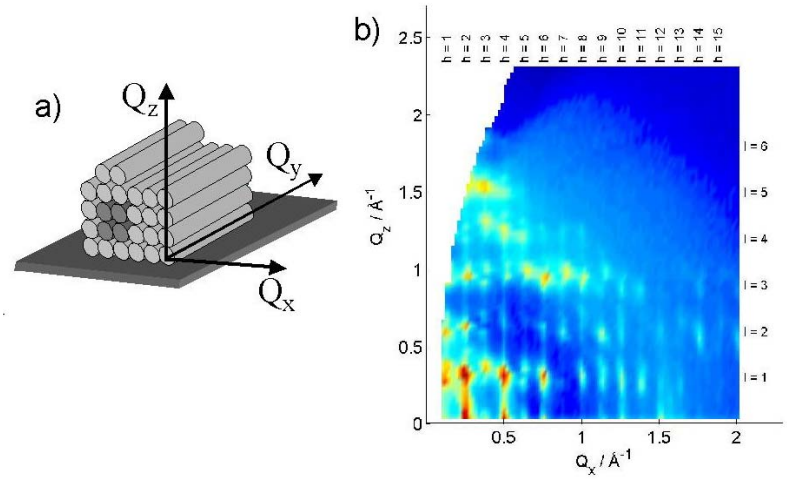

Figure 4.14. *a) Illustration of the HBC columns on the substrate and the orientation of the reciprocal coordinate system, b) picture of the Q_xQ_z plane for Q_y = 0, obtained by doing repeated scans with the point detector. The step lengths were 0.02 and 0.04 Å^{-1} in the Q_x direction and Q_z directions, respectively. The 'forbidden' region near the Q_z - axis cannot be reached by the GID technique. This kind of picture cannot be obtained using e.g. an area detector because the sample orientation differs for different reflections. The vertical streaks are crystal truncation rods. h and l denote Miller indices.*

The synthesized "picture" in Figure 4.14 shows a cross section of reciprocal space corresponding to the "equatorial" plane being perpendicular to the molecular stacks (i.e. Q_y = 0). It was obtained by taking repeated Q_x scans for increasing Q_z values using a point detector. The many higher order reflections are evidence for a well-ordered structure. The molecules were evidently highly bi-axially oriented, as indicated by the sharp peaks found in both the Q_xQ_y and the Q_xQ_z planes.

The closely spaced peaks in the Q_x direction corresponded to the intercolumnar distance of about 24.5 Å. If scanning in the Q_y direction (not shown), the only peaks were at multiples of 1.27 Å^{-1}, yielding an intracolumnar stack spacing between adjacent molecules of 4.96 Å.

In general, the columnar arrangement, the unit cell parameters and the extremely high supramolecular order were confirmed by the GID experiments. Furthermore, the side chains also revealed as well a high packing order between the aromatic columnar structures. This crystallinity of the substituents was quite surprising since the aliphatic chains were supposed to be rather disordered in the crystalline phase. But on the other hand, this is a strong evidence for the high efficiency and impact of the zone-casting technique which induced a pronounced molecular ordering. One can suggest that the HBC-C_{12} material micro-segregated to form a bi-crystalline structure with vertical ABAB… domains spanning the entire film thickness.

One could regard such an arrangement as a compromise between alkyl-chain packing and herringbone stacking of the aromatic disks. The "A" domains were approximately 16 Å wide containing the aliphatic side chains, and the "B" domains were about 9 Å of aromatic HBC stacks. As a consequence, one might expect also the top surface of the film to have regular stripes of alternating chemistry. Clearly, this invites further studies, not only of the communication between adjacent HBC stacks in the vertical direction, but also of the potential use of the films as a nano-patterned surface.[292,293]

One could also conclude an out-out-plane tilting of the molecules with respect to the support which would then led to this small observed period. In order to verify the suggested unit cell and the assumed molecular tilting on the support, a Cerius^2 simulation of the electron diffraction of two orthorhombic lattices was carried out consisting also of six molecules which possessed different tilting planes, but were arranged in the herringbone structure. The two different molecular arrangements are shown in Figure 4.15 with the corresponding equatorial reflection peak distribution of the electron diffraction. The difference of the two reflection distributions is obvious, whereby the in-plane tilting of the molecules gives an identical diffraction pattern which was experimentally observed (Figure 4.15a). It is interesting to note, that, except for the first peak position, only the even (h00) reflections appear in the simulated equatorial electron diffraction, as it is also the case in our experiment. This result additionally confirms the herringbone structure of the molecules.

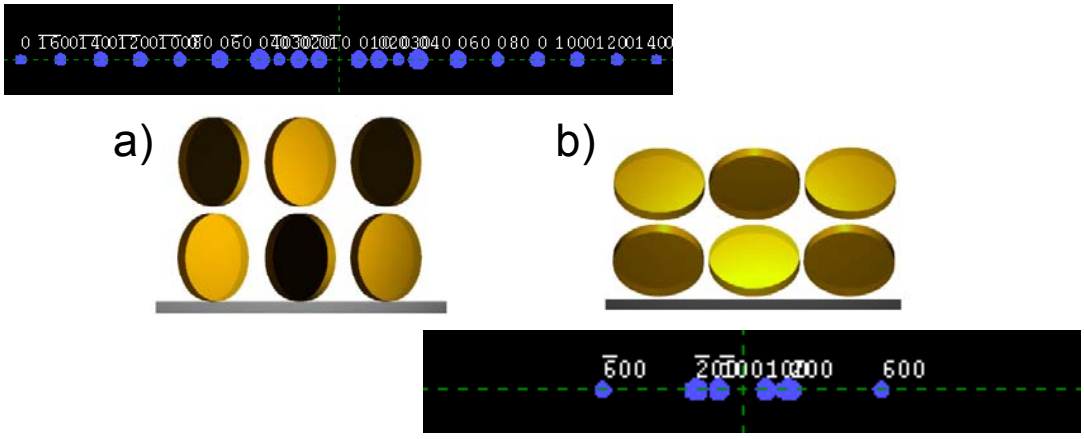

Figure 4.15. *Cerius^2 simulation of the equatorial reflection peak distribution of the electron diffraction for an orthorhombic unit cell consisting of molecules with a) an in-plane tilting and b) an out-of-plane tilting.*

It should be noted that the proposed unit cell assignment is tentative because of limits of both techniques used in this study. The X-ray diffraction measurements in reflection mode

reveals only periodicities which are arranged along the normal of the support, whereas the electron diffraction experiments gives information about the in-plane structure exposing correlation distances which are oriented parallel to the support. One can however conclude that the unit cell parameters determined by this structure investigation are significantly smaller than found for the lattice in bulk samples.[30] This significant difference in packing parameters might result from enhanced packing of the columns in the zone-cast film which was mentioned above. An additional reason is an improved peripheral organization of the alkyl chains and a slightly different tilt angle of the discs. A molecular tilting angle of approximately 30° was determined for the sample in the bulk. The significant decrease in unit cell parameters, the pronounced columnar orientation and the appearance of the characteristic intracolumnar correlation of 0.34 nm can be regarded as refined packing of the discotic molecules resulting in an improved charge carrier migration due to an enhanced overlapping of π orbitals.[294]

Bulk samples of HBC-C_{12} reveal a phase transition at 107 °C from the crystalline phase to the mesophase which is accompanied by a considerable change in the superstructure. Macroscopically oriented samples investigated by both 2D-WAXS and solid-state NMR showed in the crystalline state at room temperature a highly ordered herringbone arrangement of the discotic molecules, whereby the lateral intercolumnar organization could be assigned to the above mentioned rectangular 2D lattice with a = 6.1 nm and b = 2.38 nm.[30] Experiments at high temperatures exhibited a change in the intra- and intercolumnar organization. At the mesophase the flat cores become orthogonal to the columnar axis and the columns arrange in the typical hexagonal unit cell with a = 2.86 nm as the packing parameter. The recrystallization takes place at 82 °C accompanied by a reorganization back to the herringbone structure.

The changes in structure observed for bulk HBC-C_{12} samples were also expected to occur in the zone-cast surface layers. This phenomenon is especially interesting since the molecules are highly organized and are additionally in contact with a surface. Therefore, it is essential to investigate to which extent the structural transition will take place and if during recrystallization the structure can be recovered to the initial state or if the degree of order will be decreased by the thermal treatment. The annealing at high temperatures is an important point for any further post-processing of the films during device fabrication. Therefore, temperature dependent structure evolution was carried out by using large-area X-ray diffraction and electronic diffraction.

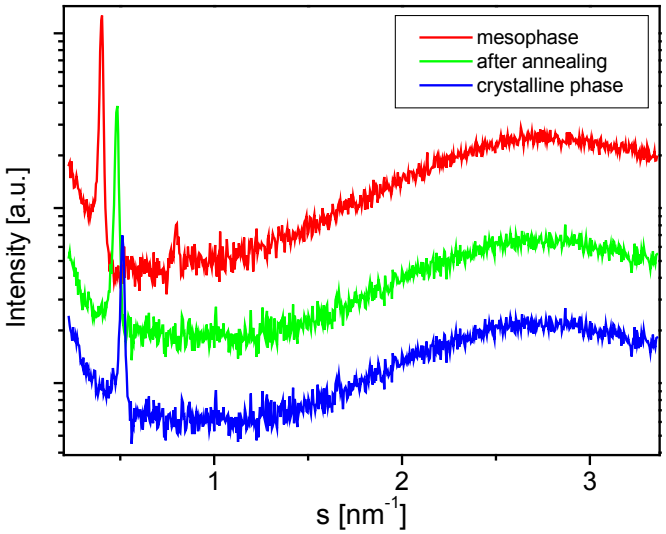

Figure 4.16. *Temperature dependent large-area X-ray diffraction in reflection mode of zone-cast HBC-C_{12} layer measured perpendicular to the columnar alignment. First, the measurement was performed at room temperature, then for the sample heated to the mesophase and finally back at room temperature in the crystalline phase.*

Figure 4.16 shows the temperature dependent large-area XRD measurements in reflection mode of the zone-cast HBC-C_{12} layer performed first in the crystalline state, then for the mesophase and finally for the sample cooled back to room temperature. When the zone-cast HBC-C_{12} film was heated to the mesophase, also one main reflection peak was observed accompanied by the second-order reflection. This indicated that the high out-of-plane intercolumnar order, which was monitored in the crystalline state, is maintained in the mesophase, despite the high molecular mobility of the aromatic core and the melting of the side chains in that phase. However, the shifting of the peak to smaller values of the scattering vector indicates an increase of the correlation distance by 0.5 nm. This relatively large value could be explained by an out-of-plane tilting of the molecules in the crystalline phase which changes in the mesophase. However, simulations described in Figure 4.15 excluded this assumption. Therefore, a more probable explanation for this expansion is the uniform distribution of the side chains around the aromatic core in the mesophase leading to the larger out-of-plane distance between the columns. Interestingly, by cooling back to room temperature one reflection peak appeared in the XRD, but shifted also to lower s values in comparison to the initial structure. It is apparent that the structure after the annealing at the mesophase does not return to its initial state completely. It can be assumed that the supramolecular arrangement might slightly differ between layers freshly zone-cast and after the thermal treatment. The indicated larger out-of-plane periodicities after annealing show

that the high packing observed after the processing is not maintained.

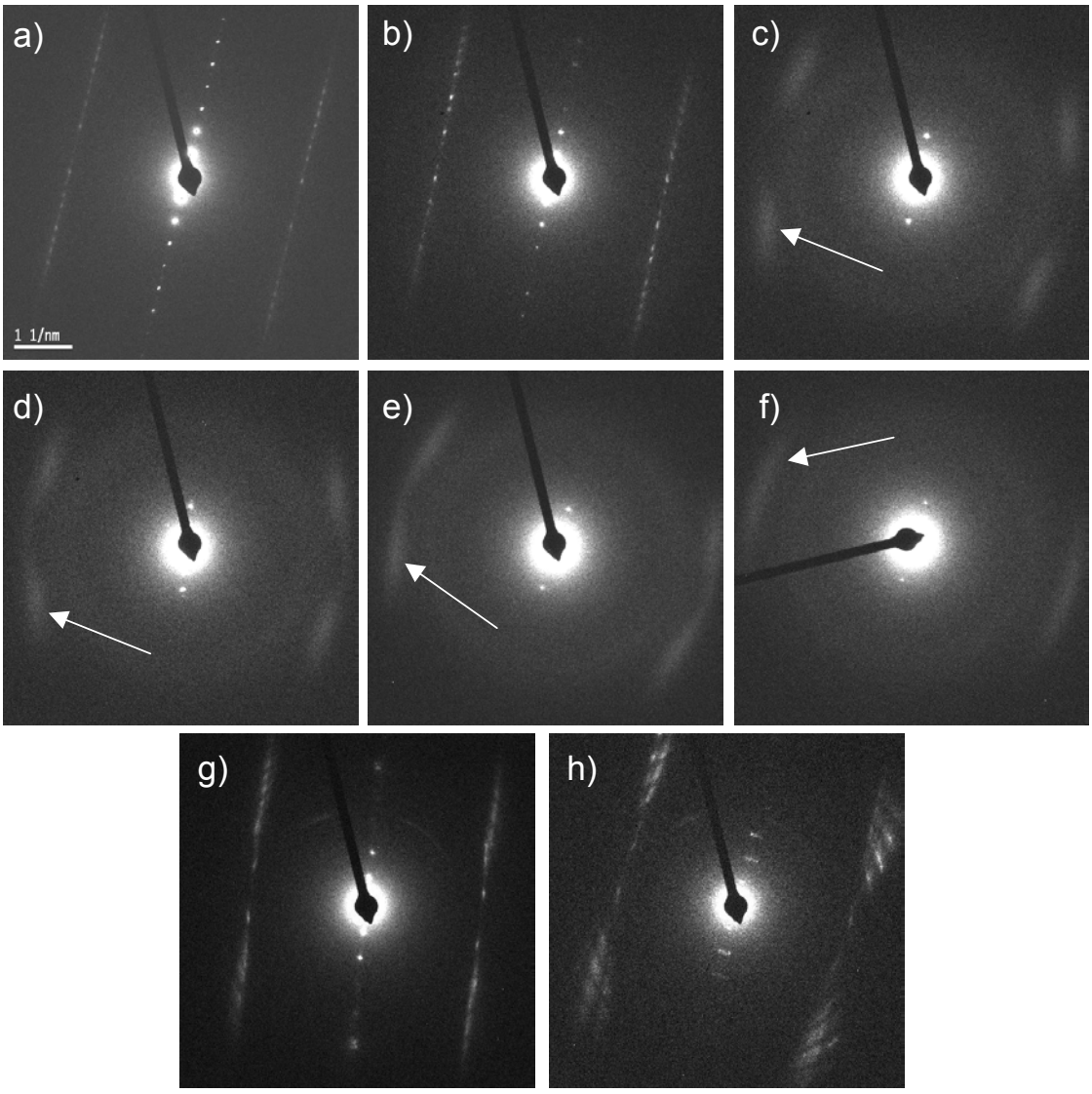

Figure 4.17. *Temperature dependent electron diffraction measurements of zone-cast HBC-C_{12} layers; image a) taken at room temperature (crystalline phase), b) at 40°C, c) – e) during further heating, f) at 130°C (mesophase), g) and h) after cooling back. The white arrows indicate the reflection peaks corresponding to the intracolumnar stacking of the discotic molecules.*

In order to obtain a deeper insight into the change in the supramolecular organization during heating of the zone-cast layers to the mesophase, temperature dependent electron diffraction was performed by monitoring the structure gradually during increasing the temperature. The diffraction patterns for the different temperatures are shown in Figure 4.17.

At room temperature the diffraction pattern revealed the characteristic reflection distribution with distinct reflection peaks of pronounced intensity indicating the high quasi single-crystalline intra- and intercolumnar order with the discotic molecules arranged in the herringbone structure. Heating the sample to 40 °C, the pattern observed at room temperature was maintained, but the intensities of the peaks changed slightly. These changes were quite obvious in the (h01) distribution line. Furthermore, most of the higher-order reflections in the equatorial vanished indicating a poorer long-range order. Heating ca 20 °C higher the zone-cast film showed considerable structural changes. The pattern suggesting the crystalline structure disappeared and a pattern implying liquid crystalline order was visible. The transition of the (h01) corresponding to the intracolumnar correlation was most impressive. The distinct peaks from the crystalline arrangement changed into two broad split and weak off-meridional reflections which were related to periodicities of 0.37 nm. At this temperature in the equatorial only one main refection corresponding to 2.52 nm and its second order peak were displayed which were related to the nearest columnar distance. During further heating the diffraction pattern did not reveal any new significant transitions. The two split off-meridional peak immerged into each other resulting finally above the phase transition in one meridional peak indicating the π-π correlation of 0.35 nm (Figure 4.17f). However, these reflection peaks were relatively diffuse and weak in comparison to the meridional reflections observed in the 2D-WAXS for an extruded filament. The equatorial reflection shifted slightly to correlation distances of 2.46 nm (2^{nd} order peak to 1.23 nm). Interestingly, at some places of the film only one peak appeared which was related to a period of 1.42 nm which is $\sqrt{3}$ times smaller than 2.46 nm. This relation confirms the hexagonal intercolumnar arrangement which was characteristic for a liquid crystalline phase. The unit cell parameters in the mesophase determined for the bulk sample were significantly larger in comparison to the packing dimensions found for the zone-cast films. This observation was also made for the room temperature phase suggesting the enhanced supramolecular order in both phases. After a controlled cooling back to the crystalline state, the high initial order of the surface layer could not be recovered. The diffraction pattern still implied the herringbone arrangement of the molecules, but the reflection peaks were significantly broader and smeared suggesting a weaker supramolecular organization of the molecules. Before annealing the sample showed an impressive homogeneous structure within the film, however after the heating to the mesophase the degree of disorder varies extremely over the sample. Some parts of the films still possessed a well-ordered alignment as in Figure 4.17g, but other had also higher columnar misalignment (Figure 4.17h) which might be the reason of different structural transitions of the different columnar layers.

The temperature dependent electron diffraction experiments revealed that the molecules

have a sufficient degree of freedom on the support to adopt the characteristic intracolumnar orthogonal disc arrangement in the mesophase. The degree of molecular rotation towards this intracolumnar organization of the discs is temperature dependent and accomplished above the temperature of 107 °C. The assigned order is typical for the liquid crystalline phase and takes place analogously to the macroscopically aligned filaments. Due to the high lateral and longitudinal fluctuations and intracolumnar rotations of the discotic molecules, a short-range order is observed. The reflections corresponding to the intracolumnar packing are surprisingly weak and diffuse at this high temperature phase indicating the relatively high degree of molecular freedom. The appearance of only the (110) reflection peak at same parts of the zone-cast layer which is related by $\sqrt{3}$ to the (100) reflection in the hexagonal organization suggests that the lateral intercolumnar arrangement might be not as uniform as at room temperature revealing also other scattering planes in the surface normal as illustrated in Figure 4.18 schematically.

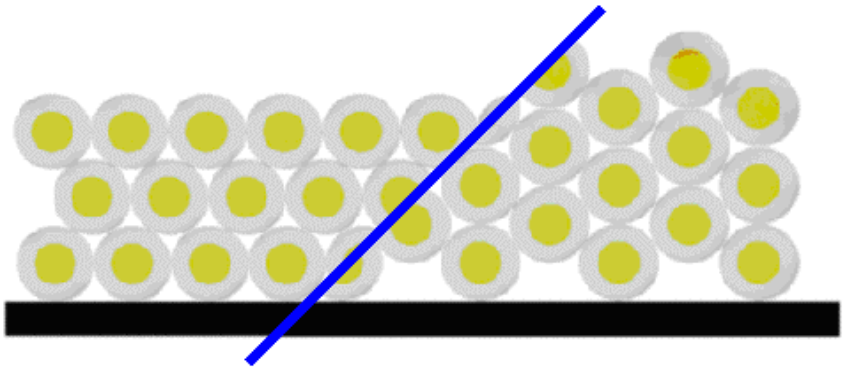

Figure 4.18. *The hexagonal lattice in the mesophase (two different packing possibilities are shown as indicated by the electron diffraction experiments). The aromatic cores are illustrated as discs and the side chains are shown as translucent surrounding.*

The recrystallization of the sample confirms the high flexibility of the molecules on the support, since the discs adopt again the herringbone structure. In general, the structure can mainly be recovered after annealing. However, obvious columnar misalignment and intracolumnar defects appear which are not homogeneously distributed over the layer. There might be several reasons for this significant decrease of order within the annealed zone-cast films. It is well known that the structure obtained from solution is different in comparison to that one obtained from the higher-temperature phases. The alignment acquired during zone-casting processing is unique and therefore heating of the sample has an effect of eliminating the structural history.

The structure evaluation has indicated that the alkyl chains are not distributed uniformly around the aromatic core in the initial crystalline phase, whereas in the mesophase they are. During the recrystallization these alkyl chains maintain distributed uniformly around the cores and prevent a complete recovering of the structure. Another important aspect is the differently strong interaction of the molecules in the different columnar layers with the surface leading to a different degree of freedom of the molecular tilting. One can assumed that the molecules at the surface perform a smaller rotation in comparison to the ones in other layers which possess relatively more rotational freedom. The third explanation is related to the mechanical factor, which is connected to the structural change at the phase transition. The molecular transformation from the herringbone structure to the orthorhombic arrangement of the discs results in a change in macroscopic dimensions as schematically shown in Figure 4.19. Theoretically, a perfectly aligned sample with molecules tilted 45° to the columnar axis should reveal at the phase transition a macroscopic shortening by ca 30% in the direction of the columnar alignment and an expansion also by 30% perpendicular to it. Such a variation in dimensions of a surface layer leads to the increase of macroscopic stresses within the sample and to the appearance of defects.

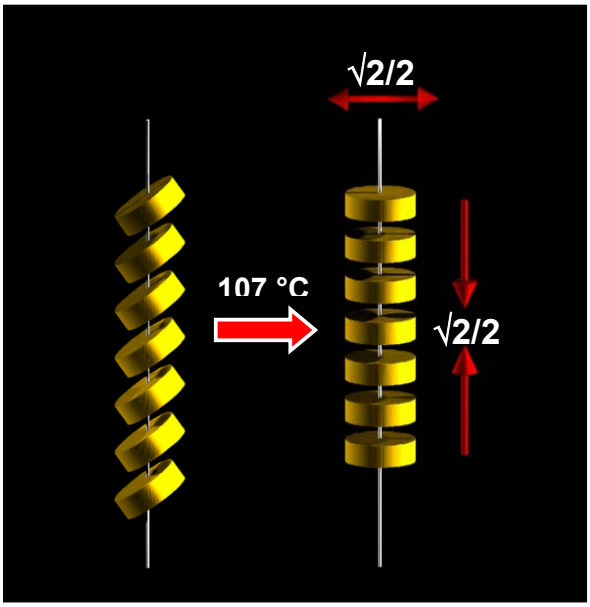

Figure 4.19. *The transformation of the intracolumnar structure from the herringbone order to the parallel arrangement of the discotic molecules leads to a macroscopic contraction of 30% of the sample along the columns and an extension perpendicular of 30% to it.*

The following experiment reveals that indeed the phase transition from the crystalline phase to the mesophase is connected to changes in macroscopic dimensions of the sample. A suspended extruded fiber of HBC-C_{12} was placed into a thermally controlled oven and the change in size was monitored temperature dependent by using a CCD camera (Figure 4.20a). Due to the resolution of the camera only the length of the sample could be monitored, whereas for a compete investigation it would be necessary to display also the change of the sample diameter. Figure 4.20b shows the length of the extruded HBC-C_{12} fiber as a function of the temperature. Heating the sample up to 80 °C leads to an elongation due to thermal expansion. The aromatic cores are still arranged in the herringbone manner, whereas the effect

of the side chains dominates, which reorganize and melt up from 42 °C. From 80 °C the length of the filament decreases first significantly and upon further temperature increase the rate of contraction exceeded a value of ~ 92%.

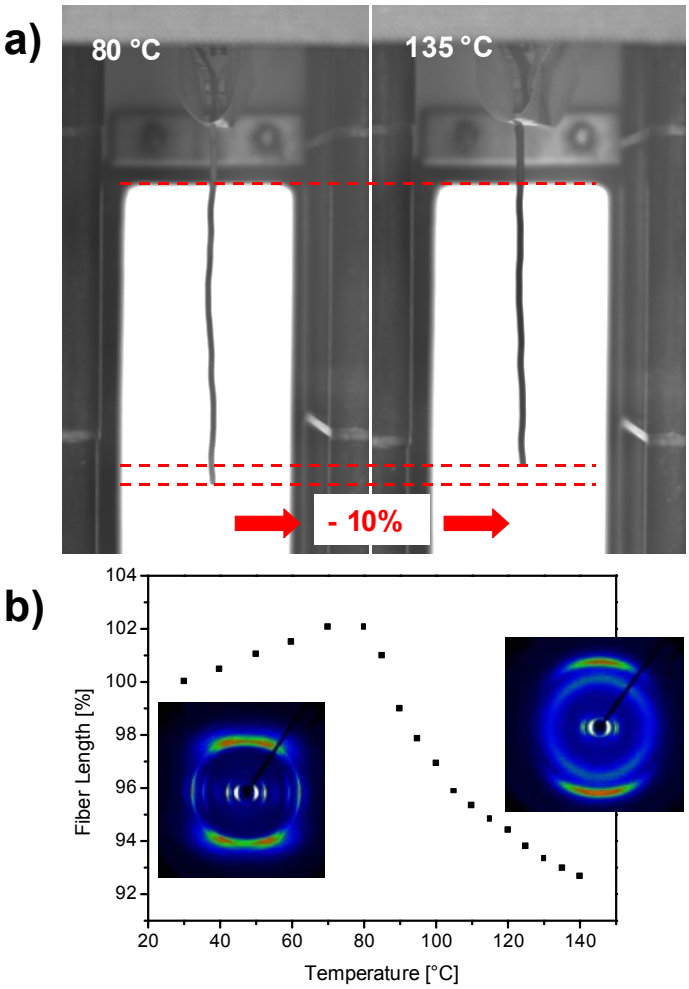

Figure 4.20. *a) A suspended extruded fiber of HBC-C_{12} at 80 °C and 135 °C upon heating, the filament is placed into a temperature controlled oven and the images were taken with a CCD camera; b) temperature dependent change in the length of the HBC-C_{12} extruded fiber (the insets show 2D-WAXS patterns at the corresponding temperatures).*

This effect is correlated with the intracolumnar reorganization of the discs which, to our surprise, takes place at considerably lower temperatures than the bulk phase transition. On the other hand, the observed structural changes in the HBC-C_{12} zone-cast film monitored by electron diffraction occurred also at lower temperatures. Both observed structural

transformations are in strong correlation. The discrepancy between the theoretical value of change in the macroscopic sample dimensions and the experimentally obtained results might be due to a not perfect order within the extruded filament. It is known that the tilting angle of the discotic molecules in the extruded filament is approximately 30° leading to a less pronounced change of the sample dimensions during heating.

The above described structure evaluation of the zone-cast HBC-C_{12} surface layers revealed that the transition from the crystalline phase to the mesophase is accompanied by a reorientation of the molecules within the columnar stacks from the tilted to the orthogonal arrangement as also observed for bulk samples. In the following experiment, this change in the intracolumnar arrangement was correlated with the macroscopic optical behavior of the zone-cast films in polarized light.

The evaluation of the optical behavior was performed in a strong collaboration with Dr. Jorge Piris from the group of Dr. John M. Warman, IRI, Delft University of Technology, The Netherlands.

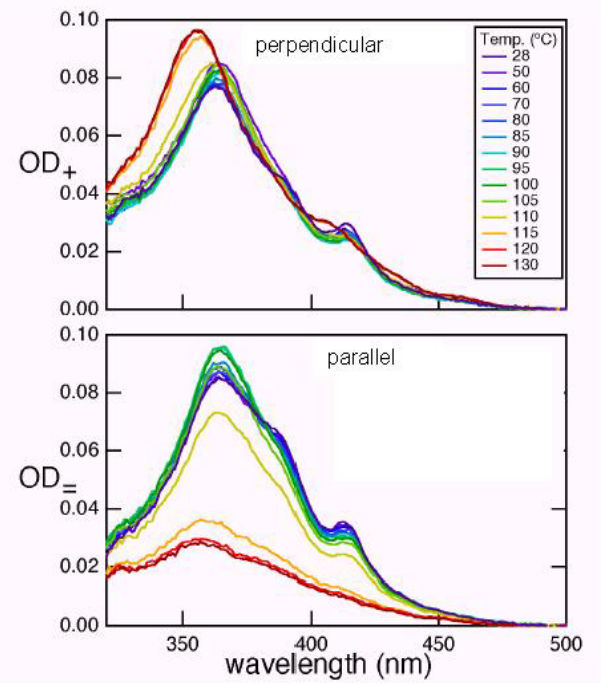

Figure 4.21. *Optical absorption spectra for the zone cast film of HBC-C_{12} on heating from 28 °C (dark blue) to 130 °C (dark red) for light polarized parallel (upper) or perpendicular (lower) to the alignment direction.*

A reversible change in optical anisotropy indeed occurred for the zone-cast film as it is shown by the optical absorption spectra in Figure 4.21, which were taken for light polarized

parallel and perpendicular to the casting direction temperature dependent during heating and cooling from room temperature to 130 °C. As can be seen, the absorption spectra at room temperature revealed only a slight preferential absorption at the spectral maximum for the parallel condition. The optical data therefore might suggest that little, if any, macroscopic columnar alignment of the HBC mesogens had been achieved by this method of preparation. The apparent anomalous lack of optical anisotropy for a clearly macroscopically well aligned film was previously also observed for certain HBC derivatives self-assembled on friction-deposited polytetrafluoroethylene primer layers.[186] As the structural investigation has proven a high order in the zone-cast layers, the explanation lies in the close to 45 degrees, herringbone stacking of the mesogens characteristic for HBC derivatives which are crystalline solids at room temperature. Since the transition dipole of the first absorption band of HBC lies in the plane of the aromatic core such a herringbone structure will result in close to zero net anisotropy even for a perfectly aligned film.

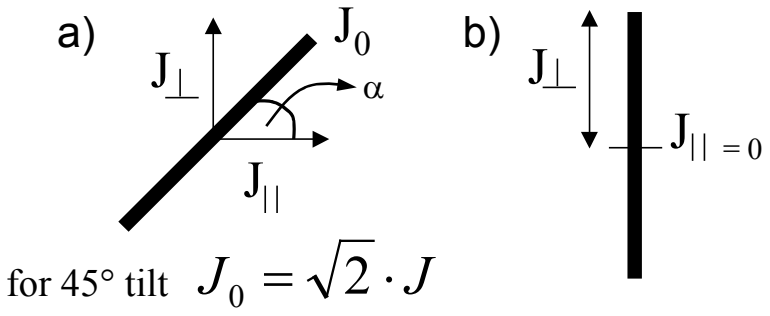

Figure 4.22. *Schematic illustration of the observed dipole moment in polarized light in a) the crystalline phase with a 45° molecular tilting and b) the mesophase with perfectly orthogonal disc arrangement.*

The heating of the zone-cast film to the mesophase induces a significant change in the optical absorption intensity for both measurements parallel and perpendicular to the columnar alignment. Since this phase transition involves a rotation of the tilted discs to form a cofacial columnar arrangement,[30] the projection of the dipole moment of light polarized parallel to the columnar axis on the core of the molecules will be reduced if such a rotation occurs in the film, whereas simultaneously the absorption perpendicular will significantly increase (schematically shown in Figure 4.22). The drop in the optical absorption for this particular polarization can be readily seen in the lower graph of Figure 4.21. From the ratio in the absorption for light polarized parallel and perpendicular to the columns before and after the phase transition, it can be estimated that the discs rotate to form a tilted columnar arrangement.

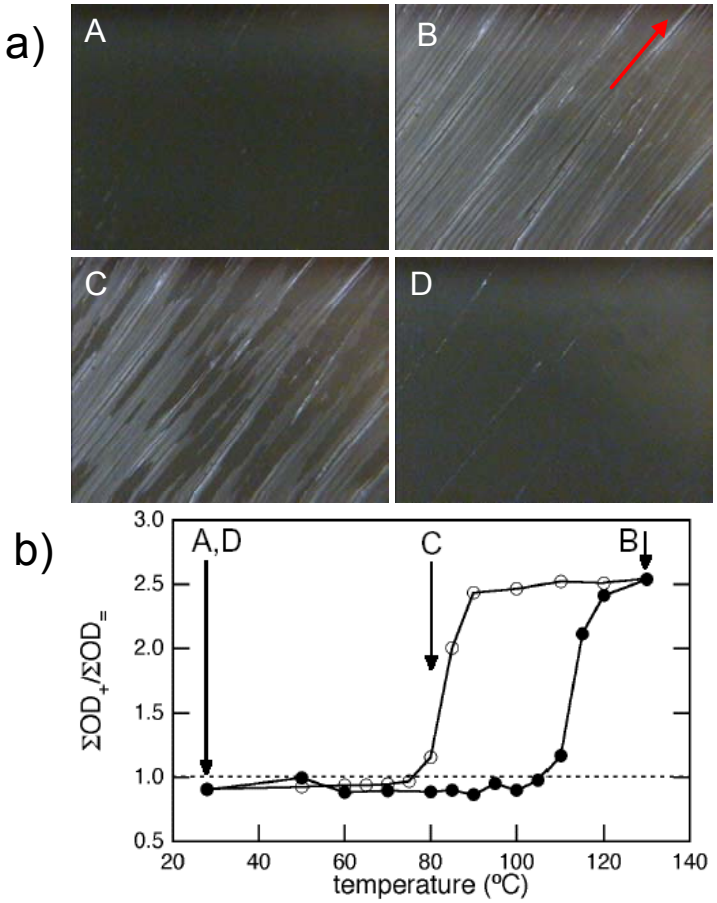

Figure 4.23. *a) Optical micrographs obtained under crossed polarizers: A, pristine sample at room temperature; B, liquid crystalline phase at 130 °C; C, at close to the phase transition temperature on cooling; D, the crystalline phase on returning to room temperature, b) temperature dependence of the ratio of the optical density of a zone-cast film of HBC-C_{12} at the absorption maximum for the incident light polarized perpendicular and parallel with respect to the casting direction.*

The dichroic ratios of the maximum optical density for perpendicular to that for parallel excitation, ODmax(+)/ODmax(=), are shown in Figure 4.23b and vary from 0.91 at room temperature to 3.30 at 130 °C and return to 0.87 after cooling back. Clearly, a considerable rotation of the molecules from their tilted, room temperature configuration has taken place at the elevated temperature. The anisotropy factor of ca 3 is still considerably smaller than the factor of 12 that has been found for a PTFE-aligned HBC derivative which is liquid crystalline and orthogonally stacked at all temperatures.[186] It is assumed therefore that reorientation to a completely orthogonal arrangement in the mesophase of the present thin-film sample probably does not occur. The values of the ratio ODmax(+)/ODmax(=) over the full heating and cooling cycle are shown in Figure 4.23b. As can be seen, the increase in the

optical density ratio occurs abruptly at close to 110 °C on heating and returns to the initial value at close to 85 °C on cooling, i.e. close to the transition temperatures found in DSC measurements for the phase transition in bulk samples. Also shown in Figure 4.23a are polarization microscopy images under crossed polarizers taken at different temperatures in the heating and cooling cycle in which the reversible change from almost no anisotropy at room temperature to a highly anisotropic medium above the temperature of the phase transition is apparent. These images provide an additional illustration of the reversible change in anisotropy occurring at the phase transition. They furthermore demonstrate the high degree of alignment that is retained in the mesophase. It is also interesting to note that the propagation of the phase transition in the zone-cast film occurs faster along the columns than perpendicular what is in contrast to the light propagation. This effect can be seen in image C in Figure 4.23a which shows the phase transition. From this observation one can assume that the thermal transport might also be favored in the columnar direction.

When the heating and cooling cycles were repeated the number of birefringent defects at room temperature increased. This effect can be explained by the results obtained from temperature dependent electron diffraction which revealed that the degree of misalignment increases significantly after the annealing of the zone-cast HBC-C_{12} layer in the mesophase. For the macroscopically oriented sample, the phase transition leads to a considerable expansion in the lateral dimensions accompanied by a decrease of the longitudinal length. The tremendous mechanical stress that this rotation implies for substrate-bound samples explains why zone-cast films do not form the thermodynamically preferred cofacial stacking at high temperatures. This behavior has consequences for the fabrication and processing of electronic devices. For instance, the principle of self-healing in the mesophase is not applicable for surface layers with phase transitions accompanied with a pronounced transformation in the supramolecular organization.

Flash photolysis time-resolved microwave conductivity (FP-TRMC) measurements indicated the relation between the macroscopic alignment of the zone-cast films and the anisotropy of the photoconductivity. The coated substrates were placed in the microwave cavity with the casting direction of the film either parallel or perpendicular to the electric field vector of the microwaves. In addition, the plane of polarization of the laser beam used to photoexcite the sample could be oriented parallel or perpendicular to the casting direction. The transient photoconductivity of the sample was monitored as a reduction in the microwave power reflected by the cavity as described in detail elsewhere.[295,296]

The anisotropy of the photoconductivity using FP-TRMC should confirm that the present HBC-C_{12} sample was in fact macroscopically aligned. This experimental technique

was also applied to films of HBC derivatives self-assembled from solution on friction-deposited PTFE.[297] As can be seen from the results in Figure 4.24, the photoconductivity transients with the casting direction parallel to the electric field vector of the microwaves are much larger than for a perpendicular orientation. The latter transients are in fact close to the noise level of detection, and the anisotropy in the conductivity is estimated to be at least a factor of 10 in favor of charge transport in the casting direction, i.e. along the axis of the columnar stacks. In agreement with the lack of optical anisotropy found in the absorption spectra, the photoconductivity is found to be almost independent of the relative orientation of the polarization of the laser beam used to photoexcite the sample. The photoconductivity results confirm therefore the high degree of columnar alignment of the discotic molecules in the present sample and the tilted, herringbone arrangement of the molecules in the columnar stacks at room temperature.

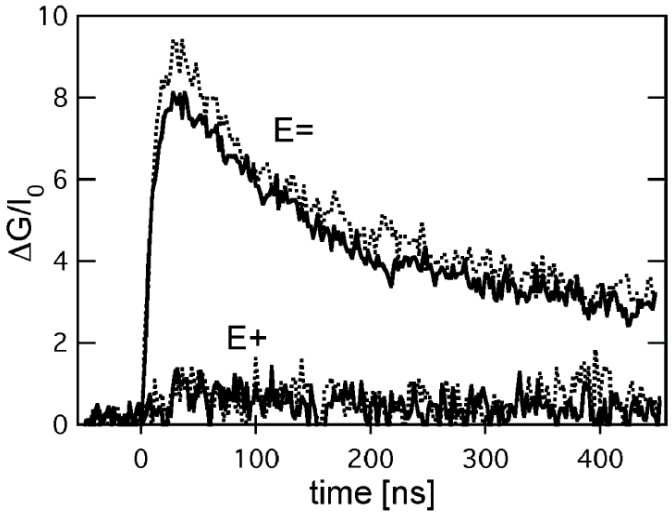

Figure 4.24. *Intensity normalized photoconductivity transients, $\Delta G/I_0$ in units of 10^{-24} S cm^{-2} per incident-photon, obtained by flash-photolysis of a zone-cast film of HBC-C_{12}. The full and dashed traces are for light polarized perpendicular or parallel to the alignment direction of the discotic columns respectively. The two upper, $E_=$, and two lower, E_+, traces are for the casting direction (columnar alignment) parallel or perpendicular to the electric field vector of the microwaves, respectively.*

It is clear that significant changes in both the optical and conductive properties of the zone-cast, thin-film sample occur in the same temperature regime as found for the bulk material. In addition, the changes are completely reversible with a hysteresis similar to that found for the bulk. This was not necessarily to be expected since the reorientation of the mesogens is accompanied by a considerable change in geometry of the material with a longitudinal shrinking and a lateral expansion with respect to the columnar director on

entering the mesophase. One explanation might be that the reorganization induced macroscopic defects which do not influence the local charge carrier mobility which is determined by this technique. A further aspect of interest in the optical data is the fact that the increase in the OD for perpendicular excitation is considerably less than the decrease in the OD for parallel excitation (Figure 4.25a). One explanation could be that the extinction coefficient for the transition is lower in a more orthogonal arrangement of the aromatic chromophores. This could be a result of excitonic interactions between neighboring cores which would also explain the slight blue-shift of the wavelength maximum on entering the mesophase.

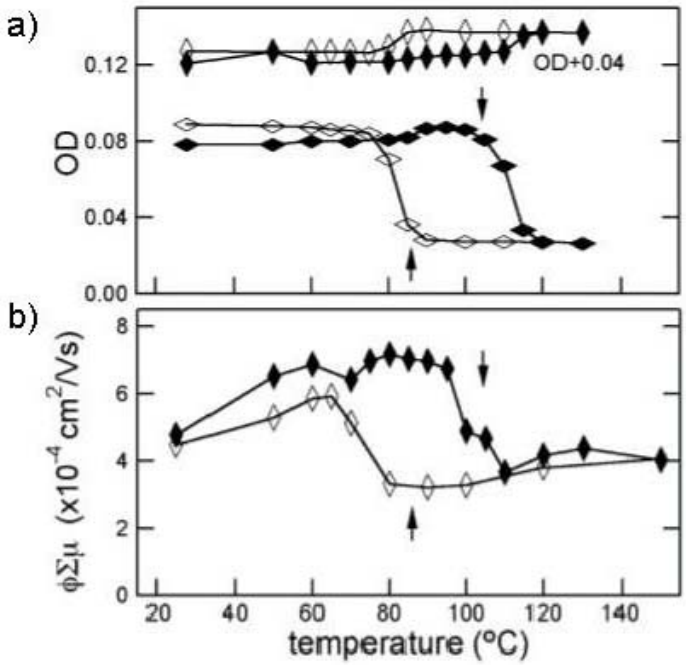

Figure 4.25. *a) The temperature dependence on heating (filled symbols) and cooling (open symbols) of the zone-cast HBC-C_{12} samples a) of the optical density at the absorption maximum (ca 360 nm) of a zone-cast film for light polarized parallel (horizontal diamonds) or perpendicular (vertical diamonds) to the casting direction and b) of the product of the quantum-yield and mobility sum, $\phi\Sigma\mu$, on (perpendicular) photoexcitation of a zone-cast film at 420 nm with the casting direction parallel to the electric field vector.*

The decrease in the photoconductivity at the phase transition temperature shown in Figure 4.25b is similar to the decrease in the one-dimensional charge mobility, $\Sigma\mu_{1D}$, determined using the pulse-radiolysis TRMC method. This decrease in mobility is attributed to an increase in the structural disorder within the columns when the saturated hydrocarbon mantle melts. The temperatures at which the decrease on heating and the subsequent increase

on cooling occur are however slightly lower than found for the bulk. Also, the change in $\Sigma\mu$ appears to be less abrupt for the film. Taking the value of $\Sigma\mu_{1D}$ to be identifiable with the value of $\Sigma\mu$ for the $E_=$ condition in the present experiments, an estimate of $0.9 \pm 0.1 \times 10^{-3}$ can be made for the quantum yield of charge carrier generation on excitation at 420 nm with perpendicularly polarized light.

As the final step, an electronic device has been constructed in order to investigate the charge carrier mobility of the zone-cast HBC-C_{12} in practical applications. Both, HBC-C_{12} which is very attractive for potential applications in devices due to its highest local charge carrier mobility of up to 1.1 cm²/Vs found for this kind of discotic systems and the processing technique which allows a fabrication of highly ordered layers of large-areas emerged to be of great interest for field-effect research. Furthermore, the relationship between supramolecular organization, revealed by the structural analysis, and the charge transport properties, obtained from field-effect transistor experiments, is studied.

In collaboration with Dr. Anoop Menon and Prof. Henning Sirringhaus, from Plastic Logic in Cambridge, the field-effect investigations of the zone-cast with HBC-C_{12} as the semiconducting material have been carried out.

The mode of operation of organic thin-film transistors parallels the one already described in the case of insulated gate field-effect transistors, based on crystalline or amorphous inorganic semiconductors. In general, the output of the FET is visualized by plotting of the drain current I_D as a function of the drain voltage V_D which characterizes the device performance. The sign of the drain current is dependent on the type of charge carriers of the active layer. When electrons migrate through the semiconductor the drain current and voltage are both positive, while when holes are the main charge carriers the current is negative. The characteristic I-V curves reveal two distinct regimes. At the first regime with low drain voltage, the current is proportional to V_D and can be described according to the Ohm's law. The linear regime can be described according to the following equation:

$$I_D = \frac{Z}{L} C_i \mu (V_G - V_0) V_D \qquad (4.1.)$$

where, Z and L are the channel width and length, C_i the capacitance per unit area of the insulator layer, μ the mobility of the majority charge carriers, V_G the gate bias and V_0 the threshold voltage. When the drain voltage increases, the device gradually enters the saturation regime where the drain current becomes independent of the drain bias. By using the following equation it is possible to calculate the saturation current.

$$I_{D,sat} = \frac{Z}{2L} C_i \mu (V_G - V_0)^2 \qquad (4.2.)$$

The charge carrier mobility in the saturation regime can be calculated from the slope of the plot of $\sqrt{|I_D|}$ versus V_G and it is one of the most important properties of a FET. But it is also possible to determine it from the linear current, whereby these both calculation methods are often in disagreement, due to assumptions which are valid for the silicon based MISFETs (metal-insulator-semiconductor field-effect transistors), but are applied to describe the organic-based TFTs (thin film transistors), although the device structure of the organic TFT's differs from that of the conventional MISFETs.[298] For instance, one assumption is that the mobility is constant over the active layer and does not depend on the gate voltage.

The most important application of the zone-casting technique in the case of HBC-C_{12} is considered to be the fabrication of a highly aligned semiconductor layer in a channel of a field-effect transistor. The uniaxially aligned HBC-C_{12} thin surface layer in the channel of the FET should have an enhancing effect as an active component on device performance. In order to demonstrate this, FETs were fabricated on top of a SiO_2 insulating layer on a silicon substrate by direct zone-casting. Under optimized zone-casting conditions, homogeneous films in the cm² range on untreated glass as well as on a hexamethyldisilazane (HMDS) modified silicon surface were obtained as presented by optical microscopy images in Figure 4.26. The increased hydrophobization of the silicon surface by HMDS was applied in order to obtain a pronounced edge-on arrangement of the discotic molecules and to avoid possible trapping sites from the oxygen located at the silicon surface.[299] It is well known that the main charge carrier migration takes place at the first monolayer or even in the bilayer at the surface of the support. Therefore, it is very sensitive on any influence from the surface as such oxygen.

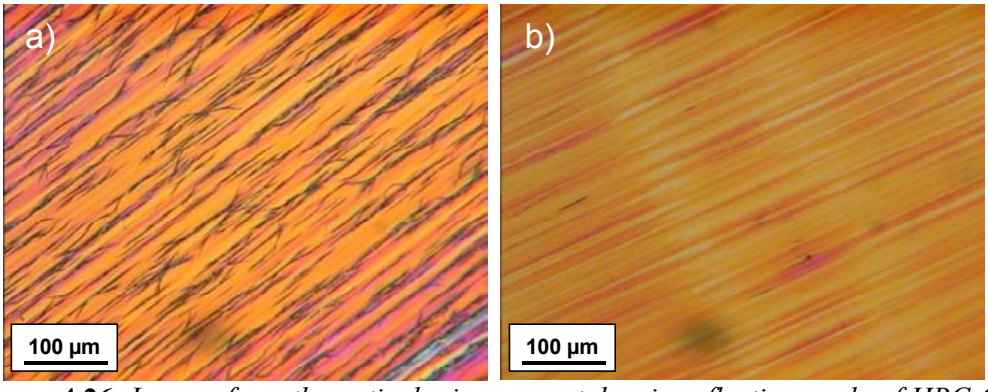

Figure 4.26. *Images from the optical microscopy taken in reflection mode of HBC-C_{12} zone-cast onto HDMS treated silicon at a) non-optimized conditions leading to the appearance of morphological defects and b) at optimized conditions with the desired homogenous morphology of the layer.*

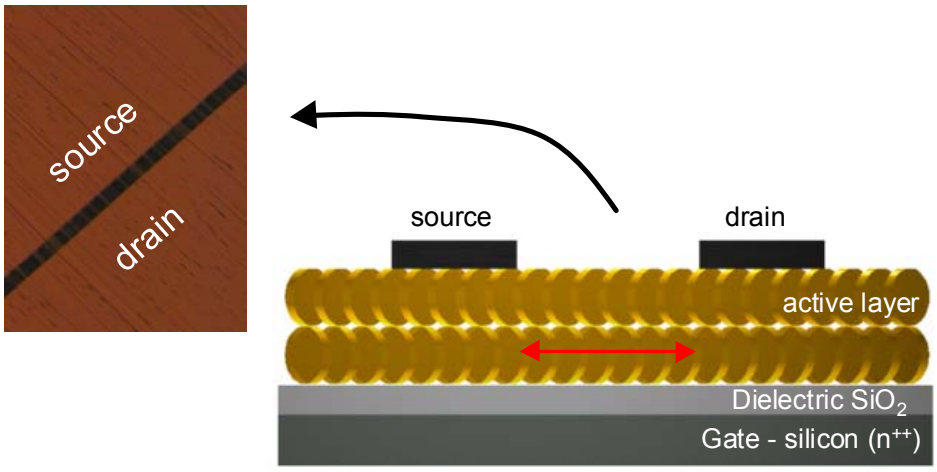

Figure 4.27. *Schematic side-view representation of the top-contact device configuration with contacts evaporated (L = 25 mm, W = 1.6 mm and d = 200 nm) onto the 20 nm thick zone-cast HBC-C_{12} aligned film, a 200nm SiO_2 dielectric and n-doped silicon substrate as gate electrode. The discs represent the tilted molecules in edge-on arrangement. The red arrow indicates the charge transport direction. The optical image shows the aligned layer in a 25 µm long channel of a FET.*

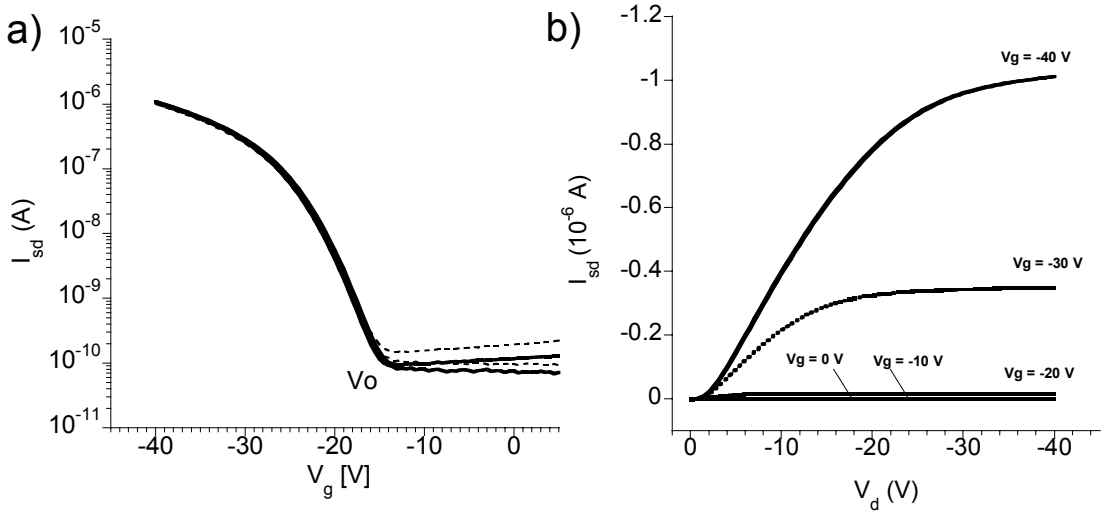

Figure 4.28. *a) Typical transfer characteristic (Vgs=-40V) of a FET with zone-cast HBC-C_{12} as an active layer. The mobilities are extracted from the saturation regime by conventional techniques, b) I-V output characteristics. Both dependencies are measured along the columnar alignment.*

The FET device was constructed with top contacts having a channel length of 25 µm between the shadow masked source and drain gold electrodes. A schematic drawing of the device design is shown in Figure 4.27. The transfer and output characteristics of the devices

measured parallel to the columnar alignment are shown in Figures 4.28a and 4.28b revealing a very good on-off ratio of 10^4, a high field-effect mobility in saturation regime at $5 \cdot 10^{-3}$ cm^2/Vs and a turn on voltage of ca. -15V. In previously reported data by van de Craats et al. it was found that the highest achievable mobility of an oriented HBC derivative on an aligned PTFE layer on silicon was $0.5 \cdot 10^{-3}$ cm^2/Vs.[185] The device dimensions reported there were similar to the current case. An order of magnitude improvement in device on currents as well as the saturation mobility by zone-casting the discotic semiconductor system has been determined. The superior device performance is attributed to highly ordered and uniformly oriented HBC-C_{12} that can be realized by the zone-casting technique. However, it should be noted that the charge carrier mobilities of HBC-C_{12} exposed in FETs are still two orders of magnitude lower than the intrinsic values obtained by pulse-radiolysis time-resolved microwave conductivity. One reason for this considerable difference concerns possible contact problems between the drain and source, and the active organic layer. During the contact deposition the organic material might be degraded at certain parts. Another contributing factor could be related to a presence of local intracolumnar packing defects which can constitute localized barriers for charge carrier motion along the columns; even at low concentrations these defects can significantly decrease the charge carrier transport over longer distances. At closer inspections of the AFM image in Figure 4.7 one can indeed observe single defects in the intracolumnar order (Figure 4.29a), for example adding or removing one column at some places (red circles). The inversion of a filtered FFT image shown in Figure 4.29b confirms the appearance of these defects and implies additionally that they are not limited to one plane, but could progress three-dimensionally. Furthermore, it is obvious in Figure 4.29b that the columnar structure accommodates these defects by column tilting and reorganization over distances of a dozen nanometers. It should be noted that the investigated layers were not thermally treated and therefore the molecular reorganization at the phase transition as the origin of the defects can be excluded in this case.

Although these defects appeared sporadically, the charge carrier transport might be influenced significantly over long ranges between the electrodes. On the other hand, the presence of local defects, for example even in organic single crystals, is extremely difficult to control by any processing technique. The device characteristics of HBC-C_{12} approach those of state of the art organic semiconductors such as dioctylfluorene-bithiophene copolymer by virtue of the highly ordered zone-cast films.[300]

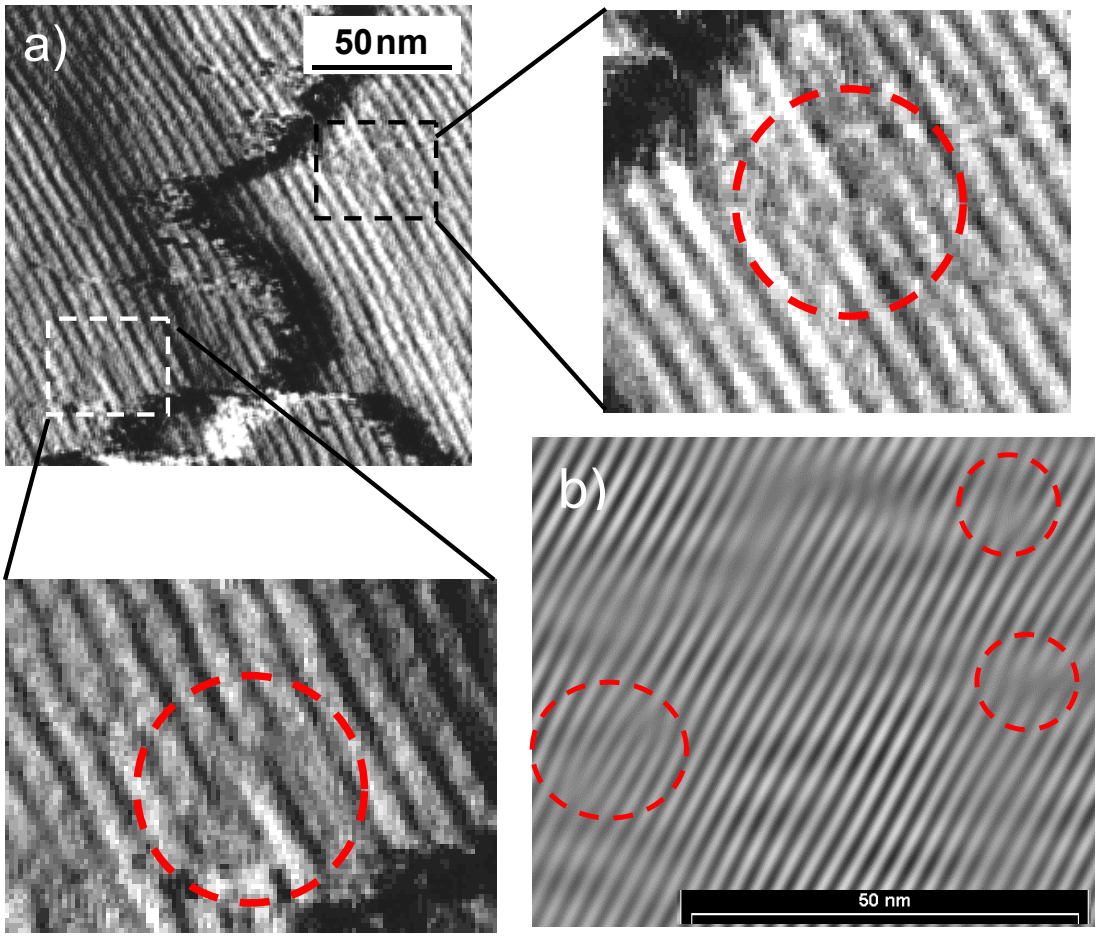

Figure 4.29. *a) AFM image of zone cast films of HBC-C_{12} from Figure 4.7 indicating the columnar defects, b) filtered IFFT image of a electron microscopy image of zone-cast HBC-C_{12}. In both cases the dashed circles indicate the intracolumnar defects.*

It can be summarized that the transfer of the self-aggregation and morphology formation onto the processing from solution was shown impressively for the zone-casting of HBC-C_{12}. One of the highest self-association constants and a pronounced pre-aggregation of HBC-C_{12} were reflected by the formation of microfibers in drop-cast films and ensured the successful alignment of this compound. Thereby, it was important that the self-organization at the surface-solvent interface of the HBC-C_{12} molecules was not effected significantly by the kinetics as proven by the use of solvents with different evaporation temperatures indicating the strong tendency to self-aggregate. The AFM topography revealed the formation of micro- or nanofibers which is known to be in strong correlation with the molecular interaction as reported for different system with π-stacking interactions. Oligo(p-phenylenevinylene)s self-assembly from solution into helical structures,[301,302] in some cases supported by hydrogen

bondings[259]. Disc-shaped molecules derived from crown ethers and phthalocyanines create helical nanofilaments.[10] Wu et al. showed that the intracolumnar packing of HBCs can be enhanced by the substitution of rigid rods leading to the formation of helical structures.[31] Due to this enhanced packing nanoribbons were observed in spin-coated films. Recently, it has been reported that amphiphilic HBCs form discrete nanotubular objects which consisted of helical arrays of π-stacked discs, whose exterior and interior surfaces were covered by the hydrophilic triethylene glycol chains.[303] All the examples from literature emphasize again the strong relationship between the self-aggregation in solution and the structure formation for π-conjugated systems.

The zone-casting method is a powerful technique for the simple fabricating of large-scale thin layers of highly oriented semiconductors. The supramolecular order of the zone-cast films is strongly related to the nucleation and growth ability of the material. According to the morphology formation of drop-cast layers, the order of the zone-cast HBC-C_{12} films attains single crystalline quality, whereby the side chains were packed between the aromatic columns and revealed a high ordering. The resulting high supramolecular alignment was proven by various experimental techniques, but the most important proof was successfully obtained by the application of the zone-cast film as an active layer in a field-effect transistor revealing up to now the highest bulk charge carrier mobility for HBC derivatives. The device performance of phthalocyanines has been intensively investigated and can be compared to the obtained results, since the charge carrier mobility determined by the PR-TRMC technique was in the same range for both species.[46] In general, the substitution alkyl chains was reflected for Pcs in a significantly lower device mobility reaching up to 10^{-4} cm²/Vs for LB aligned films.[117-121] The mobility value for the zone-cast HBC-C_{12} is in the same range as reported for vacuum deposited or PTFE aligned plain Pc-discs which showed in all cases high order.[74]

The obtained results indicate that the great advantages of the zone-casting technique are the simple processing of large surface areas. Thus, this method opens new pathways for fabricating large-scale thin layers of highly oriented semiconductors and enhancing the charge transport. This is an important step towards improving the performance of organic semiconductors in electronic devices. In order to exploit these materials in applications such as active-matrix backplanes, further studies are required into stress and environmental stability. Moreover, it is assumed that in a controlled environment for the processing it is possible to enhance significantly the charge carrier mobility,[304] since aging in the presence of oxygen can diminish the device performance[305]. Therefore, it is essential to construct the devices on the same place, where the processing is carried out. On the other hand, it is also

important to investigate the real influence of the single intracolumnar defects observed by the AFM and in the IFFT image and to develop alternative concepts to avoid the appearance of such defects. It has been reported that grain boundaries increase the resistance significantly and lower the device performance.[306,307] An additional unknown aspect is the resistance at the interface between the inorganic contacts and the organic active layer which can decrease the device performance significantly. The major influence have top-contacts which are deposited by evaporation leading to degradation of the organic semiconductor.[308]

Due to the high order with its specific herringbone arrangement unique optoelectronic properties of the films were revealed. When combined with the highly anisotropic conductive properties, this phenomenon opens up the possibility of creating optoelectronic switching devices that could be actuated by external influences such as temperature or magnetic field. In addition, there are known examples of discotic compounds, such as peripherally substituted alkoxyphenylphthalocyanines, for which the transition from a tilted crystalline phase, formed on precipitation at room temperature, to an orthogonal mesophase is irreversible.[39] Such compounds would be potential candidates for optical data storage media based on the present phenomenon. The advantage over previously reported mechanisms for switching the optical properties of columnar discotics is that the columnar arrangement remains intact, and therefore their excellent semiconductive properties could be exploited together with their unique optical behavior.[309,310] One the other hand, it is essential to examine the switching rate of the film, which is an important factor for potential applications. Furthermore, the temperature dependent structure evaluation revealed that the degree of misalignment increases with repeating heating cycles. This effect represents also a problem for the utilization of the layer for long-term switching devices.

The increase of macroscopic defects after the annealing of the film in the mesophase is an important result for the post-processing of the zone-cast layers such as self-healing which occurs in the liquid crystalline phase when the molecular mobility is relatively high. Since in the case of the zone-cast HBC-C_{12} the phase transition from the crystalline state to the liquid crystalline phase is related to a supramolecular reorganization, the self-healing procedure cannot be applied for the zone-cast layers.

4.1.2. Dove-Tailed Hexa-*peri*-hexabenzocoronenes

The results described for HBC-C_{12} show impressively the transfer of the natural nucleation and growth in/from solution into the solution processing. It was revealed that this compound possessed a very high self-aggregation and a pronounced pre-aggregation in

solution as well as a morphology formation in drop-cast films which was independent of the kinetics (the morphology did not change with different evaporation temperature of the solvents).

In the following the self-aggregation in solution of three crystalline and plastic crystalline, respectively, HBC derivatives substituted with branched side chains will be discussed. In contrast to HBC-C_{12}, the side chains influence to a high degree the interaction of the aromatic cores leading to a higher solubility. Both the thermodynamics and the kinetics play an important role during the self-organization of the molecules in drop-cast films in the surface contact.

All three HBC derivatives carrying the six branched, space-demanding alkyl side chains of different lengths, HBC-$C_{6,2}$, HBC-$C_{10,6}$ and HBC-$C_{14,10}$, showed a similar strong concentration dependence in the ^{1}H NMR spectra as observed for HBC-C_{12}, which occurred at much higher concentration values than in the case of HBC-C_{12}.[238] Below $1x10^{-5}$ M, the three HBC derivatives with the branched alkyl chains existed as monomers in solution. HBC-$C_{6,2}$ possessed the lowest solubility among the three dove-tailed HBC samples. In comparison with HBC-$C_{10,6}$ and HBC-$C_{14,10}$, it became obvious that HBC-$C_{6,2}$ was more strongly aggregated due to a chemical shift at higher field at the same concentration. Surprisingly, HBC-$C_{10,6}$ showed the lowest self-association in d^2-1,1,2,2-tetrachloroethane-d_2 at 30 °C, followed by HBC-$C_{14,10}$ with the longest alkyl substituents. Table 4.1 shows the determined association constants for the dove-tailed compounds.

Table 4.1 *Association constants for self-aggregation of the investigated HBC derivative in 1,1,2,2-tetrachloroethane-d^2 at 30 °C.*[238]

Compound	K_a / L mol^{-1}
HBC-$C_{6,2}$	13.4
HBC-$C_{10,6}$	1.8
HBC-$C_{14,10}$	2.9
HBC-C_{12}	898

When HBC-$C_{14,10}$ is spin-coated on a HOPG surface at a concentration down to 10^{-7} M, single 60 to 80 nm wide blobs with a height of ca. 3 nm appeared, which were randomly distributed over the surface (Figure 4.30a). By spin-coating HBC-$C_{14,10}$ from a 10^{-4} M THF solution, the freshly cleaved graphite surface was covered by an inhomogeneous ~100 nm thick film which showed no nanoscopic order (Figure 4.30b). From a solvent mixture of

methanol and chloroform (1:1) at the same concentration, single flat pancake shaped features with a constant thickness of ca. 2.5 nm were formed (Figure 4.30c).

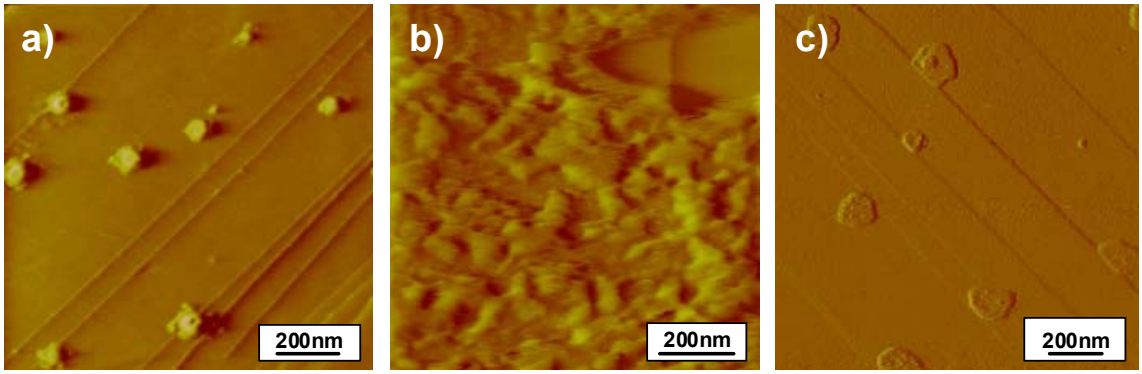

Figure 4.30. AFM images in tapping made on HOPG surface of spin-coated films of HBC-$C_{14,10}$ from a) a 10^{-7} M and b) 10^{-4} M THF solution, c) from solvent mixture of methanol and chloroform (1:1).

On the other hand, drop-cast HBC-$C_{14,10}$ and HBC-$C_{10,6}$ films from 10^{-4} M THF solutions were completely amorphous as presented in Figure 4.31a and 4.31c. By using toluene as solvent, the film morphology changed slightly revealing birefringent parts which appeared at the rim of the drop-cast films where most of the material was deposited (Figure 4.31b and 4.31d).

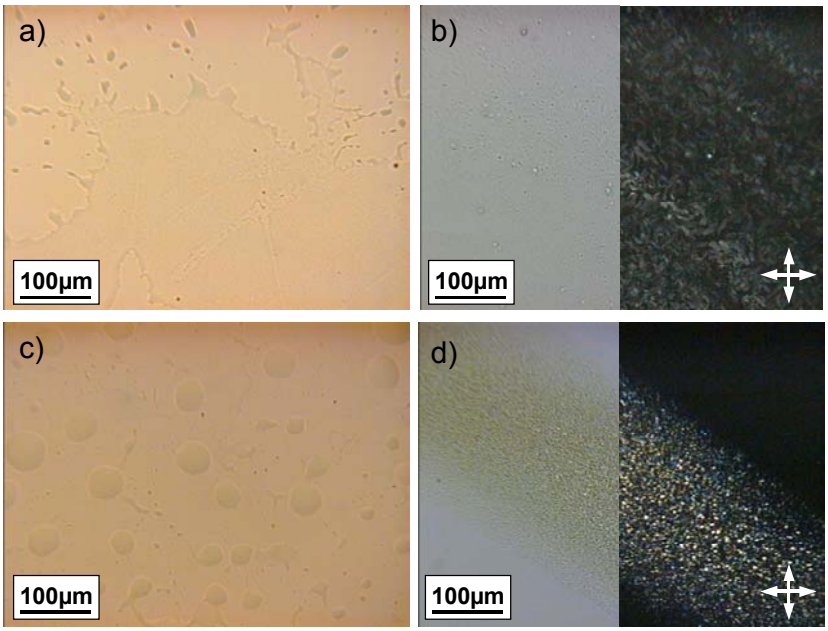

Figure 4.31. *Optical POM images of drop-cast HBC-$C_{10,6}$ from 10^{-4} M a) THF and b) toluene (right image with cross-polarizer), and of drop-cast cast HBC-$C_{14,10}$ from 10^{-4} M c) THF and d) toluene (right image with cross-polarizer).*

The drop-cast films of HBC-$C_{6,2}$ (Figure 4.32a) prepared from a 10^{-4} M THF solution also did not show any birefringence in polarized light, but small particles precipitated randomly from the solution. When the same material was processed from toluene with an identical concentration short crystalline needles appeared at the rim of the film (Figure 4.32b). These structures were highly birefringent and were mainly oriented in the direction of the drop evaporation, whereas the interior of the film revealed the same, but shorter structures. By using a comparable solvent with respect to the association such as xylene, which possesses a significant higher evaporation temperature, the length of these crystalline needles within the film interior increased considerably (Figure 4.32c). Finally, when a saturated toluene solution of HBC-$C_{6,2}$ was slowly evaporated from a small vessel, centimeter long, crystalline fibers were obtained on the bottom of the vessel (Figure 4.32d).

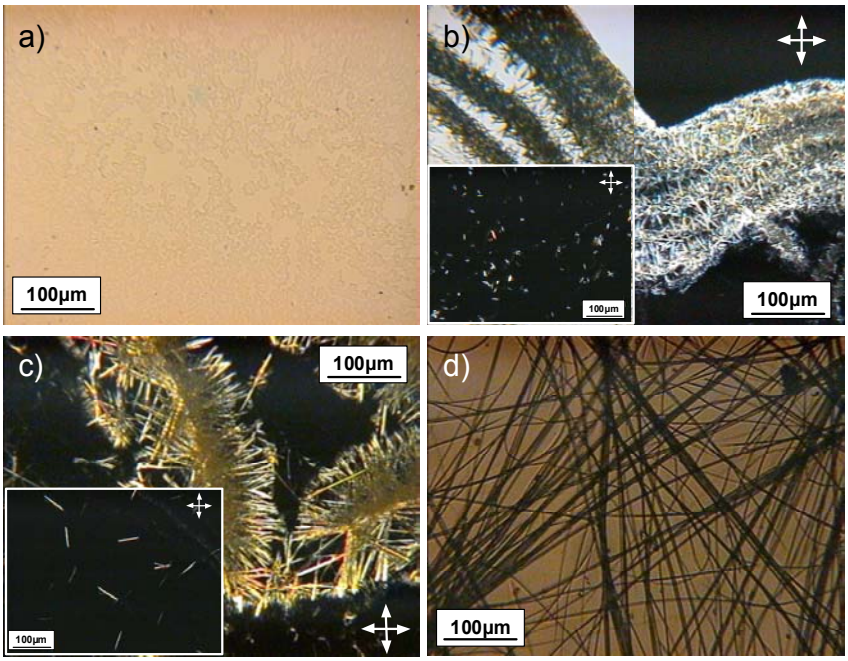

Figure 4.32. *Optical image of HBC-$C_{6,2}$ drop-cast from a) THF and POM of the rim of HBC-$C_{6,2}$ drop-cast from b) 10^{-4} M toluene (inset shows the interior of the film), c) from 10^{-4} M xylene (inset shows the interior of the film) both at a concentration of 10_{-4} M, optical image obtained after evaporation of a HBC-$C_{6,2}$ solution with a concentration close to the saturation.*

Due to this extraordinary nucleation and growth of such large crystalline needles in solution, a dipping experiment was performed in order to align these structures uniaxially as shown in Figure 4.33. Thereby, the support is slowly pulled out of the solution. At a concentration of 10^{-1} M in toluene and a low moving velocity (0.2 µm/s) of the support, a

homogenous film was acquired with indeed uniaxially oriented microfibers. The 2D-WAXS in Figure 4.33b confirmed the pronounced orientation of the columnar structures in the dipping direction. During the moving out of the support a meniscus is formed at the surface at which due to the solvent evaporating the material nucleates.

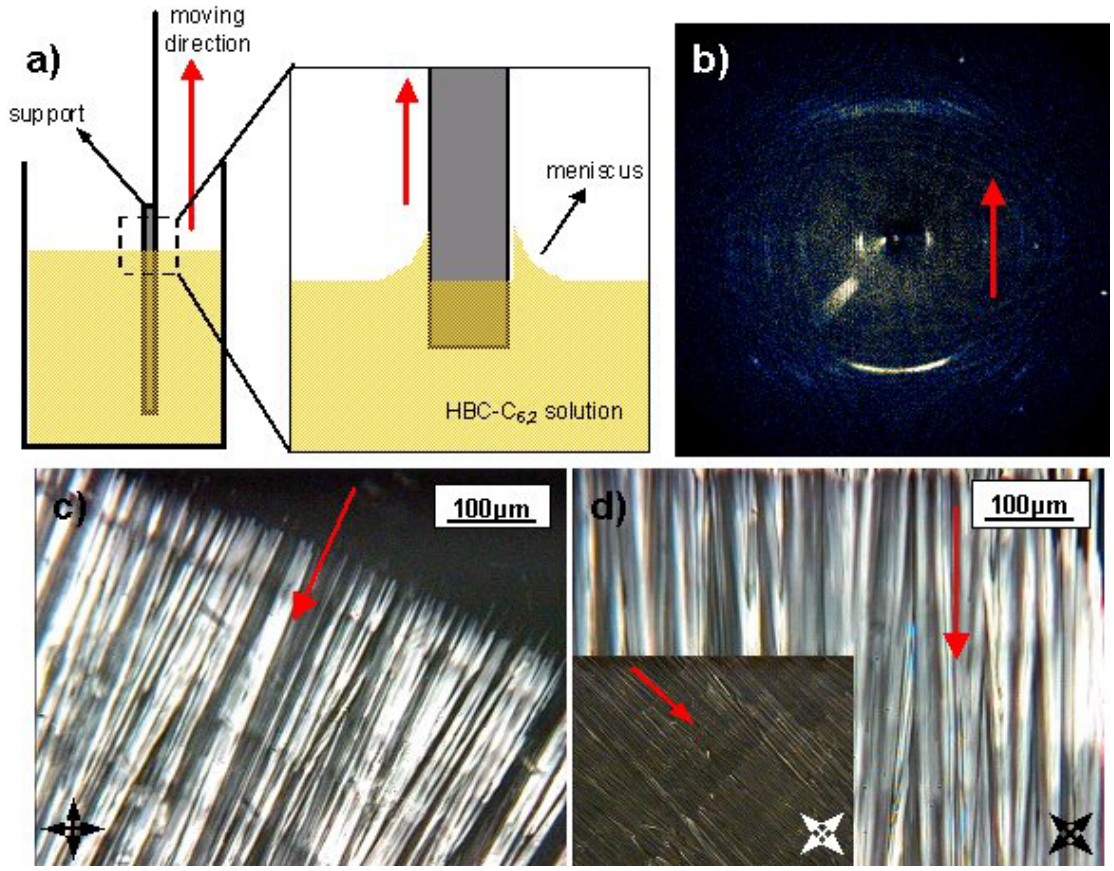

Figure 4.33. *a) Set-up for the dipping experiment of HBC-$C_{6,2}$ within a highly concentrated toluene concentration, at the deposition zone a meniscus is formed at within the material precipitates onto the moving support; b) 2D-WAXS pattern of the aligned HBC-$C_{6,2}$ film; c) POM of the nucleation site at which the structures begin to grow in the moving direction of the support; d) POM of the interior of the film revealing a uniaxial orientation of the mircofibers.*

The self-aggregation of the HBCs with branched alkyl substituents occurred in a different concentration range as compared to HBC-C_{12}. The dove-tailed side chains, which possess a large peripheral steric demand, have a significant effect on the molecular interaction disturbing the π-stacking of the aromatic cores.[311] Due to the space-filling alkyl chains the self-aggregation of these dove-tailed HBCs took place only at much higher concentrations in

comparison to HBC-C_{12}, whereby the degree of the peripheral steric hindrance was strongly dependent on the length of the branched side chains as it was also observed for tribenzocyclononenes.[312] However, an extreme elongation of the side chains to $C_{14,10}$ did not increase the steric demand and did not influence the self-aggregation in solution at room temperature. It has been reported that oligo(p-phenylenevinylene)s[313] and oligothiophenes[314] at low concentrations form golubar objects, but with a concentration increase single isolate stacks were transformed into a network structure.

The investigation of the film morphology obtained through solution casting revealed additional information about the solution behavior of the HBC derivatives. It has been found that in addition to the thermodynamical aspect, which was reflected by the self-association constant, the organization from solution is also dominated by kinetics. The latter aspect has been impressively demonstrated in the case of HBC-$C_{6,2}$, which was prepared from different solvents with different evaporation rates. The kinetics plays also an important role for the alignment of polyfluorene copolymer films on rubber polyimide layer.[315] The highest degree of orientation was obtained when the polymer was cast from solvents with very high evaporation temperatures. In general, the morphology is in close relation with the device performance as reported for vacuum deposited oligothiophenes.[316,317]

Comparing the films of HBC-$C_{6,2}$ which were drop-cast from solvents like toluene and xylene, in which the self-association is known to be very similar, one observed larger micro-objects in the case of the higher boiling xylene. The morphology of a film obtained from THF differed significantly, since only an amorphous structure was obtained. In the latter case, it should be noted that the degree of self-association is also smaller. Nevertheless, the evaporation time of the solvent in the casting process influenced significantly the macroscopic self-organization on the substrate. A slowly evaporating solvent like xylene allowed the formation of large anisotropic objects, whereas a solvent with a lower boiling point did not allow enough time to exhibit a similar organization. The role of the kinetics in the case of HBC-$C_{6,2}$ is more pronounced compared to HBC-C_{12} which revealed the micro-ribbons over the drop-cast film relatively independent of the used solvent. This effect can be explained now by the steric requirement induced by the dove-tailed alkyl substituents, which hampered the discs to approach one another. These extraordinary structures resulted on one hand from the strong self-association tendency and on the other hand from the low steric demand of the attached alkyl chains. Consequently, HBC-C_{12} has been successfully solution processed by zone-casting into highly ordered surface layers supported by the pronounced size of the pre-aggregates, which existed already before the deposition from solution. On the other hand, the alignment of HBC-$C_{6,2}$ requires more experimental effort due to its slow self-aggregation and

the necessity to use high concentrations to reach a sufficient pre-aggregation in solution. Using a high concentration accompanied by a slow solvent evaporation allowed a uniaxial orientation in surface layers, which were obtained in the dipping experiment. This method might be an alternative processing technique for materials with a strongly time dependent self-assembly. Due to the increase of the peripheral steric demand of the longer dove-tailed side chains, both compounds HBC-$C_{14,10}$ and HBC-$C_{10,6}$ did not show any tendency to create anisotropic structures from solution. Both HBC derivatives only formed small domains after the deposition, since the association rate extremely decreased compared to HBC-$C_{6,2}$.

All these results can be correlated with preliminary FET measurements of spin-coated films. HBC-C12 and HBC-C6,2 showed identical maximum charge carrier mobilities when prepared from solvents with a low evaporation rate, whereby HBC-$C_{14,10}$ and HBC-$C_{10,6}$ did not reveal any field-effect independently of the solvent used.[318]

In summery, sterically demanding dove-tailed alkyl substituents reduce significantly the self-aggregation behavior of HBC derivatives in solution comparing with dodecyl substituents. HBC-C_{12} exhibits one of the highest self-aggregation constants based only on π-stacking, due to the large π-area and unhindered stacking. The steric requirement of the dove-tailed substituents allows the regulation of the self-association in solution and opens the opportunity of the additional controlling the morphology by specific solution processing which is important for materials science during device fabrication. Morphology studies revealed that both the thermodynamical properties and kinetic aspects are important during self-aggregation in solution. These conclusions should elucidate, whether the solution association propensity can be translated to the bulk behavior and thus used for the processing of the material and device fabrication.

4.2. Solution Processing of Non-Crystalline Discotics

In the following the supramolecular organization of two polycyclic aromatic hydrocarbons, HBC-PhC_{12} and C96-C_{12} which both do not reveal a crystalline phase, after the zone-casting processing has been investigated in comparison with HBC-C_{12}. The two materials, HBC-PhC_{12} and C96-C_{12}, exhibited a considerably lower tendency to self-organize at the surface-solvent interface than HBC-C_{12}. When HBC-PhC_{12} was drop-cast from a 10^{-4} M toluene solution (Figure 4.34a), considerably shorter ribbons are formed than observed previously for HBC-C_{12} confirming the smaller tendency for self-assembly. This is also in agreement with the enhanced solubility of the compound reported elsewhere.[197] The drop-casting of C96-C_{12} at room temperature resulted in the formation of an amorphous film,

whereas the preparation of the surface layer above 45 °C led to the appearance of birefringence (Figure 4.34b). Bulk C96-C_{12} undergoes a thermal order-order transition at 38 °C, possibly related to an increased alkyl chain mobility, which could promote the formation of more ordered films under the utilization of a higher temperature.[205] At a closer inspection of the topography of the drop-cast C96-C_{12} layer by using the AFM (Figure 4.34c), one can observe several hundreds of nanometer long randomly distributed aggregates which indicate a certain degree of self-organization on the surface.

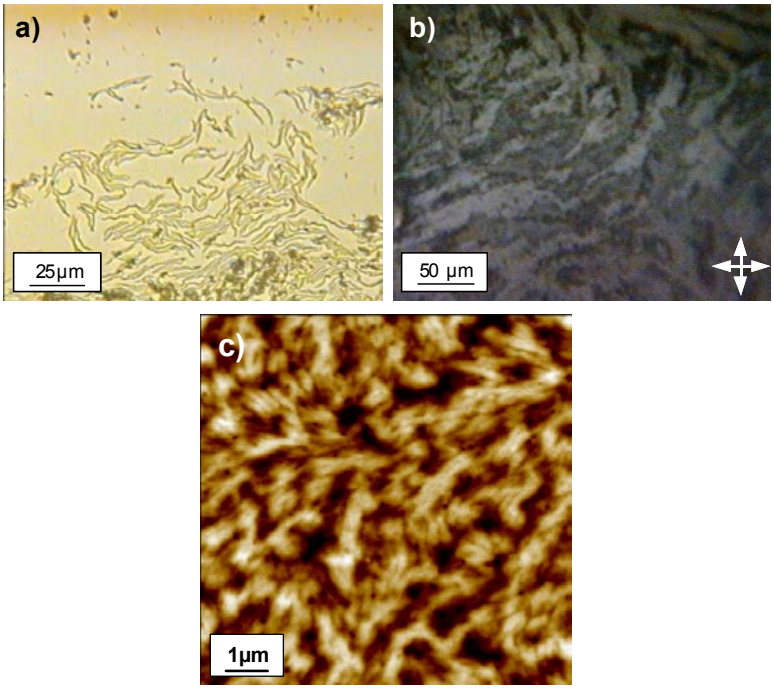

Figure 4.34. *a) Optical image of a HBC-PhC_{12} drop-cast film and b) POM of a C96-C_{12} prepared by drop-casting at 45 °C, both were cast from a 10^{-4} M THF solution, c) AFM in tapping mode of the drop-cast C96-C_{12} film.*

Because of the essentially different solubilities and apparent aggregation behavior in solution of the two compounds, the processing parameters such as the choice of the appropriate solvent, concentration and processing temperatures during zone-casting had to be optimized for each individually. In Figure 4.35 typical POM images of zone-cast HBC-PhC_{12} films obtained at different processing conditions are shown. One can notice immediately that the film morphology depends strongly on the applied parameters. The most distinct difference appears for different solvents. From toluene larger ordered domains, which reveal same orientation in the deposition direction, can be obtained (Figure 4.35a and 4.35d), whereas from THF no aligned structures can be observed (Figure 4.35f). The material just precipitates from the solvent onto the support. In general, when the concentration is too low, characteristic

periodic features are formed by the zone-casting (Figure 4.35c for toluene and 4.35e for THF).

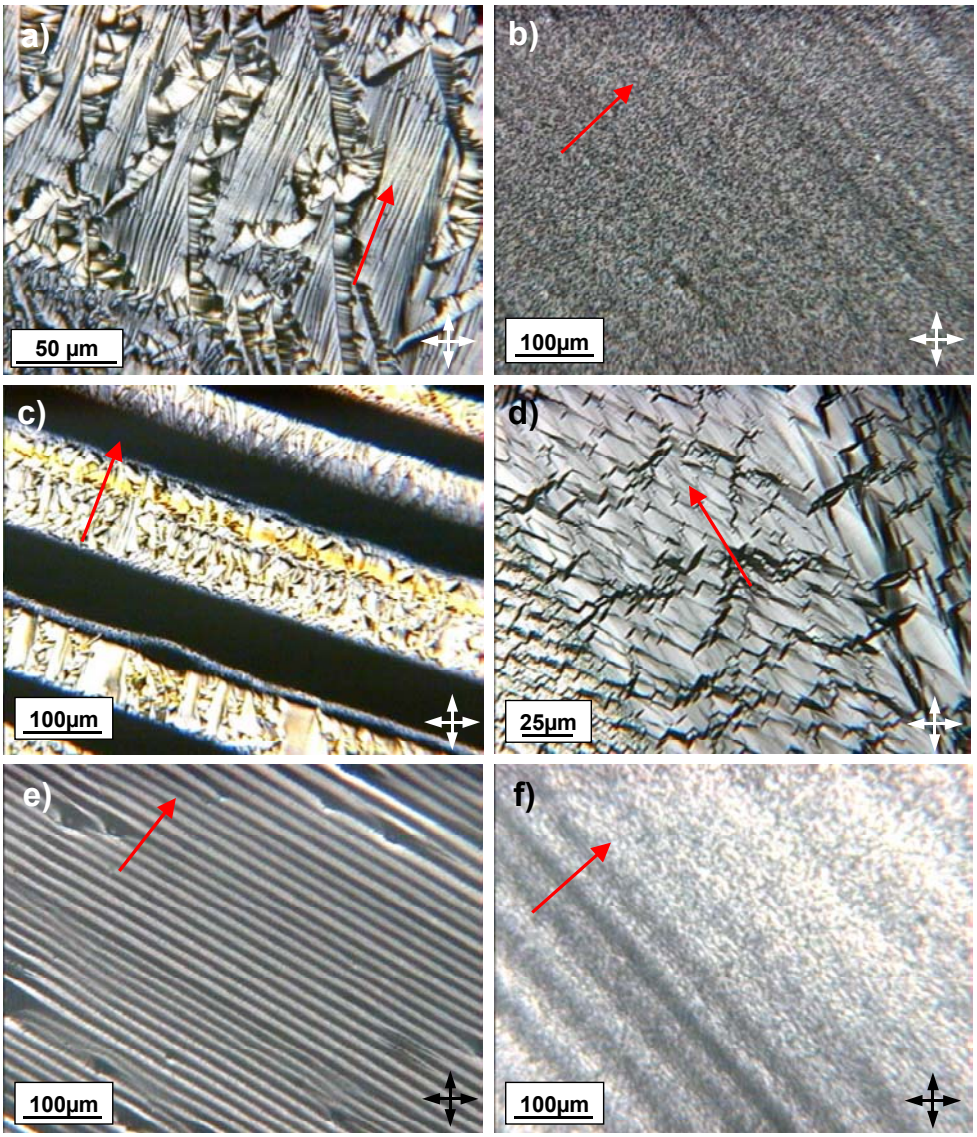

Figure 4.35. *POM images of zone-cast HBC-PhC$_{12}$ at different processing parameters from toluene at a) 90 µm/s, 95 °C/93 °C, 1.0 mg/ml (large distance between nozzle and support); b) 90 µm/s, 95 °C/93 °C, 1.0 mg/ml (small distance); c) 90 µm/s, 95 °C/93 °C, 0.5 mg/ml; d) 40 µm/s, 95 °C/93 °C, 0.5 mg/ml, and from THF at e) 0.35µm, 50 °C/40 °C, 0.5 mg/ml; f) 0.35µm, 50 °C/40 °C, 1.0 mg/ml.*

The following optimal processing parameters for HBC-PhC$_{12}$ were determined: the concentration of 1 mg/ml in a mixture of tetrahydrofuran (THF) and toluene in a ratio of 4:1, the substrate velocity 60 µm/s, the solution temperature of 55 °C and the substrate

temperature of 46 °C. The C96-C_{12} was zone-cast processed from toluene at a concentration of 1 mg/ml and a substrate velocity of 20 µm/s at temperatures of 55 °C and 45 °C for the solution and the substrate, respectively. Both compounds were zone-cast at ambient conditions directly onto an untreated glass substrate.

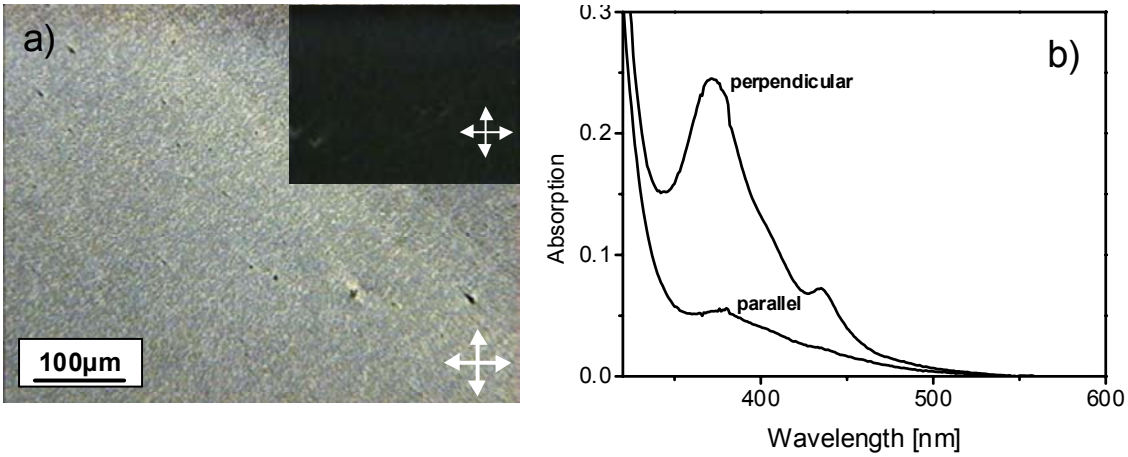

Figure 4.36. *Optical anisotropy of the zone-cast HBC-PhC_{12} a) POM images with 45° of the deposition direction related to the analyzer/polarizer axes (inset 0°) (black arrow indicates the casting direction); b) UV-Vis absorption spectra in polarized light measured with parallel and perpendicular to the casting direction.*

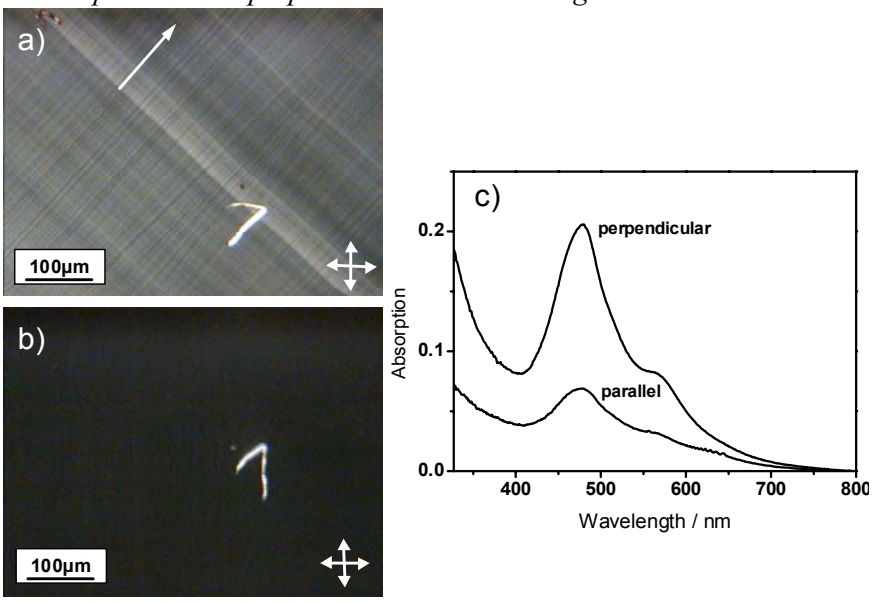

Figure 4.37. *POM images of zone-cast C96-C_{12} with a) 45° and b) 0° of the deposition direction with respect to the analyzer/polarizer axes. The number "1" confirms the same part of the sample and the same light intensity for both images (white arrow in a) indicates the zone-casting direction); c) UV-Vis absorption spectra in polarized light measured parallel and perpendicular to the casting direction.*

At these optimized conditions the zone-casting of both discotics, HBC-PhC$_{12}$ and C$_{96}$-C$_{12}$, yielded thin homogenous layers over large areas. The assignment of the optical anisotropy is one important tool in the structure characterization of the uniaxially oriented films.[90,118,182,319,320] The optical anisotropy is strongly dependent on the transition dipole moment of the molecules, which gives in turn essential information about the molecular organization. The POM images presented in Figures 4.36a and 4.37a,b indicated a high optical anisotropy of the zone-cast films. The birefringence of the surface layers under cross-polarizers was strongly dependent on the relative position of the deposition direction with respect to the analyzer/polarizer axes. The maximum birefringence appeared at an angle of 45° with respect to the deposition axis of the layers and the analyzer/polarizer axes, whereas at the coincidence of both directions a nearly complete extinction occurs. The absorption spectra, which were recorded at polarization perpendicular and parallel with respect to the deposition direction, are shown in Figures 4.37c and 4.36b for C96-C$_{12}$ and HBC-PhC$_{12}$, respectively, and verified the optical anisotropy revealing a dichroic ratio of 3.04 for C96-C$_{12}$ and 4.52 for HBC-PhC$_{12}$ The optical behavior of the zone-cast films is similar to that reported for thin HBC-PhC$_{12}$ films uniaxially oriented on friction-oriented PTFE.[186] The strong optical anisotropy of the zone-cast layers and onto PTFE aligned films can be related to the transition dipole moments which are oriented in the aromatic core plane. Since the maximum absorption occurs perpendicular to the alignment direction, one can assume a uniaxial columnar orientation along the processing direction when the discotic molecules are arranged orthogonal to the columnar axes. These results are also in close correlation to the mesophase organization of the zone-cast HBC-C$_{12}$, whereby the latter compound showed a dichroic ratio of ca 2.5 being lower than for HBC-PhC$_{12}$ and C96-C$_{12}$. This difference can be explained by the different degree of order in the corresponding films.

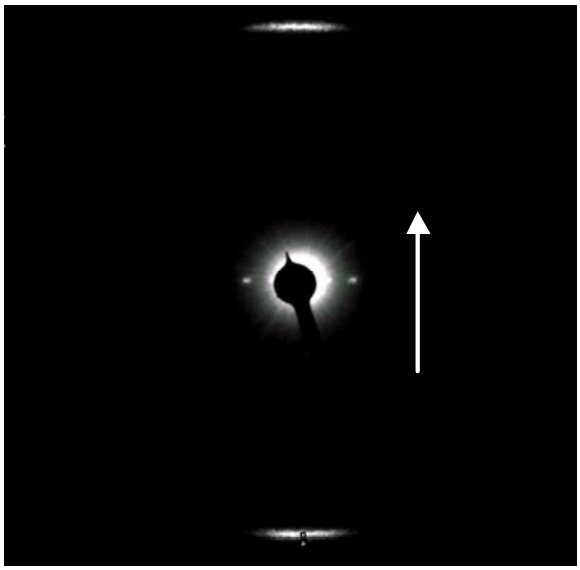

Figure 4.38. *Electron diffraction of the zone-cast HBC-PhC$_{12}$ layer (arrow indicates the casting direction).*

Figures 4.38 and 4.39 present typical electron diffraction patterns of zone-cast HBC-PhC$_{12}$ and C96-C$_{12}$, respectively. In both cases, distinct point-like equatorial reflections indicate high uniaxial intercolumnar order with orientation of columns in the casting direction. The appearance of only two equatorial reflections

(the first and second order) indicated the short-range intercolumnar correlation which is characteristic for the liquid crystalline phase accompanied by an increased molecular dynamics. The meridional reflections, corresponding to the characteristic intracolumnar distance of 0.34 nm, confirm an orthogonal intracolumnar arrangement of the discotic molecules. Moreover, the shape of the meridional reflections verify the high intracolumnar order of the molecules. Meridional arcs imply a certain degree of columnar misalignment, in contrary to the reflections in the electron diffraction patterns in Figures 4.38 and 4.39 which are only laterally extended confirming a high intracolumnar correlation, but indicating as well the absence of an intercolumnar correlation between the discs (see Figure 4.40).[321] This is in strong contrast to the electron diffraction of HBC-C_{12} at the crystalline phase exposing a large number of higher-order reflections due to a high molecular correlation.

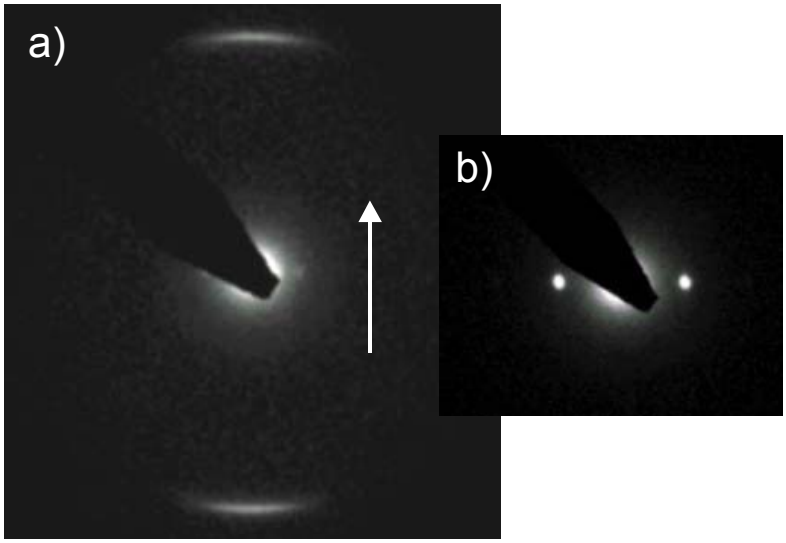

Figure 4.39. a) Electron *diffraction of zone-cast films of C96-C_{12}, b) magnification of the equatorial reflections from pattern in a). Arrow indicates the casting direction.* .

In the schematic illustration in Figure 4.40 the columnar arrangement is assumed as identical in both presented cases and therefore the equatorial scattering intensity distribution is not influenced by the modification of the intracolumnar packing.[321] Nevertheless, a variation of the structure factor, by an increase of the intracolumnar correlation of the discs, becomes obvious in a change of the meridional reflections which is schematically presented in Figure 4.40a. This supramolecular organization is characterized by meridional reflection peaks which appear as distinct spots accompanied by further higher order peaks distributed in the off-meridional. In the case of a simple intracolumnar correlation the meridional reflections remain distinct, but broaden only laterally (Figure 4.40b). The absence of an intercolumnar

disc correlation can be explained by the increased lateral and longitudinal mobility of the molecules within the stacks. A significant increase of the aromatic core and, therefore, a change in the form factor results in an identically high degree of supramolecular order in sharper meridional reflections in the scattering pattern (Figure 4.41).

The position of the first equatorial reflection in the electron diffraction pattern of zone-cast HBC-PhC_{12} appeared at a position correlated to an intercolumnar distance of 3.02 nm within a cubic lattice, whereas the nearest hexagonal columnar distance of 3.26 nm for the zone-cast C96-C_{12} was determined. Both observed intercolumnar periods were in good agreement with the lateral packing parameters obtained by X-ray diffraction for extruded filaments.[30]

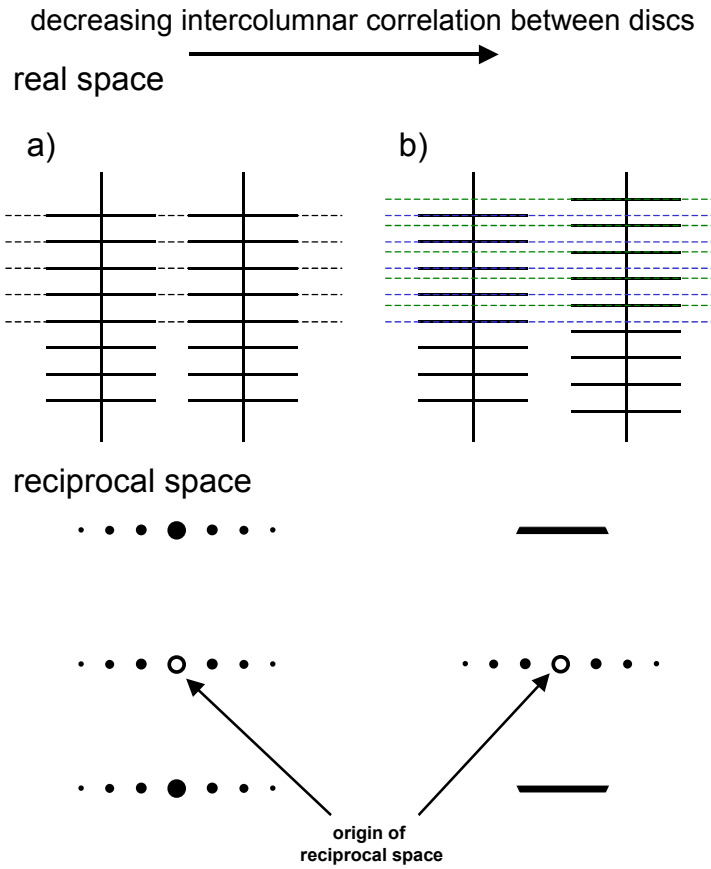

Figure 4.40. *Effect of the structure factor on the scattering pattern of discotic molecules organized in columnar structures. Relationship between the intercolumnar correlation of the discotic molecules and the resulting scattering patterns for a) a high intercolumnar correlation and b) a poor correlation.*

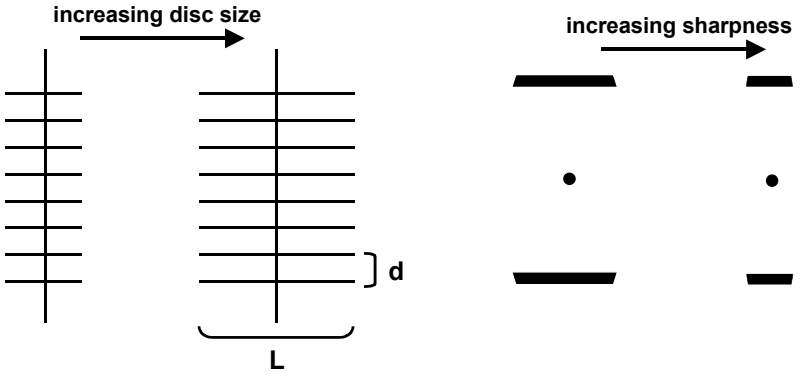

Figure 4.41. *Effect of the disc form factor on the scattering pattern of discotic molecules organized in columnar structures. Relationship between the increasing core size L and the resulting scattering pattern (the intracolumnar period d is constant).*

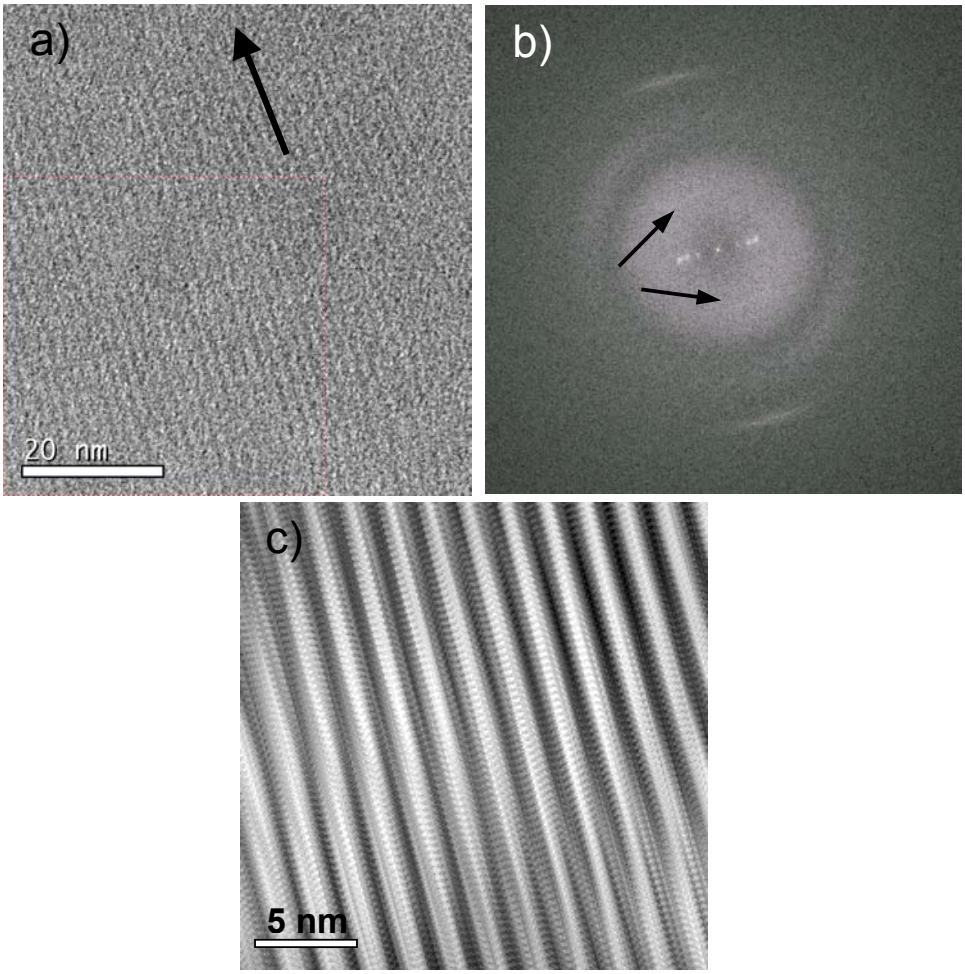

Figure 4.42. *a) HR-TEM of zone-cast HBC-PhC$_{12}$ (black arrow indicates the casting direction); b) fast Fourier-Transformation (FFT) of a) (black arrows show a higher order meridional peak) and c) inversed FFT image.*

Further insight into the supramolecular arrangement was obtained by HR-TEM shown for a zone-cast HBC-PhC_{12} film in Figure 4.42. The columns were highly uniaxially oriented in the deposition direction with a columnar length exceeding the investigated area. The Fast-Fourier transformation (FFT) image in Figure 4.42b revealed reflections corresponding to the intercolumnar as well as the intracolumnar periods found by the electron diffraction. The inverse FFT image displayed not only the uniaxial columnar alignment, but visualizes additionally the intracolumnar periods of 0.34 nm, corresponding to the molecular stacking. This period is in good agreement with the results obtained from electron diffraction experiments.

Since the electron diffraction results provide information only about the in-plane order in the zone-cast films, additional X-ray scattering experiments performed in reflection mode reveal the out-of-plane arrangement.

The X-ray diffraction of zone-cast C96-C_{12} presented in Figure 4.43 suggested a highly uniform out-of-plane structure with an intercolumnar period identical to that observed in-plane. During thermal treatment no changes in the supramolecular structure were determined. This is analogous to the behavior reported for the bulk material which also did not show any temperature dependent structural transitions.[205]

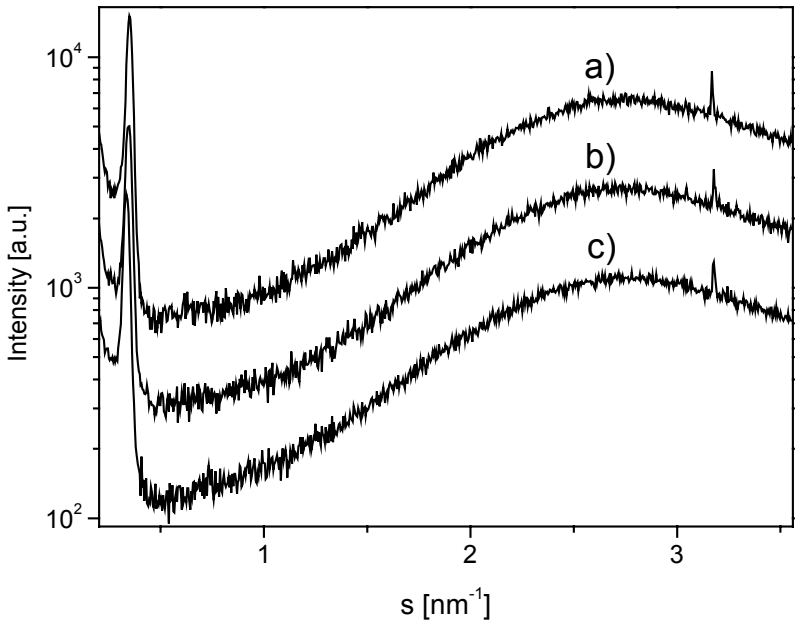

Figure 4.43. *Temperature dependent large-area X-ray diffraction in reflection mode of zone-cast C96-C_{12} a) at 30 °C, b) at 150 °C and c) at 30 °C after annealing.*

In contrast, the X-ray diffraction pattern of zone-cast HBC-PhC$_{12}$ implied a more complex and temperature dependent in-plane supramolecular arrangement. The XRD results in Figure 4.44 show a well-ordered HBC-PhC$_{12}$ zone-cast layer immediately after the zone-casting processing. The large number of higher order *(h00)* reflection peaks indicates a pronounced intercolumnar out-of-plane order in the investigated area. The peak positions could be fitted according to a 2D lateral cubic unit cell which was in good agreement with the bulk lattice of HBC-PhC$_{12}$. The appearance of a distinctive small-angle reflection related to a periodicity of 6.25 nm, which was the double distance of a simple intercolumnar distance of 3.12 nm, confirmed a highly ordered superstructure. On the other hand, weak shoulders of the (200) and (400) reflection peaks suggested a slight degree of misalignment in the out-of-plane arrangement. These reflection shoulders were attributed to mixed lattice planes which were also oriented along the out-of-plane and became therefore obvious in the XRD results. Therefore, not all columns in the successive layers lay one on top of each other inducing the appearance of these additional *(hk0)* reflections. Despite these lattice displacements, the pronounced uniaxial columnar alignment was maintained.

When the zone-cast HBC-PhC$_{12}$ layer was heated above the bulk phase transition to 130 °C, a considerable structural change was observed by the alteration of the X-ray diffraction pattern. Bulk samples revealed only a change in the intercolumnar arrangement during the heating above the phase transition at 81 °C.[30] The X-ray diffraction pattern of the zone-cast layer in the higher temperature phase showed two sharp reflections and two broad peaks which all could be fitted to a hexagonal lateral unit cell. The hexagonal unit cell parameter of a = 6.25 nm was calculated on the basis of the position of the (100) peak implying a higher order supramolecular arrangement also above the phase transition. Interestingly, the odd and even Miller's indexed reflections differed significantly in their shapes; the odd peaks were broad, whereas the even ones were sharp and distinct. An explanation might be a weaker correlation of the higher order structure than that of adjacent columns which possess the highest structural correlation resulting in the strongest contrast during the X-ray scattering. Anyway, the appearance of such a higher order columnar organization in the high temperature liquid crystalline phase of discotics has not yet been reported and is quite untypical, since the degree of order decreases significantly with the increase of lateral and longitudinal dynamics of the molecules.

After cooling back to the room temperature phase, most of the reflections observed before annealing were recovered, except the first small angle peak corresponding to 6.25 nm (Figure 4.44c) indicating that the higher order correlation disappeared after reorganization of molecules at the higher temperature phase.

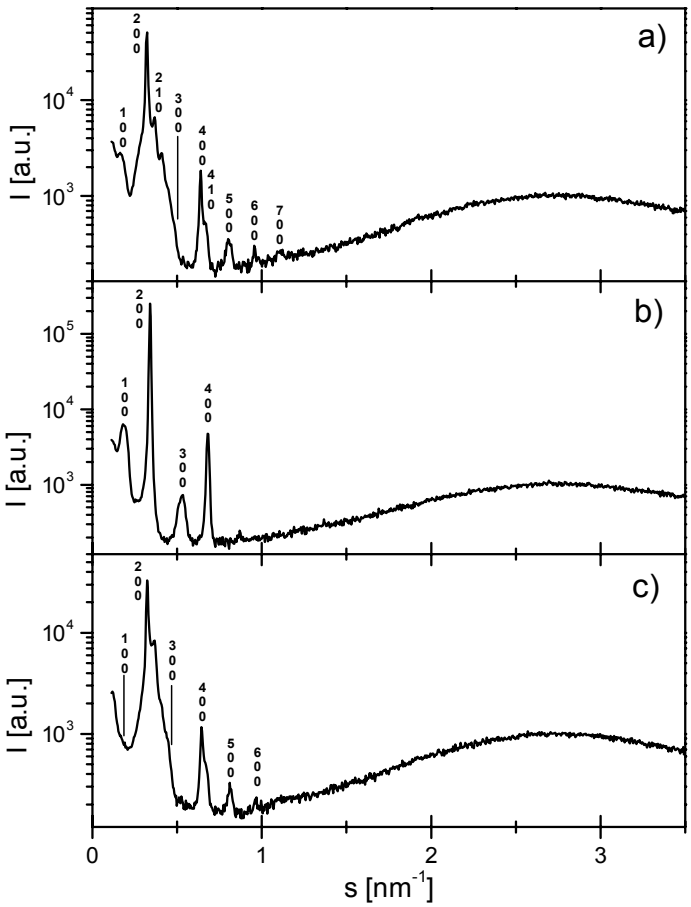

Figure 4.44. *Temperature dependent scattering intensity distribution as a function of the scattering vector acquired by large area X-ray scattering measurements of zone-cast HBC-PhC$_{12}$ at a) 30 °C, b) 130 °C and c) at 30 °C after annealing. Reflection peaks are assigned according to the Miller's indexes (hkl).*

In general, both X-ray diffractograms did not reveal the π-stacking correlation of the discotic molecules being in good structural agreement with the supramolecular arrangement on the support. In that experimental set-up the scattering vector was oriented perpendicular to the substrate, whereas the stacking correlation of the discs within the columns was aligned parallel to the support. The same observation was performed for the zone-cast HBC-C$_{12}$.

In comparison to the supramolecular organization observed for bulk HBC-PhC$_{12}$ samples, the zone-cast layer revealed a remarkably higher ordered superstructure due to a significantly more efficient alignment, whereas the packing parameters were not influenced by the alignment techniques. Both investigated planes, the in-plane and out-of-plane with respect to the substrate, exhibited the same value for the nearest intercolumnar packing of 3.12 nm fitting to a cubic arrangement. The large number of the (h00) reflection peaks in the

XRD for the HBC-PhC_{12} zone-cast layer at room temperature indicated a higher order supramolecular correlation.

The structure evaluation of the zone-cast C96-C_{12} layers revealed only one reflection peak related to the intercolumnar arrangement at an identical position in both planes. When the same hexagonal columnar organization in bulk and in the zone-cast surface layers exists, then the appearance of the same unit cell parameter in both investigated planes suggests displacements of the columnar lattice along the casting direction. A uniform hexagonal columnar order on the surface would allow the observation of the characteristic (h00) scattering intensities only in-plane or out-of-plane. Nevertheless, the results from electron diffraction proved that the C96-C_{12} columns were also highly oriented in the deposition direction.

Discotic molecules with a significantly higher solubility, which is closely related to a lower self-aggregation in solution, revealed less organized films prepared by drop-casting, but formed highly ordered and long-range, uniaxial aligned surface layers when processed by the zone-casting technique. The supramolecular structure of both zone-cast compounds was identical to the mesophase order in the zone-cast HBC-C_{12} possessing the characteristic short-range correlation due to the increased molecular dynamics in the liquid crystalline phase. Thereby, the HBC-PhC_{12} and C96-C_{12} films revealed a more pronounced intracolumnar arrangement, whereas the HBC-C_{12} seemed to lie more uniformly on top of each other. In contrast to the short-range correlation observed by electron diffraction, the HR-TEM images displayed a uniaxial alignment and the optical analysis confirmed the macroscopic ordering. It should be noted that this is the first time that liquid crystalline materials have been aligned by solution processing without the additional application of pre-oriented layers as such HBCs[185] or triphenylenes[164] on PTFE.

However, it should also be considered that the optimal processing parameters for discotic materials with poorer directional growth related to a weaker interaction between the single molecules in solution are more difficult to determine. Despite these difficulties, this study suggests that the zone-casting method is not necessarily restricted to the alignment of materials possessing a strong self-aggregation and a high nucleation, but it can be also applied to many other organic self-assembling semiconductors making this technique more versatile. These conclusions are essential for the film fabrication of other soluble organic semiconductors for the application in electronic devices. Finally, the successful alignment of HBC-PhC_{12} and C96-C_{12} as thin films opens the opportunity to employ both compounds as active layers in field-effect transistors and the investigation of their bulk electronic properties.

Chapter 5

Control of the Thermal Behavior and Processing from the Isotropic Phase

The processing from the isotropic state depends strongly on the crystallization behavior of the material and its growth ability. Therefore, before the alignment procedure, the morphology was investigated, obtained by cooling the sample, which was sandwiched between two glass slides, from the isotropic phase. Furthermore it is important that the processibility from the isotropic state can occur at reasonable temperatures which can be controlled by the introduction of space-filling side chains which considerably lowered the isotropization temperature of the HBC derivatives. The supramolecular order and molecular orientation, which have a fundamental influence on the device performance, were directed by improving the molecular affinity towards specific surfaces leading to the edge-on arrangement or homeotropic alignment of the discs. In general, the modulation of the chemical nature of the aromatic core or of the side chains opens the opportunity to increase the surface affinity of the molecules.[322]

5.1. Control of the Isotropization Temperature by the Introduction of Dove-Tailed Side Chains

The influence of the substituents on the thermal behavior of the dove-tailed HBC derivatives was followed by DSC cooling and heating rates were 10 °C/min). The results were derived from the DSC traces, which are summarized in Table 5.1. It was found that the phase behavior of the investigated HBC compounds differed significantly, indicating a strong

dependence of the thermal behavior on the length and structure of the side chains. The phase transitions were characterized in detail by using solid-state NMR (not shown) and X-ray diffraction (discussed in Chapter 3).

Table 5.1. *Thermal behavior determined by DSC of the investigated HBC derivatives. The recrystallization temperatures and the enthalpies during cooling are given in brackets.*

Compound	Temperature [°C]	Enthalpy [J/g]	Phase transition
HBC-$C_{6,2}$	97 (81)	21.4 (17.3)	C_r – Col_d
	420 (380)	–	Col_d – I
HBC-$C_{10,6}$	24 (-26)	26.1 (16.4)	Col_p – Col_d
	93 (73, 45)	2.3 (2.6, 1.0)	Col_d – I
HBC-$C_{14,10}$	46 (7)	33.4 (32.2)	Col_p – I
HBC-$C_3OC_{14,10}$	-15 (-21)	7.6 (6.7)	Col_x – Col_p
	42* ; 22 (14)	20 (22.6)	Col_p – I
HBC-$C_3OC_{10,6}$	-1 (-5)	13.8 (12.9)	Col_p – Col_{hd}
	162 (155)	2.9 (3.5)	Col_{hd} – I
HBC-$C_3OC_{6,2}$	55 (17)	10.5 (8.8)	Col_p – Col_{hd}
	~420 (~370)	-	Col_{hd} – I
HBC-$C_3OC_{8,2}$	0 (-38)	10.3 (10.6)	Col_p – Col_{hd}
	~370 (~340)	-	Col_{hd} – I

* first heating. List of abbreviations: Col_x – unassigned columnar phase, C_r – crystalline phase Col_p – plastic crystalline phase, Col_{hd} – hexagonal disordered columnar phase, I – isotropic phase.

In order to analyze the influence of dove-tailed side chains in comparison to linear alkyl chains and chains containing methylene groups, the isotropization temperature was plotted as a function of the side chain volume (Figure 5.1). Thereby, the linear and methylene containing chains are considered as cylinders and the dove-tailed ones as cones. By plotting the side chain volume onto a logarithmic scale, a linear relationship of the isotropization temperature can be observed for each type of side chain. Particularly, the dove-tailed HBC derivatives follow strictly the linearity indicated by the dashed lines. It is apparent that the number of atoms in the side chains is negligible, but the steric requirements, resulting from the high degree of rotational freedom at the branching site (verified by solid-state NMR), play a much more important role for the thermal behavior of the compounds. Thus, the dove-

tailing of the side chains led to a dramatic lowering of the isotropization temperature in comparison with the substitution of linear alkyl chains. For instance, in order to obtain an identical isotropization temperature for an HBC derivative substituted by linear side chains as for a compound bearing the dove-tailed chains, the number of carbon atoms has to be increased significantly in order to reach the same side chain volume. From Figure 5.1 it is also possible to derive that the position of branching is an additional factor for the determination of the thermal behavior. HBC derivatives substituted by side chains dove-tailed at the β-position show a lower isotropization temperature than HBCs with branched chains containing ether linkages.

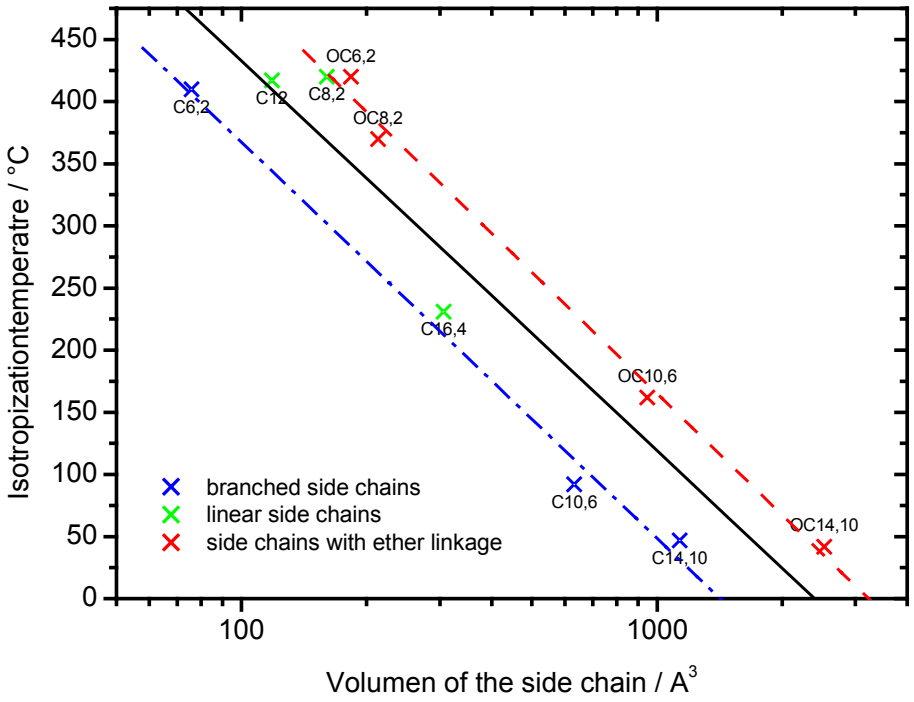

Figure 5.1. *Relation between the isotropization temperature of HBC derivatives and the volume of side chains with different architecture.*

As discussed earlier, the aggregation study in solution revealed that the introduction of the space-filling dove-tailed side chains decreases the aggregation extremely, whereby HBC derivatives substituted by linear side chains possess a solubility more than three orders of magnitude lower. The investigation of the bulk properties of these materials provided additional information about the effect of the dove-tailed side chains on the molecular interaction and self-assembly.

The simple extension of the solubilizing linear alkyl side chains did not influence the thermal properties to a high degree. This is analogous to the thermal behavior of phthalocyanines for which the extension of a linear alkyl side chain by 5 carbon atoms did not influence T_i.[323] However, introduction of oxygen into the chains had a greater influence on the thermal behavior due to the high rotational freedom,[324] whereby T_i could be lowered even down 64 °C for cobalt(II) phthalocyanines substituted by octadecyloxy chains.[325-327] The introduction of methylene groups increased the steric peripheral requirements and lowered again the clearing temperature of the discotic material.[227] Thereby, the position of the methylene also influences the thermal properties.[328,329] An alternative synthetic concept is the introduction of long branched, space-filling side chains with a higher rotational freedom thus affecting significantly the π-stacking of the aromatic cores (Figure 5.2) as it has been shown for phthalocyanines.[228]

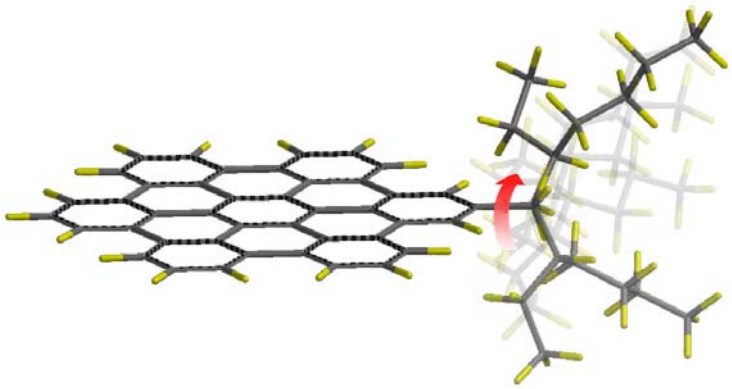

Figure 5.2. *Schematic illustration of the rotational freedom and the space-filling of a dove-tailed $C_{6,2}$ alkyl chain at different configurations in relation to the aromatic core. Due to simplicity only one side chain attached to the core is presented.*

In general, the interaction of the HBC cores was significantly decreased by the enormous steric requirements of these side chains. Furthermore, the branching site on the side chains plays an important role for the control of the isotropization temperature as well. The HBCs substituted by the β-dove-tailed chains revealed the highest steric impact during the self-assembly. The mobility of the large peripheral side chains increased with temperature, which led to repulsion of the aromatic discs due to the steric reasons and a suppression of the mesophase for HBC-$C_{14,10}$. The material melted directly from the plastic crystalline phase. Therefore, the variation the side chain length is an efficient tool to control the thermal properties. These results were in accordance with the aggregation data in solution and the

structural evaluation. The X-ray scattering results verify the effect of the bulky dove-tailed side chains onto the disc stacking. The comparison of the hexagonal packing parameter in the mesophase of the HBCs with ether linkages to HBCs substituted by linear side chains, but containing the same number of atoms, revealed that the packing parameter was significantly larger for the latter derivatives. This result was in agreement with the determined lattice parameters, since the dove-tailed side chains occupied a higher volume at the core vicinity. However, these increased steric requirements are compensated by the intracolumnar packing and a hindrance of the core interaction leading to a weak intracolumnar correlation, a disordered columnar phase (Chapter 3).

On the other hand, the observed intracolumnar disorder in the liquid crystalline phase of the homeotropically aligned HBCs highlights another crucial problem, since the major charge carrier transport takes place along the columns and encloses considerable disadvantages for applications in electronic devices. On the other hand, these bulky substituents are necessary to decrease the aggregation of the molecules and therefore to lower the processing temperature what is essential for processing. A compromise must be found between these two important properties: lowering the isotropization temperature and maintaining high columnar order at room temperature. One possibility is to displace the branching point even more from the core. This problem is a new challenge for the design of single building blocks which include both facile processing from the isotropic state resulting in the desired alignment of the material and strong self-association leading to a high supramolecular order.

5.2. Morphology Formation (edge-on arrangement) during Crystallization from the Isotropic Phase of Alkyled HBCs

The crystallization behavior from the isotropic state was investigated by means of thermally controlled POM experiments, to get a deeper insight about the supramolecular organization. For this purpose HBC-$C_{8,2}$ and HBC-$C_{6,2}$ were sandwiched between two glass slides and heated to the isotropic phase under nitrogen atmosphere. Both materials were then cooled down at a rate of 1 °C/min, exhibiting a characteristic, highly birefringent texture which appeared at a temperature from 380 °C, typical for a discotic columnar phase forming pseudo focal conic fan-shapes (Figure 5.3). This arrangement remained stable down to the crystalline state. In addition, the size of the domains was strongly dependent on the cooling rate. The size of the observed liquid crystalline domains was strongly dependent on the

cooling rate.

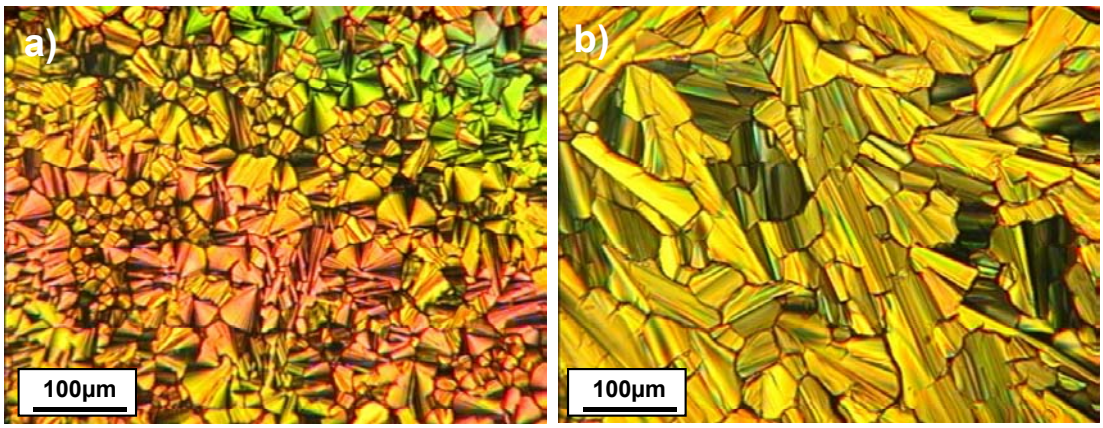

Figure 5.3. *POM images of a) HBC-$C_{8,2}$ and b) HBC-$C_{6,2}$ both cooled at 1 °C/min from the isotropic state between two glass slides.*

In contrast, HBC-$C_{10,6}$ revealed completely different textures obtained from the melt. In this case, the crystallization from the isotropization temperature and as a consequence the resulting morphology depended strongly on the surface contact. While placing the samples between two glass slides and cooled, HBC-$C_{10,6}$ formed dendritic structures as shown in Figure 5.4a. The high contrast of the image was due to the optical difference between the strong birefringence of these textures and the isotropic melt. It was remarkable that the increase in size of the dendritic domains proceeded only to a certain state, when crystallized isothermally. By lowering the crystallization temperature further, it was possible to reinitiate the growth process. The texture diversified significantly, when the material was crystallized down to room temperature as presented in Figure 5.4b. Highly ordered large domains became apparent indicating a considerable difference in the supramolecular order during the crystallization process, when the dendritic shapes began to coincide. This resulted in mosaic textures with large ordered domains which remained stable down to room temperature. The size of these domains was temperature dependent and exceeded even 500 µm.

This change of the morphology was correlated with the appearance of the second exothermic peak in the DSC at 46 °C during cooling. This might be due to an increase in density of the sandwiched material. During the early crystallization the dendritic structures were ordered, but not long-range oriented, as indicated by the absence of extinction along the polarizer/analyzer axis. When the crystallization proceeded and these features began to impinge, the density between the two glass slides simultaneously increased forcing the molecules to adopt a more favorable organization what resulted in the formation of huge

oriented domains.

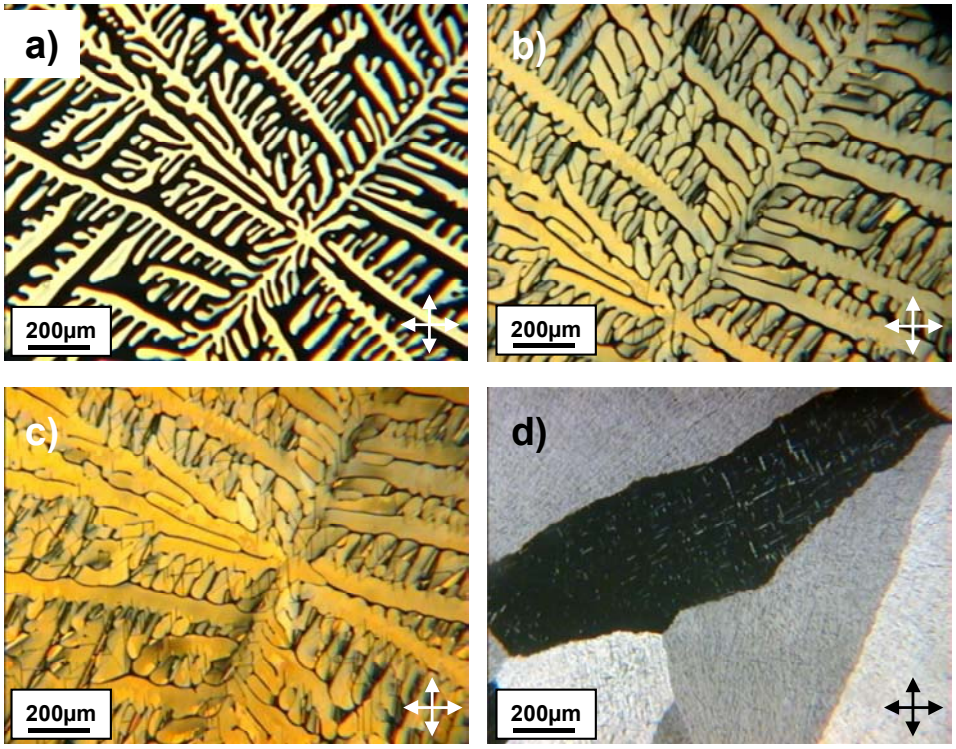

Figure 5.4. *POM image of HBC-$C_{10,6}$ between two glass slides cooled at 1 °C/min from the isotropic state at a) 95 °C, b) 88 °C, c) 70 °C and d) at room temperature.*

When crystallizing HBC-$C_{10,6}$ only on one surface, another type of texture was observed. Again, the cooling rate was again influencing the morphology. The POM images revealed small clusters at a cooling rate of 1 °C/min (Figure 5.5a). On the other hand, a finger-print texture appeared by lowering the rate to 0.05 °C/min which are presented in Figure 5.5b. Finally, at a rate to 0.01 °C/min, the material showed crystal-like features differing from the other cases (Figure 5.5c). Both the POM pictures and the topography are shown in Figures 5.5d and 5.5e, that the nucleus center was surrounded by planar rings, indicating a non-radially growth direction. The size of the crystals reaches 50-100 µm. The experiments on one surface did not show a transition in the morphology during crystallization, which confirmed the effect of density change between two glass slides. An identical phenomenon has been observed also for homeotropically aligned compounds having more significant consequences on the macroscopic ordering of the samples as it will discussed later. In the now presented cases, the HBC-$C_{10,6}$ discs adopted on one and between two surfaces an edge-on arrangement.

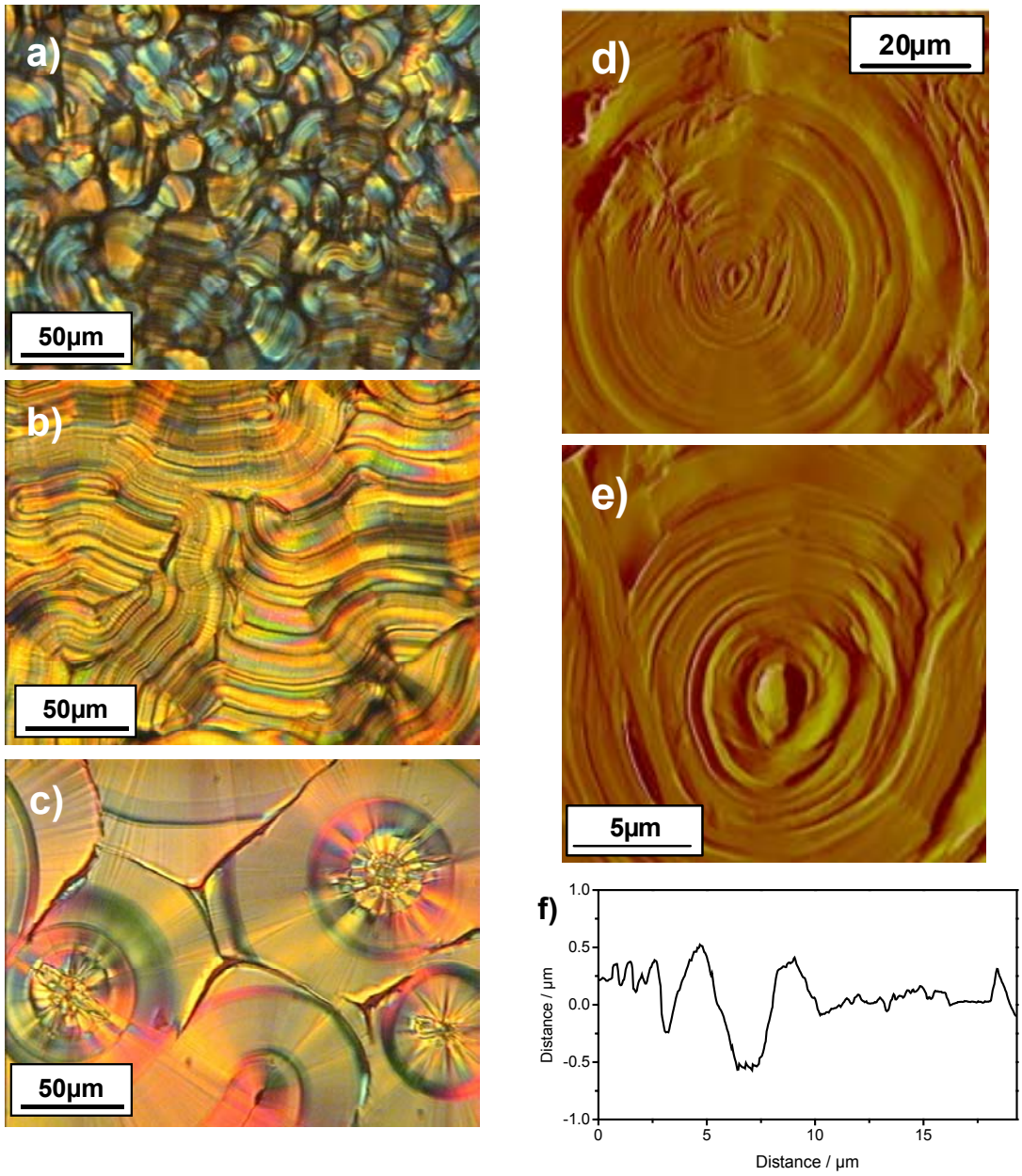

Figure 5.5. *POM images of HBC-$C_{10,6}$ on a glass surface cooled unisothermally at a rate of a) 1°C/min, b) 0.05°C and c) 0.01°C down to room temperature; d) shows the topography of a crystal and e) the nucleus by means of atomic force microscopy (AFM), f) height profile of the nucleus in e).*

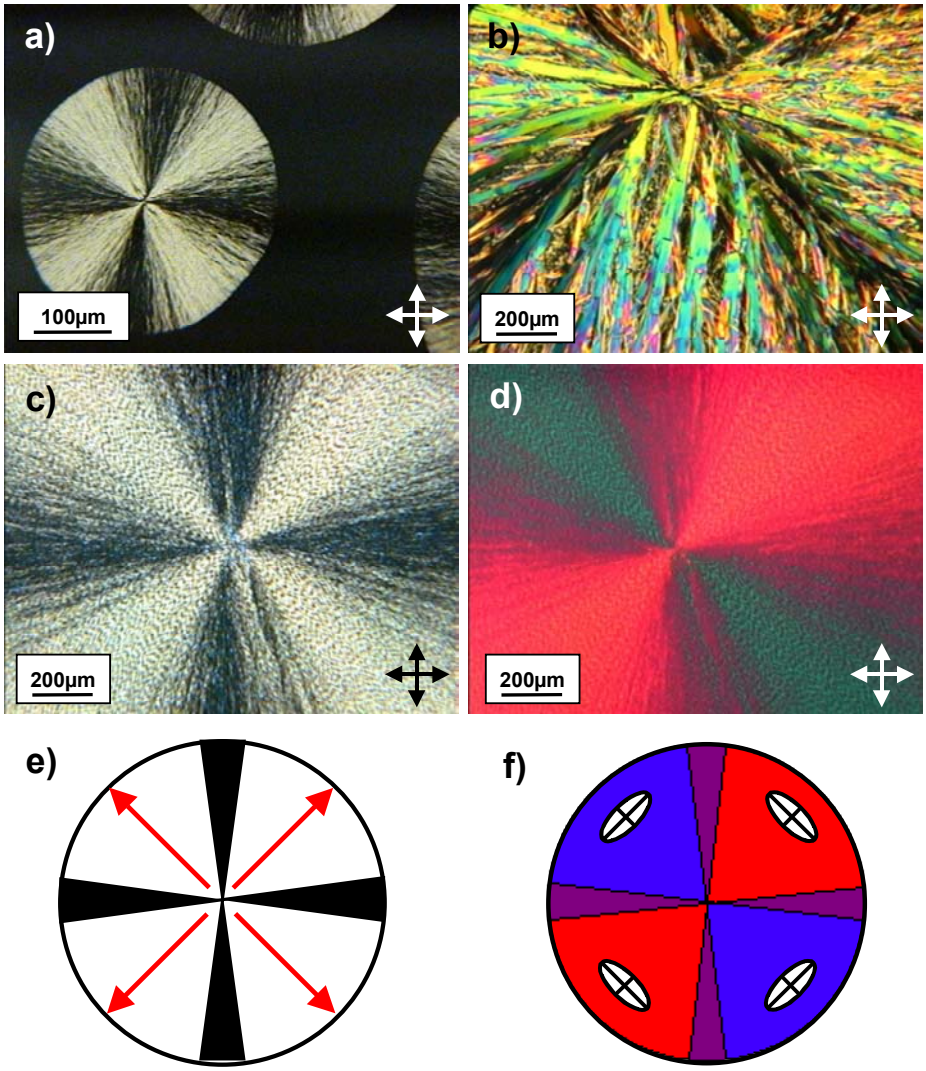

Figure 5.6. *Cross-polarized optical microscopy images of HBC-$C_{14,10}$ a) during isothermal crystallization at 35 °C, b); crystallized at 38 °C, c) crystallized at 45 °C, d) POM image from c) using a λ-plate, e) model for the radial columnar growth which results from the POM investigations, f) indication of the refractive index ellipsoid within the spherulite.*

An interesting texture was observed for the HBC derivative with the longest side chains, HBC-$C_{14,10}$. During cooling from the isotropic state, well-ordered spherulites nucleate appeared randomly distributed over the whole sample (see Figure 5.6a). This crystallization behavior was atypical for discotic systems especially for such with large aromatic cores. Spherulite formation of discotics has been published only for low molecular mass liquid crystals[330] or discotics[331] with substantially smaller cores. Bushby et al. reported spherulitic domain formation for polymeric discotic liquid crystals mixed with their monomeric

species.[332] The spherulites revealed high anisotropy and therefore coherent long-range order. This is expressed by the Maltese cross, where the isogyres followed the extinction of the analyzer/polarizer direction indicating a radial alignment of columns from the center as schematically demonstrated in Figure 5.6e. The columns were oriented in the spherulite growth direction with an edge-on arrangement of the molecules. This supramolecular order was also verified by the determination of the index of refraction. The index was smaller parallel to the radial direction than perpendicular to it as indicated by the yellow-blue distribution by using a λ-plate (Figure 5.6d and schematic representation of the index of reflection in Figure 5.6f).[333] The incident light propagated fast in the direction in the plane of the aromatic core, in which the transition dipole was oriented, than along the columnar axis. Therefore, this observation was in strong correlation with the arrangement of the molecules within the spherulitic domains where the light propagates faster radially. Finally, this phase of the material was characterized as optically negative as it can be seen in Figure 5.6d.

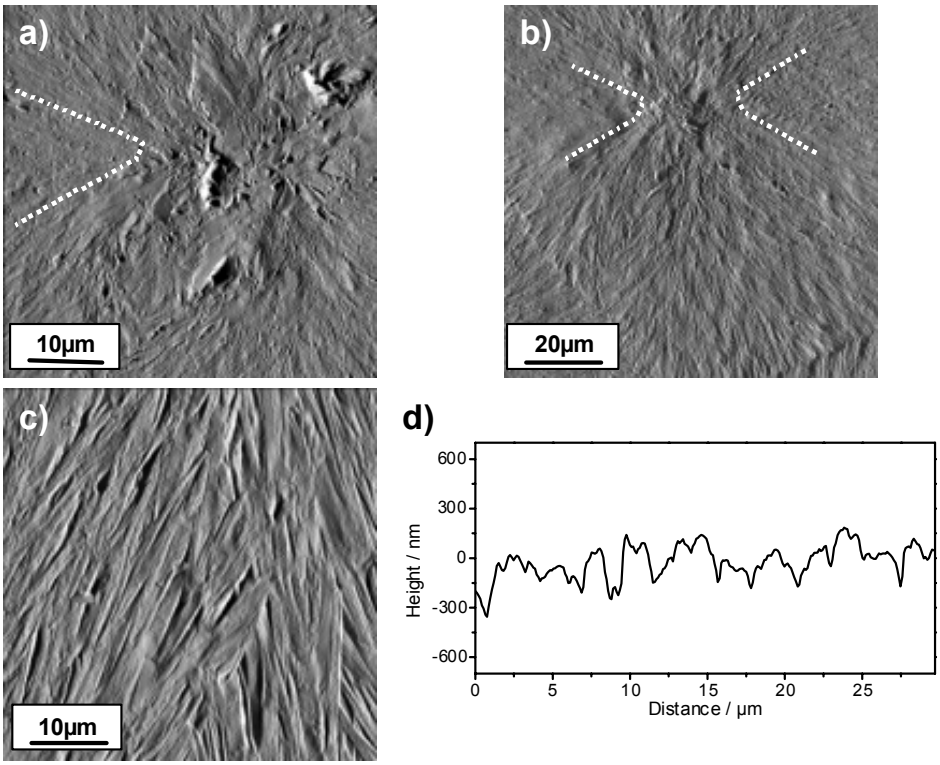

Figure 5.7. *AFM topology examples of a spherulite obtained during non-isothermal crystallization of 1°C/min showing a) the nucleus, b) the spherulite (the "eyeslets" are indicated by dashed lines) and c) impingement of two spherulites with lamellae textures and d) height cross-section of the image in c).*

AFM has been used for closer inspection of the spherulitic domains. The AFM images in Figure 5.7 showed the appearance of the so-called "eyes" at the about 10 µm huge nucleus. The origin of this phenomenon was the growing of edge-on lamellae along the perimeter from the spherulite center accompanied by an increase of strain energy leading to lamellae bending.[334] Afterwards, lamellae filled the space in the eyes in the more favorable lower energetic state in the flat-on order. The AFM image in Figure 5.7c illustrated the lamella crystal arrangement within the crystal aggregates at an impingement of two spherulites. A face-on orientation[335] was observed for many of the lamella in the image. However, it was clearly visible that most of the lamellae undergo a twisting. The twisting of crystals is a general feature of banded spherulites which were found for both synthetic[336-338] and biologic[339] polymers as well as inorganic systems[340-342] consisting of either chiral or non-chiral moieties. Although, there were significant differences in explaining the origin of the banding in polymer spherulites, it is well accepted that banding in polymer spherulites can be attributed to a twisting of crystallographic orientation about radii leading to alternative bright and dark rings under the POM which is shown in Figure 5.8a.[343] Indeed, most of the spherulitic crystals revealed a macroscopic periodicity along the radius. The periodic contrast, due to birefringent effects, appeared on single fibrous structures suggesting a helical twist of crystallites within the fibers (schematic model in Figure 5.8b and 5.8c). On the other hand, these periodic features were less pronounced than the banded textures observed for polymers.[344]

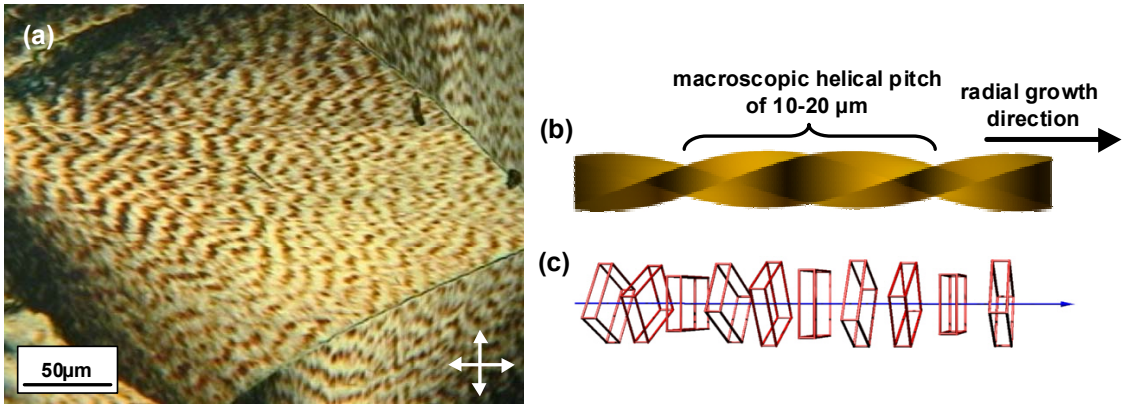

Figure 5.8. *a) An example of a cross-polarized optical microscopy image of HBC-$C_{14,10}$ illustrating the periodic features along the spherulite radius, b) schematic illustration of the helical fibrous structure and c) schematic presentation of the twist of the crystallites within the fibers.*

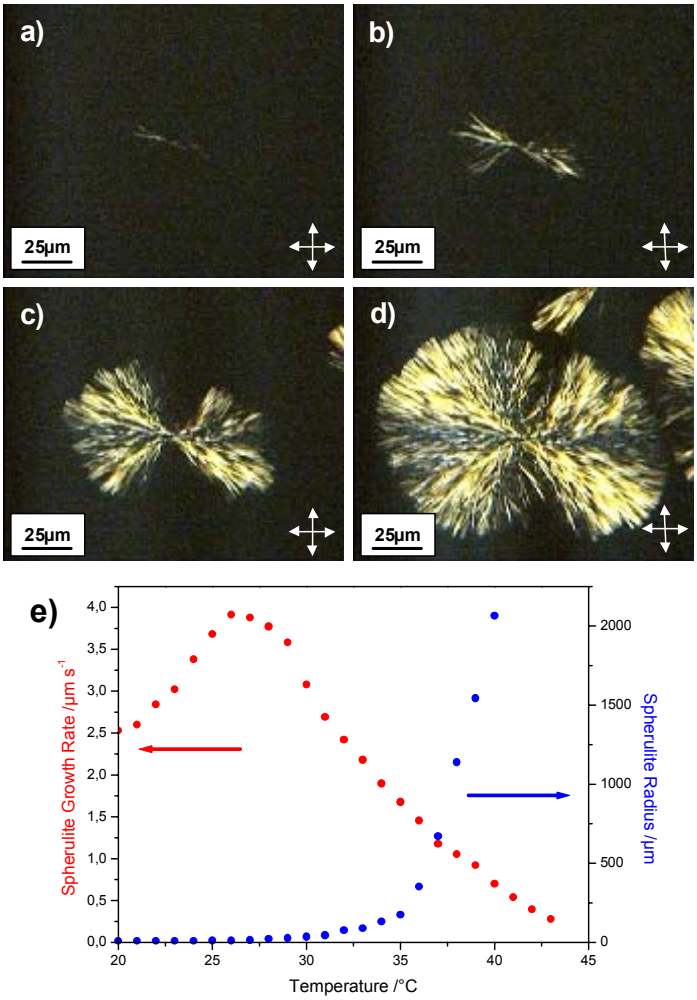

Figure 5.9. *POM images of the initial nucleation of HBC-C_{1410} crystallized isothermally at 30 °C acquired after a) 20 s; b) 24 s; c) 28 s and d) 32 s; e) spherulite growth kinetics based on isothermal crystallization, (blue) temperature depended spherulite radius and (red) temperature dependent spherulite growth rate.*

Additionally, it was possible to observe the initial nucleation process (Figure 5.9) in the POM between 30-35 °C, corresponding to the classical "sheaf of wheat" model.[345,346] In Figure 5.9a, the morphological development of a spherulite from the formation of a lamella skeleton is presented. Firstly, an embryo grew continuously into a single founding lamella which propagated in both directions. After the creation of this founding lamella, new subsidiary lamella appeared which under further growing continued to branch resulting finally in a lamella sheaf consisting of many lamellae. The onset of branching is also seen in Figure 5.9b. This lamella sheaf finally developed into a spherulite through additional branching yielding in the formation of the characteristic, above described eyelets in the interior of the

spherulites. The eyelet-type of structure (Figure 5.7b) resulted from a faster propagation of the lamellae in the forward direction than the overall growth rate at the initial nucleation, forming finally in a spherulite texture (Figure 5.9d). In general, this process usually occurred on a very small length scale and is thus only possible to monitor by temperature-controlled AFM.

The spherulite size and growth rate was determined during conventional isothermal crystallization measurements by means of the POM. The sample was cooled from the isotropic state by 50 °C/min to the desired crystallization temperature at which the spherulite radius was recorded as a function of time. The size of the spherulites varied with the crystallization temperature and was divided into two regimes: the first from 20 °C to 35 °C, where the size of the spherulites was not significantly dependent on the temperature, whereas above 35 °C the growth increased exponentially (see Figure 5.9e). While crystallizing isothermally at temperatures above 40 °C the spherulite size even exceeded 4 mm. At temperatures higher than 44 °C the spherulite texture changed, exposing a more colorful image. Both, the missing of the Maltese cross and the lower contrast of the textures reflected the absence of a long-range order.

The characteristic morphologies of the studied HBC derivatives can be explained also by the influence of the substituents. Although the three dove-tailed compounds revealed significant differences in the morphology which was obtained from the isotropic state, the discotic molecules were always oriented “edge-on” on the glass substrate, due to the long and flexible hydrophobic alkyl chains that force the molecules to minimize the contact with the polar substrates. A further aspect of the edge-on arrangement of the discs might be the high steric hindrance of the dove-tailed side chains which did not allow a face-on orientation of the molecules on the surface. HBC-$C_{6,2}$ bearing the shortest side chains formed ordered, but small domains from the isotropic state, whereas the HBC-$C_{10,6}$ possessing longer substituents revealed essentially larger ordered crystals. By the substitution of six $C_{14,10}$ chains to the HBC corona, huge domains have been observed, which were long-range oriented over several millimeters. Due to the sterically decreased π-stacking for HBC-$C_{14,10}$, the self-organization into superstructures was modulated and therefore resulted in low nucleation rates and a formation of large spherulites. In conclusion, the enhancement of the supramolecular order into large oriented domains depended on the ability to self-assemble on the time-scale leading to a strong kinetic influence. This is analogous to the importance of the kinetics during the morphology formation in drop-cast film of HBC-$C_{6,2}$. During the processing from the isotropic phase in which the molecules are present as small aggregates, the self-assembly of HBC-$C_{14,10}$ into the columnar structures leading to large domains occurred much slower than

for HBC-$C_{6,2}$ which in contrast showed small domains. This is the first time that long-range self-organization is determined by the kinetic growth of the material.

5.2.1. Processing from the Isotropic Phase

5.2.1.1. Zone-crystallization

The extraordinary self-assembly properties of compound HBC-$C_{14,10}$, consisting in nucleation and directed growth of structures and its ability to create spherulitic textures suggested the application of the zone-crystallization technique to obtain macroscopically controlled order for possible application in electronic devices. It was shown that the processing of materials from their isotropic state by using a temperature gradient is an appropriate method to control the order of supramolecular structures over large areas. Since the processing conditions depend mainly on the crystallization kinetics of the material, the optimal parameters were based on the study of the crystallization kinetics presented in Figure 5.9e. The procedure was performed at optimized processing conditions of T_1=60 °C, T_2=30 °C and a velocity of 1 μm/s. These conditions corresponded to the growth kinetics in the temperature range of 40-45 °C.

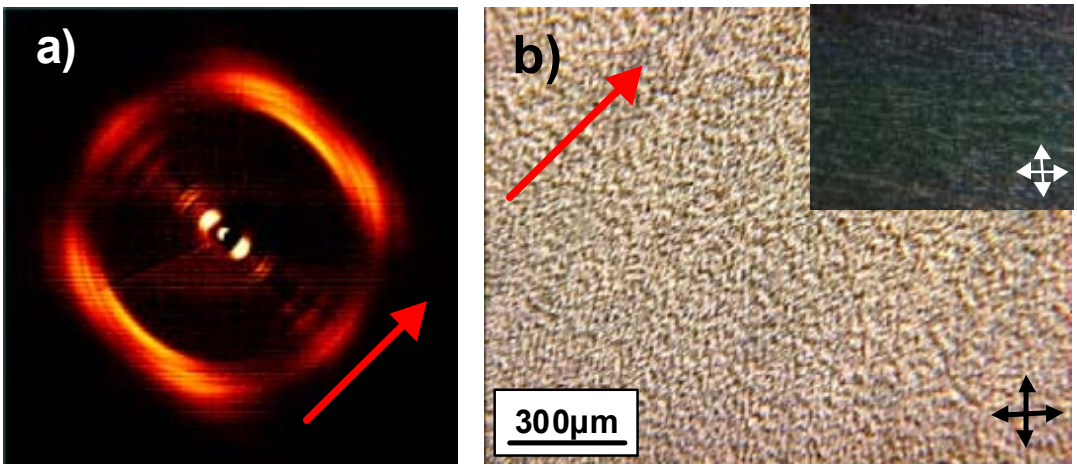

Figure 5.10. *a) 2D-WAXS of the zone-crystallized HBC-$C_{14,10}$ sample, b) POM image with an orientation of the sample alignment 45° in respect to the polarizer/analyzer axes (inset: same image at 0° to the polarizer/analyzer axes); the arrow in b) and c) indicates the moving direction of the sample along he temperature gradient.*

Indeed, after zone-crystallization processing the aligned HBC-$C_{14,10}$ sample revealed

high homogeneous structural order with columns oriented uniaxially along the temperature gradient, as could be seen in Figure 5.10a presenting the 2D-WAXS pattern. The intra- and intercolumnar arrangement within the thermally processed sample was identical as determined for the extruded filament. The discotic molecules were "edge-on" arranged with respect to the substrate. The observed high optical anisotropy of the POM images in Figure 5.10b confirmed the long-range order over large areas. The maximum birefringence appeared at an angle of 45° to the polarizer/analyzer axis suggesting that the columnar growth during crystallization took place along the temperature gradient.

The additional application of the λ-plate verified the lower index of refraction along the columnar axis, whereas the refractive index along the disc axis was larger (see Figure 5.11). Since the dipole moment was placed in the plane of the aromatic core, the light propagated faster along the core axis than along the column. Therefore, the appearance of the homogenous bleu and yellow color of the layer depended on the position with respect to the polarizer/analyzer axis indicating that the oriented film was optically negative. Moreover, the macroscopic periodicity observed in the spherical textures was also distinct in the uniaxially oriented layer. These periodicities were aligned in the direction of the temperature gradient and thus in columnar axis. Furthermore, by using the λ-plate the blue and yellow color distribution emerged homogeneously along the period. It was concluded that the optical property of the film did not depend only on the direction of the molecular dipole moment, but also on the difference of the refractive index within the crystallites. In this case these crystallites performed a macroscopic helical twist in the spherulites and in the aligned film. The obviously different index of reflection along these periods was the consequence of the twist.

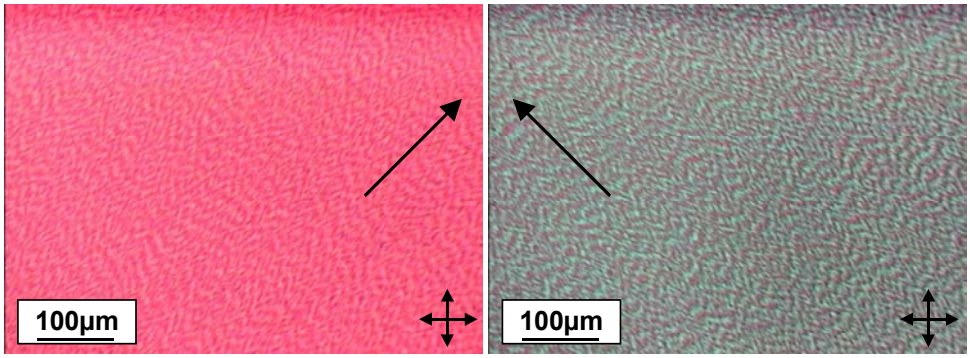

Figure 5.11. *POM images of zone-crystallized HBC-$C_{14,10}$ with the application of a λ-plate (arrow indicates the moving direction of the sample along the temperature gradient).*

The topography of the aligned layers was investigated by means of AFM which displayed a lamella morphology as shown in Figure 5.14. These structures were over several hundreds of micrometer long, 2–3 µm wide and aligned in the moving direction of the sample during the processing; the strands were threaded and entangled into each other. From the AFM image in Figure 5.14b it was obvious that most of the lamellae are face-on arranged and that a twisting of these lamellae occurs which was already displayed in the POM images.

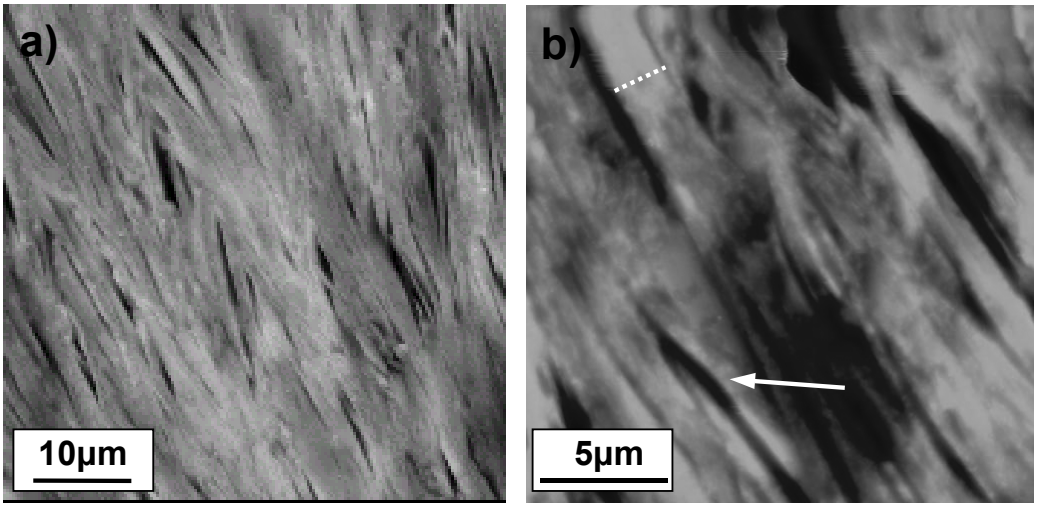

Figure 5.12. *AFM topography images of zone-crystallized HBC-$C_{14,10}$ films. Images were taken in tapping mode. The arrow in b) indicates the lamella twisting and the dashed line the lamella width of ca 2.5 µm.*

Due to the pronounced directional growth from the melt, HBC-$C_{14,10}$ was successfully oriented by using the zone-crystallization, whereby the discs were arranged edge-on in columns which were aligned in the moving direction of the sample along the temperature gradient. The optimal processing conditions depend strongly on the crystallization kinetics of the material being analogous to polymers. [347-349] This is an impressive example for the successful transfer of the natural nucleation and growth of the material onto the processing by the application of the optimum operating parameters. Bard et al. showed that steady-state short-circuit photocurrents of porphyrins were improved by several orders of magnitude by the orientation of the compound from the isotropic phase by using a similar alignment technique yielded. However, no organic devices such as FETs were until now fabricated based on such aligned layers by zone-crystallization. It is expected that an improved device performance will be achieved, since the PR-TRMC mobility was 0.47 cm²/Vs accompanied by extreme long life-times of charges.[218] Since both HBC-$C_{10,6}$ and HBC-$C_{6,2}$ did not possess such directed growth, these materials could not be oriented by this technique.

5.2.1.2. Effect of the Curvature on the Self-organization from the Isotropic Phase

The pronounced directional growth and low nucleation propensity of HBC-$C_{14,10}$ was also exploited not only in the aligning technique along a temperature gradient, but was beneficial for any other processing from the isotropic phase. It has been found that the curvature on the macro- and nanoscale can affect the growth into supramolecular structures of HBC-$C_{14,10}$. Such behavior has not been reported for many material processed from the isotropic phase.

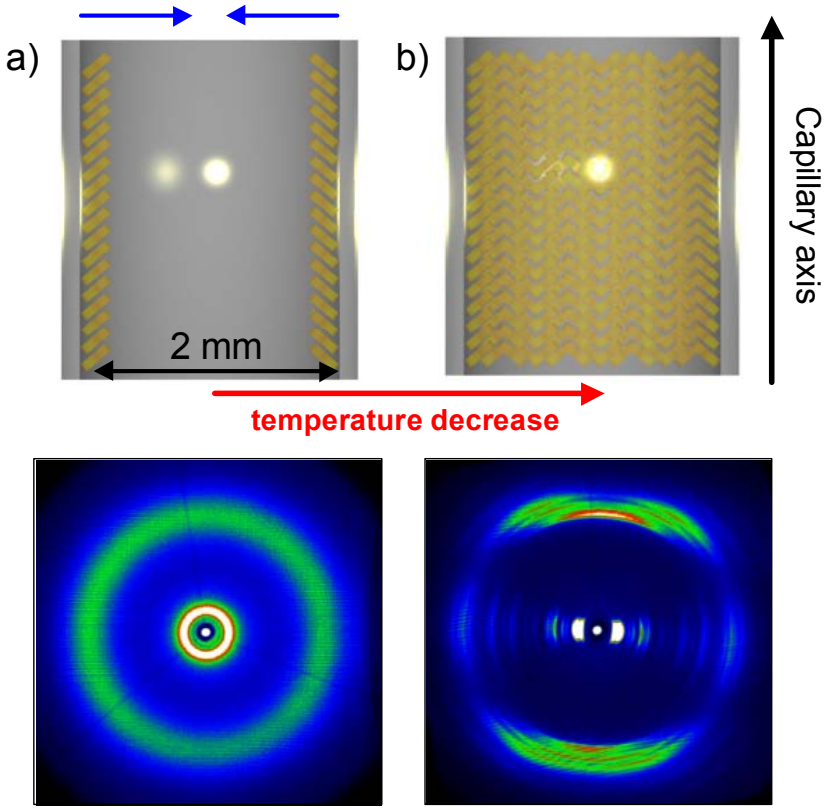

Figure 5.13. *Self-assembly of HBC-$C_{14,10}$ from the isotropic state within a macroscopic capillary, a) 2D-WAXS pattern of the isotropic phase (blue arrows indicate the crystallization direction) and b) after controlled cooling down to room temperature.*

In order to investigate the self-organization behavior in the bulk, the crystallization of the material from the isotropic phase was monitored by using 2D-WAXS experiments (Figure 5.13). Therefore, the compound was placed within a macroscopic capillary with a diameter of 2 mm and heated to the isotropic phase. As expected, the 2D-WAXS pattern in Figure 5.13a revealed a disordered phase. Afterwards the capillary was cooled down at a rate of 0.1

°C/min. After cooling the sample down to room temperature a characteristic 2D-WAXS pattern for HBC-$C_{14,10}$ was observed. The supramolecular organization was identical to that determined for the extruded HBC-$C_{14,10}$ filaments, whereas the degree of order was even higher for the capillary aligned sample. The X-ray pattern indicated a uniaxial orientation of the columnar structures along the capillary axis. Moreover, it was remarkable that the order was uniform over the whole capillary.

The mechanism of this extraordinary self-organization over long-ranges was based on the curvature effect: analogous to the homeotropic alignment the arrangement of the first monolayer at the surface was important for the overall organization. During slow cooling the first molecules initially wet the capillary wall during the slow crystallization in an edge-on respect to the capillary wall as illustrated schematically in Figure 5.13a. It seemed thermodynamically feasible for the molecules to orient along the cylindrical axis by forming highly ordered columns. As the crystallization proceeded finally into the interior of the capillary, the organization of the first layer initiated the order of the following layers. Unfortunately, it was not possible to monitor this self-organization by in-suite 2D-WAXS experiments due to a too low beam intensity leading to a too long exposition time for one pattern.

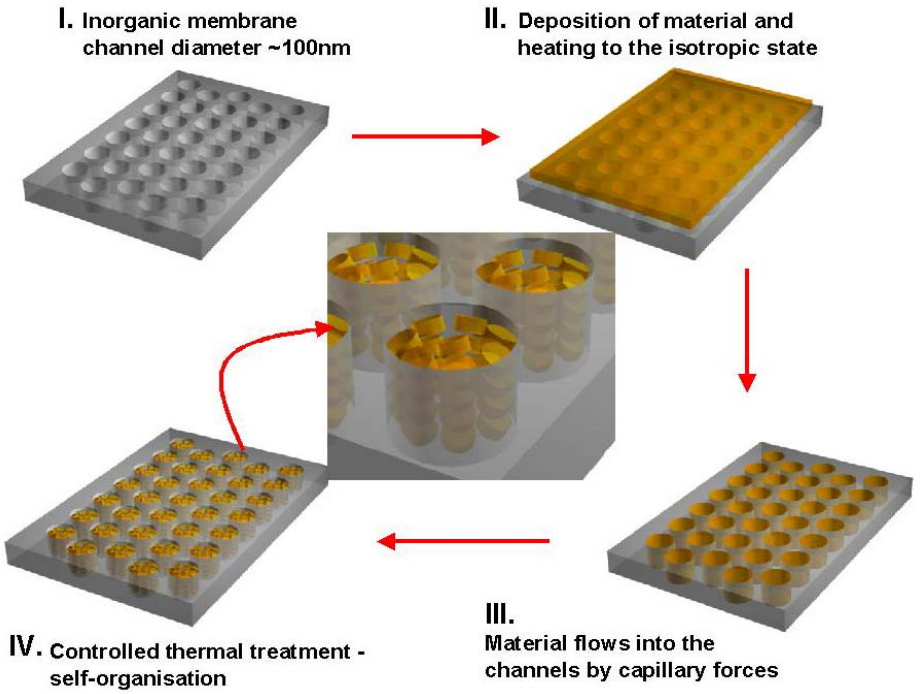

Figure 5.14. *Schematic illustration of the template processing of HBC-$C_{14,10}$ by thermal treatment.*

In order to evaluate the influence of the curvature effect on the nanoscale, this extraordinary self-organization of HBC-$C_{14,10}$ in inorganic membranes of corresponding pores sizes was monitored. The general preparation of the membrane is presented in the process flow in Figure 5.14.

As the template a commercial available inorganic aluminum oxide membrane was used. The membrane thickness was 60 µm and the pore size was ca. 100 – 200 nm. The material was placed at the pores, heated to the isotropic phase and filled into the pores by capillary forces. Afterwards the membrane was thermally treated in a vacuum oven by cooling from 60 °C down to room temperature at 0.1 °C/min. Scanning electron microscopy (SEM) images in Figure 5.15 show the membrane pores before and after the filling. It is obvious from these images that the pores were completely filled over the whole length with the compound.

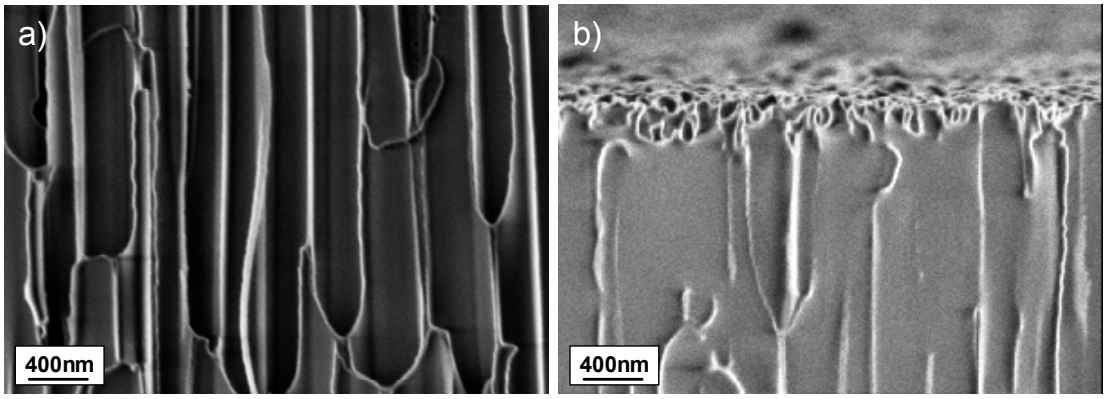

Figure 5.15. *SEM images of the aluminum oxide membrane pores a) before and b) after filling with HBC-$C_{14,10}$.*

X-ray diffraction was also in this case a powerful tool in order to assign the supramolecular order within the pores after the thermal processing. Figure 5.16a shows a large-area X-ray diffraction in reflection mode. In the diffractogram only one single distinct reflection appeared corresponding to a repetition distance of 0.49 nm. This distance was related to the intracolumnar period of tilted discotic molecules. This was in agreement with the expected supramolecular arrangement of the molecules within the pores. The schematic illustrates in Figure 5.16b confirmed that the scattering vector, which resulted from the experimental set-up, was oriented along the columnar axes. Therefore, the intracolumnar distance was the only periodicity which gave rise to the appearance of a reflection maxima.

The 2D-WAXS experiments, shown in Figure 5.17, of the crystallized HBC-$C_{14,10}$ verified the orientation of the columns along the pores. One could observe only reflections

related to the columnar arrangement, whereby reflection peaks corresponding to the intracolumnar organization were not displayed. In this experimental set-up the scattering vector was oriented perpendicular to the columnar axes. In fact, the exposed reflections were anisotropic, since the unit cell was not in correlation in the different pores.

The structural investigation indicated that the supramolecular alignment of the columnar structures could be regarded as kind of a homeotropic orientation, since the columnar axes were vertical in the pores. In general, the crystallization of polymers in membranes pores has been investigated,[350-352] but the influence of curvature is rare. The crystallites of poly(vinylidene difluoride) were reported to grow preferentially in the direction of minimal curvature.[353] In the case of the HBC derivative, one can consider charge carrier mobility investigations similar to those of homeotropically aligned samples.[354] Additionally, it might be possible to apply the self-assembled HBC-$C_{14,10}$ within the membrane pores as active material for field-emission sources used in flat-panel displays.[355-357]

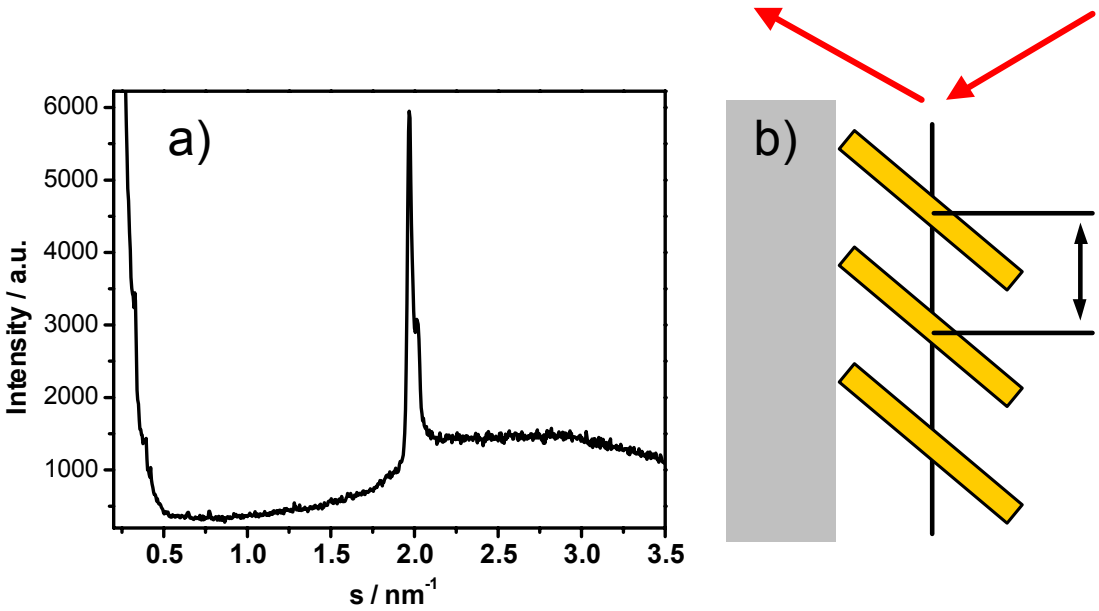

Figure 5.16. *a) Large-area X-ray diffraction in reflection mode of the template processed HBC-$C_{14,10}$ (blue: for comparison the diffraction of a plain membrane), b) schematic illustration of the molecular organization in the membrane pores and the orientation of the resulting scattering vector treatment.*

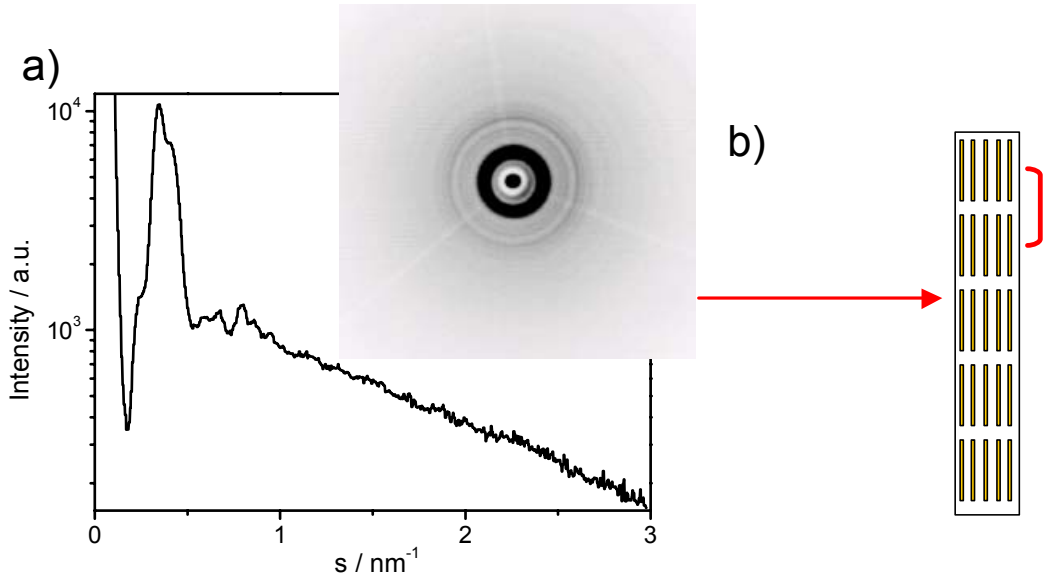

Figure 5.17. *a) 2D-WAXS pattern and the scattering intensity distribution as a function of the scattering vector, b) the experimental set-up with the X-ray beam in transmission resulting in the scattering vector perpendicular to the columnar axes.*

5.3. Control of the Thermal Behavior by Asymmetrical Substitution and the Zone-crystallization of "unwrapped" HBC

The HBC discotic molecules six-fold substituted by alkyl substituents such as HBC-C_{12} self-assemble into columnar structures. Due to the nanoseparation between the crystalline aromatic core and the disordered peripheral side-chains which acts as insulators, one can regard these superstructures as kind of "nanowires" providing an one-dimensional charge transport along the stacking direction as illustrated in Figure 5.18a. However, one-dimensionality as shown in the previous chapter is very sensitive to defects which can trap the charges and decrease the devices performance.

Therefore, one concept developed by Zhaohui Wang and Mark D. Watson suggested to extent the one-dimensional transport into three-dimensionality in order to decrease the disadvantageous effect of single defects within the columnar structures.[202] The key idea is the maintenance of the main charge transport along the columnar axes, but the introduction of intracolumnar bypasses at possible defects and domain boundaries allows also the intercolumnar hopping of charges and ensures an uninterrupted charge transport providing adequate device performance. Therefore, a new HBC derivative was designed with partially side chains stripped away. The residual flexible chains sufficient ensure solution

processibility and phase-forming properties[358,359] leading to the "unwrapped" HBC derivative presented in Figure 5.18b. Other examples for "unwrapped" HBCs are the C46-$(C_{12})_2$ and HBC-$(C_{12})_4$ (Chapter 3) which revealed a significantly higher isotropization temperature limiting the processibility. Since it is assumed that the long-range order is important for every material exploited in the device and the "by-pass" concept improves "only" the charge carrier migration between the electrodes, the thermal behavior and morphology formation of just the trialkoxy substituted HBC will be discussed. Preliminary FET results revealed that the mobility of HBC-$(C_{12})_4$ is by far lower than for HBC-C_{12} in spin-cast films prepared under identical conditions. These results indicated the strong importance of the supramolecular organization, which is not pronounced for HBC-$(C_{12})_4$ due to the asymmetrical substitution, on the device performance.[318]

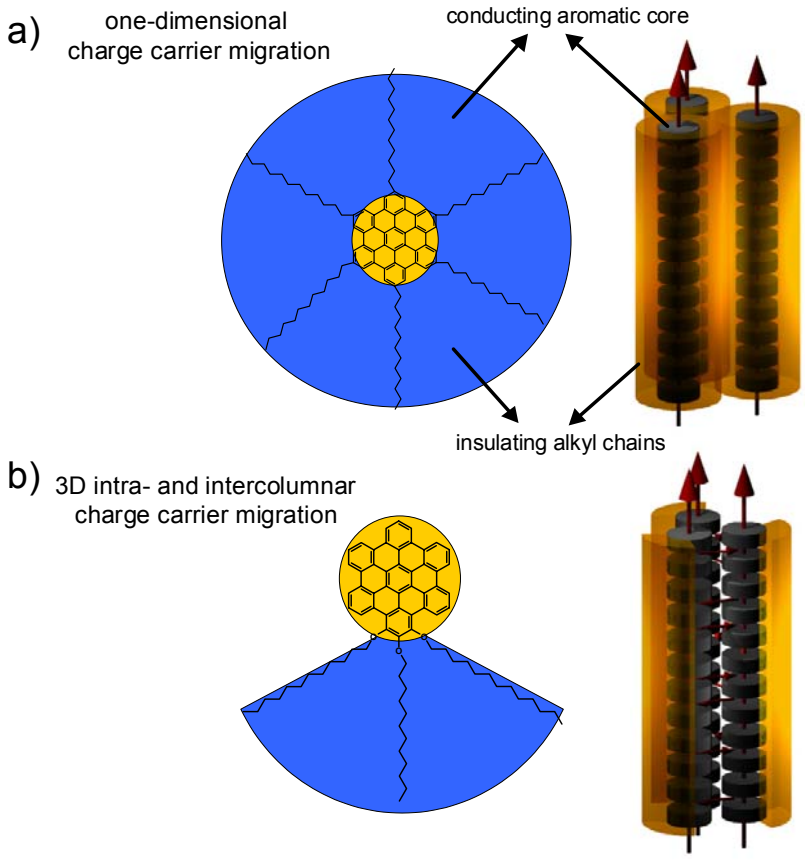

Figure 5.18. *a) Six-fold alkyl substituted HBC disc providing an one-dimensional charge migration along the columnar structures, b) new concept with the unwrapped HBC derivative allowing also intercolumnar charge hopping leading to a 3D charge transport.*

Asymmetry can be obtained by the substitution of the disc by side chains of different

length which lowers the phase transition to the isotropic phase. This has been reported for triphenylenes, phthalocyanines, HBCs and other discotics. The "unwrapping" of the HBC disc is the first time reported by Wang et al.[202] The "unwrapped" HBC derivative revealed in the DSC heating scan an endothermic phase transition at 50 °C, which was not accompanied by any structural changes, from one ordered columnar phase and to another. Furthermore, a significant decrease of the isotropization temperature to 195 °C in comparison to the alkyl substituted HBCs was observed. This drastic lowering of the isotropic phase was attributed to the reduced symmetry and the expected slight nonplanarity of the HBC mesogenic core. Such low T_i opened the possibility of processing the material by thermal means for the further exploitation in devices.

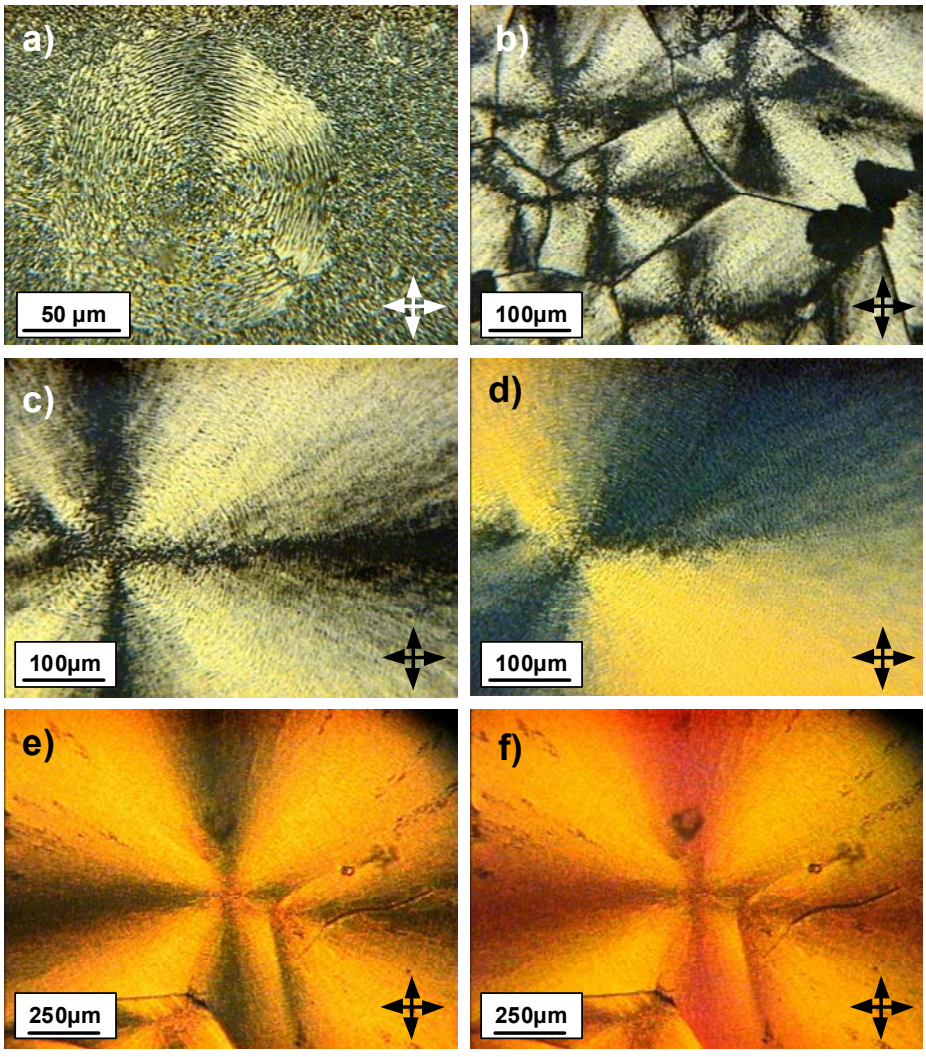

Figure 5.19. *Optical textures observed by POM for "unwrapped" HBC obtained after cooling from the isotropic state at rates of a) 20 °C/min, b) 10 °C/min, c) and d) 5 °C/min, e) and f) 1 °C/min; d) and f) are taken by using an λ-plate.*

The processing from the isotropic state depends strongly on the crystallization behavior of the material and its nucleation and growth ability. Therefore, before the alignment procedure, the morphology was investigated, obtained by cooling the sample, which was sandwiched between two glass slides, from the isotropic phase. The crystallization behavior was monitored by using thermally controlled POM and was carried out for different cooling rates.

At high cooling rates of 20 °C/min the material crystallized from the isotropic state so rapidly that only very small crystallites were formed. At some places also some larger ordered domains appeared surrounded by the fast-nucleated material (Figure 5.19a). At lower rates of 10 °C/min an optical texture untypical for discotic liquid crystals was observed displaying spherulitically ordered in 100-200 μm large domains. By further decreasing the cooling rate to 5 °C/min these spherulites nucleated randomly over the whole sample exceeding a diameter of 0.5 mm (Figure 5.19c). The spherulites revealed high anisotropy and therefore coherent long-range order. This was expressed by the Maltese cross, where the isogyres followed the extinction of the analyzer/polarizer direction indicating a radial alignment of columns from the center. Consequently, the columns were oriented in the spherulite growth direction with an edge-on arrangement of the molecules. Furthermore, at this cooling rate a weak ringed pattern appeared around the nucleation center. This poor periodic extinction pattern (radial banding) is a common observation for some polymers implying a lamellar twisting along the radial direction during crystal growth. Extinction occurs when the direction of the rotative optic axes (molecular chains) are parallel to the polarized axes. Using a λ-plate and analyzing the yellow-blue distributions in the optical spherulite image, it was possible to determine that the spherulites were optically positive i.e. with refractive index parallel to the radial direction was smaller than perpendicular to it (Figure 5.19d). At a cooling rate of 1 °C/min the spherulite size could not be monitored anymore by using the POM due to their extraordinary diameter. Interestingly, the application of the λ-plate did not reveal the same color distribution as observed for the texture obtained by cooling 5 °C/min. This could indicate a change of the optical properties of the material due to different crystallization conditions (different cooling rates) leading to slightly different superstructures. This effect is known for various polymers such as poly(ethylene adipate).[360]

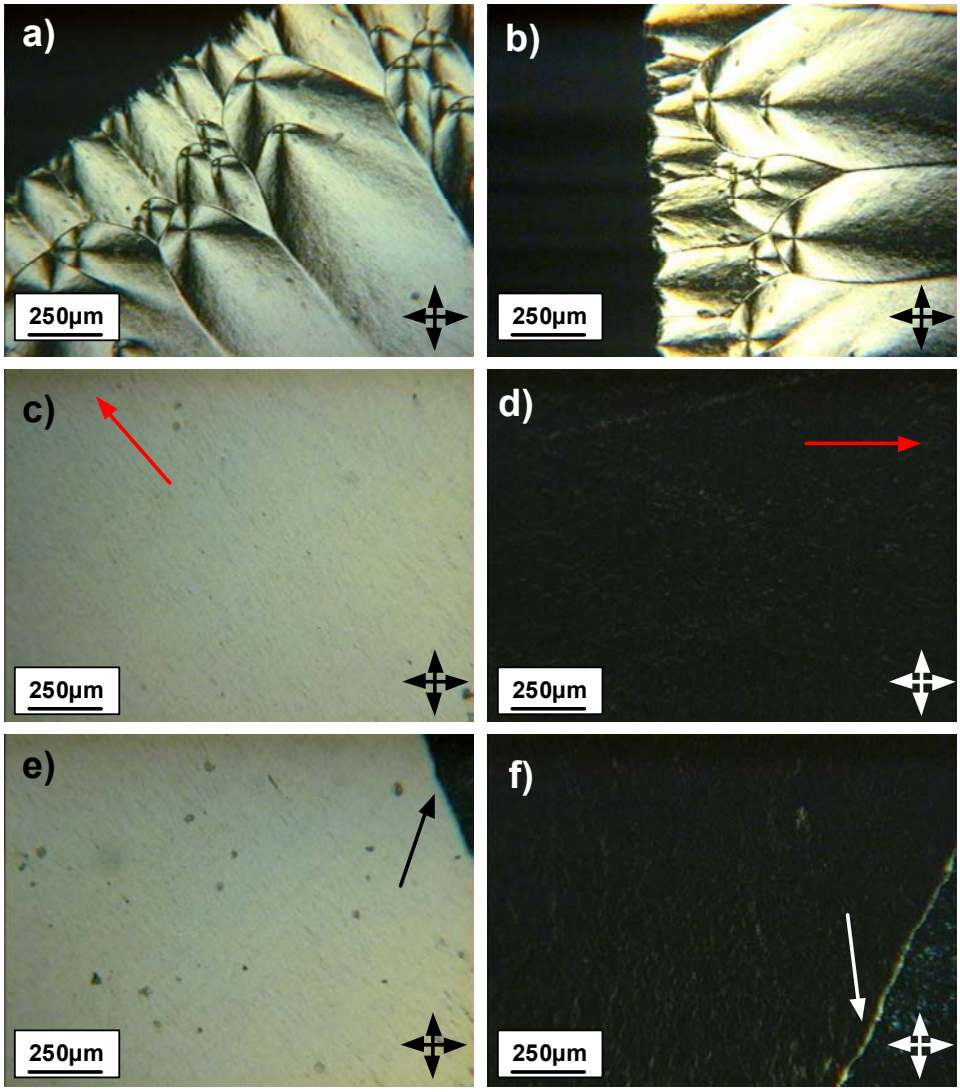

Figure 5.20. *POM of "unwrapped" HBC processed by zone-crystallization along a temperature gradient showing a) and b) the nucleation site at the film beginning, c) and d) interior the film (red arrow indicates the motion of the sample along the temperature gradient), e) and f) film edge indicating the same sample position. The image pairs were taken at two different positions (at 0° and 45°) of orientation axis of the layer with respect to the polarizer/analyzer axes.*

The formation of spherulites indicated a pronounced long-range self-organization of the molecules from the melt. Due to this strong nucleation and directional growth ability of the material it was possible to process this compound by zone-crystallization. The processing conditions depended on the crystallization kinetics of the material. The temperatures of 220 °C and 100 °C, a moving velocity of 5 µm/s and a gap between the heating blocks of 3 mm were found to be the optimal parameters for the processing of the "unwrapped" HBC. Indeed,

after one single pass along the temperature gradient, the sample revealed high optical anisotropy. The maximum birefringence appeared at the alignment direction 45° with respect to the polarizer/analyzer axes, whereas a complete extinction was observed when the alignment direction coincided with one of these axes (Figure 5.20c and 5.20d). It is important for the successful alignment by zone-crystallization that the material nucleates only at the beginning when entering into the temperature gradient. At further motion the processing parameters had to be optimized to balance between the further growth of the compound and the appearance of new nucleation sites before the growth front. The nucleation site of the sample which initiated the growth is shown in Figure 5.20a and 5.20b. The "unwrapped" HBC sample revealed a low nucleation propensity, but a pronounced growth at the above mentioned conditions resulting in large homogeneously oriented areas of more than 20 cm^2 being imposing. Moreover, the sample geometry can be varied individually and even much larger samples can be aligned as well fulfilling an important requirement of the production of large area devices.

The structural analysis was performed by using 2D-WAXS experiments of the aligned sample sandwiched between simple glass or aluminum foils (Figures 5.21a and 5.21b). In both cases strong equatorial reflections in the X-ray pattern indicated the high uniaxial orientation of the columns in the moving direction of the sample. The intercolumnar correlation distance was in agreement with the one determined for an extruded filament. The structure was extremely homogenous within the aligned film implying the pronounced long-range order with the columnar axes being in-plane to the substrate and the discotic molecules arranged edge-on with respect to the surface. Interestingly, the scattering intensities related to the intracolumnar order were unusually weak. For the sample oriented between the glass slides, the meridional reflection were even not observed. This is in contrast to the 2D-WAXS pattern attained for the extruded sample which showed the meridional reflection with a similar intensity as the equatorial reflection peaks (Figure 5.21c). The off-meridional reflections implied an intracolumnar tilted arrangement of the aromatic cores relatively to the columnar axis. The equatorial reflection distribution was fitted to a 2D rectangular unit cell with the packing parameters of a = 4.01 nm and b = 2.23 nm assigning the lateral organization of the columns.

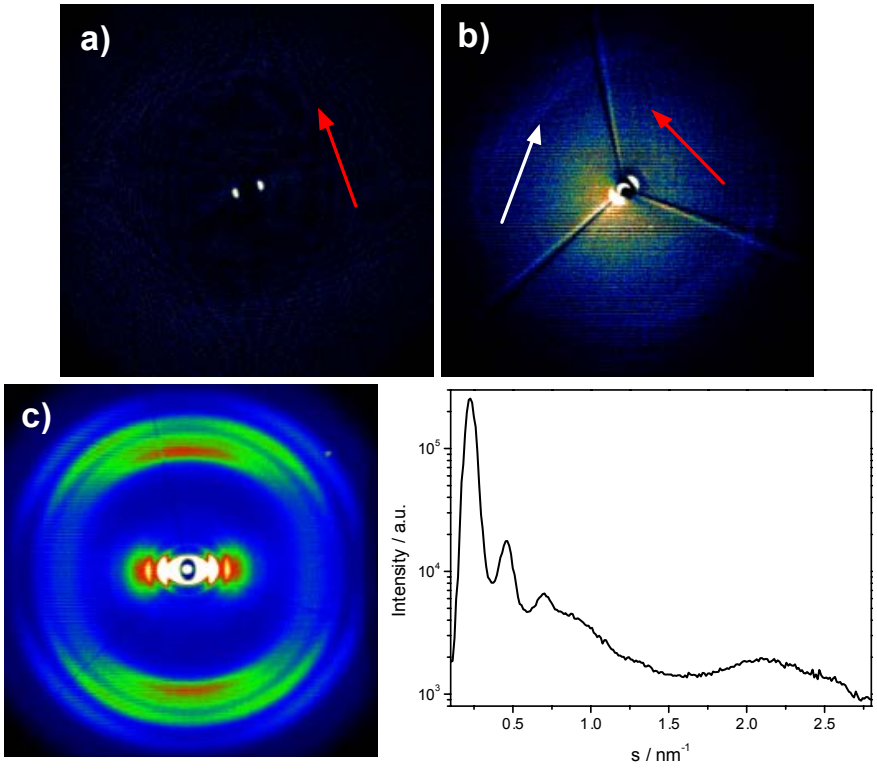

Figure 5.21. *2D-WAXS patterns of the "unwrapped" HBC aligned by zone-crystallization between a) two glass slides and b) two aluminum foils (red arrows shows the moving direction of the sample during the processing, whereas the white one indicates the weak reflections related with the π-stacking), c) oriented by filament extrusion and the equatorial scattering intensity distribution as a function of the scattering vector.*

The relatively large spacing of 4.01 nm has been explained by a lamellar arrangement of single rows of columns, whereby the space between the aromatic columns was filled the by nanophase-separated alkyloxy chains. The short side of the unit cell corresponded well to double the van-der-Waals cross-section of the HBC core, i.e. adjacent columns not separated by alkyl chains.

Unfortunately, the zone-crystallization processing did not allow the alignment of a surface layer on one single glass support, due to a strong dewetting tendency of the material in the isotropic phase changing from an initially homogeneous film to droplets on the surface. This effect could not be controlled by any known method. Therefore, for zone-crystallization the sample was sandwiched between two glass slides, whereby after the thermal treatment one of the slides was carefully removed in order not to damage the remained oriented film. This procedure allowed the investigation of the topography of the layer. In fact, the obtained

morphology was also dominated by the second glass surface, but nevertheless one can gain an insight about the type of morphology and any correlation to the alignment direction.

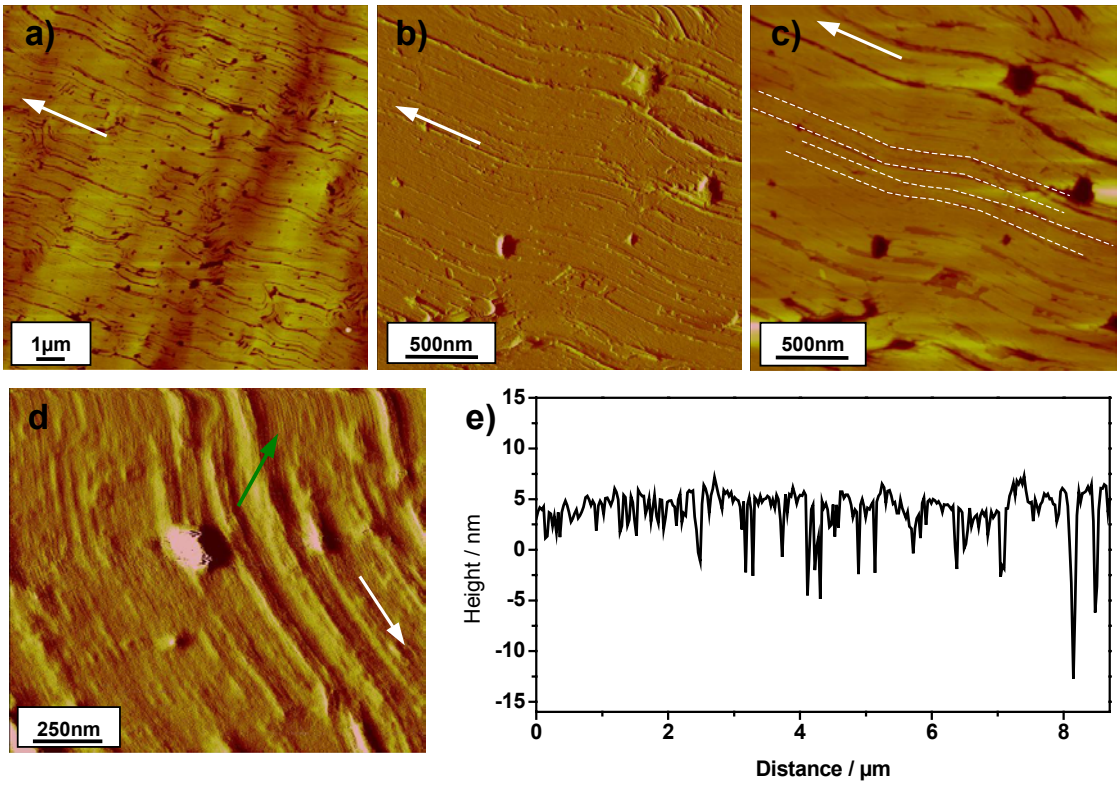

Figure 5.22. *AFM topography images taken in the tapping mode of zone-crystallized "unwrapped" HBC, a) large area scan (height image), intermediate scan with b) amplitude image and c) height image (gaps between the lamellae are indicated by dashed lines), d) small area scan (amplitude scan,nano-features are indicated by the green arrow)), (white arrows indicate the moving direction), e) cross-section of image a).*

The topography of the zone-crystallized film scanned by using AFM displayed a lamellae formation which were oriented in the moving direction (Figure 5.22). The topography of these lamellae was flat due to the contact with the second glass surface, but due to gaps between these structures, which were up to 10 nm deep (Figure 5.22e), one could distinguish these features. The morphology was very homogeneous over large areas as seen in the AFM image in Figure 5.22a with lamellae widths of approximately 100 nm and lengths exceeding the investigated area (Figure 5.22e). At a closer inspection of the topography of each lamella one could observe that these structures consisted of further features which were also aligned (Figure 5.22d indicated by the green arrow). These observations indicated a hierarchic organization with the nanoscaled columns as the basis which organized into these

100 nm wide features forming the lamellae which arranged at last in bundles of lamellae.

The lowered isotropization temperature and pronounced self-assembly of the trialkoxy substituted HBC from the isotropic state are closely related to a reduced molecular interaction due to the high asymmetry and the nonplanarity of the HBC core. The consequence was a moderate self-assembly of the molecules leading to the formation of large spherulitic domains which enabled the successful orientation of the compound by the zone-crystallization technique. In comparison, other asymmetrically substituted HBCs and other discotic molecules[244,245,361,362] did not reveal such an extraordinary self-organization. In fact, other disc molecules were symmetrically substituted, but with side chains of different length. This is the first example of the morphology for a truly asymmetrically substituted derivative. One can assume that the "degree" of asymmetry in this case for the trialkoxy substituted HBC derivative is high resulting in the significant diminishing of the π-stacking interactions. This effect is reflected also by the direct phase transition from the order phase into the isotropic state which has been only observed for HBCs bearing the longest branched side chains.

In conclusion, the uniaxial alignment of the "unwrapped" HBC derivative opens the opportunity for the design of new electronic devices such as FETs. It is therefore essential to prove the field-effect of these highly oriented surface layers which will be the next investigation step. Despite the "unwrapped" molecular architecture, the uniaxial orientation of the columns and long-range order are still important, since the major charge transport takes place along the columnar structures and the intercolumnar hopping of charges occurs only at single defects of main pathway. Therefore, anisotropy in the conductivity measured parallel and perpendicular to the columnar direction is still expected. Furthermore, it is suggested that the number of grain boundaries and single defects should be as low as possible by the alignment processing.

5.4. Control of the Homeotropic Alignment of HBCs

The control of the homeotropic alignment of discotic liquid crystals is an unsolved challenge. The exact mechanism leading to homeotropic order is not clear and therefore it is difficult to predict the successful alignment of molecules with specific architectures. Indeed, different discotic systems such as triphenylenes[363,364] and phthalocyanines[365] revealed spontaneous face-on arrangement inducing macroscopic homeotropic alignment with the columnar axis perpendicular to the substrate. This alignment occurred by cooling from the

isotropic state of compounds bearing heteroatoms which influenced strongly the supramolecular arrangement of the molecules. However, the homeotropic alignment from the isotropic state of discotic systems consisting on larger aromatic cores has not been extensively investigated, due to their prohibitively high isotropization temperatures (T_i). Until recently, the high thermal stability of the columnar phases of alkylated HBCs precluded their thermal processing within configurations suitable for electronic evaluation.[366] The alternative method was solution processing which allowed the formation of monolayers of the alkylated HBC derivatives by depositing the molecules on molybdenum disulfide[367] or highly oriented pyrolitic graphite[368] and leading to the face-on arrangement of the molecules on the substrates.

5.4.1. HBCs substituted by Dove-Tailed Side Chains with Ether Linkages

Smaller discotic systems such as triphenylenes[363,364] and phthalocyanines[365] bearing alkoxy groups at or within their core periphery, spontaneously homeotropically align when crystallized from the isotropic state. Therefore, to enhance the ability to homeotropically align HBC materials, the presence of heteroatoms into the side chains was postulated and the effect on the supramolecular order has been investigated for samples crystallized between two glass slides.

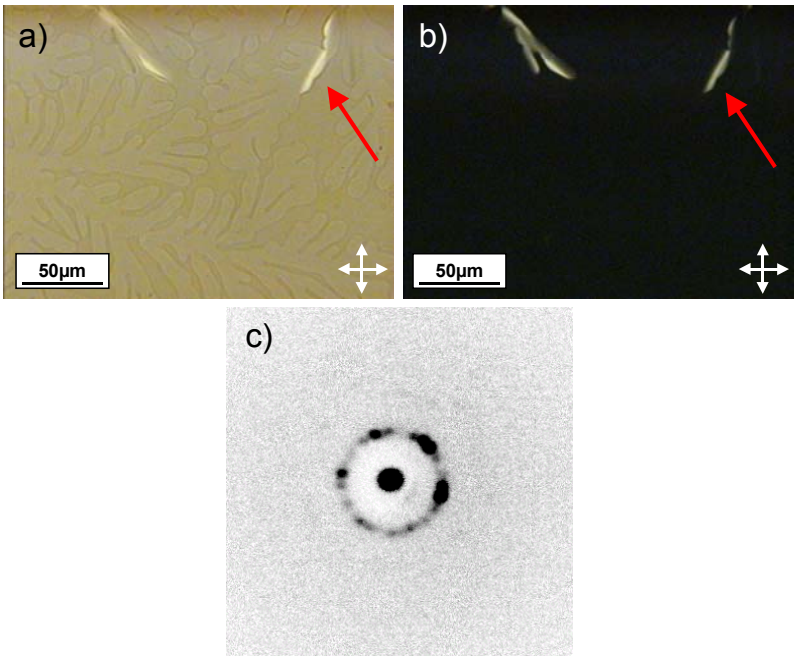

Figure 5.23. *Optical microscopy images of HBC-$C_3OC_{14,10}$ during crystallization between two glass slides a) without and b) with cross-polarizers (red arrow indicates defects in homeotropic order), c) 2D-WAXS pattern of the aligned sample.*

When slowly crystallized from their isotropic state as thin films between two polar surfaces, all discussed compounds revealed similar morphological behavior. Examples of textures observed by means of the optical microscope are presented in Figures 5.23, 5.24 and 5.27 for HBC-$C_3OC_{14,10}$, HBC-$C_3OC_{10,6}$ and HBC-$C_3OC_{8,2}$, respectively. In all cases, dendritic textures with a weak contrast with respect to the disordered material were observed in transmitted non-polarized light. However, when cross-polarizers were applied the images became black (Figure 5.23b, 5.24b and 5.27b), except some birefringent defects. This observation is characteristic for the homeotropic phase where the columnar axis is perpendicular to the substrate or for an isotropic state. In the first case, the transmitted light intensity is zero for all positions of the sample with respect to the analyzer/polarizer axis since the light propagation coincides with the optical axis and there is no anisotropy in the second case. The POM in such configuration does not allow, therefore, distinguishing uniquely between these two cases. By tilting the sample with respect to the light beam by nearly 45°, however, the dendritic areas of the homeotropically aligned sample appeared birefringent, whereas no effect for the isotropic parts was observed (Figure 5.25). Images from thermally controlled POM in Figure 5.24a display dendritic structures of HBC-$C_3OC_{10,6}$ formed during crystallization. Interestingly, the angle between the branching was consistently ca 60°, which is characteristic of hexagonal packing.

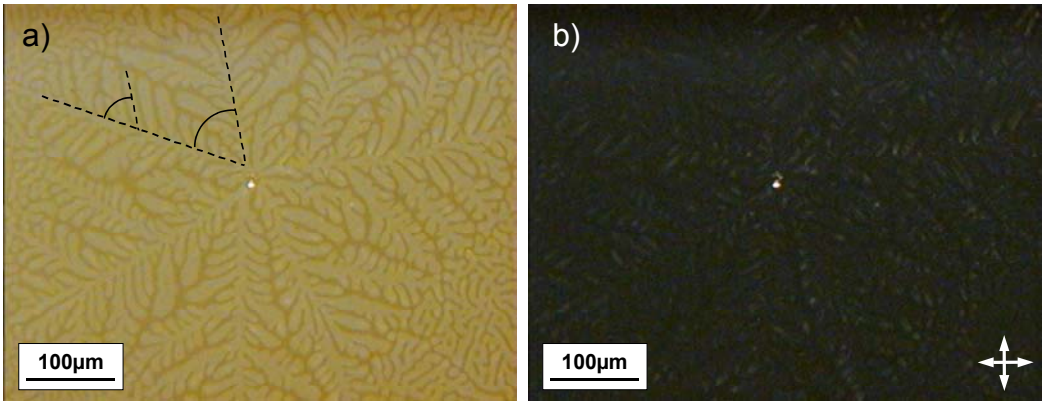

Figure 5.24. *Optical microscopy images of HBC-$C_3OC_{10,6}$ homeotropically aligned during controlled crystallization between two glass slides a) without and b) with cross-polarizers (dashed lines indicate the propagation direction of the dendritic structures).*

The homeotropic arrangement, which was implied by the lack of birefringence in the POM, was verified by 2D-WAXS measurements. In Figure 5.26a, the 2D-WAXS recorded with the incident beam perpendicular to the film surface is shown for the sample HBC-$C_3OC_{10,6}$, as an example. The diffraction pattern with the six intensive point-like first-order reflection maxima indicate uniquely the hexagonal order extending uniformly at least over the

area of the X-ray beam cross-section. This is attributed to the hexagonal arrangement of the columns with axes normal to the film surfaces and discs perpendicular to the axes of columns (homeotropic arrangement). An orientation disorder within the hexagonal packing even for areas at large distances would lead to a smearing of the six-point diagram to a ring. The complete wide-angle range of the X-ray pattern for the homeotropically aligned HBC-$C_3OC_{10,6}$ is not shown. But with this experimental set-up, only correlation distances which are exactly perpendicular to the incident beam give rise to visible reflections. Since the disc axes were orthogonal to the columnar axis, which in turn coincided with the incident beam, the typical reflections corresponding to the π-π stacking did not appear.

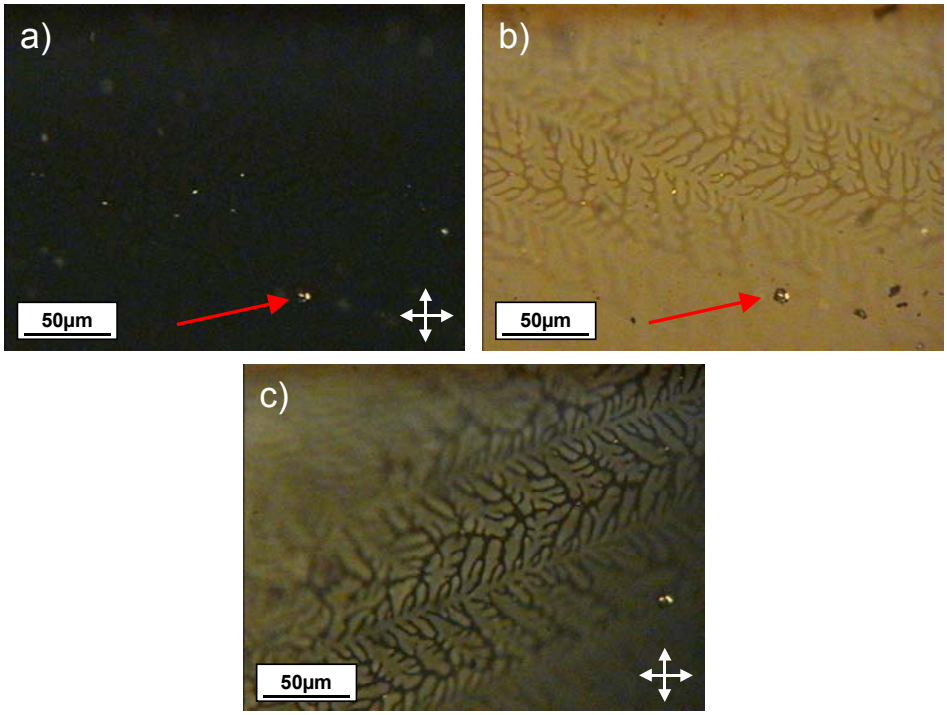

Figure 5.25. *Optical microscopy images of homeotropically aligned HBC-$C_3OC_{10,6}$ two glass slides which are tilted at 45° to the incident light a) without and b) with cross-polarizers (red line shows a particle which indicates the same position of the same), c) image in polarized light of the same position and the same tilt of the sample related to the incident light, but rotated 45° around the sample normal.*

The observed diffraction indicates a hexagonal monodomain within the scattering volume. It is interesting that this monodomain reveals a 2D dendritic form. With an appropriate exposition a less intense but distinct higher order reflections can be visualized (2^{nd}, 3^{rd} and 4^{th} order peaks) which correspond to hexagonal order, as well, and indicate a

long-range order in the hexagonal lattice. The first reflection appeared at 3.07 nm followed by the higher-order peaks was consistent with the typical relationship of hexagonal packing $1:\sqrt{3}:2:\sqrt{7}$ (Figure 5.26b). Since the disc axes were orthogonal to the columnar axis, which in turn coincided with the incident beam, the typical reflections corresponding to the π-π stacking did not appear. A schematic drawing of the homeotropic organization between the two surfaces is presented in the inset of Figure 5.26b. This supramolecular organization was in accordance with the results obtained for the bulk sample by powder diffraction. The first appearance of the homeotropic phase of HBC-$C_3OC_{10,6}$ was observed by temperature-dependent 2D-WAXS measurements at 135 °C and remained stable down to room temperature.

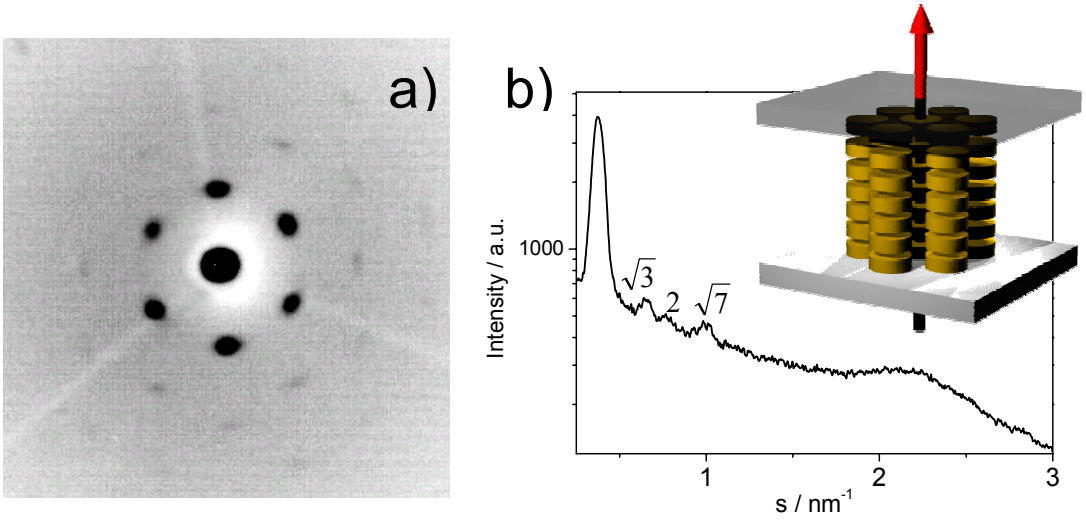

Figure 5.26. *a) 2D-WAXS pattern of HBC-$C_3OC_{10,6}$ at room temperature crystallized between two thin aluminum foils showing only the most essential intermediate 2θ range of 2°-10°; b) the intensity distribution as a function of the scattering vector (inset: schematic presentation of the homeotropic alignment between two surfaces during the X-ray experiment. The discs represent the rigid molecular cores and the red arrow assigns the X-ray beam direction).*

Both compounds HBC-$C_3OC_{14,10}$ and HBC-$C_3OC_{8,2}$ revealed a similar 2D hexagonal WAXS pattern when crystallized between the two aluminum foils. The first order reflection for HBC-$C_3OC_{14,10}$ arose at 3.55 nm, but of poorer pattern quality resulting in a less distinct packing correlation. The characteristic room temperature 2D-WAXS pattern of HBC-$C_3OC_{8,2}$ in Figure 5.27c exhibited a hexagonal intercolumnar distance of 2.78 nm being in good agreement with the unit cell parameters determined for the bulk mesophase of this compound

and verified the stability of this ordering down to room temperature. When the film of HBC-$C_3OC_{8,2}$ was cooled down quickly from the isotropic state with ca 50 °C/min, a different optical texture appeared (shown in Figure 5.27d) which revealed highly birefringent parts. It was apparent that there was limit for the cooling rate at which the homeotropical order could be obtained. This cooling rate limit was characteristic for each compound and depended on the affinity of the molecules toward the surfaces, thermal properties and viscosity in the isotropic state.

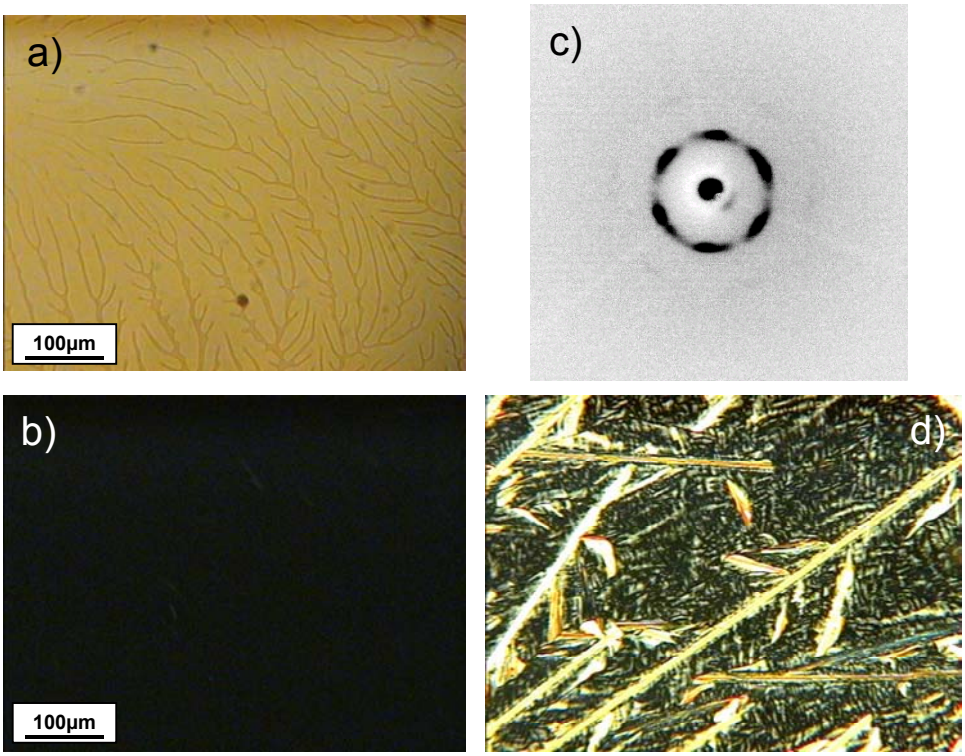

Figure 5.27. *Optical microscopy images of HBC-$C_3OC_{8,2}$ homeotropically aligned during controlled crystallization between two glass slides a) without and b) with cross-polarizers; c) 2D-WAXS pattern of HBC-$C_3OC_{8,2}$ at room temperature crystallized between two thin aluminum foils, the most essential intermediate 2θ range of 2°-10° is presented, d) POM image of HBC-$C_3OC_{8,2}$ cooled down abruptly from the isotropic state with ca 50 °C/min to room temperature.*

However during a slow crystallization between two glass slides down to room temperature also significant changes in the optical texture of HBC-$C_3OC_{8,2}$ were observed by using POM. After reaching the homeotropic phase, further crystallization caused the dendritic structures to impinge leading to more birefringent defects (Figure 5.28). First, these defects

emerged at the dendritic frontlines and upon further decreasing the temperature also appeared within these structures. Finally, at approximately 50 °C the whole optical texture changed with a significant increase in birefringence which indicated a transition in the supramolecular organization from a loss of the homeotropic order to an edge-on arrangement. This effect seems to be in contrast to the 2D-WAXS results which displayed a markedly homeotropic alignment for HBC-$C_3OC_{8,2}$ at room temperature. Since both surfaces glass and aluminum have similar surface polarities, another important feature was assumed to have significant influence on the supramolecular order. Similar observations, which are shown in Figure 5.29, were made for HBC-$C_3OC_{10,6}$ when the aligned sample was cooled below the solid-solid transition at 0 °C. Upon further lowering the temperature, the birefringence of the sample increased, but to a smaller extent than displayed for HBC-$C_3OC_{8,2}$. Interestingly, when the film was heated back to the Col_{hd} phase, the birefringence defects disappeared and the familiar black optical texture in cross-polarizers returned.

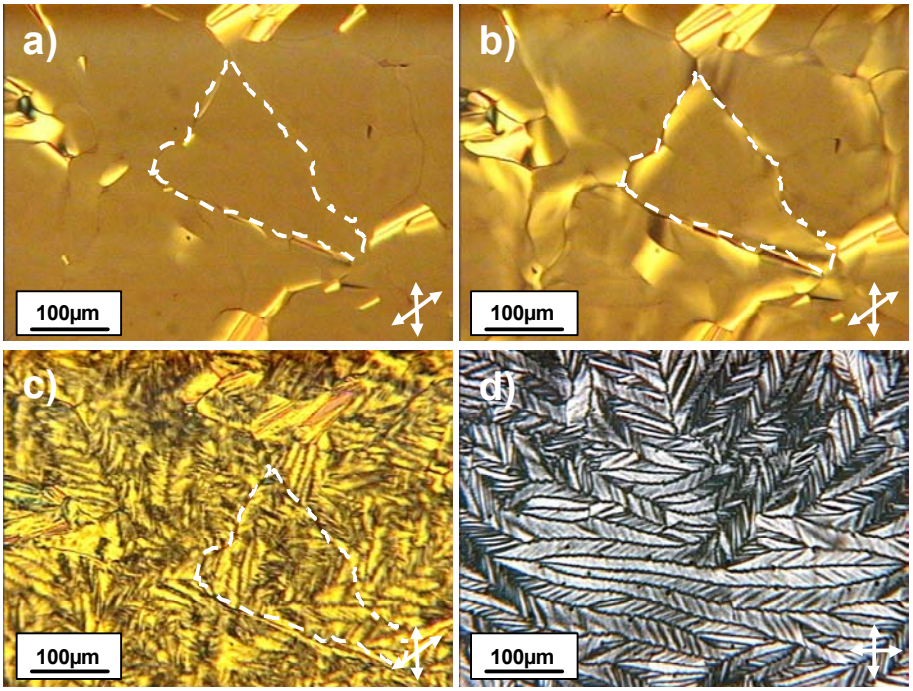

Figure 5.28. *Optical microscopy images of HBC-$C_3OC_{8,2}$ cooled at 1 °C/min from the isotropic state; Images a) – c) taken at an angle of 45° between the analyzer/polarizer axis, a) at 350 °C, b) at 290 °C and c) 100 °C (dashed lines indicate the same grain); d) cross-polarized image of a randomly chosen position of the sample after annealing it for 24hrs at room temperature.*

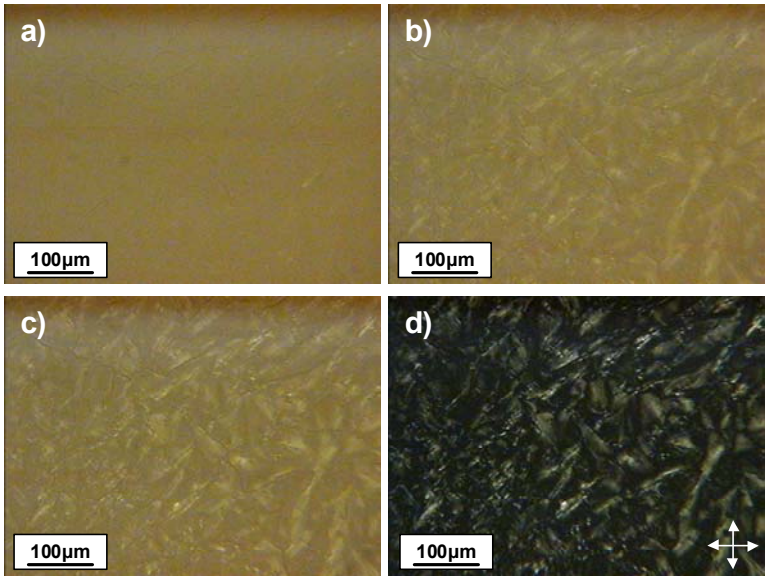

Figure 5.29. *Optical microscopy images of HBC-$C_3OC_{10,6}$ crystallized from the isotropic state; Images (a) – (c) taken with an angle analyzer/polarizer axis of 45°, (a) at 30 °C, (b) at -10 °C and (c) -30 °C; (d) cross-polarized image of (c).*

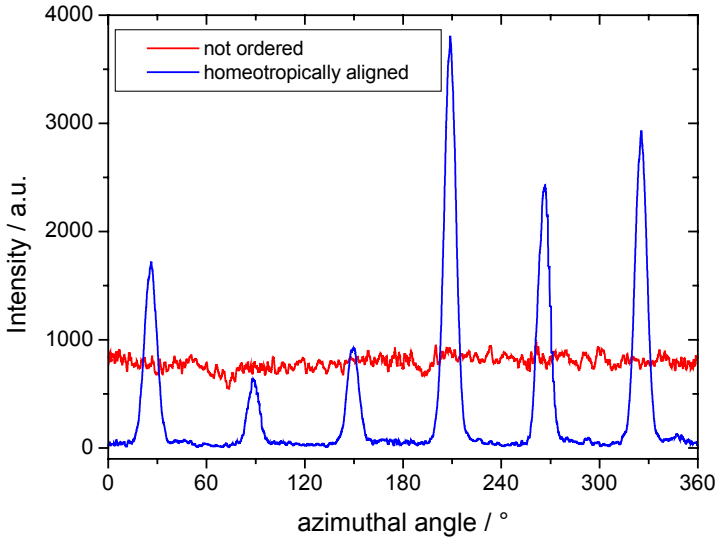

Figure 5.30. *Intensity distribution as a function of the azimuthal angle of the 1st order reflex corresponding to the a unit cell parameter of HBC-$C_3OC_{10,6}$ for a disordered surface layer shown in Figure 5.31b (red) and for a homeotropically oriented layer (blue) from Figure 5.31c.*

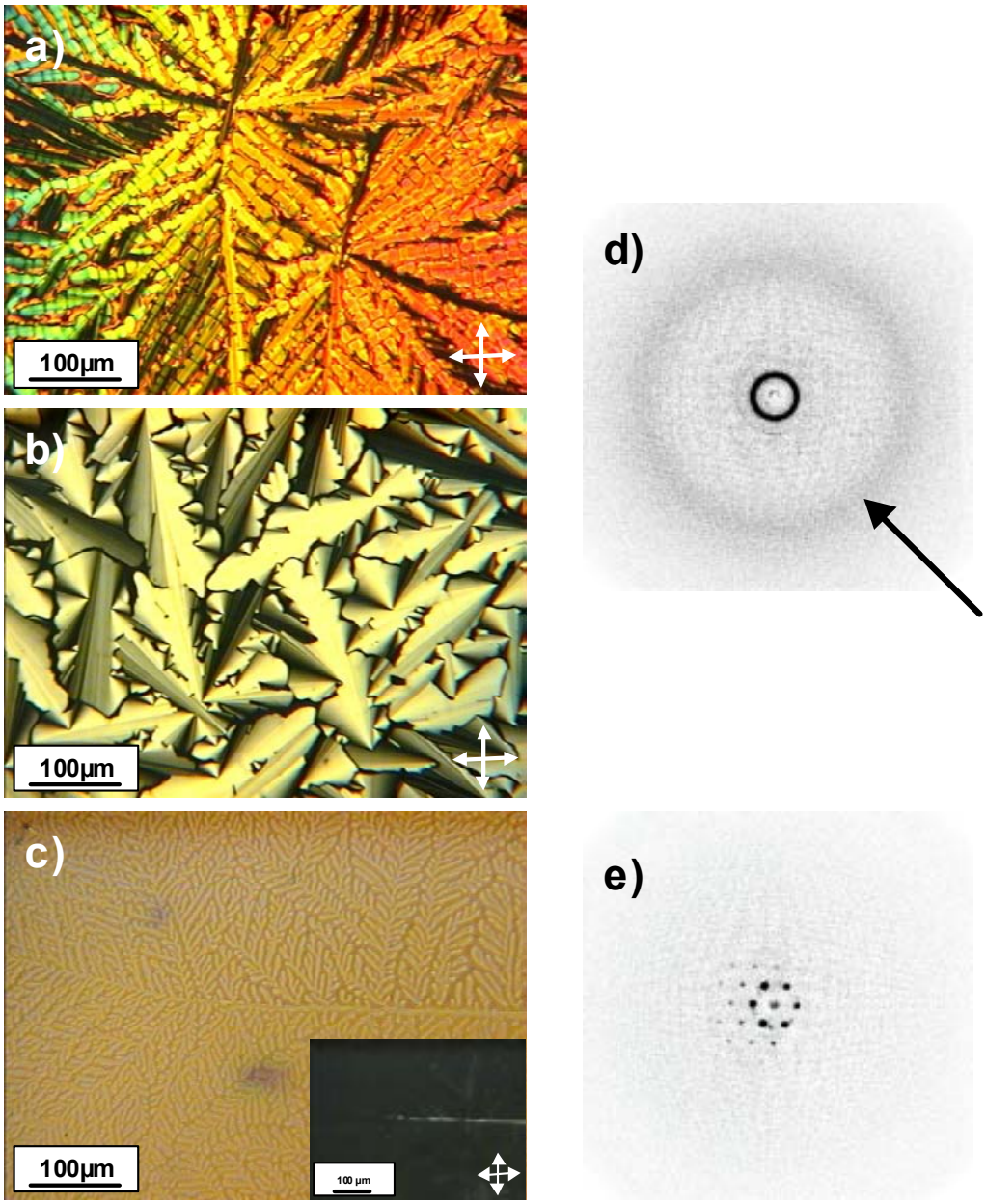

Figure 5.31. *Examples of the characteristic optical textures as a function of film thickness of HBC-$C_3OC_{10,6}$ crystallized on one glass surface at a cooling rate of 1 °C/min from the isotropic state. POM images a) and b) show the optical textures of the film with different film thickness; whereby a) presents the thickest surface layer. The optical image in c) exhibits characteristic dendritic textures formed on one surface. The same image in cross-polarizers is shown in the inset. The 2D-WAXS pattern in d) reveals the isotropic alignment within the films, which are presented in the POM images a) and b). The arrow indicates the reflection corresponding to the disordered intracolumnar disc stacking. The alignment of the layer in c) is demonstrated by the typical hexagonal 2D-WAXS pattern. Both 2D-WAXS patterns in d) and e) were recorded under identical conditions.*

Besides a facile, homeotropic alignment between two surfaces, it was of interest to design a molecule which could be ordered in the same manner on only one surface. Therefore, films of different thickness of HBC-$C_3OC_{10,6}$ were prepared on a glass slide and each sample was subjected to identical thermal treatment. As presented in Figure 5.31, the optical images revealed great differences in the optical textures of these films. When processed as a thicker film, colorful dendritic-like textures appeared, whereas a thinner surface layer revealed a characteristic, strongly birefringent, fan-shaped morphology. The 2D-WAXS (Figure 5.31d) showed edge-on alignment in both films shown in Figures 5.31a and 5.31b. The appearance of the wide-angle reflection corresponding to the intracolumnar period confirmed the molecular edge-on arrangement. Additionally, the 360° azimuthal intensity distribution of the 1st order reflection, corresponding to the *a* cell parameter, indicated a significant deviation from molecular vertical columnar alignment and suggested that the columnar axes were randomly distributed relative to the surface normal (see Figure 5.30). Finally, at an appropriate film thickness dendritic structures were observed (Figure 5.31c) which did not show any birefringence between cross-polarizers. Further structural investigations using X-ray scattering experiments (Figure 5.31e) proved an identical intercolumnar arrangement on one surface as the above-described, characteristic, homeotropic hexagonal order attained between two surfaces.

5.4.2. Homeotropic Alignment of All-Hydrocarbon HBCs

In order to evaluate the homeotropic alignment of all hydrocarbon HBC derivatives in comparison to HBCs bearing the ether linkages in the side chains, the morphology formed during crystallization from the isotropic state was studied for HBC-$C_{16,4}$, HBC-$PhC_{14,10}$ and the well known HBC-C_{12}.

The first successful approach to lower the isotropic phase transition temperature for a HBC derivative was attained by the introduction of the 3,7,11,15-tetramethylhexadecyl (HBC-$C_{16,4}$).[195] This compound revealed an isotropization temperature of 231 °C which is significantly lower in comparison to the alkylated HBCs with a T_i of 420 °C. Additionally, the phase transition from the crystalline state to the liquid crystalline phase was shifted to –36 °C. The lowered isotropization temperature allowed the processing between two ITO surfaces and the investigation of the relationship between photoconductivity and columnar alignment. Short-circuit photocurrents were fivefold higher in better-aligned regions compared to those in regions with weak orientation indicating that the charge transfer takes place along the columnar structures.

The temperature-dependent 2D-WAXS measurements of HBC-$C_{16,4}$ were discussed in

Chapter 3 and indicated a plastic crystalline state in the low temperature phase, whereby a disordered columnar phase was assigned at room temperature which was explained by the high steric demand of the bulky side chains.

Due to these increased steric requirements it was possible to process HBC-$C_{16,4}$ from the isotropic state due to the lowered isotropization temperature. When the compound was sandwiched between two glass slides and cooled under controlled conditions from the isotropic state, large dendritic domains appeared (Figure 5.32a). In cross-polarizers these optical textures were not birefringence, with the exception of same defects, indicating a uniform homeotropic alignment of the sample (Figure 5.32b). The number of defects was strongly dependent on the cooling rate. At very high rates, the homeotropic phase could be even suppressed completely resulting in an overall highly birefringent optical texture. This is the first example of an all-hydrocarbon discotic liquid crystalline compound which revealed a propensity for spontaneous homeotropic alignment from the isotropic phase. This is in contrast to all reported examples which pointed out the necessity for specific atoms within the molecular architecture for the successful orientation from the isotropic state. But this first example implies that the homeotropic order does not require the introduction of heteroatoms into the molecular structure. At this point it is too difficult to speculate about the alignment mechanism for HBC-$C_{16,4}$, since no other all-hydrocarbon discotic compounds exhibited such behavior. In contrast, all other HBC derivatives substituted by alkyl side chains showed when cooled down from the isotropic phase high birefringence in the POM indicating an edge-on arrangement of the discotic molecules with respect to the surface, whereby the columnar axes were distributed randomly in-plane.

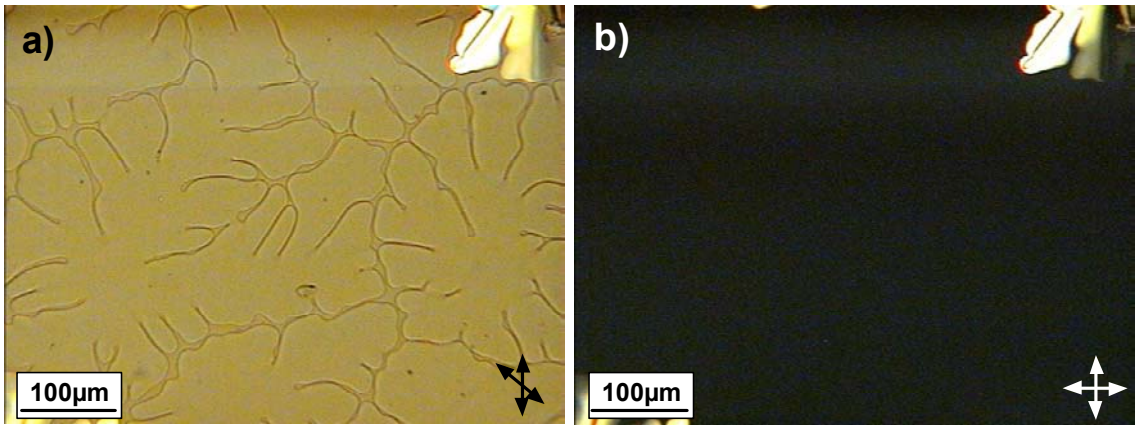

Figure 5.32. *POM images of homeotropically aligned HBC-$C_{16,4}$ cooled down from the isotropic state by 1 °C/min a) with 45° and b) 90° with respect of the polarizer/analyzer axes to each other.*

The 2D-WAXS pattern (Figure 5.33a), which exhibited the characteristic, distinct, hexagonal six-point reflections, of the aligned sample confirmed the homeotropic arrangement of the discs. Thereby, the columns are aligned in the direction of the incident X-ray beam. Interestingly, each of the reflection consisted of additional two peaks indicating that the X-ray beam was focused at a grain boundary which ran along the surface normal and along the columnar direction. The hexagonal lattice in these two domains is identical, but slightly displaced with respect to each other. The integration along the 360° azimuthal angle for each scattering vector, shown in Figure 5.33b, confirmed the hexagonal unit cell with identical packing parameters as determined for the extruded filament. Moreover, in accordance with the experimental set-up the intracolumnar correlation were not displayed in both the scattering intensity plot and in the pattern.

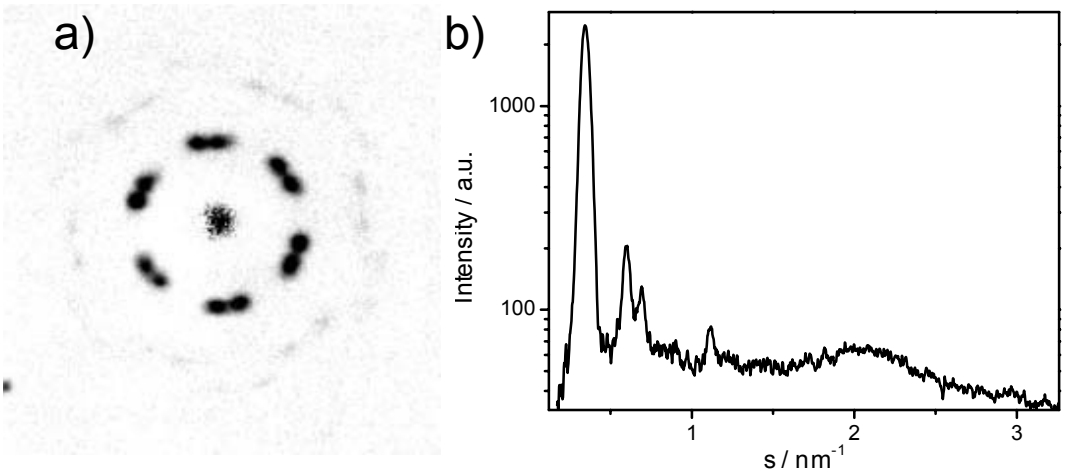

Figure 5.33. *a) Example of a 2D-WAXS pattern of a homeotropically aligned sample, whereby the columnar axes coincident with the X-ray beam, b) integration along the azimuthal angle of 360° as a function of the scattering vector.*

As an additional example for an all-hydrocarbon discotic molecule which revealed spontaneous homeotropic alignment when cooled down from the isotropic state, the supramolecular structure and the morphology of HBC-Ph$C_{14,10}$ has been investigated. The introduction of the very bulky $C_{14,10}$ side chains lowered also in this case the isotropization temperature significantly to 110 °C in comparison to HBC-PhC_{12} and HBC-PhC_8[*] which showed a T_I far above 500 °C. Since the supramolecular arrangement of this compound was not discussed in Chapter 3, the 2D-WAXS pattern of an extruded filament recorded at room temperature is presented in Figure 5.34.

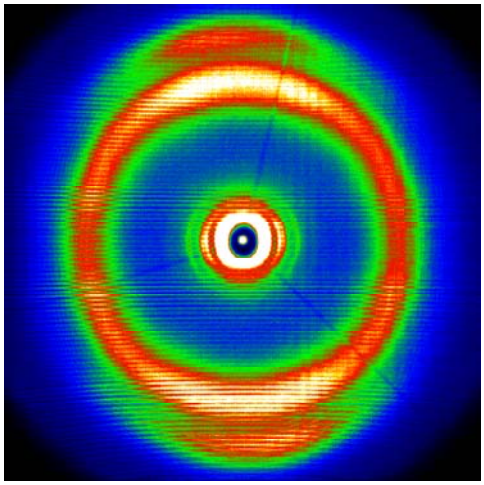

Figure 5.34. *2D-WAXS pattern of HBC-PhC$_{14,10}$ at room temperature.*

The intercolumnar arrangement could be assigned to a hexagonal lattice with 3.84 nm as the packing parameter. Despite the low degree of anisotropy of the first equatorial reflection, the meridional peaks indicate a well-ordered structure of the discotic molecules which are arranged in the non-tilted manner in the columnar stacks. However, the relatively large intracolumnar distance of 0.37 nm suggests a pronounced influence of the bulky dove-tailed side chains onto the interaction of the aromatic cores hindering an approaching to each other.

When HBC-PhC$_{14,10}$ was cooled down from the isotropic state between two glass slides, first dendritic structures appeared which finally changed into a homogenous film. At a temperature of approximately 60 °C this film did not reveal significant birefringence (Figures 5.35a and 5.35b), except few defects suggesting a macroscopic homeotropic alignment of the sample. The 2D-WAXS patterns in Figure 5.35c and 5.35d verify the orientation of columns normal to the surface. Thereby, different degrees of intercolumnar order could be observed depending on the examined position of the sample. At some positions the domains revealed an almost homogenous hexagonal arrangement of the columns, but other places at grain boundaries the hexagonal unit cell was displaced to each other. When the sample was further cooled down at a rate of 1 °C/min, the number of birefringent defects increased significantly until the optical texture of the film changed completely (Figure 5.35e) implying also a transformation of the supramolecular organization.

Finally, in order to investigate the supramolecular arrangement of an alkylated HBC derivative, as example the most prominent compound, HBC-C$_{12}$, was investigated. During cooling the sample from 420 °C above the isotropic phase between two glass slides, first

dendritic structures were espied which then created a homogenous film (Figure 5.36a), as observed for HBC-PhC$_{14,10}$. Surprisingly, the film did not show any birefringence and therefore a homeotropic alignment of the sample was suggested. Below a temperature of ca 200 °C birefringent defects appeared (Figure 5.36b) and the optical texture of the sample converted significantly (Figure 5.36c). Nevertheless, the 2D-WAXS pattern in Figure 5.36d for a sample crystallized between two aluminum foils confirmed the homeotropic alignment also at room temperature.

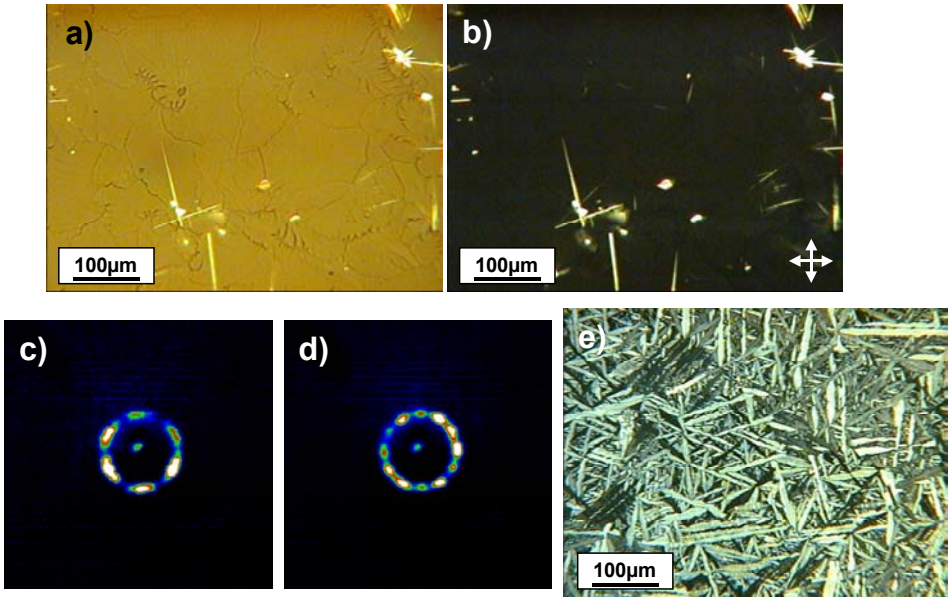

Figure 5.35. *Optical microscopy images of HBC-PhC$_{14,10}$ at ca 60 °C homeotropically aligned during controlled crystallization at 1 °C/min between two glass slides a) without and b) with cross-polarizers; 2D-WAXS pattern of HBC-PhC$_{14,10}$ at room temperature crystallized between two thin aluminum foils indicating c) one uniform domain and d) two domains (the most essential intermediate 2θ range of 2°-10° is presented), d) POM image of HBC-PhC$_{14,10}$ cooled down to room temperature at 1 °C/min.*

An additional issue was the investigation of the homeotropic order discotic molecules with respect to the support for the application in devices. One possible procedure to obtain homeotropic alignment of the sample is the introduction of polar groups into the side chains in order to increase the affinity of the molecules towards surfaces such as glasses, metals, and metal oxides. During crystallization from the isotropic state, the molecules first arrange "face-on" towards the substrate and then self-assemble homeotropically. It is assumed that this alignment should enhance the electronic performance of intracolumnar charge carrier pathways in solar cells.

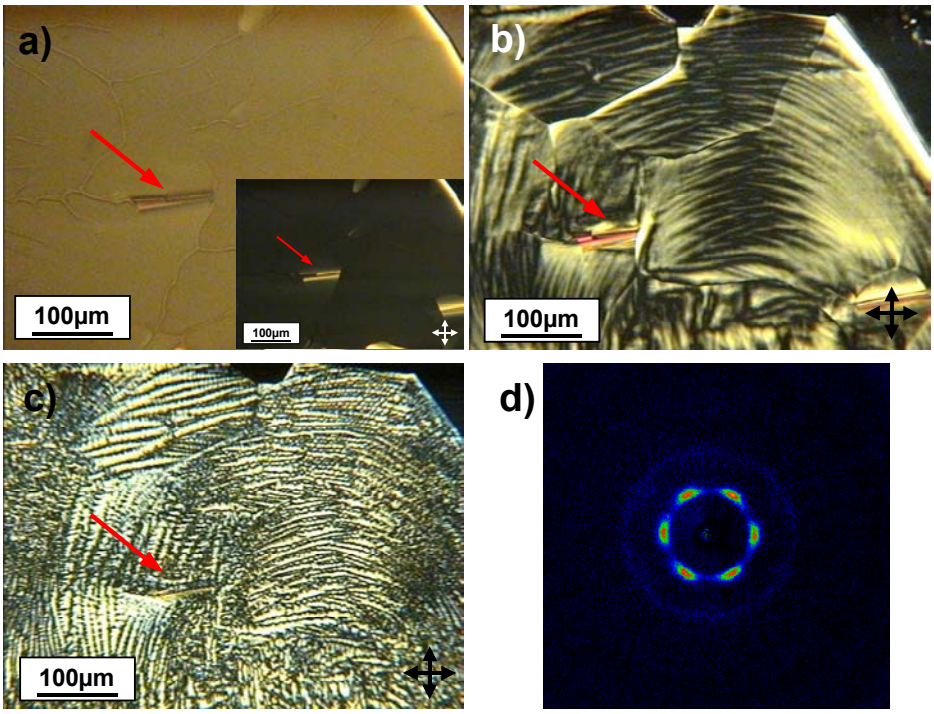

Figure 5.36. a) *Optical microscopy images of HBC-C_{12} at ca 280 °C homeotropically aligned during controlled crystallization at 2 °C/min between two glass slides (without and with cross-polarizers); b) at 180 °C and c) at room temperature (red arrow indicates a defect in order to verify the same position of the sample in all four images); d) 2D-WAXS pattern of the homeotropically aligned sample.*

Indeed, the introduction of ether groups in the side chains essentially improved the affinity of the HBC derivatives investigated toward face-on arrangement at the corresponding surface and facilitated a control of the homeotropic alignment. The presence of these polar ether units in the HBC core periphery had a fundamental influence on the self-organization behavior of the molecules on polar surfaces. These HBC derivatives presented here uniformly homeotropically aligned even at cooling rates as fast as 20 °C/min between two glass or aluminum surfaces proving the high attraction of the polar groups to this kind of surfaces. This might also suggest some self-healing of misaligned domains during solidification, evidenced by the rapid appearance and disappearance of birefringent textures during fast cooling. The strong tendency for the homeotropic alignment can be attributed to the rigid spacer between the aromatic core and the branching site of the side chains as well as to the δ position of the oxygen atom. The spacer induces stability at the δ position apart from the steric hindrance of the space-filling, dove-tailed side chains and ensures the high affinity of the molecules to the corresponding surfaces. The length of the branched side chains seems

then to be most important for the processibility of the material, rather than just for the alignment mechanism. An additional factor is an appropriate viscosity of the quasi-isotropic phase, which was proven by rheology measurements. During the processing procedure, the interaction of the first molecules with the surface plays a crucial role. Upon further decreasing the temperature, the crystallization progresses and other molecules stack upon the pre-arranged discs at the surface creating in this way the desired macroscopic order.

Due to its distinct homeotropic alignment, the self-orientation behavior of HBC-$C_3OC_{10,6}$ deserves attention. During crystallization between two glass surfaces the material created dendritic textures which nucleated sporadically and grew at structure edges with columns arranging perpendicularly with respect to the growing front, contrary to other cases with the directional growth. The 2D-WAXS confirmed the hexagonal homeotropic arrangement which indeed was closely related to the optical texture. Since the X-ray beam used in the WAXS experiment had a diameter of nearly 1 mm, the POM images displayed only a minor part of the by X-ray examined area. Therefore, the structure evaluation suggested an extremely uniform and quasi defect-free hexagonal order without apparent replacements of the lattice over the whole investigated range of the sample. On the other hand, this is in excellent correlation with powder diffraction experiments which showed that even the bulk material at room temperature forms a well ordered supramolecular structure with a strong dependence on thermal processing. The only relationship between the macro- and nanoscopic organization is the characteristic 60° angle which appears in both the hexagonal 2D lattice and the dendritic morphology. Despite the directional growth and the anisotropic morphology of these structures, no supramolecular orientation in this growth direction was induced.

Moreover, the strong affinity towards the surface was demonstrated by the successful orientation of the material on only one surface. Since thicker films did not reveal this specific arrangement, there is evidently some critical thickness above which the governing influence of the surface layer is lost within the bulk of the film or at the upper surface, whereby random columnar growth becomes dominant. The schematic model which is assumed for the different columnar growth is presented in Figure 5.37. So, the supramolecular order changes at a certain columnar height from homeotropic oriented molecules to an edge-on arrangement with columns lying on the surface. In contrast, all-hydrocarbon HBC-$C_{16,4}$, which showed homeotropic alignment between two surfaces, did not reveal similar crystallization behavior on one surface at any film thickness or by any approach. This implies that the introduction of heteroatoms increases the affinity towards polar surfaces significantly, overcoming even the high thermodynamical limits forcing the molecules to lie flat on the support.

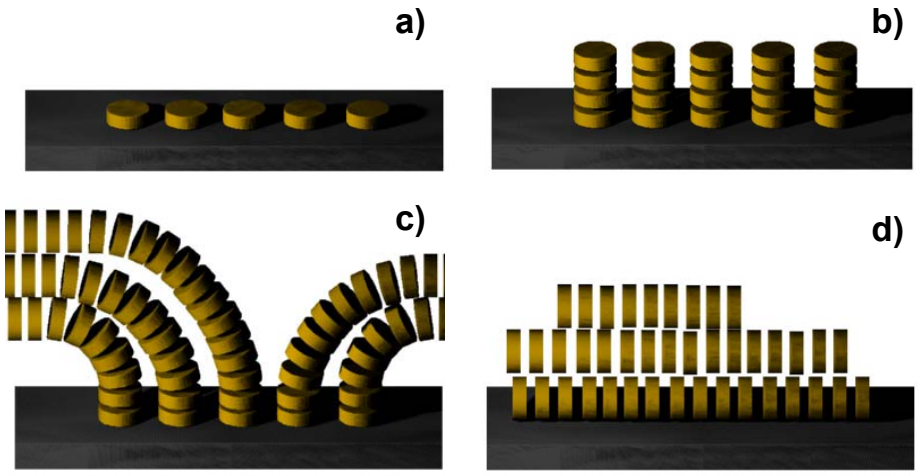

Figure 5.37. *Schematic model of the molecular arrangement on one surface during crystallization form the isotropic phase with a) the first face-on arranged molecules at which during further crystallization additional discs aggregate forming the desired homeotropical order as observed for HBC-$C_3OC_{10,6}$. Other compounds did not reveal such self-assembly behavior on one surface and organize in a different way such as proposed in c) with the first molecules face-on arranged, but with progress of the columnar growth the disc change the order to edge-on or d) with already edge-on oriented molecules at the surface.*

Due to the synthetic limitations for other discotic materials, the homeotropic order of all-hydrocarbon discotics has never been investigated. For triphenylenes and phthalocyanines, bearing heteroatoms in their side chains, it was claimed that the presence of these atoms provide homeotropic order.[50,363] In contrast, the successful homeotropic alignment of the all-hydrocarbon HBC-$C_{16,4}$ and HBC-$PhC_{14,10}$ indicated that heteroatoms are not necessary. The reason for this specific alignment might be not only the affinity increase by the introduction of ether linkages into the side chains. It is assumed that the origin of the face-on arrangement is the influence of the side chains. The investigated all-hydrocarbon samples which revealed homeotropic orientation, the side chains were bulk and space-filling leading to a relatively disordered intracolumnar packing. During crystallization from the isotropic phase, these space-filling side chains wet the surface and forced the aromatic core to the face-on arrangement. Afterwards the next aromatic cores interacted with the already face-on arranged molecules leading to the self-assembly interior the film and finally macroscopic homeotropic order. However, when the steric requirement of the side chains was too high, as in the case of the dove-tailed HBC-$C_{14,10}$, HBC-$C_{10,6}$ and HBC-$C_{6,2}$, the molecules are hindered to approach the surface and therefore organized in the edge-on manner. By the introduction of a spacer between the aromatic core and the branching of the dove-tailed chains, as in the cases of

HBC-$C_3OC_{14,10}$, HBC-$C_3OC_{10,6}$, HBC-$C_3OC_{6,2}$ and HBC-$PhC_{14,10}$, the high steric demand at the core vicinity was lowered and enabled a lying down of the aromatic core.

Same samples revealed changes in the homeotropic alignment during cooling, whereas for other compounds the order was stable down to room temperature. In general, each phase transition implies a considerable structural change, which in turn is associated with a density alteration and related to changes in macroscopic dimensions of the sample. A thermal phase transition induces changes in supramolecular order towards a more thermodynamically favorable organization for given molecules. This alteration is considerable for any material contained in a limited volume. When water is crystallized from the liquid to the solid state in a closed glass bottle, the density increase of the material can be high enough to burst the glass vessel. Such a phenomenon was observed during the crystallization of HBC-$C_3OC_{8,2}$ between two glass slides which can be considered as fixed surfaces limiting the volume relaxation in the sample. The texture of the sample transformed from a homeotropic alignment indicated by the black POM image to a highly birefringent mosaic texture at lower temperatures implying a significant change in the order. On the other hand, 2D-WAXS experiments provided a contradicting result for the same material crystallized between two aluminum foils revealing the homeotropic order at room temperature. If these foils can be considered as flexible surfaces then one can assume that during the crystallization they can compensate for the density and macroscopical changes maintaining the homeotropic orientation. Based on these observations, the stability of the homeotropic phase can be regarded as a mechanical problem consisting in adjustment of stiffness and thermal expansion of the materials as illustrated in Figure 5.38.

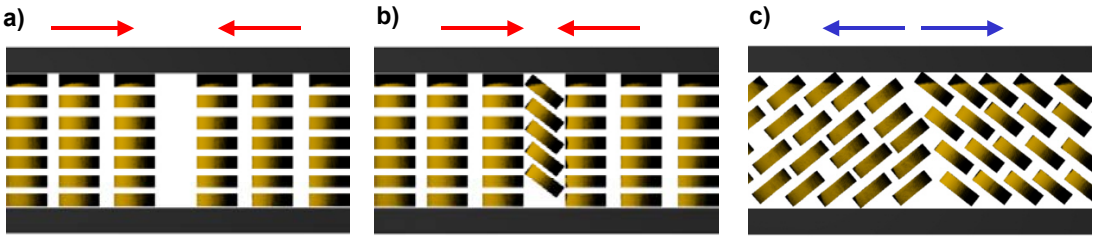

Figure 5.38. *Schematic representation of the change in the supramolecular organization within two adjacent crystalline grains during crystallization of a homeotropically aligned sample such as HBC-$C_3OC_{8,2}$ with a) the crystallization fronts of the two grains growing towards each other, b) impingement of the growth fronts and c) the resulting change in the order within the two grains due to the impingement (red arrows indicate the growth direction and the blue ones show the acting forces).*

The homeotropic phase of HBC-$C_3OC_{10,6}$ was stable upon cooling to room temperature,

but at 0 °C the material underwent structural changes at the solid-solid transition which was combined with an alteration in the inter- and intracolumnar packing behavior. Since the homeotropic order is formed during the transition from the isotropic state to the mesophase, a hexagonal two-dimensional lateral intercolumnar arrangement appears, which is characteristic for the liquid-crystalline state. Any change in this intercolumnar organization induces defects in the homeotropic alignment which was possible to observe by POM by cooling the sample below 0 °C. At the low temperature phase the morphology and macroscopic orientation of the homeotropically aligned sample diminished. Therefore, the absence of significant thermal and structural transitions between the orientation process and application is another important requirement for this kind of supramolecular order. These requirements are fulfilled for HBC-$C_3OC_{10,6}$, which was confirmed to be in the Col_{hd} phase at room temperature. However, the low extent of birefringence below 0 °C indicated that the main homeotropic alignment was stable. This suggests a strong and tight surface contact of the molecules, since the bulk compound revealed a considerable structural change at this solid – solid phase transition. Heating the sample back to the higher temperature phase revealed a significant decrease of the birefringent defects and a reversible appearance of the homeotropical texture.

5.4.3. Binary Mixtures of Discotics with Different Molecular Architecture

The results of the last section indicate that mainly the degree of the steric demand of alkyl side chains determines the tendency for homeotropic alignment of discotics. This assumption was based on the different supramolecular arrangement of the β-dove-tailed HBCs in comparison to HBC substituted by linear or methylene containing side chains. The introduction of the phenyl rings between the aromatic core and the long branched $C_{14,10}$ alkyl chains led to the decrease of the peripheral steric requirements resulting in homeotropic order. In order to gain a final proof for this conclusion the following experiments have been carried out during which implicitly the effect of the space-filling reduction of the side chains was investigated. Therefore, the idea was to intercalate disc molecules, bearing a small number of side chains, between HBC-$C_{10,6}$ building blocks in order to enlarge the distance between the HBC molecules. In this way, the space-filling effect of the bulky $C_{10,6}$ alkyl chains should be diminished leading hopefully to the desired macroscopic self-organization.

In general, a novel concept in the design of materials might be the mixing of two different discotic materials with each other. Accordingly to the blending of two linear

polymers various effect can be expected reaching from a phase separation in the blend to the formation of a one-phase mixture. For two polymers the blending enthalpy determines whether the mixture will be homogenous or phase separated.[369] The blending of materials based on single building blocks which self-assembly into superstructures is, however, more complex, since the molecular architecture controls the interaction between the molecules. Therefore, various different supramolecular structures can be formed in a mixture including nano- as well micro-separation as illustrated in Figure 5.39.

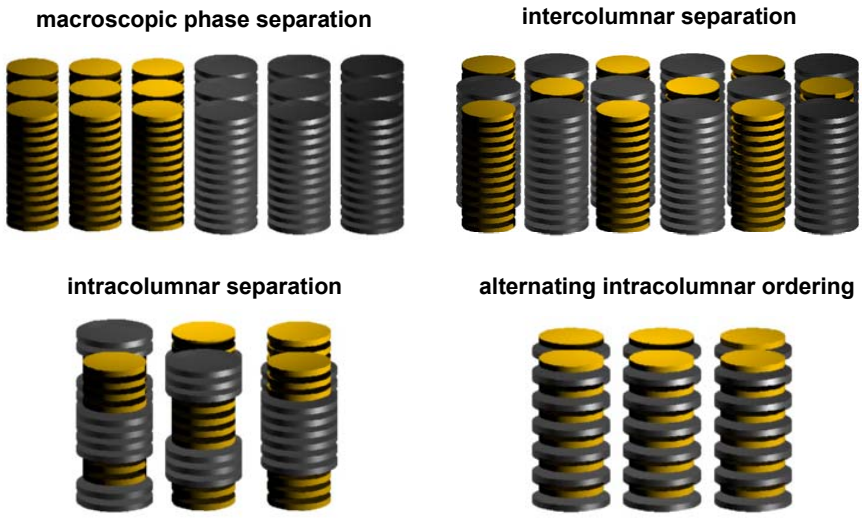

Figure 5.39. *Schematic illustration of different supramolecular structures in mixtures consisting of two different discotic compounds.*

The blending of two discotic compounds has not been investigated intensively. Bushby and Boden studied the effects of blending hexakis(hexyloxy)triphenylene with azatriphenylene or hexakis(phenylhexyloxy)triphenylene, both mixtures at a molar ratio of ½.[370,371] The preparation of the samples was not reported. The mixtures revealed a homogenous phase, whereby the isotropization temperature of the blends was higher than of the pure compounds. From the structure evaluation of the blends it was assumed that an alternating intracolumnar arrangement was formed, which was more ordered and much more stable. Time-of-flight experiments verified these results and showed a significantly higher charge carrier mobility in the blend than for the pure compounds.[372,373] The formation of alternating stacking of donor and acceptors equimolar mixtures for mixtures of triphenylene with trinitrofluorenone[122] or triimides[374] resulting in the increase of intracolumnar order.

In this study, the effect of blending two discotic materials, which differ significantly in their electronic properties has been studied. While hexa-*peri*-hexabenzocoronene substituted by long, branched alkyl chains (HBC-$C_{10,6}$) is an electron donating agent, perylene diimide[375]

(PDI) or terrylene diimide derivative (TDI) are strong acceptors. Therefore, the molecules allowed a weak electronic interaction between the two components; one expected a stabilization due to alternating stacking in the columnar structure and thus an induction of ordering in this donor-acceptor mixture. Additionally, the blended molecules were compatible in size permitting a matched intracolumnar packing, leading to a different propensity to self-organize on a surface.

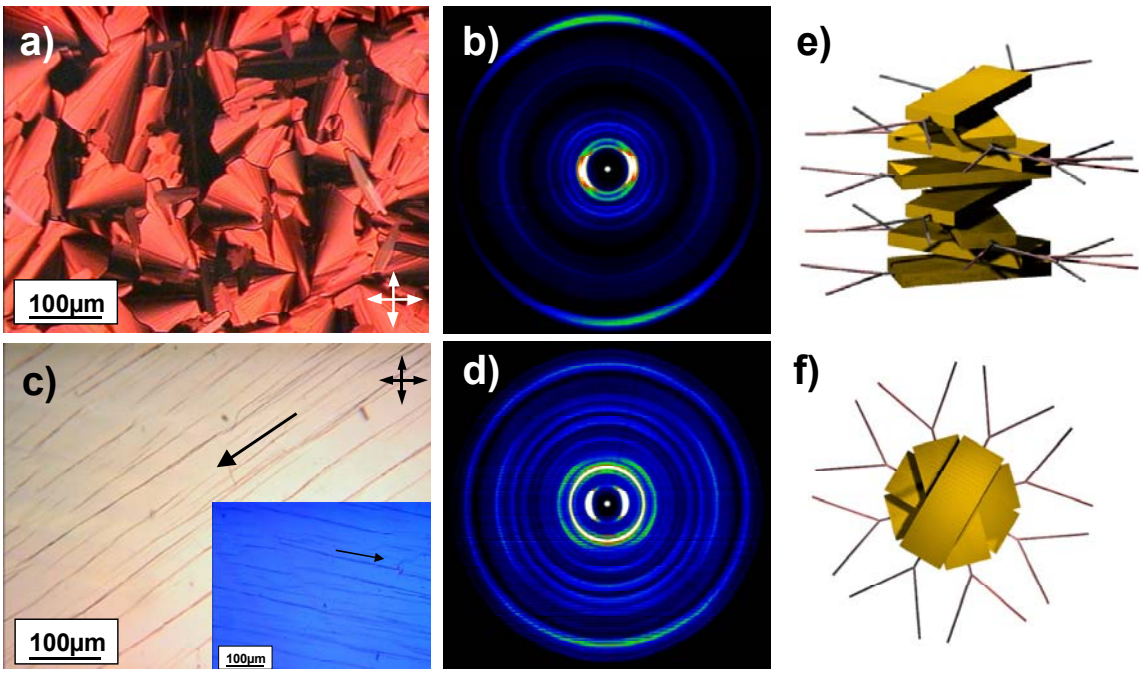

Figure 5.40. *a) POM image of the optical texture of PDI obtained by cooling down at 2 °C/min from the isotropic phase, b) 2D-WAXS pattern of PDI at room temperature, c) POM image of TDI cooled down at 2 °C/min from the isotropic state, d) 2D-WAXS pattern of TDI, e) Schematic illustration of the intracolumnar packing model for PDI and TDI, f) top view of the columnar organization.*

As discussed earlier, HBC-$C_{10,6}$ revealed a herringbone structure at room temperature (plastic crystalline phase) and a disordered columnar phase at temperature higher than 40 °C. When cooled down from the isotropic phase (T_i = 96 °C) highly birefringent dendritic structures appeared which indicated an edge-on arrangement of the molecules. For PDI an optical texture with pseudo focal conic fan-shapes (Figure 5.40a) during crystallization (T_i = 130°C)[375] was observed suggesting the formation of a discotic LC phase, where the molecules were orthogonally arranged with respect to the stacking axis. Furthermore, the 2D-WAXS (Figure 5.40c) indicated that the cofacially oriented perylene molecules pack with a slight rotation between neighboring molecules within a columnar stack (Figure 5.40e and 5.40f).

Such an intracolumnar organization has been already reported and was explained by the intermolecular dipole-dipole interactions between the carbonyl groups of the imide moieties.[376,377] An identical intracolumnar arrangement was determined for TDI (Figure 5.40d) which formed large ordered domains during cooling from the isotropic phase with molecules edge-on oriented (Figure 5.40b). In general, the substitution of rylene derivatives by alkyl side chains opens the opportunity to control their solubility and thermal behavior, both properties which are essential for the device processing.[378] Device mobilities up to 0.6 cm²/Vs have been reported for alkyled perylene diimide films prepared by evaporation.[379]

The pure compounds were blended at a molar ratio first in the solution, but afterwards in the isotropic phase. From the investigation of the thermal behavior it was evident that all mixtures formed a macroscopic, homogenous thermal phase. But it should be noted that it was possible to separate the compounds by chromatographic methods. Additionally, the supramolecular structure was investigated by 2D-WAXS and the morphology by thermally controlled POM experiments.

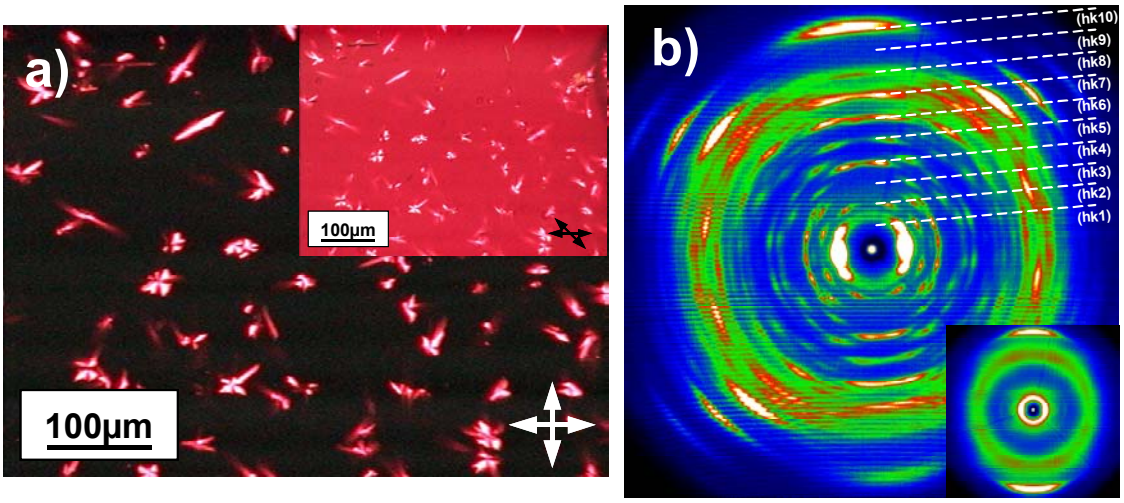

Figure 5.41. *a) POM of the mixture of HBC-$C_{10,6}$ and PDI at a molar ratio of 1-1 at room temperature after cooling from the isotropic phase in cross-polarizers (inset: 45° of the polarizer/analyzer), b) 2D-WAXS pattern of the mixture after annealing at ambient conditions for 48hrs (inset: directly after filament extrusion).*

In Figure 5.41a the optical texture of the mixture of HBC-$C_{10,6}$ and PDI at a molar ratio of 1-1 is shown. The isotropization temperature was determined at 50.0 °C. When the sample crystallized, a homogenous film was formed with an optical texture which did not show significant birefringence in polarized light, despite few defects. The morphology of the blend differed fundamentally from that observed for the pure compounds. The 2D-WAXS pattern of

the mixture indicated also a significant difference in the supramolecular arrangement. After the sample preparation (Figure 5.41b) the pattern showed an almost isotropic first equatorial reflection, a pronounced meridional peak and a clear amorphous halo. But after annealing the extruded sample for 48 hours at ambient conditions, the X-ray pattern changed, whereby the number of distinct reflections increased dramatically. Plenty of new higher order reflections emerged which indicated a highly complex arrangement of the two different discotic molecules. The transformation of the first equatorial reflection was thereby particularly impressive which converted from the isotropic shape to three sharp peaks implying that the reorganization occurred also intercolumnar and was not limited to single molecules. In order to assign the structure in more detail, the 2D-WAXS patterns of other blend ratios have been investigated as well.

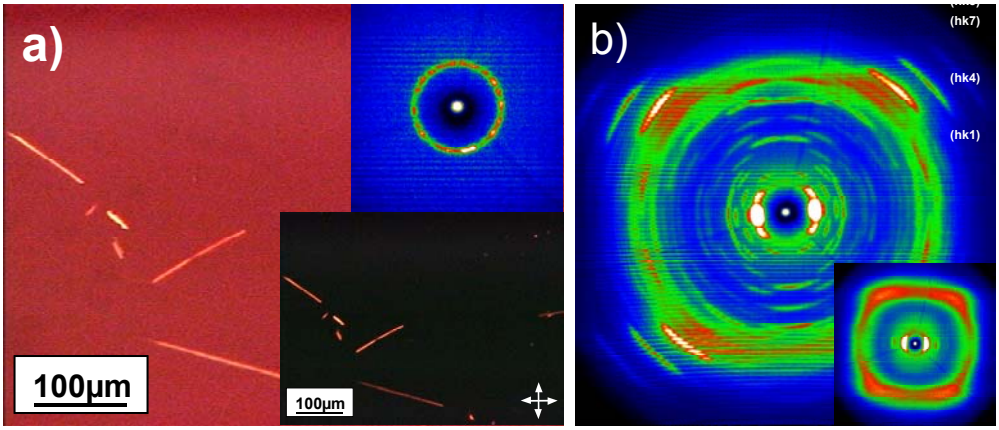

Figure 5.42. a) *POM of the mixture of HBC-$C_{10,6}$ and PDI at a molar ratio of 2-1 at room temperature after cooling from the isotropic phase in cross-polarizers (lower inset: in 45° of the polarizer/analyzer, upper inset: 2D-WAXS pattern of the mixture at room temperature crystallized between two thin aluminum foils, the most essential intermediate 2θ range of 2°-10° is presented), b) 2D-WAXS pattern of the mixture after annealing at ambient conditions for 48hrs (inset: directly after filament extrusion).*

When the molar content of HBC-$C_{10,6}$ in the blend was greaten to 2-1, the degree of homeotropic alignment increased for a sample, prepared under identical conditions as described above, and the number of birefringent defects of the film diminished, (Figure 5.42a), whereas the morphology did not change significantly. The 2D-WAXS pattern in Figure 5.42a confirmed the homeotropic orientation, however, the domains were less ordered than observed for the pure HBC derivatives with homeotropic order. The different domains showed the same hexagonal unit cell which was highly displaced in the lateral plane, but with a uniform packing parameter. But in the same time, the columnar arrangement was consistent

along the surface normal. The isotropization temperature of this sample was determined at 55.7 °C and therefore somewhat higher than for the 1-1 blend.

The 2D-WAXS pattern in Figure 5.42b of the freshly extruded mixture of HBC-$C_{10,6}$ and PDI at a molar composition of 2-1 differed from the pattern for the 1-1 blend. However, after the same annealing time of 48 hours the supramolecular structure improved significantly, too. Interestingly, reflections at the same correlation positions appeared, whereby the intensity between these peaks was different. A similar result was obtained for the mixture at a complementary molar ratio of 1-2 which revealed identical reflections, but of other intensity distribution, after the structural reorganization within the 48hrs (Figure 5.42b). Summarizing the structural results, all three investigated mixtures revealed identical correlation distances in the 2D-WAXS pattern, which differed in intensity. In contrast to the other mixtures, the 1-2 blend showed dendritic textures during crystallization in the optical microscopy, which were at great parts highly birefringent (Figure 5.43a), and a considerably higher isotropization temperature of 150 °C. At few positions the homeotropic alignment could be assumed.

The investigation of mixtures with a much higher content of one compound revealed that the degree of homeotropic order decreased significantly as well as the appearance of the complex supramolecular structure (results not shown). The thermotropic behavior of the mixtures became more similar to the properties of the starting materials, whereas the T_i of the 1-3 blend was still considerably higher than of the pure compounds.

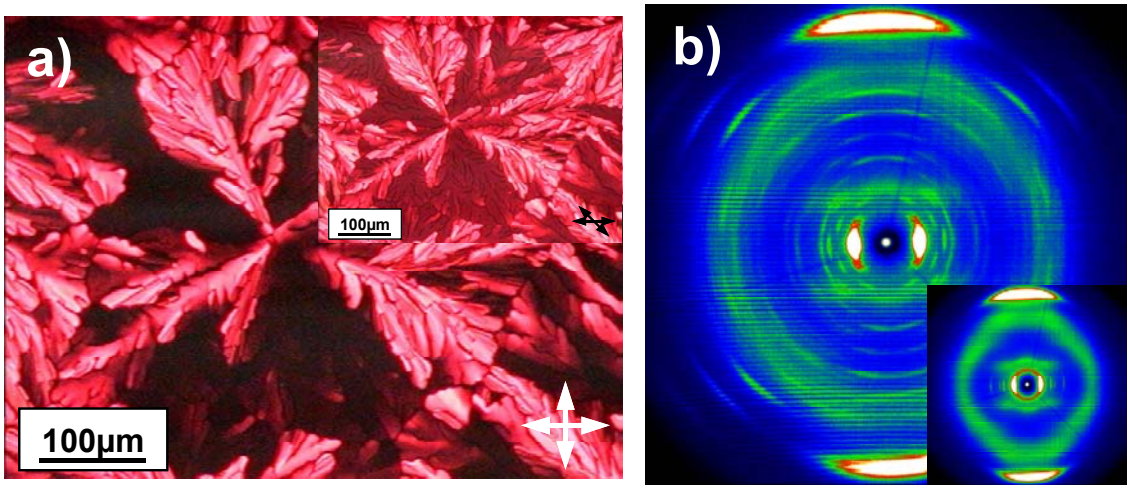

Figure 5.43. *a) Room temperature POM of the mixture of HBC-$C_{10,6}$ and PDI at a molar ratio of 1-2 after cooling from the isotropic phase in cross-polarizers (inset: in 45° of the polarizer/analyzer), b) 2D-WAXS pattern of the mixture after annealing at ambient conditions for 48hrs (inset: directly after filament extrusion).*

The structural comparison of the three presented mixtures gives more insight into the arrangement of the two different discotic molecules. The analysis of the thermal behavior revealed a homogeneous mixture and therefore one can exclude macroscopic phase separation. Nevertheless, the comparison of the 2D-WAXS patterns suggests that the molecules are not fully mixed. The meridional reflection at the corresponding distance of 0.34 nm was assigned to the perylene diimide, whereby the intensity of this peak increased for mixtures with higher PDI content. Furthermore, the off-meridional reflections at an azimuthal angle of ca 40° and a corresponding distance of 0.39 nm were related to the tilting of the HBC-$C_{10,6}$ discs. Accordingly, the new additional reflections indicating the superstructure of the mixture reached their maximum intensity for the 1-1 ratio. The set of new higher order reflections indicated an exceptional long-range order and a complex helical arrangement of the two discotic species within the columnar stacks. The layered distribution of the reflections in the meridional direction in the WAXS pattern in Figure 5.41b is identified by the Miller's indices (hkl) which were assigned to the intracolumnar packing. The nearest intracolumnar repeating distance between single building blocks was 0.34 nm and related to the meridional reflection, which determined the number of 10 molecules per helical pitch, indicating strong correlations over long distances (helical pitch distance 3.4 nm). This corresponds to an identical helical pitch as observed for the B-DNA.[246] The suggested model for the supramolecular arrangement is illustrated in Figure 5.44. It is assumed that an alternating molecular packing gave rise to the helical organization. Thereby, the PDI molecules intercalated between the HBC-discs, which were rotated with respect to each other by 12° providing the necessary contrast for the helical pitch. This molecular rotation was induced by the space demand of the attached alkyl chains in both derivatives.

It is therefore reasonable to conclude that columns consisting of one kind of discotic species do not exist. The columns were created from both type of molecules, whereby the discs were randomly distributed along the columns (at the 1-1 molar ratio alternatingly). Since the 2D-WAXS pattern of all extruded samples revealed reflections at identical positions as observed for the 1:1 blend, but with different reflection intensities, which depended on the composition ratio, one can suggest that homo-sequences of excess components were present in the non-equimolar mixtures. It is important to remember that the dove-tailed HBC derivatives form small stacks in the isotropic state and are not monomeric in the melt. This can be assumed also for the perylene diimide. Therefore, the formation of both homo- and heterosequences in a non-equimolar mixture is a logical consequence. The columnar stacks are formed by both types of molecules leading to different sequence distributions along the columns. Since X-ray diffraction experiments indicated that both compounds HBC-$C_{10,6}$ and the perylene diimide are not monomeric in the isotropic state, but create small stacks, the

preparation of the mixtures in the melt can never result in only an alternating intracolumnar arrangement. Since the positions of the reflections were independent from the blend composition, three different sequences within the columns appeared: sequences consisting of the pure components and the sequence with the alternating organization containing the HBC and perylene molecules in the same ratio. The length of the sequences and the distribution along the columnar structures varied with the composition and determines the reflection intensities. The reflections with the highest intensity related to the helical arrangement appeared for the 1:1 mixture. The superstructure of the mixture became identical to the pure compounds when the content of one component is increased significantly.

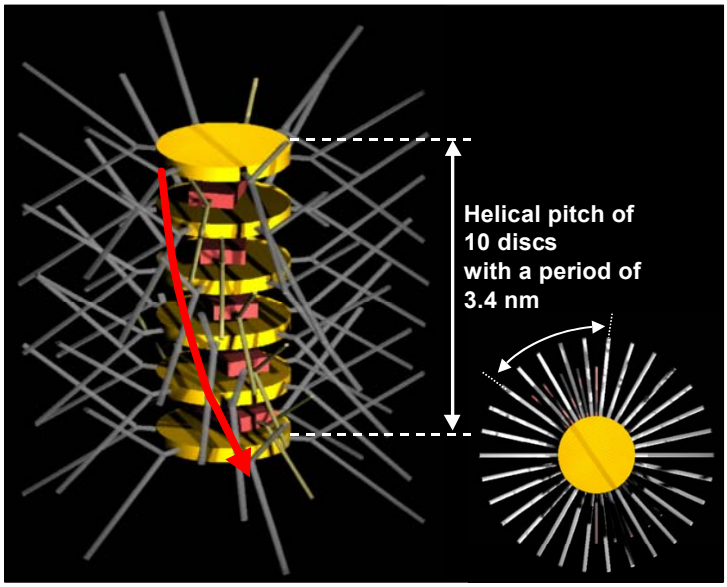

Figure 5.44. Schematic packing model of an alternating intracolumnar arrangement for the binary mixture. The PDI molecules are intercalated between HBC discs which was displaced by 12° with respect to each other leading to the formation of a helical pitch of 3.4 nm.

In order to examine the influence of the core size on the superstructure of the mixture and the alignment effect, mixtures of HBC-$C_{10,6}$ and terrylene diimide were investigated as well. The morphology of blends with a molar composition of 1-1 and 2-1 of HBC-$C_{10,6}$ and terrylene diimide is shown in Figure 5.45. The isotropization temperature for the 1-1 mixture increased to ca 410 °C and to 350 °C for the 2-1 molar ratio (in comparison to the pure materials; the T_i of TDI was 278 °C). After cooling from the isotropic phase down to room temperature, the samples revealed also a homeotropic orientation, whereby the number of defects decreased for the sample with a higher HBC content. The dendritic textures indicate the nucleation and growth of a hexagonal columnar growth. Indeed, the 2D-WAXS pattern of

this mixture as an extruded filament (not shown) revealed discs stacked in a non-tilted manner in the columns which were organized laterally in a hexagonal unit cell with a packing parameter of 2.58 nm. After annealing no superstructure, as in the blends with perylene diimide, could be observed for these samples. Due to the significant shift of the T_i to higher temperatures of the 1-1 mixture it was not possible to prepare the blend in the isotropic state and to investigate the structure by the X-ray scattering. However, by increasing the content of one component, the morphology of the blend changed significantly leading to completely other optical textures.

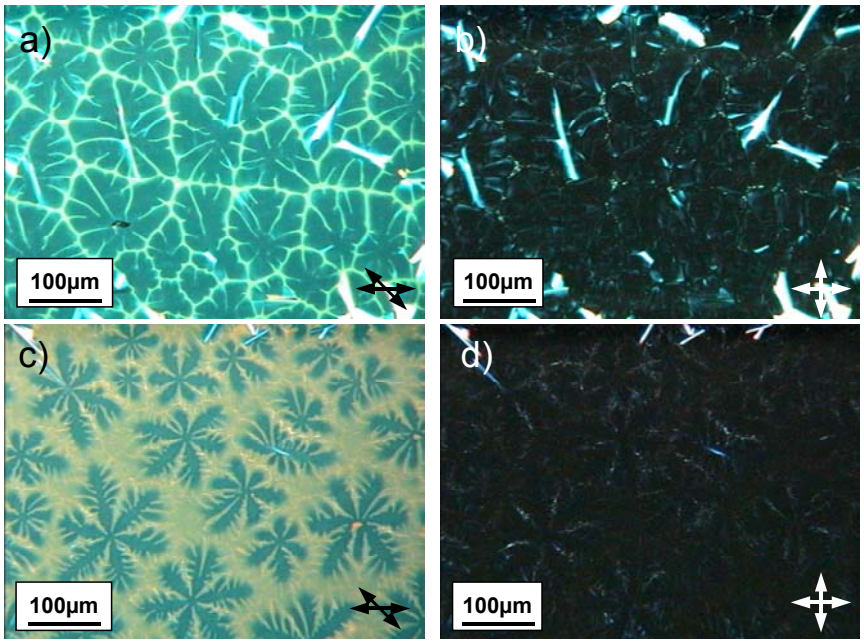

Figure 5.45. *Optical images of the mixture of HBC-$C_{10,6}$ and TDI at a molar ratio of 1-1 at room temperature cooled down at 1 °C/min (a) polarizers at 45° and b) with cross-polarizers), optical images of the mixture of HBC-$C_{10,6}$ and TDI at a molar ratio of 2-1 at room temperature cooled down at 1 °C/min (c) polarizers at 45° and d with cross-polarizers).*

The formation of the homeotropic order for mixtures of discotics is not restricted to blends between discs of different size. This kind of alignment from the isotropic state is also possible for mixtures of HBC derivatives. Thereby, HBC-$C_{10,6}$ was mixed with the "unwrapped" trialkoxy HBC-$(OC_{12})_3$, which created spherulitic structures during crystallization, at a molar composition of 1-1. Despite the appearance of few birefringent defects, the homeotropic orientation was stable down to room temperature which was confirmed again by 2D-WAXS experiments.

The morphology formation during crystallization was also investigated for mixture

containing HC-$C_{14,10}$ instead of HBC-$C_{10,6}$ with the same composition. However, for all discussed blends no homeotropic alignment could be observed. In same cases phase separation occurred.

As summery of the most important results, the space demanding alkyl substituents on the β-dove-tailed HBCs hindered the molecules to approach the surface in a face-on manner, leading to an edge-on orientation (Figure 5.46a). In the mixture, the smaller PDI and TDI, respectively, intercalated between HBC-$C_{10,6}$, and acted as spacer to allow the face-on approach of the aromatic molecule to the surface (Figure 5.46b). For the more space demanding HBC-$C_{14,10}$, the mixture did not form a homeotropic film, since the perylene diimide did not compensate the steric demand of the long 2-decyl-tetradecyl chains, when approaching the surface.

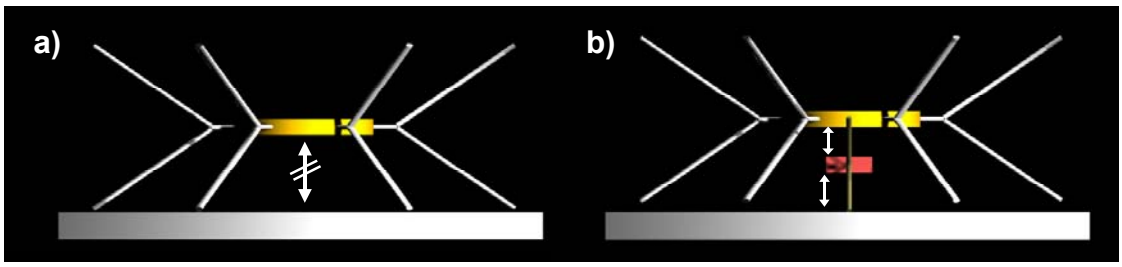

Figure 5.46. *Schematic explanation of the different behavior on surfaces during cooling from the isotropic phase, a) the dove-tailed side chains hinder an approaching of the molecule to the surface, whereas homeotropic order is formed when a perylene molecule intercalates between the surface and the HBC disc.*

In conclusion, it was shown that supramolecular organization in a binary mixture differed strongly from the one of the homo-components. Strictly alternating stacks were formed spontaneously upon cooling from the isotropic state, due to the weak donor-acceptor interactions between the electron rich HBC and the electron poor rylene dyes PDI and TDI. These interactions led to an enormous ordering in the self-organized columnar stacks. The molecules in the mixture revealed a homeotropic orientation, due to an auxiliary effect of the smaller aromatic molecule while forming the first monolayer of the sterically demanding HBCs on the surface. These results confirm the conclusions of the section before that the main driving force are side chains which wet the surface during the self-assembly of the molecules from the isotropic phase. This is the first time that the mechanism for homeotropic alignment of discotic molecules has been discussed and contradicts the conclusions found in literature.[365]

5.4.4. Outlook for TOF Measurements on Homeotropically Aligned Samples

One of the most essential objectives is the relation between the organization of the discotic materials and the charge carrier mobility in order to gain information about their electronic performance. Therefore, the optoelectronic properties of the homeotropically aligned HBC compounds are determined by time-of-flight (TOF) measurements which can be performed dependent on the macroscopic organization to obtain the anisotropy of the mobility, and on the thermal behavior, to relate the intracolumnar order to the charge migration. TOF experiments were reported up to now only for triphenylene derivatives, but without any correlation to the supramolecular alignment of the sample in the cell. In the following an example for TOF measurements on HBC-$C_{16,4}$ at room temperature is described.

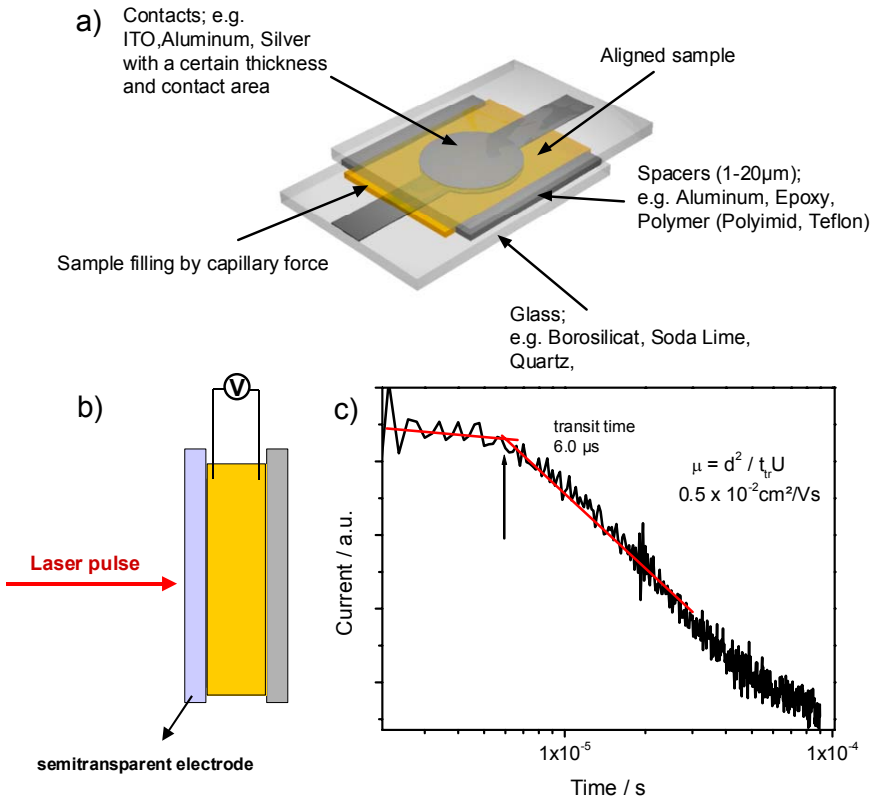

Figure 5.47. *a) Schematic illustration of the ITO cell and b) the experimental set-up for time-of-flight, c) example for characteristic transient time of charges of a homeotropically oriented HBC-$C_{16,4}$ sample at room temperature.*

Before the measurements, special cells were constructed by using glass covered on one side with semitransparent ITO contacts (Figure 5.47a). Glass spheres of ca 5.3 µm in diameter were used as spacers which were distributed uniformly onto one of the ITO glass slides by

spin-coating. Afterwards the second one was carefully placed on top of the distributed glass spheres and the two glass substrates were glued together with epoxy cement. The exact distance between the electrodes was determined by using interference patterns from a typical UV-Vis spectrometer. The electrodes were contacted with silverpaste and thin wires. The compound was filled into the cells by means of capillary forces.[380-382] Therefore, HBC-$C_{16,4}$ was placed at the opening between the ITO pieces, the whole cell was put into a vacuum oven and heated to a temperature of 250 °C, where the compound underwent into the isotropic liquid phase which allowed the cell filling. Afterward the homeotropic alignment was obtained by controlled thermal treatment within a thermally controlled heating stage under nitrogen atmosphere in order to avoid possible degradation of the compound.

Since the charge carriers are rapidly scavenged by oxygen and strictly oxygen free conditions are required for the TOF measurements. Therefore, the measurements were performed in vacuum down to 10^{-4} mbar and indeed experiments at ambient conditions did not shown any success. For photoexcitation of the charge carriers a laser pulse, with a width of 10 ns at a wavelength of 336 nm as a third harmonics, was generated by a YAG nitrogen laser. The laser irradiation at the main absorption band is expected to create electron-hole pairs with a certain quantum yield (Figure 5.47b). Under the influence of an externally applied field at the sample, electrons or holes as the major charge carriers will drift through the sample to the other electrode. This displacement current is recorded by means of a Techtronix oscilloscope.

Figure 5.47c exhibits a typical transient plot for the photogenerated charges at room temperature. In this case the majority of charge carriers were holes, whereas by applying the opposite electric field no electrons was observed. Therefore, this is the first indication that this compound is mainly an n-type semiconductor. The transient plot showed three characteristic regimes. At the beginning of the plot a sharp peak was attributed to the photogeneration by the laser pulse. The drift of the charges through the sample was characterized by a narrow plateau of the photocurrent which decreased at a transit time of 5 μs. By taking into taking account the applied field of 12 V and a film thickness of ca 6 μm it was possible to determine the charge carrier mobility by the following equation:

$$\mu = \frac{d^2}{U \cdot t_{tr}} \qquad (5.1.)$$

which revealed a room temperature mobility of holes along the columnar stacks of 0.5×10^{-2} cm²/Vs. Moreover, the plateau implied a nondispersive transport of charges, and therefore, a relatively low concentration of defects, domain boundaries or significant disorder which could trap the charges. This result became more meaningful with the combination of the structural investigations. Therefore, it is apparent that in the disordered columnar phase, which was

assigned on the basis of the 2D-WAXS experiments, the intracolumnar arrangement of the discotic molecules was high enough to ensure the one-dimensional charge migration along the columnar structures corresponding to a bandlike transport mechanism.

The plateau is followed by slow decline of the photocurrent. This slow decline might indicate that a small number of charges were trapped. Such assumption might be realistic, since the discotic molecules are known to possess in this "high" temperature phase a high degree of lateral and longitudinal mobility within the columns. However, it should be noted that for stressing out the three plot regimes only the current intensity is presented on a logarithmic scale, whereas it is common to show the transients in a double-logarithmic diagram in order to enlarge the plateau and shorten the current decline.

Since, the charge carrier mobility and the transport mechanism are strongly dependent on the evaluated temperature and thermal phase of the compound, it is expected that high mobilities with a more distinct bandlike transport of charges might occur in the low temperature phase of HBC-$C_{16,4}$.

This basic result should be described in relation with other discotic derivatives. Since the charge transport of only triphenylenes was discussed comprehensively in literature, the results for these compounds will be compared. In general, the most essential factors in determining the magnitude of the charge carrier mobility are: the degree of order within the column, the size of the aromatic core and the extent of electronic overlap between adjacent molecules.[218,383] The mobility for triphenylene derivatives in the hexagonal columnar phase increases from 10^{-4} cm²/Vs for a compound substituted by C_{11} alkyl side chains to 10^{-3} cm²/Vs bearing C_5.[384,385] This increase was attributed to the improved intracolumnar order with decreasing side chains length, however the supramolecular order was not investigated in this context. For triphenylenes with shorter side chains mobility as high as 10^{-1} cm²/Vs were even observed. Such high values were correlated with the helical arrangement of the discotic molecules leading to an enhanced molecular orbital overlap. This is an important indication for conclusions related to the organization within columnar superstructures.

Conclusions

In conclusion, the macro- and microscopic properties of the discotic HBC materials can be effectively manipulated by controlling the aggregation. The strong interaction between the aromatic cores leads to the self-assembly into columnar supramolecular structures. By using different peripheral substituents it is possible to reduce this molecular interaction, resulting in a change of the thermal properties, increase of solubility, influence on the charge carrier transport along these columnar structures and control of the morphology. These properties are essential parameters in the design of efficient electronic devices which are based on these organic semi-conducting materials. Therefore, the investigation of the relationship between these parameters is an important issue and is schematically illustrated in Figure 6.1.

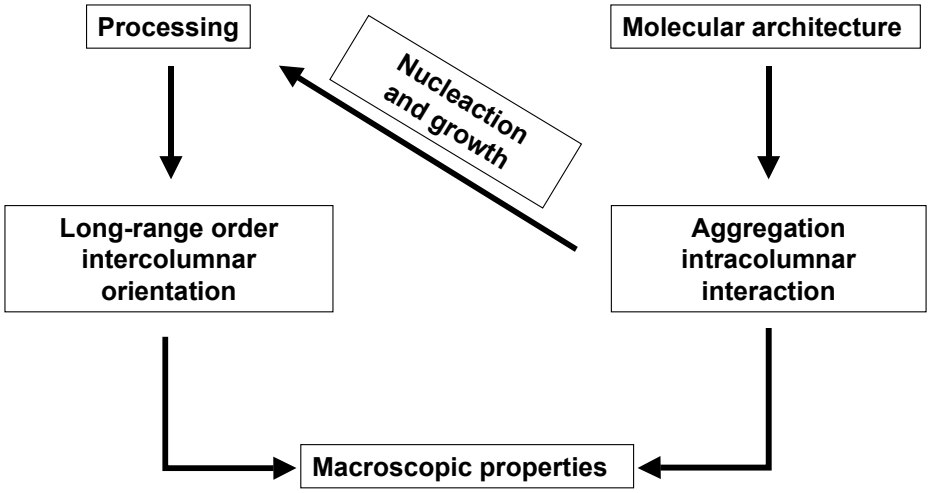

Figure 6.1. *Relation between molecular architecture, processing and the properties of discotic materials based on polycyclic aromatic hydrocarbons.*

The molecular architecture determines the self-aggregation between the single building blocks, and the relation between the π-stacking interaction of the aromatic cores and steric requirement of the side chains controls the bulk properties. The steric demand of the side chains is determined by their volume and their space-filling effect. Thereby, the dove-tailing of long alkyl chains is an effective route to reduce the interaction between the aromatic cores. The modification of the self-aggregation has fundamental consequences onto the solubility, thermal behavior and morphology formation from both solution and the isotropic state. The nucleation and growth of the materials determine the optimal processing conditions. High self-aggregation and pronounced pre-aggregation in solution, leading to the formation of highly anisotropic structures in drop-cast layers, are requirements for the zone-casting method and ensure a processing of long-range ordered surface layers. On the other hand, the reduction

of the interaction between the molecules results in a drastic solubility increase, providing high purity of the material and long half-life times of charge carriers, and in the lowering of the isotropization temperature, which is necessary for the processing from the melt. The morphology formation during crystallization is strongly affected by degree of self-assembly, whereby compounds with high self-aggregation form small domains and the creation of huge spherulitic domains was observed when the self-assembly is slow and modulated. The transfer of this extraordinary growth was impressively demonstrated by the successful alignment along the temperature gradient during the zone-crystallization. Finally, the establishment of the organic materials into electronic devices and their high performance verify the long-range order and uniaxial orientation of the superstructures verifying the high potential for practical applications. Nevertheless, single defects can trap the charges and decrease the device efficiency.

For the first time it was possible to control the self-organization of the HBC derivatives as thin films in sandwich geometries between two polar surfaces. Homeotropic alignment is most likely nucleated at, and grows from, face-on monolayers at surfaces, whereby the steric requirement of the side chains determines the molecular arrangement. Heteroatoms in the side chains increase the affinity of the molecule to glass and aluminum surfaces, but are not a requirement for the alignment. Molecules bearing heteroatoms allowed homeotropic alignment even at fast cooling rates and more significantly, on a single surface, which has till now been unattainable with all-hydrocarbon HBC's. Homogeneous nucleation and growth of non-oriented columns occurs away from the surface in thicker films, and in films of the weakly interacting disks when not sandwiched between two surfaces. Alignment on single surfaces should enable construction of multilayer devices via subsequent processing of additional layers. These two issues, practical processability and control over alignment of charge-carrier pathways connecting large-area flat electrodes (e.g. in solar cells), are essential for the optimal potential application of columnar-type materials in electronic devices.

Experimental Appendix

Structure Analysis

The structure investigation was performed using a two-dimensional wide-angle X-ray scattering (2D-WAXS) setup which is shown schematically in Figure 7.1. The sample was positioned perpendicular to the incident X-ray beam. From the reflection positions in the 2D-WAXS pattern, it is possible to obtain information about the intra- and intercolumnar supramolecular organization. Since the fibers are placed vertically with respect to the incident X-ray beam, the meridional reflections correspond to the correlations resulting from disc stacking and the equatorial reflections distribution provide information about the intercolumnar order.

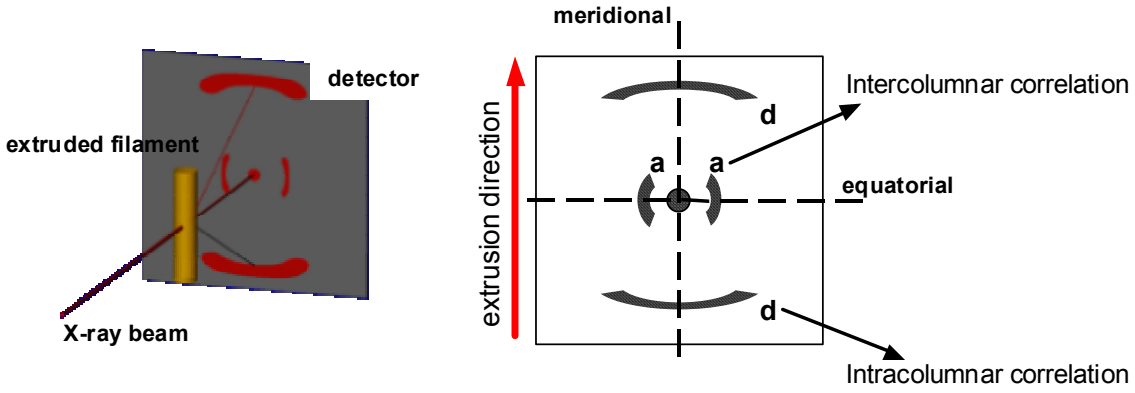

Figure 7.1. *Schematic illustration of the experimental set-up (left) and the characteristic 2D-WAXS pattern of an extruded filament based on discotic molecules (right).*

The 2D-WAXS experiments were performed by means of a rotating anode (Rigaku 18 kW) X-ray beam with a pinhole collimation and a 2D Siemens detector with a beam diameter of ca 1 mm. A double graphite monochromator for the Cu-K_α radiation (λ=0.154 nm) was used.

Large-area X-ray diffraction was performed on a theta-theta Philips PW 1820 Kristalloflex diffractometer with a graphite-monochromized CuK_α X-ray beam of a zone-cast HBC-C_{12} film on a pure glass substrate at room temperature in both casting directions (parallel and perpendicular). The temperature dependent X-ray diffraction measurements were

performed at various temperatures in order to investigate the supramolecular structure of the zone-cast compounds at different phases. A θ-θ Siemens D500 Kristalloflex with a graphite-monochromatized CuK_α X-ray beam was used. The diffraction patterns were recorded in the 2θ range from 1° to 32° and are presented as functions of the scattering vector s; with $s=2\sin\theta/\lambda$ where 2θ is the scattering angle.

High-Resolution Transmission Electron microscopy was carried out on a FEI TECNAI F30 ST at 300 kV under liquid N2 cryo conditions. Electron diffraction was recorded using a Philips CM 12 electron microscope at 120 kV acceleration voltage. In both cases the films were first cast onto a carbon film evaporated onto a glass substrate. Then the HBC-C_{12}/carbon film was removed from the glass using a dilute aqueous HF solution and carefully mounted onto a TEM copper grid.

Other Techniques

Differential scanning calorimetry (DSC) was measured on a Mettler DSC 30 with heating and cooling rates of 10 K/min.

A Zeiss microscope equipped with polarizing filters and equipped with a Hitachi KP-D50 Colour digital CCD camera was used in order to investigate the optical textures of the compounds. The samples were sandwiched between two glass slides or doctor bladed as a film on one glass surface and then thermally treated on a Linkam hotstage fitted with a Linkam TMS 91 temperature controller.

Dynamic mechanical measurements were performed by means of the Rheometric Scientific RMS-800 mechanical spectrometer. Shear deformation was applied under conditions of controlled deformation amplitude, always remaining in the range of the linear viscoelastic response of studied sample. The storage (G') and loss (G'') shear moduli were measured at various temperatures at a frequency of 10 rad/s. A geometry of parallel plates with diameters of 6 mm was used with a gap of about 1 mm between plates (sample thickness). Experiments were performed under dry nitrogen atmosphere.

Atomic force microscopy was performed by using a Nanoscope IIIa MultiMode scanning probe microscope; Digital Instruments, Santa Barbara, CA. For AFM imaging of the zone-cast HBC-C_{12} samples simple glass support was applied.

Optical absorption studies were carried out using a Perkin-Elmer Lambda 800 spectrometer equipped with a Glan-Thomson polarizer.

Field-effect investigations were performed in collaboration with Dr. Anoop Menon and Prof. Henning Sirringhaus, from Plastic Logic in Cambridge, where the HMDS treated Si(n++) / SiO2 wafer were prepared, the substrates were plasma cleaned in an oxygen plasma for 30 seconds. After this, the HMDS was spin-cast at 2000 rpm on the substrate followed by a 30 minute bake at 100 °C. Field-effect transistors were fabricated by zone casting HBC-C12 on a HMDS treated Si(n++) / SiO2 wafer using the procedure described earlier. Source drain contacts were made on top of the HBC films by a shadow mask evaporation, yielding a channel length of 25 μm and a width of 1.6 mm. The gate dielectric is SiO2 with a thickness of 200 nm. All device characteristics were measured at room temperature with a semiconductor parameter analyzer HP 4155B in a glovebox in a dry nitrogen atmosphere (H20 < 1 ppm, O2 < 5 ppm).

References

(1) Dürkop, T.; Getty, S. A.; Cobas, E.; Fuhrer, S. M. *Nanoletters* **2004**, *4*, 35.

(2) Takagi, S.-H.; Toriumi, A.; Iwase, M.; Tango, H. *IEEE Trans. Electron. Devices* **1994**, *41*, 2357.

(3) Chandrasekhar, S.; Sadashiva, B. K.; Suresh, K. A. *Pramana* **1977**, *9*, 471.

(4) Sandquist, H. *Chem. Ber.* **1915**, *48*, 2054.

(5) Chandrasekhar, S.; Ranganath, G. S. *Rep. Prog.* **1990**, *53*, 57.

(6) Buess, C. M.; Lawson, D. D. *Chem. Rev.* **1960**, *60*, 313.

(7) Perez, D.; Guitian, E. *Chem. Soc. Rev.* **2004**, *33*, 274.

(8) Henderson, P.; Kumar, S.; Rego, J. A.; Ringsdorf, H.; Schuhmacher, P. *J. Chem. Soc.-Chem. Com.* **1995**, 1059.

(9) Musgrave, O. C.; Webster, C. J. J. C. S. C., 1397. *J. Chem. Soc. (C)* **1971**, 1397.

(10) Engelkamp, H.; Middelbeek, S.; Nolte, R. J. M. *Science* **1999**, *284*, 785.

(11) Armstrong, N. R. *J. Porphyrins Phthalocyanines* **2000**, *4*, 414.

(12) Vannostrum, C. F.; Picken, S. J.; Schouten, A. J.; Nolte, R. J. M. *J. Am. Chem. Soc.* **1995**, *117*, 9957.

(13) Eichhorn, H. *J. Porphyrins Phthalocyanines* **2000**, *4*, 88.

(14) Gregg, B. A.; Fox, M. A.; Bard, A. J. *J. Chem. Soc.-Chem. Com.* **1987**, 1134.

(15) Shimizu, Y.; Miya, M.; Nagata, A.; Ohta, K.; Matsumura, A.; Yamamoto, I.; Kusabayashi, S. *Chem. Lett.* **1991**, 25.

(16) Watson, M. D.; Fechtenkötter, A.; Müllen, K. *Chem. Rev.* **2001**, *101*, 1267.

(17) Simpson, C. D.; Wu, J.; Watson, M. D.; Müllen, K. *J. Mater. Chem.* **2004**, *14*, 494.

(18) Grimsdale, A. C.; Müllen, K. *Chem. Rec.* **2001**, *1*, 243.

(19) Bushey, M. L.; Nguyen, T.-Q.; Zhang, W.; Horoszewski, D.; Nuckolls, C. *Angew. Chem. Int. Ed.* **2004**, *43*, 5446.

(20) Simpson, C. D. *Dissertation* **2003**, Johannes Gutenberg University, Mainz.

(21) Levelut, A. M. *J. Chem. Phys.* **1983**, *88*, 149.

(22) Levelut, A. M. *J. Phys.Lett. (Paris)* **1979**, *40*, L-81.

(23) Prins, L. J.; Reinhoudt, D. N.; Timmermann, P. *Angew. Chem. Int. Ed.* **2001**, *40*, 2382.

(24) Sherrington, D. C.; Taskinen, K. A. *Chem. Soc. Rev.* **2001**, *30*, 83.

(25) Ky Hirschberg, J. H. K.; Brunsfeld, L.; Ramzi, A.; Vekemans, J. A. J. M.; Sijbesma, R. P.; Meier, E. W. *Nature* **2000**, *407*, 167.

(26) van Gorp, J. J.; Vekemans, J.; Meijer, E. W. *J. Am. Chem. Soc.* **2002**, *124*, 14759.

(27) Gearba, R. I.; Lehmann, M.; Levin, J.; Ivanov, D. A.; Koch, M. H. J.; Barbera, J.; Debije, M. G.; Piris, J.; Geerts, Y. H. *Adv. Mater.* **2003**, *15*, 1614.

(28) Nguyen, T.-Q.; Martel, R.; Avouris, P.; Bushey, M. L.; Brus, L.; Nuckolls, C. *J. Am. Chem. Soc.* **2004**, *126*, 5234.

(29) Würthner, F.; Thalacker, C.; Sautter, A. *Adv. Mater.* **1999**, *11*, 754.

(30) Fischbach, I.; Pakula, T.; Minkin, P.; Fechtenkötter, A.; Müllen, K.; Spiess, H. W.; Saalwachter, K. *J. Phys. Chem. B* **2002**, *106*, 6408.

(31) Wu, J. S.; Watson, M. D.; Zhang, L.; Wang, Z. H.; Müllen, K. *J. Am. Chem. Soc.* **2004**, *126*, 177.

(32) Fontes, E.; Heiney, P. A.; de Jeu, W. H. *Phys. Rev. Lett.* **1988**, *61*, 1202.

(33) Lehmann, M.; Fischbach, I.; Spiess, H. W.; Meier, H. *J. Am. Chem. Soc.* **2003**, *126*, 772.

(34) Fischbach, I.; Ebert, F.; Spiess, H. W.; Schnell, I. *ChemPhysChem* **2004**, *5*, 895.

(35) Piris, J. *Dissertation, Delft University of Technology, the Netherlands* **2004**.

(36) Schouten, P. G.; Warman, J. M.; Dehaas, M. P.; Vannostrum, C. F.; Gelinck, G. H.; Nolte, R. J. M.; Copyn, M. J.; Zwikker, J. W.; Engel, M. K.; Hanack, M.; Chang, Y. H.; Ford, W. T. *J. Am. Chem. Soc.* **1994**, *116*, 6880.

(37) van de Craats, A. M.; Siebbeles, L. D. A.; Bleyl, I.; Haarer, D.; Berlin, Y. A.; Zharikov, A. A.; Warman, J. M. *J. Phys. Chem. B* **1998**, *102*, 9625.

(38) Horowitz, G. *J. Mater. Chem.* **1999**, *9*, 2021.

(39) Warman, J. M.; Van de Craats, A. M. *Mol. Cryst. Liq. Cryst.* **2003**, *396*, 41.

(40) Boden, N.; Bushby, R. J.; Clements, J. *J. Chem. Phys.* **1993**, *98*, 5920.

(41) Boden, N.; Bushby, R. J.; Clements, J.; Movaghar, B.; Donovan, K. J.; Kreouzis, T. *Phys. Rev. B* **1995**, *52*, 13274.

(42) Simmerer, J.; Glusen, B.; Paulus, W.; Kettner, A.; Schuhmacher, P.; Adam, D.; Etzbach, K. H.; Siemensmeyer, K.; Wendorff, J. H.; Ringsdorf, H.; Haarer, D. *Adv. Mater.* **1996**, *8*, 815.

(43) Adam, D.; Schuhmacher, P.; Simmerer, J.; Haussling, L.; Siemensmeyer, K.; Etzbach, K. H.; Ringsdorf, H.; Haarer, D. *Nature* **1994**, *371*, 141.

(44) Adam, D.; Closs, F.; Frey, T.; Funhoff, D.; Haarer, D.; Ringsdorf, H.; Schuhmacher, P.; Siemensmeyer, K. *Phys. Rev. Lett.* **1993**, *70*, 457.

(45) van de Craats, A. M.; Warman, J. M.; Müllen, K.; Geerts, Y.; Brand, J. D. *Adv. Mater.* **1998**, *10*, 36.

(46) van de Craats, A. M.; Warman, J. M. *Adv. Mater.* **2001**, *13*, 130.

(47) vandeCraats, A. M.; Warman, J. M.; deHaas, M. P.; Adam, D.; Simmerer, J.; Haarer, D.; Schuhmacher, P. *Adv. Mater.* **1996**, *8*, 823.

(48) vandeCraats, A. M.; deHaas, M. P.; Warman, J. M. *Synth. Met.* **1997**, *86*, 2125.

(49) Warman, J. M.; Kroeze, J. E.; Schouten, P. G.; van de Craats, A. M. *J. Porphyrins Phthalocyanines* **2003**, *7*, 342.

(50) Ohta, K.; Hatsusaka, K.; Sugibayashi, M.; Ariyoshi, M.; Ban, K.; Maeda, F.; Naito, R.; Nishizawa, K.; van de Craats, A. M.; Warman, J. M. *Mol. Cryst. Liq. Cryst.* **2003**, *397*, 325.

(51) Schouten, P. G.; Chen, W. M.; Warman, J. M.; Dehaas, M. P.; Vanderpol, J. F.; Zwikker, J. W. *Synth. Met.* **1991**, *42*, 2665.

(52) van de Craats, A. M.; Warman, J. M.; Fechtenkötter, A.; Brand, J. D.; Harbison, M. A.; Müllen, K. *Adv. Mater.* **1999**, *11*, 1469.

(53) Seguy, I.; Jolinat, P.; Destruel, P.; Farenc, J.; Mamy, R.; Bock, H. J.; Nguyen, T. P. *J. Appl. Phys.* **2001**, *89*, 5442.

(54) Boden, N.; Bushby, R. J.; Martin, P. S.; Evans, S. D.; Owens, R. W.; Smith, D. A. *Langmuir* **1999**, *15*, 3790.

(55) Haarer, D.; Adam, D.; Simmerer, J.; Closs, F.; Funhoff, D.; Haussling, L.; Siemensmeyer, K.; Ringsdorf, H.; Schuhmacher, P. *Mol. Cryst. Liq. Cryst. Science and Technology Section a-Mol. Cryst. Liq. Cryst.* **1994**, *252*, 155.

(56) Bunning, J. C.; Donovan, K. J.; Kreouzis, T.; Scott, K.; Bushby, R. J.; Boden, N.; Lozman, O. R. *Mol. Cryst. Liq. Cryst.* **2003**, *397*, 563.

(57) Boden, N.; Bushby, R. J.; Cammidge, A. N.; Clements, J.; Luo, R.; Donovan, K. J. *Mol. Cryst. Liq. Cryst.***1995**, *261*, 251.

(58) Tsumura, A.; Koezuka, T. *Appl. Phys. Lett* **1986**, *49*, 1210.

(59) Xu, B.; Fichou, D.; Horowitz, G.; Garnier, F. *Adv. Mater.* **1991**, *3*, 150-153.

(60) Garnier, F.; Horowitz, G.; Peng, X. H.; Fichou, D. *Adv. Mater.* **1990**, *2*, 592.

(61) Dimitrakopoulos, C. D.; Malenfant, P. R. L. *Adv. Mater.* **2002**, *14*, 99.

(62) de Boer, R. W. I.; Gershenson, M. E.; Morpurgo, A. F.; Podzorov, V. *Phys. Stat. Sol.* **2004**, *201*, 1302.

(63) Sundar, V. C.; Zaumseil, J.; Podzorov, V.; Menard, E.; Willett, R. L.; Someya, T.; Gershenson, M. E.; Rogers, J. A. *Science* **2004**, *303*, 1644.

(64) W., W.; Karl, N. *Phys. Rev. B* **1985**, *32*, 1172.

(65) Karl, N.; Martanner, J. *Mol. Cryst. Liq. Cryst.* **2001**, *355*, 149.

(66) Podzorov, V.; Pudalov, V. M.; Gershenson, M. E.; 82. *Appl. Phys. Lett.* **2003**, *82*, 1739.

(67) Takeya, J.; Goldmann, C.; Haas, S.; Pernstich, K. P.; Ketterer, B.; Batlogg, B. *J. Appl. Phys.* **2003**, *94*, 5800.

(68) Nelson, S. F.; Lin, Y.-Y.; Gundlach, D. J.; Jackson, T. N. *Appl. Phys. Lett.* **1998**, *72*, 1854.

(69) Dimitrakopoulos, C.; Purushothaman, S.; Kymissis, J.; Callegari, A.; Shaw, J. M. *Science* **1999**, *283*, 822.

(70) Katz, H. E.; Laquindanum, J. G.; Lovinger, A. J. *Chem. Mater.* **1998**, *10*, 633.

(71) Sirringhaus, H.; Friend, R. H.; Li, X. C.; Moratti, S. C.; Holmes, A. B.; Feeder, N. *Appl. Phys. Lett.* **1997**, *71*, 3871.

(72) Dimitrakopoulos, C. D.; Furman, B. K.; Graham, T.; Hegde, S.; Purushothaman, S. **1998**, *92*, 47.

(73) Guillaud, G.; Simon, J. *Chem. Phys. Lett.* **1994**, *219*, 123.

(74) Bao, Z.; Lovinger, A. J.; Dodabalapur, A. *Appl. Phys. Lett.* **1996**, *69*, 3066.

(75) Bao, Z. N.; Lovinger, A. J.; Dodabalapur, A. *Adv. Mater.* **1997**, *9*, 42.

(76) Fuchigami, H.; Tsumura, A.; Koezuka, H. *Appl. Phys. Lett.* **1993**, *63*, 1372.

(77) Sirringhaus, H.; Tessler, N.; Friend, H. R. *Synth. Met.* **1999**, *102*, 857.

(78) Blodgett, K. B. *J. Am. Chem. Soc.* **1935**, *57*, 1007.

(79) Langmuir, I. *J. Am. Chem. Soc.* **1917**, *39*, 1848.

(80) Blodgett, K. B.; Langmuir, I. *Phys. Rev.* **1937**, *51*, 964.

(81) Bj¢rnholm, T.; Greve, D. R.; Reitzel, N.; Hassenkam, T.; Kjaer, K.; Howes, P. B.; Larsen, N. B.; B¢gelund, J.; Jayaraman, M.; Ewbank, P. C.; McCullough, R. D. *J. Am. Chem. Soc.* **1998**, *120*, 7643.

(82) Paloheimo, J.; Stubb, H.; Yli-Lahti, P.; Dyreklev, P.; Inganäs, O. *Thin Solid Films* **1992**, *210/211*, 283.

(83) Xu, G.; Bao, Z.; Groves, J. T. *Langmuir* **2000**, *16*, 1834.

(84) Li, C.; Imae, T. *Langmuir* **2003**, *19*, 779.

(85) da Silva, A. M. G.; Viseu, M. I.; Romao, R. I. S.; Costa, S. M. B. *Phys. Chem. Chem. Phys.* **2002**, *4*, 4754.

(86) Viseu, M. I.; da Silva, A. M. G.; Antunes, P.; Costa, S. M. B. *Langmuir* **2002**, *18*, 5772.

(87) Qian, D. J.; Nakamura, C.; Miyake, J. *Thin Solid Films* **2001**, *397*, 266.

(88) Richardson, T. H.; Dooling, C. M.; Worsfold, O.; Jones, L. T.; Kato, K.; Shinbo, K.; Kaneko, F.; Treggoning, R.; Vysotsky, M. O.; Hunter, C. A. *Thin Solid Films* **2001**, *393*, 259.

(89) Tronin, A.; Strzalka, J.; Kneller, L. R.; Chen, X.; Blasie, J. K.; Dutton, P. L. *Biophys. J.* **2000**, *78*, 284A.

(90) Ni, Y. H.; Puthenkovilakom, R. R.; Huo, Q. *Langmuir* **2004**, *20*, 2765.

(91) Zhang, Z. J.; Lal Verma, A.; Nakashima, K.; Yoneyama, M.; Iriyama, K.; Ozaki, Y. *Thin Solid Films* **1998**, *326*, 211.

(92) Mindyuk, O. Y.; Heiney, P. A. *Adv. Mater.* **1999**, *11*, 341.

(93) Mertesdorf, C.; Ringsdorf, H. *Liq. Cryst.* **1989**, *5*, 1757.

(94) Shutt, J. D.; Batzel, D. A.; Sudiwala, R. V.; Rickert, S. E.; Kenney, M. E. *Langmuir* **1988**, *4*, 1240.

(95) Valkova, L. A.; Shabyshev, L. S.; Borovkov, N. Y.; Feigin, L. A.; Rustichelli, F. *J. Inclusion Phenom. Macrocyclic Chem.* **1999**, *35*, 243.

(96) Fouriaux, S.; Armand, F.; Araspin, O.; RuaudelTeixier, A.; Maya, E. M.; Vazquez, P.; Torres, T. *J. Phys. Chem.* **1996**, *100*, 16984.

(97) Fukui, M.; Katayama, N.; Ozaki, Y.; Araki, T.; Iriyama, K. *Chem. Phys. Lett.* **1991**, *177*, 247.

(98) Mohammed, M. A.; Ottenbreit, P.; Prass, W.; Schnurpfeil, G.; Wohrle, D. *Thin Solid Films* **1992**, *213*, 285.

(99) Nakahara, H.; Sun, K. Z.; Fukuda, K. *J. Mater. Chem.* **1995**, *5*, 395.

(100) Cook, J. M. *J. Mater. Chem.* **1996**, *6*, 677.

(101) Cook, M. J.; McMurdo, J.; Miles, D. A.; Poynter, R. H.; Simmons, J. M.; Haslam, S. D.; Richardson, R. M.; Welford, K. *J. Mater. Chem.* **1994**, *4*, 1205.

(102) Bryant, G. C.; Cook, M. J.; Ruggiero, C.; Ryan, T. G.; Thorne, A. J.; Haslam, S. D.; Richardson, R. M. *Thin Solid Films* **1994**, *243*, 316.

(103) Zhou, S. Q.; Liu, Y. Q.; Qiu, W. F.; Xu, Y.; Huang, X. B.; Li, Y. S.; Jiang, L.; Zhu, D. B. *Adv. Funct. Mater.* **2002**, *12*, 65.

(104) Liu, Y. Q.; Hu, W. P.; Xu, Y.; Liu, S. G.; Zhu, D. B. *J. Phys. Chem. B* **2000**, *104*, 11859.

(105) Armand, F.; Cabezon, B.; MartinezDiaz, M. V.; RuaudelTeixier, A.; Torres, T. *J. Mater. Chem.* **1997**, *7*, 1741.

(106) Tans, S. J.; Miedema, R.; Geerligs, L. J.; Dekker, C.; Wu, J.; Wegner, G. *Synth. Met.* **1997**, *84*, 733.

(107) Ferencz, A.; Armstrong, N. R.; Wegner, G. *Macromolecules* **1994**, *27*, 1517.

(108) Gattinger, P.; Rengel, H.; Neher, D.; Gurka, M.; Buck, M.; van de Craats, A. M.; Warman, J. M. *J. Phys. Chem. B* **1999**, *103*, 3179.

(109) Silerova, R.; Kalvoda, L.; Neher, D.; Ferencz, A.; Wu, J.; Wegner, G. *Chem. Mater.* **1998**, *10*, 2284.

(110) Smolenyak, P.; Peterson, R.; Nebesny, K.; Torker, M.; O'Brien, D. F.; Armstrong, N. R. *J. Am. Chem. Soc.* **1999**, *121*, 8628.

(111) Smolenyak, P. E.; Osburn, E. J.; Chen, S. Y.; Chau, L. K.; Obrien, D. F.; Armstrong, N. R. *Langmuir* **1997**, *13*, 6568.

(112) Osburn, E. J.; Chau, L. K.; Chen, S. Y.; Collins, N.; Obrien, D. F.; Armstrong, N. R. *Langmuir* **1996**, *12*, 4784.

(113) Zangmeister, R. A. P.; O'Brien, D. F.; Armstrong, N. R. *Adv. Funct. Mater.* **2002**, *12*, 179.

(114) Donley, C. L.; Xia, W.; Minch, B. A.; Zangmeister, R. A. P.; Drager, A. S.; Nebesny, K.; O'Brien, D. F.; Armstrong, N. R. *Langmuir* **2003**, *19*, 6512.

(115) Bourgoin, J. P.; Doublet, F.; Palacin, S.; Vandevyver, M. *Langmuir* **1996**, *12*, 6473.

(116) Granito, C.; Goldenberg, L. M.; Bryce, M. R.; Monkman, A. P.; Troisi, L.; Pasimeni, L.; Petty, M. C. *Langmuir* **1996**, *12*, 472.

(117) Xiao, K.; Liu, Y. Q.; Huang, X. B.; Xu, Y.; Yu, G.; Zhu, D. B. *J. Phys. Chem. B* **2003**, *107*, 9226.

(118) Locklin, J.; Shinbo, K.; Onishi, K.; Kaneko, F.; Bao, Z. N.; Advincula, R. C. *Chem. Mater.* **2003**, *15*, 1404.

(119) Liu, Y. Q.; Hu, W. P.; Qiu, W. F.; Xu, Y.; Zhou, S. Q.; Zhu, D. B. *Sensors Actuators B* **2001**, *80*, 202.

(120) Hu, W. P.; Liu, Y. Q.; Xu, Y.; Liu, S. G.; Zhou, S. Q.; Zhu, D. B. *Synth. Met.* **1999**, *104*, 19.

(121) Hu, W. P.; Liu, Y. Q.; Xu, Y.; Liu, S. G.; Zhou, S. Q.; Zeng, P. J.; Ben Zhu, D. *Sensors Actuators B* **1999**, *56*, 228.

(122) Tsukruk, V. V.; Wendorff, J. H.; Karthaus, O.; Ringsdorf, H. *Langmuir* **1993**, *9*, 614.

(123) Karthaus, O.; Ringsdorf, H.; Tsukruk, V. V.; Wendorff, J. H. *Langmuir* **1992**, *8*, 2279.

(124) Vandevyver, M.; Albouy, P. A.; Mingotaud, C.; Perez, J.; Barraud, A.; Karthaus, O.; Ringsdorf, H. *Mol. Cryst. Liq. Cryst.***1993**, *234*, 333.

(125) Maliszewskyj, N. C.; Heiney, P. A.; Josefowicz, J. Y.; McCauley, J. P.; Smith, A. B. *Science* **1994**, *264*, 77.

(126) Josefowicz, J. Y.; Maliszewskyj, N. C.; Idziak, S. H. J.; Heiney, P. A.; McCauley, J. P.; Smith, A. B. *Science* **1993**, *260*, 323.

(127) Gidalevitz, D.; Mindyuk, O. Y.; Heiney, P. A.; Ocko, B. M.; Henderson, P.; Ringsdorf, H.; Boden, N.; Bushby, R. J.; Martin, P. S.; Strzalka, J.; McCauley, J. P.; Smith, A. B. *J. Phys. Chem. B* **1997**, *101*, 10870.

(128) Henderson, P.; Beyer, D.; Jonas, U.; Karthaus, O.; Ringsdorf, H.; Heiney, P. A.; Maliszewskyj, N. C.; Ghosh, S. S.; Mindyuk, O. Y.; Josefowicz, J. Y. *J. Am. Chem. Soc.* **1997**, *119*, 4740.

(129) Vaes, A.; Van der Auweraer, M.; De Schryver, F. C.; Laguitton, B.; Jonas, A. *Langmuir* **1998**, *14*, 5250.

(130) Maliszewskyj, N. C.; Heiney, P. A.; Josefowicz, J. Y.; Plesnivy, T.; Ringsdorf, H.; Schuhmacher, P. *Langmuir* **1995**, *11*, 1666.

(131) Janietz, D.; Festag, R.; Schmidt, C.; Wendorff, J. H. *Liq. Cryst.* **1996**, *20*, 459.

(132) Tsukruk, V. V.; Bengs, H.; Ringsdorf, H. *Langmuir* **1996**, *12*, 754.

(133) Janietz, D.; Festag, R.; Schmidt, C.; Wendorff, J. H.; Tsukruk, V. V. *Thin Solid Films* **1996**, *285*, 289.

(134) Wittman, J. C.; Smith, P. *Nature* **1991**, *352*, 414.

(135) Tanigaki, N.; Kyotani, H.; Wada, M.; Kaito, A.; Yoshida, Y.; Han, E. M.; Abe, K.; Yase, K. *Thin*

Solid Films **1998**, *331*, 229.

(136) Damman, P.; Fougnies, C.; Dosiere, M.; Wittmann, J. C. *Macromolecules* **1995**, *28*, 8272.

(137) Schafer, O.; Greiner, A.; Pommerehne, J.; Guss, W.; Vestweber, H.; Tak, H. Y.; Bassler, H.; Schmidt, C.; Lussem, G.; Schartel, B.; Stumpflen, V.; Wendorff, J. H.; Spiegel, S.; Moller, C.; Spiess, H. W. *Synth. Met.* **1996**, *82*, 1.

(138) Novillo, F. A.; Fujita, M.; Tsuji, M.; Kohjiya, S. *Sen-I Gakkaishi* **1998**, *54*, 544.

(139) Wittmann, J. C.; Meyer, S.; Damman, P.; Dosiere, M.; Schmidt, H. W. *Polymer* **1998**, *39*, 3545.

(140) Tanigaki, N.; Yoshida, Y.; Kyotani, H.; Kaito, A.; Yase, K. *Kobunshi Ronbunshu* **2002**, *59*, 623.

(141) Gao, X.; Liu, R. G.; Yu, Y.; Jin, M.; Bus, H. S. *Journal of Polymer Science Part B-Polymer Physics* **2004**, *42*, 296.

(142) Mathieu, C.; Thierry, A.; Wittman, J. C.; Lotz, B. *J Polym Sci: Part B, Polym Phys* **2000**, *38*, 3088.

(143) Zhang, Y.; Katoh, T.; Endo, A. *J. Phys. Chem. B* **2000**, *104*, 6212.

(144) Tanabe, K.; Shiojiri, M. *Dyes and Pigments* **1997**, *34*, 121.

(145) Tanaka, T.; Matsuoka, M. *Thin Solid Films* **2001**, *393*, 148.

(146) Wittmann, J. C.; Straupe, C.; Meyer, S.; Lotz, B.; Lang, P.; Horowitz, G.; Garnier, F. *Thin Solid Films* **1998**, *333*, 272.

(147) Gill, R. E.; Hadziioannou, G.; Lang, P.; Garnier, F.; Wittmann, J. C. *Adv. Mater.* **1997**, *9*, 331.

(148) Lang, P.; Horowitz, G.; Valat, P.; Garnier, F.; Wittmann, J. C.; Lotz, B. *J. Phys. Chem. B* **1997**, *101*, 8204.

(149) Wittmann, J. C.; Straupe, C.; Meyer, S.; Lotz, B.; Lang, P.; Horowitz, G.; Garnier, F. *Thin Solid Films* **1997**, *311*, 317.

(150) Wittmann, J. C.; Straupe, C.; Meyer, S.; Lotz, B.; Lang, P.; Horowitz, G.; Garnier, F. *Thin Solid Films* **1997**, *303*, 207.

(151) Brinkmann, M.; Graff, S.; Straupe, C.; Wittmann, J. C.; Chaumont, C.; Nuesch, F.; Aziz, A.; Schaer, M.; Zuppiroli, L. *J. Phys. Chem. B* **2003**, *107*, 10531.

(152) Ofuji, M.; Inaba, K.; Omote, K.; Hoshi, H.; Takanishi, Y.; Ishikawa, K.; Takezoe, H. *Japan. J. Appl. Phys. Part 1* **2003**, *42*, 7520.

(153) Brinkmann, M.; Wittmann, J. C.; Barthel, M.; Hanack, M.; Chaumont, C. *Chem. Mater.* **2002**, *14*, 904.

(154) Nakamura, M.; Matsunobe, T.; Tokumoto, H. *J. Appl. Phys.* **2001**, *89*, 7860.

(155) Chen, X. L.; Lovinger, A. J.; Bao, Z. N.; Sapjeta, J. *Chem. Mater.* **2001**, *13*, 1341.

(156) Nagamatsu, S.; Takashima, W.; Kaneto, K.; Yoshida, Y.; Tanigaki, N.; Yase, K. *Macromolecules* **2003**, *36*, 5252.

(157) Nagamatsu, S.; Tanigaki, N.; Yoshida, Y.; Takashima, W.; Yase, K.; Kaneto, K. *Synth. Met.* **2003**, *137*, 923.

(158) Nagamatsu, S.; Takashima, W.; Kaneto, K.; Yoshida, Y.; Tanigaki, N.; Yase, K. *Appl. Phys. Lett.* **2004**, *84*, 4608.

(159) Saito, T.; Ueda, Y.; Harada, K.; Fukunishi, K. *Mol. Cryst. Liq. Cryst.* **2003**, *407*, 553.

(160) Cuminal, M. P.; Touhari, F.; Brunet, M.; Cohen-Solal, G. *Mol. Cryst. Liq. Cryst.***1999**, *333*, 181.

(161) Campanelli, E.; Faetti, S.; Nobili, N. *Eur. Phys. J. E* **2003**, *11*, 199.

(162) Lester, G.; Hanmer, J.; Coles, H. *Mol. Cryst. Liq. Cryst.* **1995**, *262*, 149.

(163) Mallon, J. J.; Adams, P. M. *Mol. Cryst. Liq. Cryst.* **1992**, *213*, 173.

(164) Zimmermann, S.; Wendorff, J. H.; Weder, C. *Chem. Mater.* **2002**, *14*, 2218.

(165) Ge, J. J.; Li, C. Y.; Xue, G.; Mann, I. K.; Zhang, D.; Wang, S. Y.; Harris, F. W.; Cheng, S. Z. D.; Hong, S. C.; Zhuang, X. W.; Shen, Y. R. *J. Am. Chem. Soc.* **2001**, *123*, 5768.

(166) Neuber, C.; Giesa, R.; Schmidt, H. W. *Adv. Funct. Mater.* **2003**, *13*, 387.

(167) Borzsonyi, T.; Akamatsu, S. *Phys. Rev. E* **2002**, *66*.

(168) Sirringhaus, H.; Wilson, R. J.; Friend, H. R.; Inbasekaran, M.; Wu, W.; Woo, E. P.; Grell, M.; Bradley, D. D. C. *Appl. Phys. Lett.* **2000**, *77*, 406.

(169) Sirringhaus, H.; Kawase, T.; Friend, H. R.; Shimoda, T.; Inbasekaran, M.; Wu, W.; Woo, E. P. *Nature* **2000**, *290*, 2123.

(170) Lovinger, A. J.; Gryte, C. C. *Macromolecules* **1976**, *9*, 247.

(171) Schulze, G. E. W.; Naujeck, T. R. *Colloid Polym. Sci.***1991**, *269*, 695.

(172) Pawlak, A.; Piorkowska, E. *Colloid Polym. Sci.***2001**, *279*, 939.

(173) Peev, N. S. *Crystl. Res. Technol.* **1986**, *21*, 319.

(174) Peev, N. S.; Tairov, Y. M.; Smirnova, N. A.; Kalnin. *Crystl. Res. Technol.* **1987**, *22*, 783.

(175) Liu, C. Y.; Bard, A. J. *Chem. Mater.* **2000**, *12*, 2353.

(176) Burda, L.; Tracz, A.; Pakula, T.; Ulanski, J.; Kryszewski, M. *J. Phys. D: Appl. Phys.* **1983**, *16*, 1737.

(177) Tracz, A.; Jeszka, J. K.; Kryszewski, M.; Shafee, E. E. *Mater. Sci.***1988**, *14*, 181.

(178) Matsushita, S.; Miwa, T.; Fujishima, A. *Langmuir* **1997**, *13*, 2582.

(179) Yagi, Y.; Matsushita, S. I.; Tryk, D. A.; Koda, T.; Fujishima, A. *Langmuir* **2000**, *16*, 1180.

(180) Reitzel, N.; Hassenkam, T.; Balashev, K.; Jensen, T. R.; Howes, P. B.; Kjaer, K.; Fechtenkötter, A.; Tchebotareva, N.; Ito, S.; Müllen, K.; Bjornholm, T. *Chem. Eur. J.* **2001**, *7*, 4894.

(181) Kubowicz, S.; Thunemann, A. F.; Geue, T. M.; Pietsch, U.; Watson, M. D.; Tchebotareva, N.; Müllen, K. *Langmuir* **2003**, *19*, 10997.

(182) Kubowicz, S.; Pietsch, U.; Watson, M. D.; Tchebotareva, N.; Müllen, K.; Thunemann, A. F. *Langmuir* **2003**, *19*, 5036.

(183) Thüneman, A. F.; Ruppelt, D.; S., I.; Müllen, K. *J. Mater. Chem.* **1999**, *9*, 1055.

(184) Laursen, B. W.; Norgaard, K.; Reitzel, N.; Simonsen, J. B.; Nielsen, C. B.; Als-Nielsen, J.; Bjornholm, T.; Solling, T. I.; Nielsen, M. M.; Bunk, O.; Kjaer, K.; Tchebotareva, N.; Watson, M. D.; Müllen, K.; Piris, J. *Langmuir* **2004**, *20*, 4139.

(185) van de Craats, A. M.; Stutzmann, N.; Bunk, O.; Nielsen, M. M.; Watson, M.; Müllen, K.; Chanzy, H. D.; Sirringhaus, H.; Friend, R. H. *Adv. Mater.* **2003**, *15*, 495.

(186) Piris, J.; Debije, M. G.; Stutzmann, N.; van de Craats, A. M.; Watson, M. D.; Müllen, K.; Warman, J. M. *Adv. Mater.* **2003**, *15*, 1736.

(187) Bunk, O.; Nielsen, M. M.; Solling, T. I.; van de Craats, A. M.; Stutzmann, N. *J. Am. Chem. Soc.* **2003**, *125*, 2252.

(188) Schmidt-Mende, L.; Watson, M.; Müllen, K.; Friend, R. H. *Mol. Cryst. Liq. Cryst.***2003**, *396*, 73.

(189) Schmidt-Mende, L.; Fechtenkötter, A.; Müllen, K.; Friend, R. H.; MacKenzie, J. D. *Physica E* **2002**, *14*, 263.

(190) Schmidt-Mende, L.; Fechtenkötter, A.; Müllen, K.; Moons, E.; Friend, R. H.; MacKenzie, J. D. *Science* **2001**, *293*, 1119.

(191) Petritsch, K.; Friend, R. H.; Lux, A.; Rozenberg, G.; Moratti, S. C.; Holmes, A. B. *Synth. Met.* **1999**, *102*, 1776.

(192) Kim, J. Y.; Bard, A. J. *Chem. Phys. Lett.* **2004**, *383*, 11.

(193) Fechtenkötter, A.; Tchebotareva, N.; Watson, M.; Müllen, K. *Tetrahedron* **2001**, *57*, 3769.

(194) Herwig, P.; Kayser, C. W.; Müllen, K.; Spiess, H. W. *Adv. Mater.* **1996**, *8*, 510.

(195) Liu, C. Y.; Fechtenkötter, A.; Watson, M. D.; Müllen, K.; Bard, A. J. *Chem. Mater.* **2003**, *15*, 124.

(196) Kastler, M. - *private communication*.

(197) Fechtenkötter, A.; Saalwachter, K.; Harbison, M. A.; Müllen, K.; Spiess, H. W. *Angew. Chem. Int. Ed.* **1999**, *38*, 3039.

(198) Samori, P.; Fechtenkötter, A.; Jackel, F.; Bohme, T.; Müllen, K.; Rabe, J. P. *J. Am. Chem. Soc.* **2001**, *123*, 11462.

(199) Kastler, M.; Wasserfallen, D. - *private communication*.

(200) Kastler, M.; Pisula, W.; Wasserfallen, D.; Pakula, T.; Müllen, K. *J. Am. Chem. Soc.* 2005, *127*, 4268.

(201) Pisula, W.; Tomovic; El Hamaoui, B.; Watson, M. D.; Pakula, T.; Müllen, K. *Adv. Funct. Mater.* **- in press**.

(202) Wang, Z. H.; Watson, M. D.; Wu, J. S.; Müllen, K. *ChemComm.* **2004**, 336.

(203) Iyer, V. S.; Yoshimura, K.; Enkelmann, V.; Epsch, R.; Rabe, J. P.; Müllen, K. *Angew. Chem. Int. Ed.* **1998**, *37*, 2696.

(204) Simpson, C. D. *Dissertation, Johannes Gutenberg Universität* **2004**.

(205) Tomovic, Z.; Watson, M. D.; Müllen, K. *Angew. Chem. Int. Ed.* **2004**, *43*, 755.

(206) Tomovic, Z. - *private communication*.

(207) Nolde, F.; Kohl, C. - *private communication*.

(208) Lukaschek, M.; Grabowski, D. A.; Schmidt, C. *Langmuir* **1995**, *11*, 3590.

(209) Liu, L.; Singh, M.; John, V. T.; McPherson, G. L.; He, J.; Agarwal, V.; Bose, A. *J. Am. Chem. Soc.* **2004**, *126*, 2276.

(210) Tokita, M.; Tokunaga, K.; Funaoka, S.; Osada, K.; Watanabe, J. *Macromolecules* **2004**, *37*, 2527.

(211) Ramos, L.; Molino, F.; Porte, G. *Langmuir* **2000**, *16*, 5846.

(212) Allen, M. T.; Harris, K. D. M.; Kariuki, B. M.; Kumari, N.; Preece, J. A.; Diele, S.; Lose, D.; Hegmann, T.; Tschierske, C. *Liq. Cryst.* **2000**, *27*, 689.

(213) Allen, M. T.; Diele, S.; Harris, K. D. M.; Hegmann, T.; Kariuki, B. M.; Lose, D.; Preece, J. A.; Tschierske, C. *J. Mater. Chem.* **2001**, *11*, 302.

(214) Warman, J. M.; Schouten, P. G. *J. Phys. Chem.* **1995**, *99*, 17181.

(215) Ban, K.; Nishizawa, K.; Ohta, K.; de Craats, A. M. V.; Warman, J. M.; Yamamoto, I.; Shirai, H. *J. Mater. Chem.* **2001**, *11*, 321.

(216) van de Craats, A. M.; Warman, J. M. *Synth. Met.* **2001**, *121*, 1287.

(217) Crispin, X.; Cornil, A.; Friedlein, R.; Okudaira, K. K.; Lemaur, V.; Crispin, A.; Kestemont, G.; Lehmann, M.; Fahlman, M.; Lazzaroni, R.; Geerts, Y.; Wendin, G.; Ueno, N.; Bredas, J. L.; Salaneck, W. R. *J. Am. Chem. Soc.* **2004**, *126*, 11889.

(218) Lemaur, V.; Da Silva Filho, D. A.; Coropceanu, V.; Lehmann, M.; Geerts, Y.; Piris, J.; Debije, M. G.; Van de Craats, A. M.; Senthilkumar, K.; Siebbeles, L. D. A.; Warman, J. M.; Bredas, J. L.; Cornil, J. *J. Am. Chem. Soc.* **2004**, *126*, 3271.

(219) Gray, G. W.; Winsor, P. A. *Liq. Cryst. & Plastic Crystals*; Ellis Horwood: Chichester, 1974; Vol. 1.

(220) Ungar, G. *Polymer* **1993**, *34*, 2050.

(221) Glusen, B.; Heitz, W.; Kettner, A.; Wendorff, J. H. *Liq. Cryst.* **1996**, *20*, 627.

(222) Glusen, B.; Kettner, A.; Wendorff, J. H. *Mol. Cryst. Liq. Cryst.* **1997**, *303*, 115.

(223) Hindmarsh, P.; Hird, M.; Styring, P.; Goodby, J. W. *J. Mater. Chem.* **1993**, *3*, 1117.

(224) Kurihara, S.; Nonaka, T. *Mol. Cryst. Liq. Cryst.* **1994**, *238*, 39.

(225) Ohta, K.; Watanabe, T.; Tanaka, S.; Fujimoto, T.; Yamamoto, I.; Bassoul, P.; Kucharczyk, N.; Simon, J. *Liq. Cryst.* **1991**, *10*, 357.

(226) Gurek, A. G.; Ahsen, V.; Heinemann, F.; Zugenmaier, P. *Mol. Cryst. Liq. Cryst.* **2000**, *338*, 75.

(227) Schouten, P. G.; Vanderpol, J. F.; Zwikker, J. W.; Drenth, W.; Picken, S. J. *Mol. Cryst. Liq. Cryst.* **1991**, *195*, 291.

(228) Tant, J. *Dissertation, Universite Libre de Bruxelles, Belgium* **2004**.

(229) Warman, J. M.; de Haas, M. P.; Dicker, G.; Grozema, F. C.; Piris, J.; Debije, M. G. *Chem. Mater.* **2004**, *1^6*, 4600.

(230) Brunsveld, L.; Folmer, B. J. B.; Meijer, E. W.; Sijbesma, R. P. *Chem. Rev.* **2001**, *101*, 4071.

(231) Suarez, M.; Lehn, J.-M.; Zimmermann, S. C.; Skoulios, A.; Heinrich, B. *J. Am. Chem. Soc.* **1998**, *120*, 9526.

(232) Kleppinger, R.; Lillya, C. P.; Yang, C. M. *J. Am. Chem. Soc.* **1997**, *119*, 4097.

(233) Lee, C. J.; Lee, S. J.; Chang, J. Y. *Tetrahedron Lett.* **2002**, *43*, 3863.

(234) Kübel, C. *Dissertation, Johannes Gutenberg Universität* **1998**.

(235) Brand, J. D. *Dissertation, Johannes Gutenberg Universität* **2000**.

(236) Brand, J. D.; Kubel, C.; Ito, S.; Müllen, K. *Chem. Mater.* **2000**, *12*, 1638.

(237) Brown, S. P.; Schnell, I.; Brand, J. D.; Müllen, K.; Spiess, H. W. *Phys. Chem. Chem. Phys.* **2000**, *2*, 1735.

(238) Kastler, M.; Pisula, W.; Wasserfallen, D.; Pakula, T.; Müllen, K. *J. Am. Chem. Soc.* **2005**, *127*, 4268.

(239) Tchebotareva, N. *Dissertation, Johannes Gutenberg Universität* **2003**.

(240) Tchebotareva, N.; Yin, X. M.; Watson, M. D.; Samori, P.; Rabe, J. P.; Müllen, K. *J. Am. Chem. Soc.* **2003**, *125*, 9734.

(241) Rego, J. A.; Kumar, S.; Dmochowski, I. J.; Ringsdorf, H. *ChemComm.* **1996**, 1031.

(242) Rego, J. A.; Kumar, S.; Ringsdorf, H. *Chem. Mater.* **1996**, *8*, 1402.

(243) Cross, S. J.; Goodby, J. W.; Hall, A. W.; Hird, M.; Kelly, S. M.; Toyne, K. J.; Wu, C. *Liq. Cryst.* **1998**, *25*, 1.

(244) McKeown, N. B.; Leznoff, C. C.; Richardson, R. M.; Cherodian, A. S. *Mol. Cryst. Liq. Cryst.* **1992**, *213*, 91.

(245) Corsellis, E. A.; Coles, H. J.; McKeown, N. B.; Weber, P.; Guillon, D.; Skoulios, A. *Liq. Cryst.* **1997**, *23*, 475.

(246) Watson, J. D.; Crick, F. H. *Nature* **1953**, *171*, 737.

(247) Brunsfeld, L.; Lohmeijer, B. G. G.; Vekemans, J.; Meijer, E. W. *Journal of Inclusion Phenomena and*

Macrocyclic Chemistry **2001**, *41*, 61.

(248) Nuckolls, C.; Katz, T. J.; Castellanos, J. *J. Am. Chem. Soc.* **1996**, *118*, 3767.

(249) Nuckolls, C.; Katz, T. J.; Verbiest, T.; Van Elshocht, S.; Kuball, H. G.; Kiesewalter, S.; Lovinger, A. J.; Persoons, A. *J. Am. Chem. Soc.* **1998**, *120*, 8656.

(250) Nuckolls, C.; Katz, T. J. *J. Am. Chem. Soc.* **1999**, *121*, 79.

(251) Katz, T. J. *Angew. Chem. Int. Ed.* **2000**, *39*, 1921.

(252) Cuccia, L. A.; Lehn, J.-M.; Homo, J.-C.; Schmutz, M. *Angew. Chem. Int. Ed.* **2000**, *39*, 233.

(253) Fox, J. M.; Katz, T. J.; Van Elshocht, S.; Verbiest, T.; Kauranen, M.; Persoons, A.; Thongpanchang, T.; Krauss, T.; Brus, L. *J. Am. Chem. Soc.* **1999**, *121*, 3453.

(254) van Nostrum, C. F.; Picken, S. J.; Nolte, R. J. M. *Angew. Chem., Int. Ed. Engl.* **1994**, *33*, 2173.

(255) Green, M. M.; Peterson, N. C.; Sato, T.; Teramoto, A.; Lifson, S. *Science* **1995**, *268*, 1860.

(256) Palmans, A. R. A.; Vekemans, J. A. J. M.; Havinga, E. E.; Meijer, E. W. *Angew. Chem., Int. Ed. Engl.* **1997**, *36*, 2648.

(257) Brunsveld, L.; Schenning, A. P. H. J.; Broeren, M. A. C.; Janssen, H. M.; Vekemans, J. A. J. M.; Meijer, E. W. *Chem. Lett.* **2002**, 292.

(258) Schenning, A. P. H. J.; Jonkheijm, P.; Peeters, E.; Meijer, E. W. *J. Am. Chem. Soc.* **2001**, *123*, 409.

(259) Würthner, F.; Chen, Z.; Hoeben, F. J. M.; Osswald, P.; You, C.-C.; Jonkheijm, P.; v. Herrikhuyzen, J.; Schenning, A. P. H. J.; van der Schoot, P. P. A. M.; Meijer, E. W.; Beckers, E. H. A.; Meskers, S. C. J.; Janssen, R. A. J. *J. Am. Chem. Soc.* **2004**, *126*, 10611.

(260) Brunsveld, L.; Lohmeijer, B. G. G.; Vekemans, J.; Meijer, E. W. *ChemComm.* **2000**, 2305.

(261) Green, M. M.; Ringsdorf, H.; Wagner, J.; Wustefeld, R. *Angew. Chem. Int. Ed.* **1990**, *29*, 1478.

(262) van Nostrum, C. F.; Bosman, A. W.; Gelinck, G. H.; Schouten, P. G.; Warman, J. M.; Kentgens, A. P. M.; Devillers, M. A. C.; Meijerink, A.; Picken, S. J.; Sohling, U.; Schouten, A.-J.; Nolte, R. J. M. *Chem. Eur. J.* **1995**, *1*, 171.

(263) Clar, E. *Ber. Dtsch. Chem. Ges.* **1936**, *69*, 607.

(264) Fischbach, I.; Ebert, F.; Spiess, H. W.; Schnell, I. *Chemphyschem* **2004**, *5*, 895.

(265) Goodby, J. W. *J. Mater. Chem.* **1991**, *1*, 307.

(266) Voigtmartin, I. G.; Garbella, R. W.; Schumacher, M. *Liq. Cryst.* **1994**, *17*, 775.

(267) Voigtmartin, I. G.; Durst, H.; Brzezinski, V.; Krug, H.; Kreuder, W.; Ringsdorf, H. *Angew. Chem. Int. Ed.* **1989**, *28*, 323.

(268) Barbera, J.; Cavero, E.; Lehmann, M.; Serrano, J.-L.; Sierra, T.; Vazquez, J. T. *J . Am. Chem. Soc.* **2003**, *125*, 4527.

(269) Wu, J. H.; Watson, M. D.; Müllen, K. *Angew. Chem. Int. Ed.* **2003**, *42*, 5329.

(270) Percec, V.; Glodde, M.; Bera, T. K.; Miura, Y.; Shiyanovskaya, I.; Singer, K. D.; Balagurusamy, V. S. K.; Heiney, P. A.; Schnell, I.; Rapp, A.; Spiess, H. W.; Hudson, S. D.; Duan, H. *Nature* **2002**, *419*, 384.

(271) Percec, V.; Ahn, C. H.; Ungar, G.; Yeardley, D. J. P.; Möller, M.; Sheiko, S. S. *Nature* **1998**, *391*, 161.

(272) Iribarren, I.; Aleman, C.; Bou, J. J.; MunozGuerra, S. *Macromolecules* **1996**, *29*, 4397.

(273) Hobson, R. J.; Windle, A. H. *Polymer* **1993**, *34*, 3582.

(274) Liu, J.; Geil, P. H. *J. Poly. Sci.Part B - Poly. Phys.*, *35*, 1575.

(275) Shenhar, R.; Wang, H.; Hoffman, R. E.; Frish, L.; Avram, L.; Willner, I.; Rajca, A.; Rabinovitz, M. *J. Am. Chem. Soc.* **2002**, *124*, 4685.

(276) Terekhov, D. S.; Nolan, K. J. M.; McArthur, C. R.; Leznoff, C. C. *J. Org. Chem.* **1996**, *61*, 3034.

(277) Hindmarsh, P.; Watson, M. J.; Hird, M.; Goodby, J. W. *J. Mater. Chem.* **1995**, *5*, 2111.

(278) Zhao, D. H.; Moore, J. S. *Chem.Comm.* **2003**, 807.

(279) Zhao, D. H.; Moore, J. S. *J. Org. Chem.***2002**, *67*, 3548.

(280) Tobe, Y.; Utsumi, N.; Kawabata, K.; Nagano, A.; Adachi, K.; Araki, S.; Sonoda, M.; Hirose, K.; Naemura, K. *J. Am. Chem. Soc.* **2002**, *124*, 5350.

(281) Phillips, K. E. S.; Katz, T. J.; Jockusch, S.; Lovinger, A. J.; Turro, N. J. *J. Am. Chem. Soc.* **2001**, 11899.

(282) Nakamura, K.; Okubo, H.; Yamaguchi, M. *Org. Lett.* **2001**, *3*, 1097.

(283) Kano, K.; Fukuda, K.; Wakami, H.; Nishiyabu, R.; Pasternack, R. F. *J. Am. Chem. Soc.* **2000**, *122*, 7494.

(284) Schutte, W. J.; Sluytersrehbach, M.; Sluyters, J. H. *J. Phys. Chem.* **1993**, *97*, 6069.

(285) Law, W. F.; Lui, K. M.; Ng, D. K. P. *J. Mater. Chem.* **1997**, *7*, 2063.

(286) Nguyen, T. Q.; Bushey, M. L.; Brus, L. E.; Nuckolls, C. *J. Am. Chem. Soc.* **2002**, *124*, 15051.

(287) Klok, H.-A.; Jolliffe, K. A.; Schauer, C. L.; Prins, L. J.; Spatz, J. P.; Möller, M.; Timmermann, P.; Reinhoudt, D. N. *J. Am. Chem. Soc.* **1999**, *121*, 7154.

(288) Jonkheijm, P.; Hoeben, F. J. M.; Kleppinger, R.; van Herrikhuyzen, J.; Schenning, A.; Meijer, E. W. *J. Am. Chem. Soc.* **2003**, *125*, 15941.

(289) Tracz, A.; Wostek, D.; Kucinska, I.; Jeszka, J. K.; Watson, M.; Müllen, K.; Pakula, T. *In NATO Advanced Study Institute Series; Graja, A., Bu³ka, . R., Kajzar, F., Eds., Kluwer:, Dordrecht, 2002: p. 315*.

(290) Goddard, R.; Haenel, M. W.; Herndon, W. C.; Krüger, C.; Zander, M. *J. Am. Chem. Soc.* **1995**, *117*, 30.

(291) Breiby, D. W.; Bunk, O.; Pisula, W.; Sølling, T. I.; Tracz, A.; Nielsen, M. M.; Pakula, T.; Müllen, K. -

submitted.

(292) Whang, D.; Jin, S.; Lieber, C. M. *Nano Lett.* **2003**, *3*, 951.

(293) Stamou, D.; Musil, C.; Ulrich, W.-P.; Leufgen, K.; Padeste, C.; David, C.; Gobrecht, J.; Duschl, C.; Vogel, H. *Langmuir* **2004**, *20*, 3495.

(294) Curtis, M. D.; Cao, J.; Kampf, J. W. *J. Am. Chem. Soc.* **2004**, *126*, 4318.

(295) Kroeze, J. E.; Savenije, T. J.; Vermeulen, M. J. W.; Warman, J. M. *J. Phys. Chem. B* **2003**, *107*, 7696.

(296) Grozema, F. C.; Savenije, T. J.; Vermeulen, M. J. W.; Siebbeles, L. D. A.; Warman, J. M.; Meisel, A.; Neher, D.; Nothofer, H.-G.; Scherf, U. *Adv. Mat.* **2001**, *13*, 1627.

(297) Piris, J.; Debije, M. G.; Stutzmann, N.; Laursen, B. W.; Pisula, W.; Watson, M. D.; Bjornholm, T.; Müllen, K.; Warman, J. M. *Adv. Funct. Mater.* **2004**, *14*, 1053.

(298) Horowitz, G. *Adv. Mater.* **1998**, *10*, 365.

(299) Zangmeister, R. A. P.; Smolenyak, P. E.; Drager, A. S.; O'Brien, D. F.; Armstrong, N. R. *Langmuir* **2001**, *17*, 7071.

(300) Sirringhaus, H.; Wilson, R. J.; Friend, R. H.; Inbasekaran, M.; Wu, W.; Woo, E. P.; Grell, M.; Bradley, D. D. C. *Appl. Phys. Lett* **2000**, *77*, 406.

(301) George, A. J.; Ajayaghosh, A.; Jonkheijm, P.; Schenning, A. P. H. J.; Meijer, E. W. *Angew. Chem. Int. Ed.* **2004**, *43*, 3421.

(302) Jonkheijm, P.; Miura, A.; Zdanowska, M.; Hoeben, F. J. M.; De Feyter, S.; Schenning, A. P. H. J.; De Schryver, F. C.; Meijer, E. W. *Angew. Chem. Int. Ed.* **2004**, *43*, 74.

(303) Hill, J. P.; Jin, W.; Kosaka, A.; Fukushima, T.; HIchihara, I.; Shimomura, T.; Ito, K.; Hashizume, T.; Ishii, N.; Aida, T. *Science* **2004**, *304*, 1481.

(304) Tada, H.; Touda, H.; Takada, M.; Matsushige, K. *J. Porphyrins Phthalocyanines* **1999**, *3*, 667.

(305) Clarisse, C.; Riou, M.-T. *J. Appl. Phys.* **1991**, *69*, 3324.

(306) Chwang, A. B.; Frisbie, C. D. *J. Appl. Phys.* **2001**, *90*, 1342.

(307) Chwang, A. B.; Frisbie, C. D. *J. Phys. Chem. B* **2000**, *104*, 12202.

(308) Leufgena, M.; Bassa, U.; Muckb, T.; Borzenkoa, T.; Schmidta, G.; Geurtsa, J.; Wagnerb, V.; Molenkampa, L. W. *Synth. Met.* **2004**, *146*, 341.

(309) Monobe, H.; Kiyohara, K.; Terasawa, N.; Heya, M.; Awazu, K.; Shimizu, Y. *Adv. Funct. Mater.* **2003**, *13*, 919.

(310) Monobe, H.; Kiyohara, K.; Heya, M.; Awazu, K.; Shimizu, Y. *Mol. Cryst. Liq. Cryst.* **2003**, *397*, 359.

(311) Shetty, A. S.; Zhang, J. S.; Moore, J. S. *J. Am. Chem. Soc.* **1996**, *118*, 1019.

(312) Luz, Z.; Poupko, R.; Wachtel, E. J.; Zimmermann, H.; Bader, V. *Mol. Cryst. Liq. Cryst.* **2003**, *397*, 367.

(313) Jonkheijm, P.; Hoeben, F. J. M.; Klappinger, R.; van Herrikhuyzen, J.; Schenning, A. P. H. J.; Meijer, E. W. *J. Am. Chem. Soc.* **2003**, *125*, 15941.

(314) Leclere, P.; Surin, M.; Viville, P.; Lazzaroni, R.; Kilbinger, A. F. M.; Henze, O.; Feast, W. J.; Cavallini, M.; Biscarini, F.; Schenning, A. P. H. J.; Meijer, E. W. *Chem. Mater.* **2004**, *16*, 4452.

(315) Banach, M. J.; Friend, R. H.; Sirringhaus, H. *Macromolecules* **2004**, *37*, 6079.

(316) Deman, A.-L.; Tardy, J.; Nicolas, Y.; Blanchard, P.; Roncali, J. *Synth. Met.* **2004**, *146*, 365.

(317) Schoonvald, W. A.; Stok, R. W.; Weijmans, J. W.; Vrijmoeth, J.; Wildeman, J.; Klapwijk, T. M. *Synth. Met.* **1997**, *84*, 583.

(318) Pinto, J. - *private communication, Cavendish Laboratory, Cambridge*.

(319) Wang, Y.; Zhou, Y. Q.; Wang, X. P.; Chen, W. Q.; Xi, S. Q. *J. Chem. Soc.-Chem. Com.* **1992**, 873.

(320) Iverson, I. K.; Casey, S. M.; Seo, W.; Tam-Chang, S. W.; Pindzola, B. A. *Langmuir* **2002**, *18*, 3510.

(321) Pakula, T.; Saijo, K.; Kawai, H.; Hashimoto, T. *Macromolecules* **1985**, *18*, 1294.

(322) Jung, H.-T.; Kim, S. O.; Ko, Y. K.; Yoon, D. K.; Hudson, S. D.; Percec, V.; Holerca, M. N.; Cho, W.-D.; Mosier, P. E. *Macromolecules* **2002**, *35*, 3717.

(323) Engel, M. K.; Bassoul, P.; Bosio, L.; Lehmann, H.; Hanack, M.; Simon, J. *Liq. Cryst.* **1993**, *15*, 709.

(324) Collard, D. M.; Lillya, C. P. *J. Org. Chem.* **1991**, *56*, 6064.

(325) van der Pol, J. F.; Neeleman, E.; Zwikker, J. W.; Nolte, R. J. M.; Drenth, W.; Aerts, J.; Visser, R.; Picken, S. J. *Liq. Cryst.* **1989**, *6*, 577.

(326) Sleven, J.; Cardinaels, T.; Binnemans, K.; Nelis, D.; Müllens, J.; Hinz-Hubner, D.; Meyer, G. *Liq. Cryst.* **2003**, *30*, 143.

(327) Sleven, J.; Cardinaels, T.; Binnemans, K.; Guillon, D.; Donnio, B. *Liq. Cryst.* **2002**, *29*, 1425.

(328) Collard, D. M.; Lillya, C. P. *J. Am. Chem. Soc.* **1991**, *113*, 8577.

(329) Collard, D. M.; Lillya, C. P. *J. Am. Chem. Soc.* **1989**, *111*, 1829.

(330) Hutter, J. L.; Bechhoefer, J. *J. Crystal Growth* **2000**, *217*, 332.

(331) Bushey, M. L.; Hwang, A.; Stephens, P. W.; Nuckolls, C. *J. Am. Chem. Soc.* **2001**, *123*, 8157.

(332) Boden, N.; Bushby, R. J.; Cooke, G.; Lozman, O. R.; Lu, Z. B. *J. Am. Chem. Soc.* **2001**, *123*, 7915.

(333) Hamley, I. W.; Castelletto, V.; Castillo, R. V.; Müller, A. J.; Martin, C. M.; Pollet, E.; Dubois, P. *Macromolecules* **2005**, *38*, 463.

(334) Lei, Y.-G.; Chan, C.-M.; Wang, Y.; Ng, K.-M.; Jiang, Y.; Lin, L. *Polymer* **2003**, *44*, 4673.

(335) Beekmans, L. G. M.; van der Meer, D. W.; Vancso, G. J. *Polymer* **2002**, *43*, 1887.

(336) Liu, J.; Zhang, F.; He, T. *Macromol. Rapid Commun.* **2001**, *22*, 1340.

(337) Lindsell, W. E.; Preston, P. N.; Seddon, J. M.; Rosair, G. M.; Woodman, T. A. *J. Mater. Chem.* **2000**, *12*, 1572.

(338) Weng, X.; Li, C. Y.; Jin, S.; Zhang, D.; Zhang, J. Z.; Bai, F.; Harris, F. W.; Cheng, S. Z. D. *Macromolecules* **2002**, *35*, 9678.

(339) Thomas, B. N.; Lindemann, C. M.; Corcoran, R. C.; Cotant, C. L.; Kirsch, J. E.; Persichini, P. J. *J . Am. Chem. Soc.* **2002**, *124*, 1227.

(340) Imai, H.; Oaki, Y. *Angew. Chem. Int. Ed.* **2004**, *43*, 1363.

(341) Oaki, Y.; Imai, H. *J. Am. Chem. Soc.* **2004**, *126*, 9271.

(342) Kim, W. J.; Yang, S. M. *Adv. Mater.* **2003**, *13*, 1191.

(343) Schultz, J. M. *Polymer* **2003**, *44*, 433.

(344) Xu, J.; Guo, B.-H.; Zhang, Z.-M.; Zhou, J.-J.; Jiang, Y.; Yan, S.; Li, L.; Wu, Q.; Chen, G.-Q.; Schultz, J. M. *Macromolecules* **2004**, *37*, 4118.

(345) Beekmans, L. G. M.; Vancso, G. J. *Polymer* **2000**, *41*, 8975.

(346) Li, L.; Chan, C.-M.; Yeung, K. L.; Li, J.-X.; Ng, K.-M.; Lei, Y. *Macromolecules* **2001**, *34*, 316.

(347) Asano, T.; Imaizumi, K.; Tohyama, N.; Yoshida, S. *J. Macromol. Sci.-Phys.* **2004**, *B43*, 639.

(348) Pawlak, A.; Piorkowska, E. *Colloid Polym.Sci.* **2001**, *279*, 939.

(349) Motomatsu, M.; Nie, H. Y.; Mizutani, W.; Tokumoto, H. *Polymer* **1996**, *37*, 183.

(350) Steinhart, M.; Wendorff, J. H.; Greiner, A.; Wehrspohn, R. B.; Nielsch, K.; Schilling, J.; Choi, J.; Gösele, U. *Science* **2002**, *296*, 1997.

(351) Cepak, V. M.; Martin, C. R. *Chem. Mater.* **1999**, *11*, 1363.

(352) Moon, S. I.; McCarthy, T. J. *Macromolecules* **2003**, *36*, 4253.

(353) Steinhart, M.; Senz, S.; Wehrspohn, R. B.; Gösele, U.; Wendorff, J. H. *Macromolecules* **2003**, *36*, 3646.

(354) Donovan, K. J.; Kreouzis, T.; Scott, K.; Bunning, J. C.; Bushby, R. J.; Boden, N.; Lozman, O. R.; Movaghar, B. *Mol. Cryst. Liq. Cryst.* **2003**, *396*, 91.

(355) Milne, W. I.; Teo, K. B. K.; Amaratunga, G. A. J.; Legagneux, P.; Gangloff, L.; Schnell, J.-P.; Semet, V.; Thien Binh, V.; Groening, O. *J. Mater. Chem.* **2004**, *14*, 933.

(356) Gangloff, L.; Minoux, E.; Teo, K. B. K.; Vincent, P.; Semet, V. T.; Binh, V. T.; Yang, M. H.; Bu, I. Y. Y.; Lacerda, R. G.; Pirio, G.; Schnell, J. P.; Pribat, D.; Hasko, D. G.; Amaratunga, G. A. J.; Milne, W. I.; Legagneux, P. *Nano Letters* **2004**, *4*, 1575.

(357) Teo, K. B. K.; Lee, S.-B.; Chhowalla, M.; Semet, V.; Thien Binh, V.; Groening, O.; Castignolles, M.; Loiseau, A.; Pirio, G.; Legagneux, P.; Pribat, D.; Hasko, D. G.; Ahmed, H.; Amaratunga, G. A. J.; Milne, W. I. *Nanotechnology* **2003**, *14*, 204.

(358) Lee, S. J.; Ho, S. H.; Park, K.-M.; Kim, H.; Zin, W.-C.; M.-G., C.; Kim, K. *Chem. Mater.* **1998**, *10*,

1889.

(359) Keinan, E.; Kumar, S.; Moshenberg, R.; Ghirlando, R.; Wachtel, E. J. *Adv. Mater.* **1991**, *3*, 251.

(360) Murayama, E. *Polymer Preprints Japan* **2002**, *51*, 460.

(361) Bengs, H.; Karthaus, O.; Ringsdorf, H.; Baehr, C.; Ebert, M.; Wendorff, J. H. *Liq. Cryst.* **1991**, *10*, 161.

(362) Castella, M.; Lopez-Calahorra, F.; Velasco, D. *Liq. Cryst.* **2002**, *29*, 559.

(363) Terasawa, N.; Monobe, H.; Kiyohara, K.; Shimizu, Y. *Chem. Comm.* **2003**, 1678.

(364) Cammidge, A. N.; Gopee, H. *J. Mater. Chem.* **2001**, *11*, 2773.

(365) Hatsusaka, K.; Ohta, K.; Yamamoto, I.; Shirai, H. *J. Mater. Chem.* **2001**, *11*, 423.

(366) Ito, S.; Wehmeier, M.; Brand, J. D.; Kubel, C.; Epsch, R.; Rabe, J. P.; Müllen, K. *Chem.Eur.J.* **2000**, *6*, 4327.

(367) Friedlein, R.; Crispin, X.; Simpson, D.; Watson, M. D.; Jäckel, F.; Osikowicz, W.; Marciniak, S.; Jong, M. P. d.; Samori, P.; Jönsson, S. K. M.; Fahlman, M.; Müllen, K.; Rabe, J. P.; Salaneck, W. R. *Phys. Rev. B* **2003**, *68*, 195414.

(368) Samori, P.; Keil, M.; Friedlein, R.; Birgerson, J.; Watson, M.; Müllen, K.; Salaneck, W. R.; Rabe, J. P. *J. Phys. Chem. B* **2001**, *105*, 11114.

(369) Scott, R. L. *J. Chem Phys.* **1949**, *17*, 279.

(370) Boden, N.; Bushby, R. J.; Lu, Z. B.; Lozman, O. R. *Liq. Cryst.* **2001**, *28*, 657.

(371) Arikainen, E. O.; Boden, N.; Bushby, R. J.; Lozman, O. R.; Vinter, J. G.; Wood, A. *Angew. Chem. Int. Ed.* **2000**, *39*, 2333.

(372) Wegewijs, B. R.; Siebbeles, L. D. A.; Boden, N.; Bushby, R. J.; Movaghar, B.; Lozman, O. R.; Liu, Q.; Pecchia, A.; Mason, L. A. *Phys. Rev. B* **2002**, *65*.

(373) Pecchia, A.; Lozman, O. R.; Movaghar, B.; Boden, N.; Bushby, R. J.; Donovan, K. J.; Kreouzis, T. *Phys. Rev. B* **2002**, *65*.

(374) Park, L. Y.; Hamilton, D. G.; McGehee, E. A.; McMenimen, K. A. *J. Am. Chem. Soc.* **2003**, *125*, 10586.

(375) Langhals, H.; Yürük, I. R. O. *Tetrahedron* **2000**, *56*, 5435.

(376) Struijk, C. W.; Sieval, A. B.; Dakhorst, J. E. J.; van Dijk, M.; Kimkes, P.; Koehorst, R. B. M.; Donker, H.; Schaafsma, T. J.; Picken, S. J.; van de Craats, A. M.; Warman, J. M.; Zuilhof, H.; Sudholter, E. J. R. *J. Am. Chem. Soc.* **2000**, *122*, 11057.

(377) Liu, S.-G.; Sui, G.; Cormier, R. A.; Leblanc, R. M.; Gregg, B. A. *J. Phys. Chem. B* **2002**, *106*, 1307.

(378) O'Neill, M.; Kelly, M. *Adv. Mater.* **2003**, *15*, 1135.

(379) Malenfant, P. R. L.; Dimitrakopoulos, C. D.; Gelorme, J. D.; Kosbar, L. L.; Graham, T. O.; Curioni, A.; Andreoni, W. *Appl. Phys. Lett.* **2002**, *80*, 2517.

(380) Liu, C. Y.; Pan, H. L.; Tang, H. J.; Fox, M. A.; Bard, A. J. *J. Phys. Chem.* **1995**, *99*, 7632.

(381) Liu, C.-Y.; Bard, A. J. *J. Am. Chem. Soc.* **1998**, *120*, 5575.

(382) Liu, C.-Y.; Bard, A. J. *Acc. Chem. Res* **1999**, *32*, 235.

(383) Cornil, J.; Lemaur, V.; Calbert, J. P.; Bredas, J. L. *Adv. Mater.* **2002**, *14*, 726.

(384) Bengs, H.; Closs, F.; Frey, T.; Funhoff, D.; Ringsdorf, H.; Siemensmeyer, K. *Liq. Cryst.* **1993**, *15*, 565.

(385) Kreouzis, T.; Scott, K.; Donovan, K. J.; Boden, N.; Bushby, R. J.; Lozman, O. R.; Liu, Q. *Chem. Phys.* **2000**, *262*, 489.

List of Publications & Presentations

1. J. Piglowski, M. Trelinska-Wazlak, I. Gancarz, W. Pisula, *Structure and properties of polyamide-6/isotactic poly(propylene) blends compatibilized with reactive copolymers based on polyethylene,* Applied Macromolecular Chemistry and Physics *269*, 61, **1999**

2. W. Pisula, J. Piglowski, C. Kummerlöwe, *Preparation and characterization of copolyesters of poly(tetramethylene succinate) and poly(butylenes terephthalate),* Polymery, accepted, **2005**

3. A. Tracz, J. K. Jeszka, M. D. Watson, W. Pisula, K. Müllen, T. Pakula, *Uniaxial alignment of the columnar super-structure of a hexa (alkyl) hexa-peri-hexabenzocoronene on untreated glass by simple solution processing,* Journal of the American Chemical Society *125*, 1682, **2003**

4. J. Piris, W. Pisula, A. Tracz, T. Pakula, K. Müllen J. M. Warman, *Thermal Switching of the Optical Anisotropy in a Macroscopically Aligned Film of a Discotic Liquid Crystal,* Liquid Crystals *31*, 993, **2004**

5. W. Pisula, M. Kastler, D. Wasserfallen, T. Pakula, K. Müllen, *Exceptionally Long-Range Self-Assembly of Hexa-peri-hexabenzocoronene with Dove-Tailed Alkyl Substituents,* Journal of the American Chemical Society *126*, 8074, **2004**

6. J. Piris, M. G. Debije, N. Stutzmann, B. W. Laursen, W. Pisula, M. D. Watson, T. Bjørnholm, K. Müllen, J. M. Warman, *Aligned Thin Films of Discotic Hexabenzocoronenes: Anisotropy in the Optical and Charge Transport Properties,* Advanced Functional Materials *14*, 1053, **2004**

7. J. Piris, W. Pisula, J. M. Warman, *Anisotropy of the Optical Absorption and Photoconductivity of a Zone-Cast Film of a Discotic Hexabenzocoronene,* Synthetic Metals *147*, 85, **2004**

8. W. Pisula, A. Menon, M. Stepputat, I. Lieberwirth, U. Kolb, A. Tracz, H. Sirringhaus, T. Pakula, K. Müllen, *Highly ordered columnar zone-cast Hexa-peri-hexabenzocoronene surface layers and their applications in field-effect transistors,* Advanced Materials *17*, 684, **2005**

9. W. Pisula, Ž. Tomović, B. El Hamaoui, M. D. Watson, T. Pakula and K. Müllen, *Control of the homeotropic order of discotic hexa-peri-hexabenzocoronenes,* Advanced Functional Materials *15*, 893, **2005**

10. W. Pisula, Ž. Tomović, M. Stepputat, U. Kolb, T. Pakula, K. Müllen, *Uniaxial alignment of liquid crystalline discotics by solution processing,* Chemistry of Materials *17*, 2641, **2005**

11. M. Kastler, W. Pisula, D. Wasserfallen, T. Pakula, K. Müllen, *Influence of alkyl substituents on the solution aggregation of hexa-peri-hexabenzocoronene derivatives,* Journal of the American Chemical Society *127*, 4268, **2005**

12. D. Wasserfallen, I. Fischbach, N. Chebotareva, M. Kastler, W. Pisula, F. Jäckel, M. D. Watson, I. Schnell, J. P. Rabe, H. W. Spiess, K. Müllen, *Influence of Hydrogen-Bonds on the Supramolecular Order of Hexa-peri-hexabenzocoronene Derivatives,* Advanced Functional Materials, accepted, **2005**

13. W. Pisula, M. Kastler, D. Wasserfallen, M. Mondeshki, J. Piris, I. Schnell, J. M. Warman, T. Pakula, K. Müllen, *Investigation of the Structure-Morphology Relation and Charge Carrier Mobility of Dove-Tailed Hexa-peri-hexabenzocoronene Derivatives,* Journal of the American Chemical Society, to be submitted

14. W. Pisula, Ž. Tomović, C. Simpson, M. Kastler, T. Pakula, K. Müllen, *Relationship between Core Size, Side Chains Length and the Supramolecular Organization in Polycyclic Aromatic Hydrocarbons,* Chemistry of Materials, in press, **2005**

15. D. W. Breiby, O. Bunk, W. Pisula, T. I. Sølling, A. Tracz, M. M. Nielsen, T. Pakula, K. Müllen, *The Structure of Zone-cast Hexabenzocoronene,* Journal of the American Chemical Society, accepted, **2005**

16. D. W. Breiby, F. Hansteen, O. Bunk, W. Pisula, T. Pakula, M. M. Nielsen, *In-situ Studies of Phase Transitions in Discotic Thin Films,* Macromolecules, to be submitted

17. L. Gherghel, W. Pisula, U. Kolb, F. Bonino, K. Müllen, *Nanoporous carbon-based Materials obtained by Pyrolysis*, Advanced Materials, to be submitted

18. W. Pisula, M. Kastler, D. Wasserfallen, F. Nolde, C. Kohl, T. Pakula, K. Müllen, *Pronounced Supramolecular Order in Discotic Donor-Acceptor Mixtures,* Angewandte Chemie International Edition, submitted, **2005**

19. D. Wasserfallen, M. Kastler, W. Pisula, Y. Fogel, Z. Wang, K. Müllen, *Synthesis and Characterization of Distorted Polycyclic Aromatic Hydrocarbons,* Angewandte Chemie International Edition, to be submitted

20. J. M. Warman, J. Piris, W. Pisula, M. Kastler, D. Wasserfallen, K. Müllen, *Charge Recombination via Intercolumnar Electron Tunnelling through the Lipid-like Mantle of Discotic Hexabenzocoronenes*, Journal of the American Chemical Society, submitted, **2005**

21. W. Pisula, M. Kastler, D. Wasserfallen, T. Pakula, K. Müllen, *Homeotropic Alignment of All-Hydrocarbon Hexa-peri-hexabenzocoronenes,* in preparation

22. A. Menon, W. Pisula, A. Tracz, T. Pakula, K. Müllen, H. Sirringhaus, *Organic Field Effect Transistors based on zone-cast discotic semiconductors,* in preparation

23. W. Pisula, D. W. Breiby, A. Tracz, M. Stepputat, U. Kolb, M. M. Nielsen, T. Pakula, K. Müllen, *Zone-casting of Hexa-peri-hexabenzocoronenes,* in preparation

24. J. Wu, W. Pisula, K. Müllen, *Nano-sized Graphene Molecules as Materials for Electronics* (Review)*,* to be submitted

25. J. Li, M. Kastler, , J. Robertson., W. Pisula, D. Wasserfallen, A. Grimsdale, J. Wu, K. Müllen, S*olar Cells based on HBCs: Effect of Alkyl Substiutents,* in preparation

Oral conference contributions

1. W. Pisula, A. Tracz, T. Pakula, K. Müllen, *Long-Range Order of Polycyclic Aromatic Hydrocarbons,* NATO Macromolecules 2003, 6–10 October 2003, Tirrenia (Pisa), Italy

2. W. Pisula, Z. Tomowic, A. Tracz, M. Watson, T. Pakula, K. Müllen, *Supramolecular Arrangement of Discotic Mesogenes in Thin Film,* Materials Congress 2004, 30 March - 1 April 2004, London, UK

3. D. W. Breiby, W. Pisula, O. Bunk, T. I. Sollling, M. M. Nielsen, T. Pakula, K. Müllen, *Superstructures along self-assembled molecular wires,* 6th International Symposium on Functional pi-Electron Systems (Fpi6), 14-18 June 2004, Ithaca, NY

4. W. Pisula, T. Pakula, K. Müllen, *Columnar Self–Organized Liquid Crystal Semiconductors based on Discotic Hexabenzocoronenes,* Conference on new Concepts and Materials for Molecular Electronics and Nanotechnology (CMME '04), 11–15 September 2004, Poznan, Poland

5. W. Pisula, T. Pakula, K. Müllen, *Long-range Order of Columnar Discotic Systems,* Molecular Crystals 2004, 21–25 September 2004, Czestochowa, Poland

6. W. Pisula, T. Pakula, K. Müllen, *Supramolecular Structure and Processing of Organic Semiconductors based on Alkyl substituted Polycyclic Aromatic Hydrocarbons,* The 6th Minerva Student Symposium on Molecular Based Devices, 6-8 March 2005, Weizmann Institute of Science, Rehovot, Israel

7. W. Pisula, T. Pakula, K. Müllen, *Supramolecular organization of discotic liquid crystals,* 229th American Chemical Society National Meeting, 13-17 March 2005, San Diego, CA

8. W. Pisula, T. Pakula and K. Müllen, *Control of the Supramolecular Organization of Organic Semiconductors based on Polycyclic Aromatic Hydrocarbons for Device Fabrication*, International Conference on Organic Electronics (ICOE), 21-23 June 2005, the Conference Centre High Tech Campus, Eindhoven, The Netherlands

9. D.W. Breiby, J.W. Andreasen, M. Drews, M.M. Nielsen, F. Hansteen, O. Bunk, W. Pisula, T. Pakula, K. Müllen, Self-Organization in Discotics Studied by Grazing Incidence X-ray Diffraction and Ellipsometry, International Conference on Organic Electronics (ICOE), 21-23 June 2005, the Conference Centre High Tech Campus, Eindhoven, The Netherlands

Oral presentations at the DISCEL project meetings*:*

- Max-Planck-Institute for Polymer Research, Mainz, Germany, 21-22 March 2003
- Technical University of Lodz, Lodz, Poland, 27-28 August 2003
- Interfaculty Reactor Institute of the Delft University of Technology, Delft, the Netherlands, 12-13 January 2004

Oral presentations at the NAIMO project meetings:

– Clare College, Cambridge, UK, 4 – 6 April 2005

Poster contributions

1. W. Pisula, M. D. Watson, K. Müllen, T. Pakula, *Macroscopic orientation of columnar structures based on discotic liquid crystalline HBCs,* Molecular Crystals 2002, 17–21 September 2002, Warsaw, Poland

2. A.Tracz, W.Pisula, D.Wostek, J.K.Jeszka, M.Watson, K.Müllen, T.Pakula, *Preparation of different morphological and structural forms of hexa (alkyl)-hexa-peri-hexabenzocoronene,* 7th European Conference on Molecular Electronics (ECME 7), 10–14 September 2003, Avignon, France

3. W. Pisula, M. Kastler, D. Wasserfallen, T. Pakula, K. Müllen, *Processing Techniques for Macro- and Nano-Scale Columnar Alignment of Hexa-peri-Hexabenzocoronene Derivatives,* 7th International Conference on Nanostructured Materials, 20–24 June 2004, Wiesbaden, Germany

4. A. Tracz, J. K. Jeszka, T. Pakula, W. Pisula, C. Tang, T. Kowalewski, *Fabrication of Long-Range-Ordered Thin Organic Films by Solution Zone Casting*, Polymers (East), 19-24 June, 2005, Mount Holyoke College, South Hadley, MA